Scour investigation around a bridge pier founded in cohesive soil

Jana Zaidan

Normandie Université

THÈSE

Pour obtenir le diplôme de doctorat

Spécialité GENIE CIVIL

Préparée au sein de l'Université Le Havre Normandie

Scour investigation around a bridge pier founded in cohesive soil
Etude des phénomènes d'affouillement autour d'une pile de pont fondée sur un sol cohésif

Présentée et soutenue par
JANA ZAIDAN

Thèse soutenue publiquement le 14/12/2023
devant le jury composé de

MME CLAIRE CHASSAGNE	ASSOCIATE PROFFESSOR, TU DELFT	Rapporteure
M. DAMIEN PHAM VAN BANG	PROFESSEUR DES UNIVERSITÉS, UNIVERSITÉ DU QUÉBEC	Rapporteur
M. PHILIPPE GONDRET	PROFESSEUR DES UNIVERSITÉS, UNIVERSITÉ PARIS-SACLAY	Examinateur
M. VINCENT REY	PROFESSEUR DES UNIVERSITÉS, UNIVERSITÉ DE TOULON	Examinateur
M. CHRISTOPHE CHEVALIER	CHARGÉ DE RECHERCHE, IFSTTAR	Membre Invité
M. FRANÇOIS MARIN	PROFESSEUR DES UNIVERSITÉS, UNIVERSITÉ LE HAVRE NORMANDIE	Co-encadrant
M. ADRIEN POUPARDIN	CHARGÉ DE RECHERCHE, ESTP PARIS	Co-encadrant
M. ABDELKRIM BENNABI	CHARGÉ DE RECHERCHE, ESTP PARIS	Co-encadrant
M. AHMED BENAMAR	MAÎTRE DE CONFÉRENCES (HDR), UNIVERSITÉ LE HAVRE NORMANDIE	Directeur de thèse

Thèse dirigée par AHMED BENAMAR (Laboratoire Ondes et Milieux Complexes)

UNIVERSITÉ LE HAVRE NORMANDIE

591 ED PSIME

LOMC

Acknowledgements

Sincere gratitude to my supervisory team for their exceptional support and guidance throughout my research work. I am very grateful to my thesis director, Ahmed Benamar, and my supervisors François Marin, Adrien Poupardin, and Abdelkrim Bennabi. Your collective expertise has played a crucial role in shaping my research journey, helping me develop both academically and personally. I appreciate your permanent encouragement, your belief in me, and your kindness. You have always been there for me to discuss even the smallest details. I appreciate your valuable comments, which have significantly enhanced the quality of the work. I've greatly enjoyed working with you; it's been a pleasure!

Furthermore, I would like to express my gratitude to each member of the jury for reading my manuscript and accepting to evaluate my thesis work. I wish to thank Philippe Gondret for having accepted to be the president of the dissertation committee, Claire Chassagne and Damien Pham Van Bang, who agreed to judge this manuscript as rapporteurs. I also thank Vincent Rey and Christophe Chevalier, for having accepted to be part of the jury. I am sincerely thankful for your relevant questions after my presentation, and your insightful and constructive discussions.

I would like also to acknowledge the financial supporters of my PhD study: ESTP Fondation and Normandie Region. My thanks also go to R&D vision company for the Scilab code for refraction correction provided with the scanner and their training.

I also wish to thank Mitia, Hugo and Eder for their hard work during their interships. Their results have been useful to my work, and its supervisions have been a particularly rewarding experiences.

I would like to express my sincere thanks to my colleagues at ESTP (Fréderic, Claire, Lamisse, Shadi, Abdelatif, Om Kathoum, Othman, Maroua, Jean Bruce, Baba Hassan..), and at LOMC laboratory (Mohammed, Youssef, Moustafa, Hanan, Anaïs, Juliette, Hussein, Joseph, Richard, Ahmad ..) and my friends at GREAH laboratory (Ye, Joyce, Hoda, Batoul, Hussein, Gloria ..)

for the time we spent together, the exchanges and the unforgettable moments. Special thank to my neighbors and my friends outside the thesis framework (in particular Maryam and Souad) for the motivation you gave me.

I cannot close this page without expressing my deepest appreciation to my wonderful family. Dear parents, my dear mother, Sonia and my dear father, Abdel Nasser, thank you for supporting me throughout my studies, for always supporting my choices and encouraging me, for your immeasurable loves and sacrifices. I thank also my brother, Abdallah and my sisters, Hanine and Farah, who have always given me all kinds of support. A tender thought to my niece, Loujayn and my nephew, Yazan who embellished my life by their innocence. I also wish to thank my uncles, aunts and cousins. In particular, a big thank to my uncle, Fadi and my cousin, Wadad. To ensure that no one is overlooked, I would like to extend my gratitude to all those who have contributed in any way to my achievement.

Finally, I dedicate my achievement in the thesis to my dear husband, my second half, Abdullah, who was always present despite the geographical distance that separated us. I would like to say thank you for your patience, your helps, your love and your sacrifices.

Contents

Nomenclature

α_s Side slope of the scour hole

γ_s Specific weight of sediment ($M^1L^{-2}T^{-2}$)

γ_w Specific weight of water ($M^1L^{-2}T^{-2}$)

Φ_* Dimensionless angle of repose ($M^0L^0T^0$)

Φ_c Angle of repose or internal friction for cohesive sediment

Φ_s Angle of repose or internal friction for sand

ρ_{dop} Dry optimum Proctor unit density ($M^1L^{-3}T^0$)

ρ_d Dry unit density ($M^1L^{-3}T^0$)

τ_{cr} Critical shear stress at the incipient condition ($M^1L^{-1}T^{-2}$)

B Width of the scour hole ($M^0L^1T^0$)

b Diameter of the pier ($M^0L^1T^0$)

C_* Dimensionless Cohesion ($M^0L^0T^0$)

C_u Cohesion at optimum moisture content ($M^1L^{-1}T^{-2}$)

$Comp.$ Percentage of soil Compaction

d_{50} Arithmetic mean size of sediment ($M^0L^1T^0$)

Fr Froude number based on the water depth ($M^0L^0T^0$)

$Fr_{(pier)}$ Pier Froude number based on the pier diameter ($M^0L^0T^0$)

h Flow depth ($M^0L^1T^0$)

IWC Initial Water Content

IWC_* Initial moisture content required to saturate the soil sample
For plastic soil: IWc_*= soil liquid limit

P_c Cohesive soil content in a soil mixture

PI Plasticity Index

Re_b Number of Reynolds based on the diameter of the pier ($M^0L^0T^0$)

t Time ($M^0L^0T^1$)

$t*$ Dimensionless time ($M^0L^0T^0$)

UCS Unconfined Compressive Strength of cohesive soils ($M^1L^{-1}T^{-2}$)

$UCS*$ Dimensionless Unconfined Compressive Strength of cohesive soils ($M^0L^0T^0$)

V Approach velocity ($M^0L^1T^{-1}$)

$V_{cr(sand)}$ Critical velocity at the incipient condition for the sand used in the soil mixture ($M^0L^1T^{-1}$)

V_{cr} Critical velocity at the incipient condition ($M^0L^1T^{-1}$)

VS Vane shear strength ($M^1L^{-1}T^{-2}$)

$Z_{cs(side)}$ Equilibrium maximum scour depth around the pier founded at the side region in cohesive sediment ($M^0L^1T^0$)

$Z_{cs(wake)}$ Equilibrium maximum scour depth around the pier founded at the wake region in cohesive sediment ($M^0L^1T^0$)

Z_{cs} Equilibrium maximum scour depth around the pier founded in cohesive sediment ($M^0L^1T^0$)

Z_s Equilibrium maximum scour depth around the pier founded in cohesionless sediment ($M^0L^1T^0$)

The list above provides the nomenclature of symbols used in table I.2

General Introduction

BACKGROUND AND MOTIVATION

Bridges are essential connections, linking communities and enabling the efficient movement of goods and people. They are the reliable support of our modern infrastructure, allowing us to cross rivers, valleys, and landscapes with ease. Despite their indispensability, bridges faced with a threat known as "bridge scour".
The bridge scour refers to the erosive process in which sediment is removed from the bed and banks of a waterway or a river, particularly around bridge piers and abutments. This phenomenon is a consequence of the dynamic interaction between flowing water and the sediment bed. Over time, scour can deepen the riverbed, exposing bridge foundations, and destabilizing these transportation structures, leading to its failure. The destruction of a bridge causes significant material damages and economic losses.

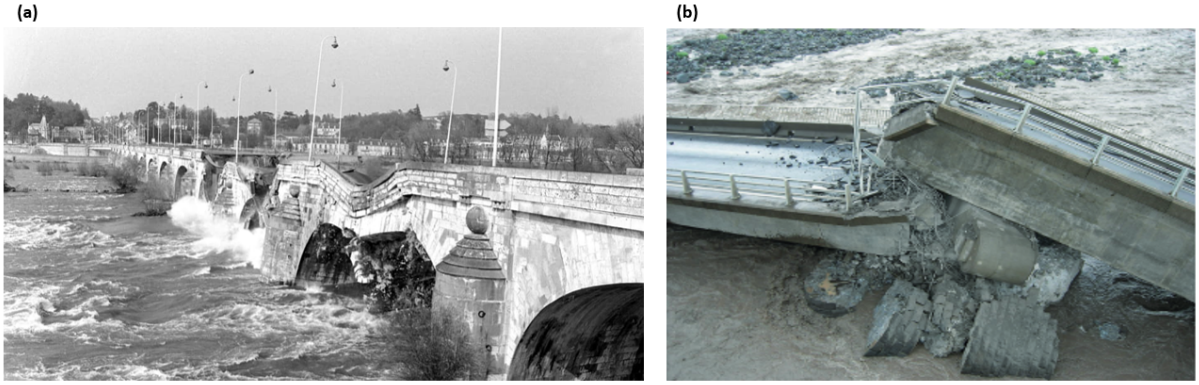

Figure 1: Examples of French bridge collapse due to scour : (a): Wilson bridge in Tours (1978) [200], (b): the bridge over the Saint-Étienne river on Reunion Island (2007) [62]

Bridge scour is considered as the primary risk of bridge collapse in the United States. Shirole and Holt. 1991 [232] found that 60% of bridge failures in the United States between 1989 and 2000 are due to scour. The annual cost for repairing flood damage to highways by the federal

support system averages $50 million [144]. An example of a bridge collapse in the United States due to pier scour is the bridge over Schoharie Creek in the state of New York in 1987, where 10 people died [131]. There are approximately 20,000 bridges classified as "scour critical" and an additional same number of bridges as "scour susceptible" [101]. In France, where there are around 8,000 river crossings integrated into the national rail network, 1,700 of them are susceptible to scour issues [149]. The risks are even higher for the national road system [149]. Noteworthy scour-related bridge failures in France include the collapses of the Wilson Bridge in Tours in 1978 (Figure 1 (a)), the St. Louis Bridge on Reunion Island in 2007 (Figure 1 (b)), and, more recently, the Coarraze railway embankment failure on the Gave de Pau River in 2013 [71]. These events motivated in France the funding of studies on the scour around bridge foundations, opening new line of research. This work constitutes the first PhD research on the *pier scour project* carried out at the ESTP (Ecole Spéciale des Travaux Publics) and Le Havre university. It is co-financed by the ESTP foundation and the Normandy region.

OBJECTIVES

The main objectives of this research can be summarized as follows:

1. **Instrumentation Development:** The study addresses the lack of robust and standard instrumentation for monitoring local scour around bridge piers in laboratory settings. It aims to develop a method based on the use of a 3D Laser Scanner for monitoring the temporal evolution of scour.

2. **Scour investigations in cohesive bed:** While extensive research exist for bridge piers scour in cohesionless soils, limited literature exist in the case of cohesive beds. This study expand the understanding of the dynamics of local scour process by investigating its occurrence around circular piers founded in a cohesive bed, with particular emphasis on the influence of increasing clay/silt ratio.

3. **Scour Depth Prediction:** Prediction methods for scour depth used in engineering design are conservative and not adjusted to cohesive soils, affecting construction costs. Cohesive soils can erode at a rate that is up to 1000 times slower than cohesionless soils [48, 56]. To optimize the design bridge, the time should be taken into consideration while estimating the scour depth in a cohesive bed. This study evaluates the predictive methods proposed for cohesive beds (mainly SRICOS-EFA method) to accurately predict the maximum scour depth.

ORGANIZATION OF THE THESIS

The manuscript of the thesis comprises four chapters, with a "General Introduction" and a "General Conclusion and Perspectives". The details of the chapters and the "General Conclusion and Perspectives" are as follows:

- Chapter I provides an overview of the current state of the art related to the phenomenon of pier scour. First, it covers the basic concepts of scour and the flow patterns around a vertical emerged circular pier. Next, it examines the existing techniques for monitoring local pier scour in laboratory settings. The chapter also discusses earlier researches on pier scour in both cohesionless and cohesive bed conditions. In addition, it documents the available methods for predicting the maximum scour depth, including the SRICOS-EFA method. Remarkably, there is a noticeable less number of studies addressing pier scour on cohesive beds compared to cohesionless beds. This scarcity, underscores the contribution and novelty of the research presented in this thesis.

- Chapter II devotes to the experimental set-ups, featuring the physical model of pier scour implemented in the hydraulic flume that facilitated our tests. It describes all the measurement instruments employed during the work, for measuring the sediment and flow characteristics and monitoring the sediment bed deformation during the scour process. Furthermore, it outlines the experimental protocol of the pier scour test developed during the thesis. It details the characteristics of the flow and the materials used during the work. This chapter also presents the chosen experimental conditions and the various measurements conducted.

- Chapter III dedicates to the assessment of the validity of a 3D Laser Scanner Technique for continuous monitoring of local scour around a pier. The chapter provides a detailed presentation of the proposed data processing methodology, including the used software. Following this, the chapter presents the results of preliminary flume tests on local scour, conducted by using medium sand in clear water, which serves as a benchmark test. The repeatability of these tests is also examined. Finally, the chapter explores the influence of the glass plate placed on the water surface during the pier scour measurement and the water evacuation on the topography of the scouring hole.

- Chapter IV documents the experimental investigation of pier scour on cohesive beds. It focuses on the temporal evolution of local scour hole shape around the pier with increasing the clay/silt ratio content. It presents the erosive properties of the investigated tested soils. This chapter explores the dynamic propagation of the scour process, the scour patterns,

profiles, scour hole horizontal plane dimensions and volumes. The study also compares the deepest scour depth measured to the predicted one by available empirical relationships (including the SRICOS-EFA method).

- "General Conclusion and Perspectives" summarizes the main conclusions by emphasizing the key findings. It gives also suggestions for future research in this topic.

Chapter I :

State of art

INTRODUCTION

This chapter aims to review the basic concepts of scouring, flow pattern around a circular pier, instrumentation used for pier scour monitoring mainly in laboratory, the impact of ice cover on pier scour, studies on pier scour founded in cohesionless and cohesive sediments as well as empirical methods for estimating the maximum scour depth. Finally, a discussion of the literature results presents the knowledge available to date in relation to the present PhD work, in order to clarify the objectives of this thesis.

I.1 BACKGROUND ON SCOURING

I.1.1 *Definition of scour*

Scour refers to the process of erosion or removal of sediment material from the surface of a bed, such as a riverbed, streambed, or coastal area. It can result in the deepening or widening of channels, the formation of depressions, and changes in the landscape or underwater features. Scour can have significant impacts on the stability of infrastructure, such as bridges, and is an important consideration in engineering.

I.1.2 *Type of scour*

According to Wang 2004 [258], in the vicinity of a bridge support, different scouring processes sometimes overlap.
Figure I.1 shows the different types of scour identified:

- *Generalized scour*: This type corresponds to an overall decrease in the elevation of a stream bed. It results from a change in the flow regime caused by natural phenomena (flooding, climate change) or human activity (construction of a dam or reservoir). The degradation of the sedimentary bottom can occur rapidly (short term) or gradually over a period of several years (long term) [70]. This phenomenon is independent of the presence of a structure.

- *Contraction scour*: This type concerns the erosion of the area where there is a narrowing of the stream width, either natural or due to the presence of a structure. As the watercourse narrows, the flow velocity increases, resulting in a stronger erosive force. This causes the sediment in the contraction zone to be carried away, leading to a localized lowering of the riverbed.

- *Local scour*: This type deals with the erosion in the immediate vicinity of an obstacle (abutments or piers) in the flow. It results from the interaction between the fluid, the sediments and the structure. Since pier local scour is a key focus of this study, it will be discussed in more detail in the following sections.

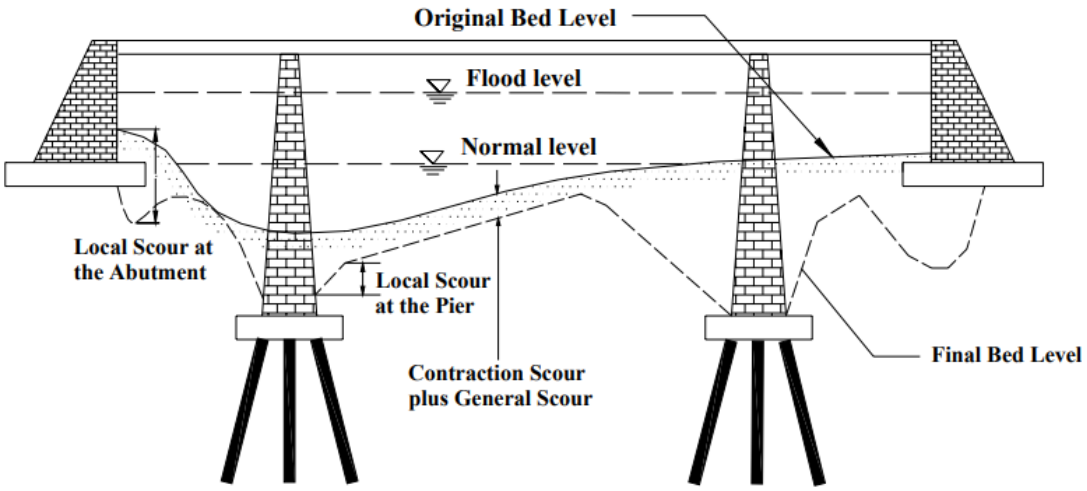

Figure I.1: Sketch of the various types of scour in a bridge cross-section; Wang 2004 [258]

It was be noted that the total scour depth at the pier is only equal to the sum of the pier scour depth and the contraction scour depth, but the total scour depth at the abutment is equal to the abutment scour depth (Figure I.1).

I.1.3 *Regime of pier scour*

Two distinct regimes of pier local scour have been defined, *Clear water scour* and *Live bed scour* [63, 97, 167], whether the bed sediment transport occurs usptream of the pier. This can be determined depending on the ratio of approaching water flow velocity (V) to the critical flow velocity that initiate the sediment motions (V_{cr}) (Figure I.2 (a)).

- Clear water scour: If, $V/V_{cr} \leq 1$, erosion is limited to the immediate vicinity of the obstacle, while sediments located further away from the obstacle remain undisturbed.
- Live bed scour : If $V/V_{cr} \succ 1$, erosion occurs throughout the entire bed and intensified near the obstacle. There is a continuous supply of sediment from upstream to downstream in the form of bed load.

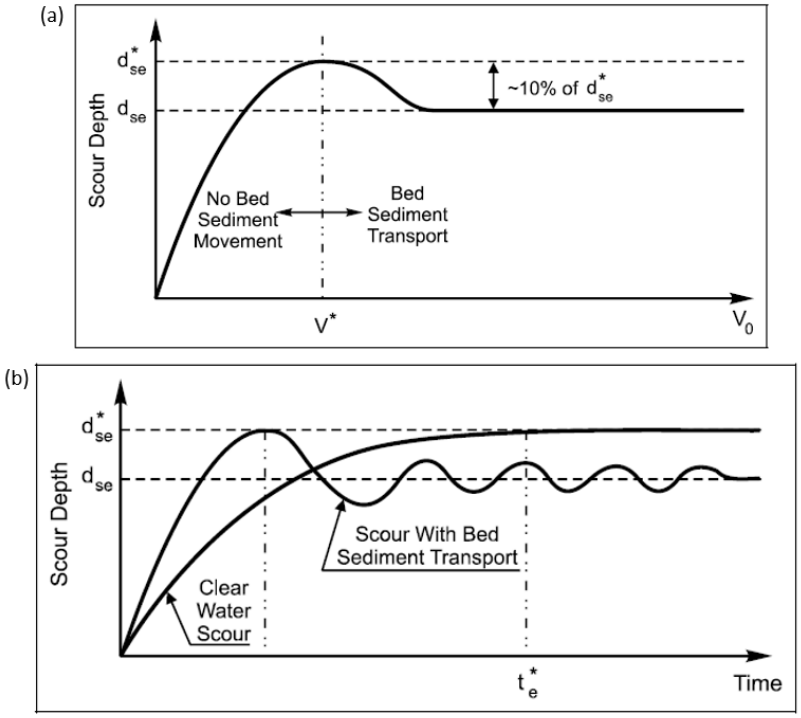

Figure I.2: Scour depth function (a) of flow velocity and (b) of time in sand bed; V* refers to the critical velocity Vcr, Vo is the flow velocity, dse and dse* corresponds to the equilibrium scour depth in live bed regime and clear water regime respectively; Ettema et al. 2006 [97]

The scouring regime has a direct influence on the scouring depth and the time required to reach it, as shown in Figure I.2 (b). In clear water scour, scour depth increases initially slowly till reaching an equilibrium value dse* (equilibrium scour depth). In contrast, for live bed scour, the maximum scour depth initially increases rapidly, then fluctuates around an equilibrium value dse,

which is due to the interaction between sediments supplied from upstream and those removed by erosion in the scour hole [35]. The amplitude of the fluctuation is less than half of the height of the bed form [225]. This dse value (for live bed regime) is 10% lower than the dse* value (for clear water regime) [14, 97] (Figure I.2 (a)). For non-uniform sediment, [169] identified an armor velocity Va instead of Vc, which is larger than Vc, for the transition from clear water scour to live bed scour. In cohesive bed, clear water scour is always occurring because once particles are eroded, they remain in suspension [97, 173].

The scouring mechanism in clear water scour was decomposed into three steps [78, 94, 183]. An initial stage, characterized by a rapid scouring rate, a development stage and finally a stage corresponding to the equilibrium state. Several researchers (e.g. [181, 209]) have conducted their experiments within a limited time frame because achieving equilibrium scour can be a time-consuming process. [167, 171, 230] stated that equilibrium state was attained when the scour depth increases by no more than 5% of the pier diameter (D) within a 24-hour period. The experiment was stopped when the scour depth remained below 1 mm for a continuous period of 3 hours by [137] and 4 hours by [94]. [157] stopped the experiment when scour rate was less than the median diameter d50 of tested sand per hour. [33, 125] reported that a scouring period of 2 hours was found to be sufficient for reaching the equilibrium state. Conversely, [5] observed that data collected over a shorter duration, such as 10 hours, could underestimate the scour depth by up to 50% compared to the equilibrium scour depth. Nevertheless, many researchers [61, 146, 192, 233] believed that equilibrium should be determined on the basis of fitted curves.

I.2 FLOW FIELDS AROUND A VERTICAL CIRCULAR PIER

The presence of an obstacle disturbs the current streamlines and results in an entirely three-dimensional flow. Figure I.3 shows the case of a emmerged vertical circular pier, which is characterized by the following main flow patterns: *Down flow* at the front of the pier, *surface roller* ahead of the pier, *horseshoe vortex* system at the upstream of the pier, and *wake vortex* shedding downstream of the pier.

When the flow interacts with the pier, it creates a pressure gradient [113]. Unger and Hager. 2007 [253] observed a stagnant point on the upstream face of the cylinder dividing the water flow into two parts: one ascending and the other descending. Guo. 2012 [113] observed that the stagnation point was at 10% of the flow depth from the bottom. The descending flow acts as a vertical jet on the sedimentary bed, causing the formation of a new stagnant point, which is the origin of a weak micro horseshoe vortex that initiates erosion at the base of the cylinder

[253]. On the other hand, at the free water surface, a continuous presence of surface roller with a rotational sense opposite to the primary horseshoe vortices is created [253].

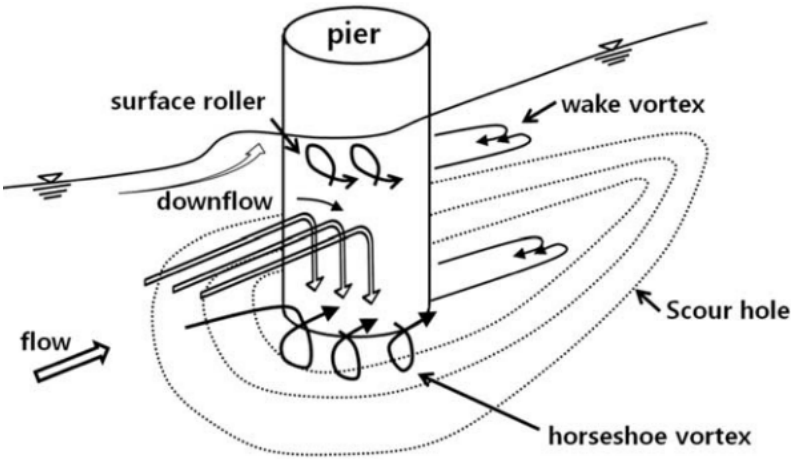

Figure I.3: Schematic sketch of flow patterns around a vertical emmerged circular pier; Choi and Choi 2016 [72]

The formation of the horseshoe vortex system is due to the separation of the incoming boundary layer induced by adverse pressure gradients. The system appears as a collection of U-shaped necklace vortices (Figure I.4) [88, 129, 272]. Dargahi. 1989 [77] studied the vortical patterns surrounding a circular cylinder with a flat bottom. The number of vortices in front of the cylinder was discovered to be dependent on the cylinder Reynolds number, $Reb = Vb/\nu$, where V is the flow velocity, b is the pier diameter and ν is the kinematic viscosity of the water.

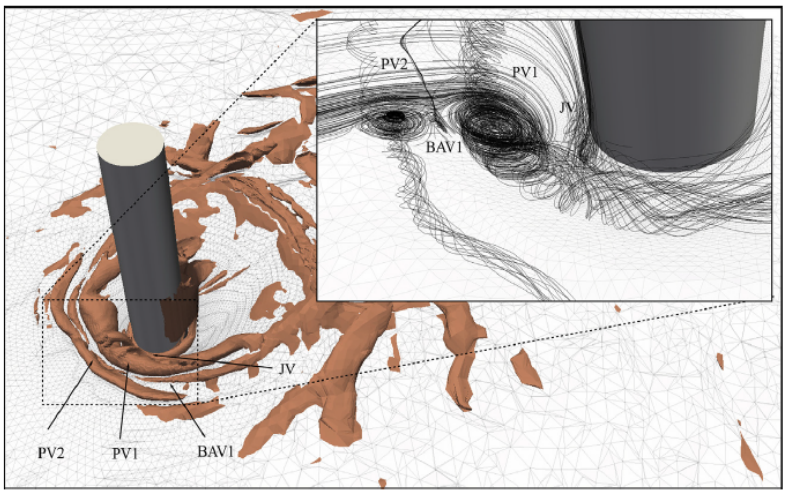

Figure I.4: Numerical simulation showing necklace vortices inside the scour hole for live bed scour regime (Re_b=46000); JV: Joint Vortex, PV: Primary Vortex, BAV: Bottom-Attached Vortex, SV: Secondary Vortex; Zhang et al. 2020 [272]

The flow in the vicinity of the cylinder accelerates at the sides and detaches downstream. This results in the formation of periodic vertical-axis vortices, widely recognized since the early 20th century, known as Bénard Von Kàrmàn vortices [22, 23, 255]. The classification of [105] gave the different wake regimes depending on the pier Reynolds number (*Reb*) (Figure I.5). The frequency of emission (or detachment) of these vortices (f) was characterized by the Strouhal number ($St = fb/V$) [240]. Based on several experiments in different regimes, the Strouhal number St was related to the pier Reynolds number Reb [93].

Studies of the flow around a cylinder were carried out within scour hole at the equilibrium state, e.g. [79, 88, 110, 129] and others in a scour hole during its development, e.g. [18, 78, 111, 178, 272]. Some of them were experimental [88, 111, 129, 178] while others were numerical [18, 129, 272]. Kirkil et al. 2008 [129] identified bimodal chaotic oscillations inside the HV (horseshoe vortex) systems and uplift events and strong ejection in the wake region of a cylinder. Dey and Raikar. 2007 [88] observed an increase in the horseshoe vortex with an increase in the scour, and a decrease in the circulation zone of the vortex with an increase in the azimuthal angle relative to its origin being in the flow direction. In their experiments the maximum downflow in the scour hole do not exceed 0.6 times the approach flow velocity. Dargahi. 1990 [78] and Niedoroda and Dalton. 1982 [183] noted that the scouring mechanism was mainly due to the horseshoe vortex. Baykal et al. 2015 [18] observed that the effect of wake vortex shedding were only present during the very early stages of the scouring process. Figure I.6 provides a schematic sketch of clear water scour hole developed by the system of horseshoe vortex [78]. The sediment was mainly eroded by the primary vortices (V2, V4). The position of vortex V1 is almost constant over time, whereas vortices V2, V3, V4, and V5 oscillate back and forth in the horizontal plane of symmetry. As a result, the erosion holes and deposition zones vary spatially over the time. The V1 and V2 vortices then merge (Figures I.6 f and g). The depressions beneath vortices V2 and V4 form two tiny slopes (Figure I.6 h) and the system tends to a single erosion hole with two different slopes of comparable length as time passes (Figure I.6 k). Zhang et al. 2020 [272] simulated the evolution of the horseshoe vortex HV system and the wake vortex in live bed regime. They observed that at the initial stage the HV structure is unstable, then grows in size as the scour hole forms, but loses strength until it reaches a state of equilibrium and becomes more stable. Some authors have observed experimentally [15, 38, 220] and numerically [198, 272], the existence of a secondary vortex with a horizontal-axis in the wake zone. Ahmed and Rajaratnam. 1998 [4] observed the impact of the bed roughness with and without scour hole. Their findings showed that the down flow and the shear stress at the cylinder base increased with the bed roughness and the scour depth.

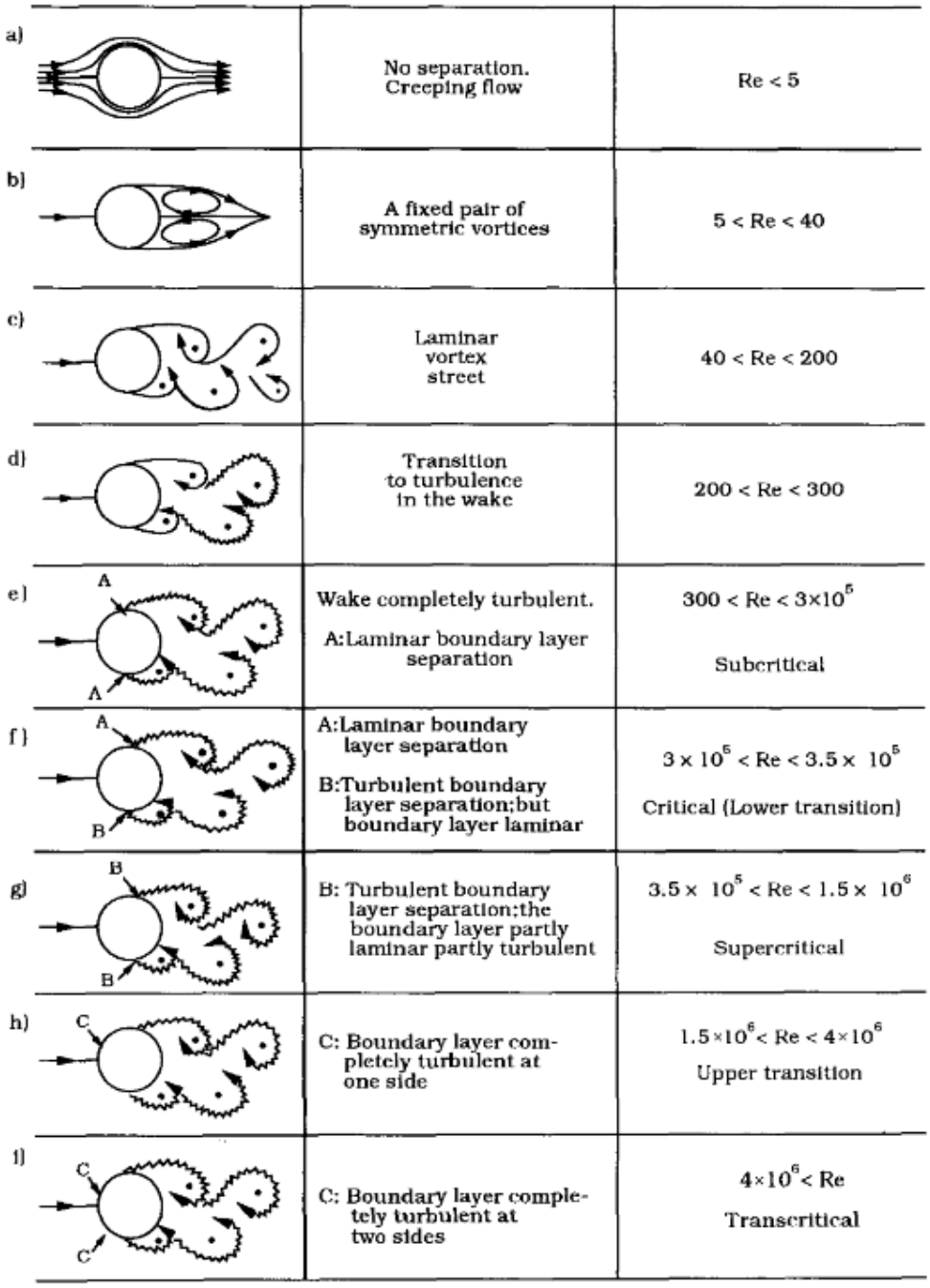

Figure I.5: Classification of the wake regime around a cylinder depending on the pier Reynolds number; Sumer and Fredsoe 2006 [105]

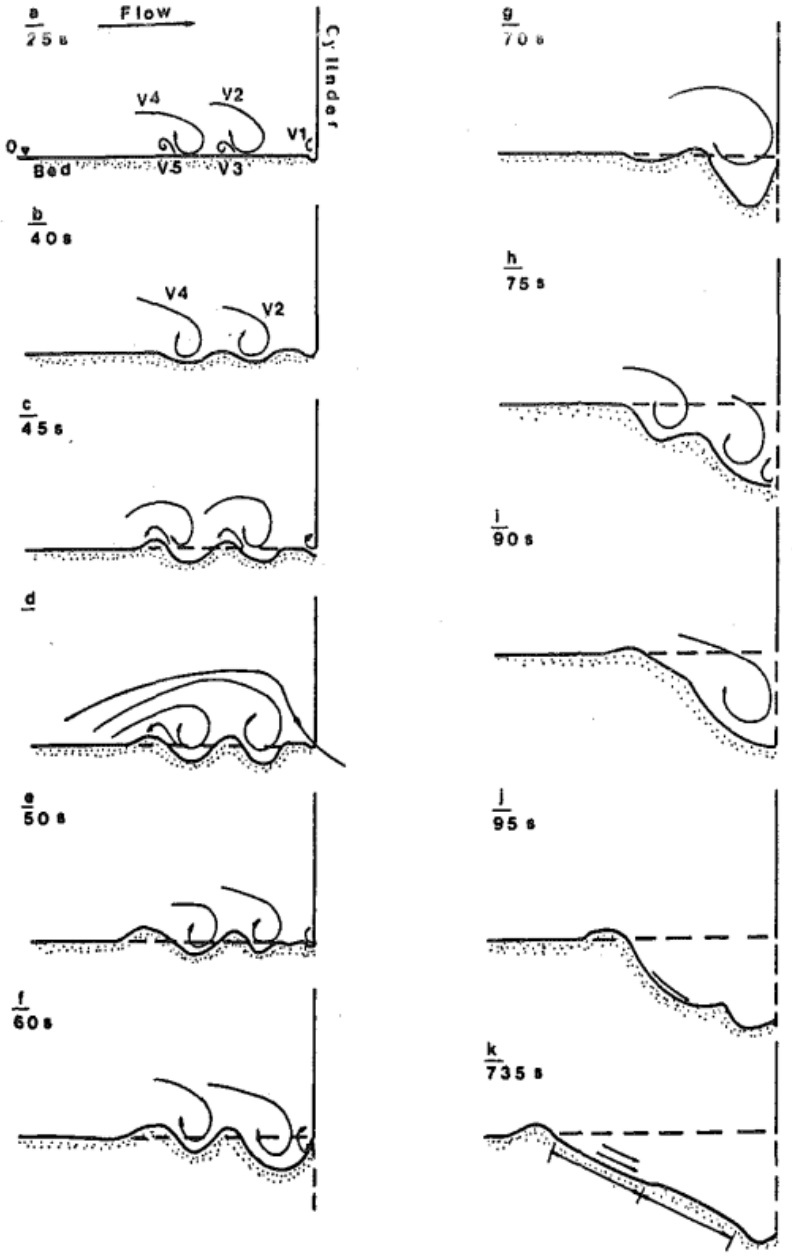

Figure I.6: Schematic sketch of clear-water scour hole formed by the horseshoe vortex (Re_b=39000); Dargaghi et al. 1990 [78]

If the circular pier was immersed in water, the flow pattern was different [126, 134, 194, 197, 245, 246]. At the free end of the obstacle, the development of boundary layers lead to the formation of small-sized vortices known as *tip vortex*. Another, observed modification was the absence of alternating shedding of von Kármán vortices and the presence of an *arched vortex* structure behind the obstacle.

I.3 LABORATORY TECHNIQUES FOR PIER SCOUR MEASUREMENT

In the last two decades, significant progress has been made in the research of bridge scour in the laboratory in order to better understand the physical mechanisms and to investigate under controlled conditions the impact of different factors on the scour development. In addition, it enables formulas for estimating scour depth to be developed or evaluated, and methods for scour mitigation to be developed. To effectively monitor the pier scour during laboratory tests, it is crucial to employ an appropriate measurement technique. Consequently, the literature reports the use of a wide variety of instruments for this purpose. We will present some of them, highlighting their benefits and drawbacks.

The simplest approach for studying the development of a scour hole was the use of gauges [99, 136, 147, 191]; or scales attached or marked on pier models [64, 80, 98, 162, 171, 203, 266]. The later can be monitored visually or by cameras set-up that were placed inside transparent pier models. The scour depth was measured using micro-cameras under clear water scour by [64] and using endoscopic camera under live bed conditions by [98] through an image processing technique. In [65–67, 80, 82] studies on soil mixtures containing clay, the authors used a camera connected to a computer mounted on a carriage unit having vertical and rotational degrees of freedom to record the time variation of scour depth with respect to the position of the attached scales (Figure I.7 (a) and (b)). After siphoning off the water, they further used a point gauge with a graduated traverse arrangement in the three coordinate directions to acquire the precise geometry of the scour hole at equilibrium (scour depth, lateral extension, and longitudinal extension).

The acoustic signal detection technology was based on identifying the interface between the water and the bed. A dense array of fixed ultrasonic sensors which allowed simultaneous and continuous measurements [37, 76, 165, 205] and a strip of ultrasonic sensors mounted on an automated trolley that moves at a constant speed on a rail [16, 68, 193] (Figure I.7 (c)), were widely used to measure the bed geometry around a pier. The latter method does not ensure a proper synchronization of the measures particularly in the early stage when the rate of erosion was quite high. Consequently, measurements were done only at the end of the test, considered as the equilibrium state by [16]. Another acoustic technique was based on the use of echo sounders (sonar) [52, 101, 203, 216, 229, 230]. Sheppard. 2003 (a), (b) [226, 227] used an acoustic transducer and two video cameras in order to obtain the 3D data of the scour hole in clear water and in live bed regime for a large-scale experiments in sand bed (Figure I.7 (d)). All the acoustic

measurement techniques should be submerged in the water which could cause disturbances in the flow field, and then alter the natural behavior of the phenomenon.

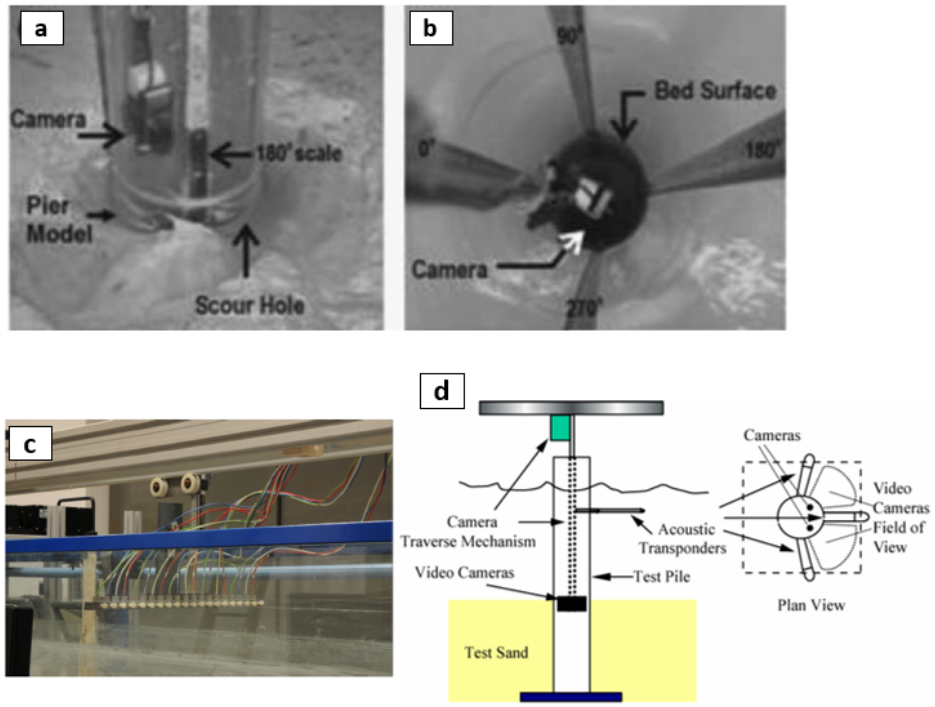

Figure I.7: Experimental technique for pier scour measurement (a) Side view, (b) Top view of a camera inside a pier with attached scale; Chaudhari et al. 2013 [65]; (c): strip of ultasonic sensors; Auzerais 2017 [15], (d): diagram of local scour measuring (Acoustic Transponders and video cameras); Sheppard 2003 (a),(b) [226, 227]

There are several efforts employed in the application of photogrammetry in a variety of set-ups to monitor the evolution of pier scour bed topography [17, 31, 203, 243, 252]. The concept of this approach involves identifying the precise location of any point detectable by analyzing two images captured by one or more cameras at different positions. The method reported in [203, 252] required the flow to be stopped and the model to be drained during photo acquisition. This method can become quite laborious and time-consuming if the bed is measured at multiple instances. Additionally, this water interruption may cause disruptions that affect the erosional processes. Also, measuring the bed elevation intermittently assumes that the behavior of the bed during the intervening periods can be estimated through interpolation. However, this assumption may not always be accurate, as the rate of scour may vary over time and at different locations. Summer et al. 2013 [243] and Baglio et al. 2001 [17] have used a common stereovision approach with a laser or a light projector to create a grid with dot nodes on the surface of the bed (Figure I.8 (a)). The dots are the target points where the temporal erosion evolution was tracked. According to [103], utilizing a grid lens on a sand surface was not appropriate and could lead to a reduction

of accuracy. Furthermore, results from [17] were less accurate since they didn't take into account lens distortions and light refraction via air, glass, and water interfaces. Summer et al. 2013 [243] did account for lens aberrations but still did not replicate refraction through the flume wall properly. Bouratsis et al. 2013 [31] introduced a stereo vision technique for the three-dimensional characterization of the bed morphology continuously and at high resolution. The method is based on the use of two calibrated and partially submerged cameras that capture the sediment bed changes over time. This approach takes into account the sediment bed texture and eliminates the need for targets or structured light. To ensure accurate surface reconstruction, a series of computer-vision and image-processing algorithms were developed. The effectiveness of this technique was also demonstrated in [32] study, where it was used to quantify the spatio-temporal characterization of the scouring at the base of a circular pier.

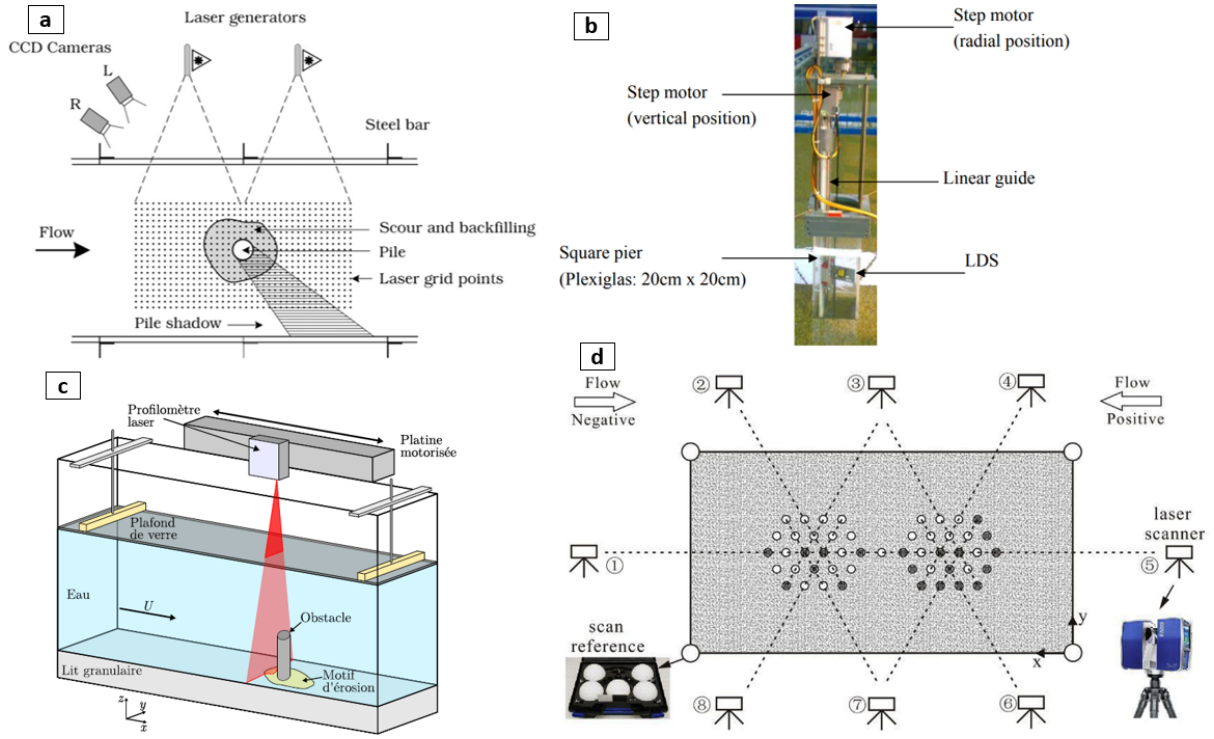

Figure I.8: Experimental techniques for pier scour measurement (a) Stereo-vision measuring scheme adopted by Summer et al. 2013 [243]; (b): Laser Distance Sensor (LDS) system for square pier; Diab 2011 [90]; (c): Profilometer Laser Technique scheme adopted by LaChaussée 2018 [142] ; (d): Laser scanner scheme adopted by Ma et al. 2018 [162]

Link et al. 2008 [157] used a Laser Distance Sensor (LDS), placed inside a plexiglass pier founded in sand, to measure scour hole radius at different depths (Figure I.8 (b)). The device was oriented horizontally in radial direction to avoid refraction caused by the cylinder wall during measurement. The sensor was driven in the vertical and azimuthal directions by a stepper-motor with an accuracy of $\pm 1/50$ mm and $\pm 1/100^{\circ}$ respectively. This allows the distance sensor to

turn around in the scour hole and take various vertical profiles in different azimuthal half-planes. In this way, the scour hole geometry beneath the initial flatbed is automatically measured, with an accuracy of ± 0.4 mm. This LDS worked well in live bed condition with a flow intensity (V/Vc) of 2. The flow intensity is defined as the ratio between the flow velocity (V) and the velocity of incipient motion (Vc). Measurements in gravel by [89] and sand-clay mixture by [156] were conducted using the same methodology. However, it was expected that the accuracy of LDS measurements was affected by high turbidity or suspended fine sediment, which may limit its usefulness under certain supercritical flow conditions.

An et al. 2017 [9] used a Contact Image Sensor (CIS), an optical sensor that detects the temporal evolution of the interface between water and sand by measuring the difference in the reflectivity of the light from the two different media. The CIS should be buried in the bed and make only punctual measurements at distinct points in space. The CIS, which had a spatial resolution of 0.086 mm, did not need to be calibrated for every test. It was founded that the sensor was not sensitive to water temperature in the range of 2-30°C. However, a concentration of suspended sediment higher than 40 kg/m^3 affected the accuracy of sensor readings. Since the CIS camera was not resistant to ambient light, it was reported that the entire test region should be completely covered with opaque polystyrene sheets. The sensor was found to successfully measure the local scour development around a vertical pier in laboratory under steady current covering three regimes of scour (clear water scour, rippled bed scour, and scour in sheet flow conditions) and under tidal current condition.

Scour experiments conducted by [142, 143, 202, 217, 248] were recorded using a laser with receiver, such as a camera. Poggi and Kurdyavtseva. 2019 [202] conducted continuous measurements of the scour pit depth over time. However, their data was limited to 2D information and did not capture the entire formation process of the scour pit. Lachaussée et al. 2018 [143] used a profilometer laser technique consisting of a laser sheet and a receptor cell which was mounted on a carriage translation plate (Figure I.8 (c)). A horizontal glass plate was placed on the water surface to minimize signal noise caused by fluctuations. The laser sheet was emitted perpendicularly to the bed surface. A systematic corrective factor of 1.3 to the measured elevation values was used to compensate refraction error [141]. This monitoring technology allowed for the automatic tracking of erosion development without the need to interrupt flow. Limitations included an unresolved blind zone in the vicinity of the obstacle that prevents access to erosion topography in that region. This technique was applied in similar laboratory studies, including continuous evolving breach geometries of non-cohesive fluvial dikes by [214], morphology changes bed resulting from tur-

bulent wall jets with a planar configuration by [269] and sand waves that were migrating by [121].

Kinect device is composed of three main components: an infrared projector, an infrared camera, and a digital camera [73]. The infrared projector emits a speckle pattern which is then reflected on the surface of the object being scanned. The infrared camera captures the pattern and sends the information to a computer for processing. The digital camera provides color information that can be superimposed onto the 3D image generated by the system. Chourasiya et al. 2017 [73] conducted research on the use of the Kinect sensor for the purpose of measuring 3-D bed profiles in a continuous manner. The study found that the method was non-intrusive, and a viable option for continuous 3-D bed profiling without the need for expensive cameras or complex image analysis. However, the method is limited by the fact that it can operate over small areas ($\leq$ 100 cm x 75 cm) and is susceptible to errors caused by rough water surfaces, high turbidity, illuminance, and reflections from the target surface. Bento et al. 2022 [26] reported that Kinect sensor was shown to be just as accurate as close-range photogrammetry while being simpler, faster, and cheaper for studying pier scour topography.

Nagarajan and Arockiasamy. 2020 (a), (b) [179, 180], and Raju et al. 2022 [207] tested the feasibility of a terrestrial scanner green laser in a pool with pier and fabricated scour hole, under water and in static conditions. Kaolinite powder was added progressively to the water, resulting in turbidity levels ranging from 1.2 to 20.8 NTU (Nephelometric Turbidity Units). The findings indicated that the bed topography were clearly visible at turbidity levels below 6.4 NTU. However, at higher turbidity levels, the bed topography remained invisible even with a reduced water depth. The most well-known advantage and disadvantage reported by various authors related to the use of the laser scanner [27, 162, 234, 254, 264] was the high level of accuracy and the requirement of the water drainage prior measurement respectively. Ma et al. 2018 [162], Sirianni et al. 2022 [234] and Valela et al. 2021 [254] used laser scanner at different stations. The scans were then combined using reference coordinates from fixed markers that could be seen in all scans to produce the 3D point cloud model (Figure I.8 (d)). Xing et al. 2021 [161] used an underwater laser 3D scanner to measure the scour bed morphology around a monopier. The presence of the scanner in the water may affect significantly the scour process.

I.4 EFFECT OF ICE COVER ON PIER SCOUR

In our tests, in the vicinity of the pier, the flow is influenced by surface waves that diffracted the laser scanner beams. To mitigate this phenomenon, a plexiglass plate is required to be used on the water surface during measurements (see in chapter II, Figure II.18). The presence of this plate simulates the extreme cases of local scour near bridge piers which are most commonly observed in regions with cold climates, where the flow surface is covered by ice.

The ice cover gradually thickens and develops a smooth surface in contact with the water when it forms naturally under cold temperatures and mild flow conditions [271]. When the ice cover is created mechanically, such as by shoving during freeze-up or break-up periods, it typically consists of many broken fragments that come together to form a rough surface [3, 19]. Zare et al. 2016 [3] conducted a study aiming to quantify the roughness characteristics of the Manning's coefficient under an ice cover. To achieve this, they employed a bottom-mounted Acoustic Doppler Current Profiler (ADCP) that continuously monitored velocity profiles for several months. By fitting the time-averaged velocity profiles to the log-law, [3] determined that the Manning roughness coefficient at the bottom of the ice cover ranged from nearly zero to as high as 0.08. Consequently, the underside of an ice cover can exhibit either a smooth or considerably rough surface. The ice was modelled experimentally using various materials. For example, Polyvinyl Chloride (PVC) and Polypropylene plate by [25], a sheet of Styrofoam by [182, 263], plywood that possesses sanded faces for smooth bottom surface and with PVC acoustic wall panels of 0.02 m maximum elevation that cover the smooth bottom to create the appropriate roughness of 0.013m estimated using logarithmic law of the wall by [234, 254], natural ice cover, plywood cover and plywood covered with "Mactac" by [135] and a hollow Plexiglas acrylic block with a rounded leading edge by [8]. The presence of ice cover significantly complicates the interactions between the ice cover, fluid flow and channel geometry in a river. These interactions can have a significant impact on the sediment transport process [117].

The velocity profile changes when an ice cover forms at the surface of the water in a river. Some studies made measurements of the flow field around pier under ice covered conditions e.g. [74, 123, 176, 234, 254, 259, 271]. The velocity profile acts like in a pipe flow, with velocity decreasing at the top and bottom borders and peaking in the center of the flow depth [152, 254, 263] (Figure I.9). The upper portion of the flow was primarily influenced by the ice cover resistance while the lower portion of the flow was affected by the channel bed resistance [123]. The position of the maximum flow velocity beneath ice cover varied based on the ratio between

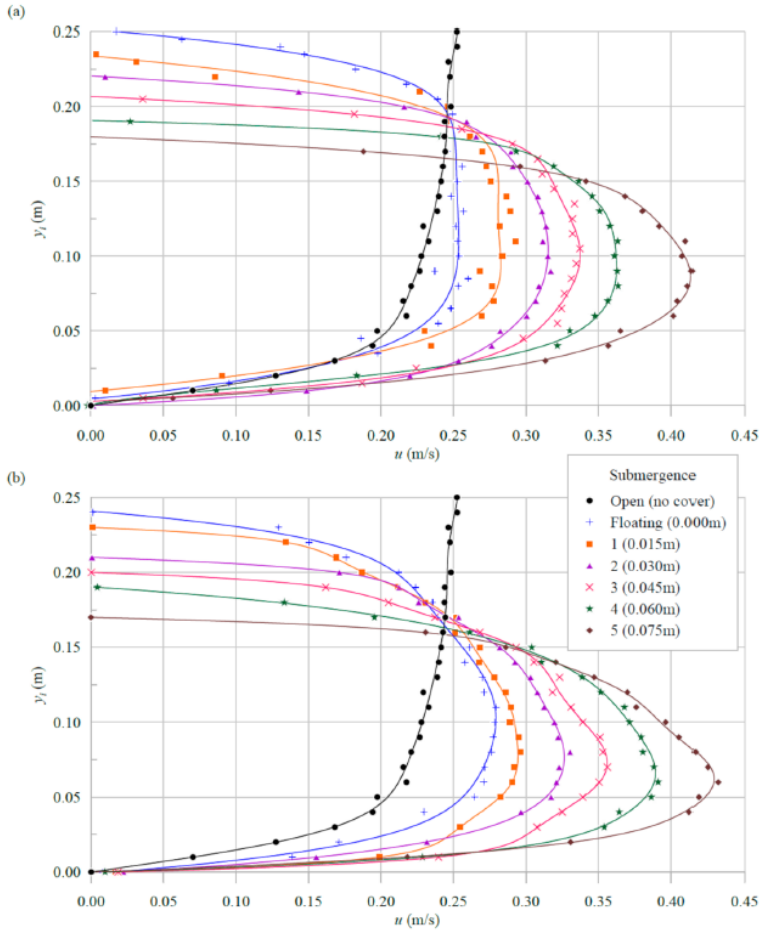

Figure I.9: Velocity profiles for open, floating, and various depth of submerged attached conditions under (a) smooth ice cover and (b): rough ice cover; Valela et al. 2021 [254]

the ice resistance coefficient (related to the roughness) and the bed resistance coefficient [74]. As the ice resistance coefficient increases, it was expected that the maximum flow velocity will shift closer to the channel bed, causing the near bed velocity to increase [254, 259, 263] (Figure I.9). The measured maximum velocity under smooth cover was approximately situated at 0.8 y_1, whereas the maximum velocity under rough cover was approximately at 0.6 y_1 by [176], where y_1 is the approach flow depth (as indicated in Figure I.9). In addition to the roughness of the ice cover, whether or not the ice cover is attached to the banks of the flume, can also have an impact on the velocity profile and the amount of scour. The ice cover can adjust its elevation to account for changes in water levels when it is floated on the water surface [8]. The ice cover cannot respond to rises in water level when it is attached to the banks, which can lead to pressured flow conditions beneath the ice cover [271]. When comparing the velocity profiles between the floating and submerged (fixed) ice covers, the disparity observed is minimal, apart from the influence of submersion depth (Figure I.9). Valela et al. 2021 [254] investigated pier scour under progressively increasing submergence of the ice cover. As submergence increased

under the ice cover, there is an observed increase in the maximum velocity, accompanied by a downward shift in the location of the maximum velocity [254] (Figure I.9).

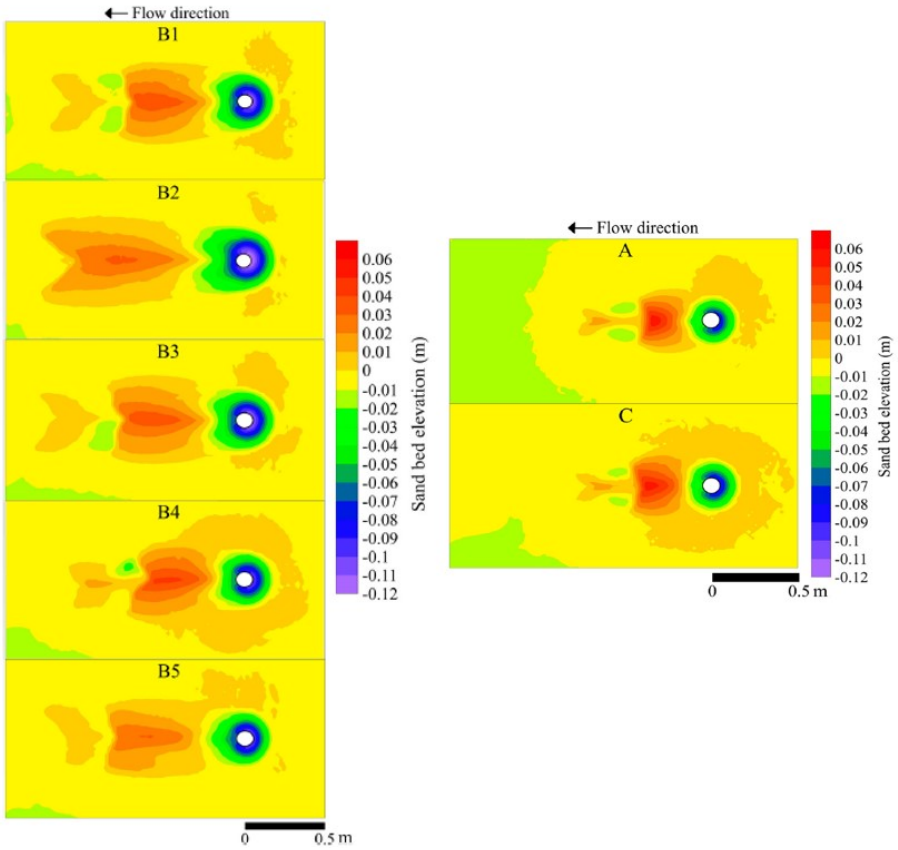

Figure I.10: Scour bathymetry: open channel scour (A), growing ice cover scour (B) where the upstream lengths are 0, 0.63, 1.33, 2.66 and 5.32 m for B1, B2, B3, B4 and B5 respectively and local jamming scour (C); Sirianni et al. 2022 [234]

The existence of an ice covering surrounding the bridge pier was found to amplify pier scour by various authors [234, 254, 263]. Sirianni et al. 2022 [234] examined pier scour from a circular localized cover, simulating jam initialisation and various channel-spanning ice cover lengths, simulating several stages of ice cover development. Five upstream lengths were tested ranging from 0 m to 5.32 m, all with cover downstream of the pier. The local cover had a diameter three times larger than the pier in the upstream part. For the growing ice cover, the 2.66 m length, case B4 Figure I.10, causes the most scour and near bed Reynolds stress with larger scour depth and volume by 46.9% and 238% respectively, compared to free-surface flow condition . However, the local cover, case C Figure I.10, provided the least scour depth and volume increase by 4.94 % and 14.8 % respectively, compared to free-surface flow condition. Other studies considered a fully developed ice cover [254, 263]. As the flow depth increased, the effect of ice cover decreases [254, 263]. A rough ice cover resulted in greater scour depths compared to a smooth ice cover

for each level of submersion [254]. Under both open channel and ice-covered flow conditions, empirical equations of scour depth and radius were established as function of the relative bed coarseness, flow shallowness, and pier Froude number by [263]. Ackermann et al. 2002 [2] observed that for equivalent averaged flow velocities, the presence of an ice cover could raise the local scour depth scour by 25% to 35% from the free surface condition. In live bed scour state where the flow velocity, V, is 1.5 to 2 times the critical velocity for bed movement,V_{cr}, the difference was the greatest. The scour action observed in [270] diminished when the ice sheet transitioned from attached into a state of free-floating. Hains. 2004 [117] found similar depths of equilibrium scour for fixed and floating covers during clear-water conditions, up to 21% higher than those observed in free water surface.

I.5 ERODIBILITY OF SEDIMENTS

The skeleton of sand grains is a dominant factor in the mechanical behavior of a soil below a specific level of fine particle content (fcm (%)). The mechanical behavior is dominated by fines particles when the fines content exceeds this threshold value, and the sand grains taken into account as void [21] (Figure I.11 (a)). The transition from a non-cohesive bed to a cohesive bed happens for small proportion mud content in the sediment mixture in the range of 3 to 15 % by weight, depending on the clay mineral type and the compaction level applied [172]. The mud refers to clay and silt particles which are less than 63 μm in size according to British Soil Classification System. Cohesive sediment erosion mechanisms are very different from those of non-cohesive sediments [84]. The erodibility behavior in cohesive soils is controlled by the complex interaction of physical, geochemical and biological properties [109]. Winterwerp and van Kesteren 2004 [262] suggest that elevated pH levels can heighten sediment erodibility. This is due to the reduction of H+ ions, leading to expanded double layer thicknesses and intensified repulsive forces. Kohyari and Jain. 2008 [132] point out the existence of three modes of erosion for cohesive sediment mixtures, particle or floc erosion, surface erosion and mass erosion.

There are various forces exerted on a grain subjected to a flow. The destabilizing force of the flow, which corresponds to the combination of two forces, the lift force FL, directed normally to the flow, which tends to move the grain upwards, and the drag force FD, parallel to the flow direction, tending to move the grain downstream. The stabilizing force is the particle's weight (W) in the case of a non-cohesive soil. On the other hand, in the case of a cohesive soil, an additional stabilizing effect is added due to the bound between particules which is governed by

electro-chemical attractive forces (Fc) such as Van der Waals forces [262] (Figure I.11 (b)). The result is a higher resistance to erosion in cohesive soils than in non-cohesive soil.

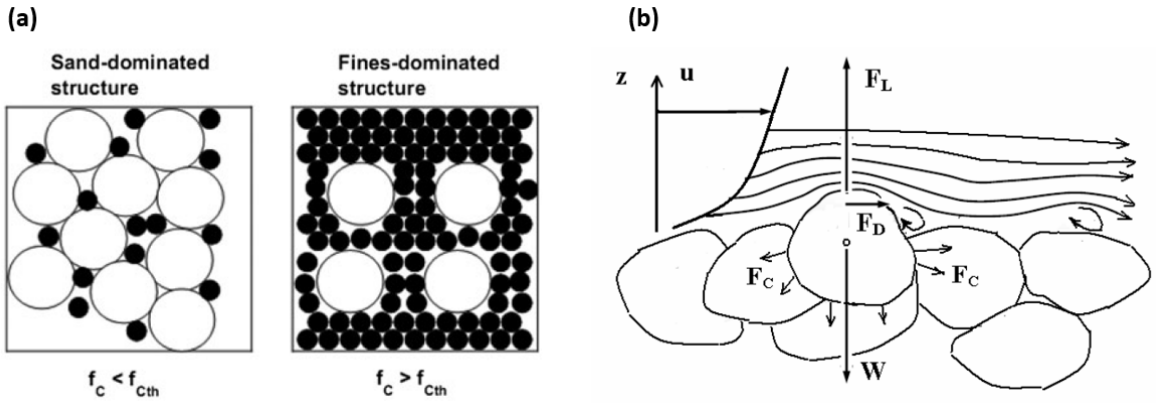

Figure I.11: Schemes of (a): structure configurations of mixtures containing sand and fines; Benahmed et al. 2015 [21], (b): forces exerted on a grain in a cohesive soil; Debnath and Chaudhuri 2010 (c) [81]

The Shields number θ [231] establishs the non-dimensional relationship between the destabilizing forces and the stabilizing forces.

For non-cohesive bed, the Shields number θ is given by the equation I.1.

$$\theta = \frac{{u_*}^2}{(s-1)gd_{50}} = \frac{\tau_0}{\rho_f(s-1)gd_{50}} \tag{I.1}$$

Where, $u_*(m/s)$ is the bottom friction velocity, $g(m/s^2)$ is the acceleration of gravity, $s = \rho_s/\rho_w$ with s, $\rho_s(kg/m^3)$ and $\rho_w(kg/m^3)$ are the relative density of the sediment, the volumetric mass of the sediment and the volumetric mass of the water respectively, $\tau_0(N/m^2)$ is the basal shear stress and $d_{50}(m)$ is the median diameter of the grain.
The critical threshold of movement θ_{cr} beyond which sediments move is given by the equation I.1 with the corresponding critical bottom friction velocity u_{*cr} or the critical basale shear stress τ_{0cr}.
Soulsby. 1997 [236] proposed a formula for directly calculating the critical threshold θ_{cr} from the dimensionless sedimentological diameter D_* (equation I.2).

$$\theta_c = \frac{0,3}{1+1,2D_*} + 0,055\left[1-\exp\left(-0,02D_*\right)\right] \tag{I.2}$$

Where,

$$D_* = \left[\frac{g(s-1)}{\nu^2}\right]^{1/3} d_{50} \tag{I.3}$$

Where ν is the kinematic viscosity of the water

For cohesive soil sediments, It is hard to predict the incipient flow condition. Some authors reported that erosion threshold did not exist for cohesive sediments [151, 195]. Rijn. 2020 [215] proposed simple equations for critical shear stress for eroding particles of the sand and mud fraction which were in good agreement for those of soils at low to medium density, but with an underestimate for the critical shear stress for soils at medium to high density beds. General expression for the Shields number assuming that cohesion was proportional to the yield strength, quantified by tensile tests at which there will be particle detachment, was proposed by [58]. This expression is valid only for weakly cohesive granular materials. Ternat et al. 2008 [247] proposed a model that related the critical Shields number of saturated natural cohesive sediments (θ_c) to the particle Reynolds number (Re_*) including the electrostatic surface forces. The particle Reynolds number (Re_*) is defined by $u_* k_s / \nu$, where $k_s = 2.5 d_{50}$ is the roughness length of the bed and d_{50} is the mean size of the sediment.

The simplest general way to determine the erodibility properties, in particular the incipient velocity or shear stress for cohesive soils is by taking measurements using erosion tests, such as the EFA test (Erosion Function Apparatus) [24, 50, 55], or the HET test (Hole Erosion Test) [20, 30, 60], or the JET test (Jet Erosion Test) [7, 104, 127]. The erosion parameters obtained from an erosion curve defined by [54, 222, 224] are the following : the critical erosion velocity v_{cr}, the critical erosion stress τ_{cr}, the initial slope in the curve of erosion velocity E_v, the initial slope in the curve of shear stress E_τ and the erosion category EC.
Figure I.12 shows the procedure used to determine τ_{cr}, E_τ and EC. The τ_{cr} is the shear stress corresponding to threshold erosion. It is associated to an arbitrary low erosion rate 0.1 mm/hr according to EFA measurements (Figure I.12 (a)). The E_τ represents the slope of the erosion curve when erosion is initiated. It indicates the rate at which the soil erodes at the critical shear stress (Figure I.12 (a)). The same procedure is used to determine v_{cr} and E_v in the erosion rate versus velocity erosion chart. The erosion category (EC) of soils illustrated by linear limits on the logarithmic plots of erosion rate function of shear stress or flow velocity was defined by [40, 50]. The position of the median point of the erosion curve on the established limits in erosion rate against shear stress in the logarithmic chart is used to determine the representative value for EC (Figure I.12 (b)).

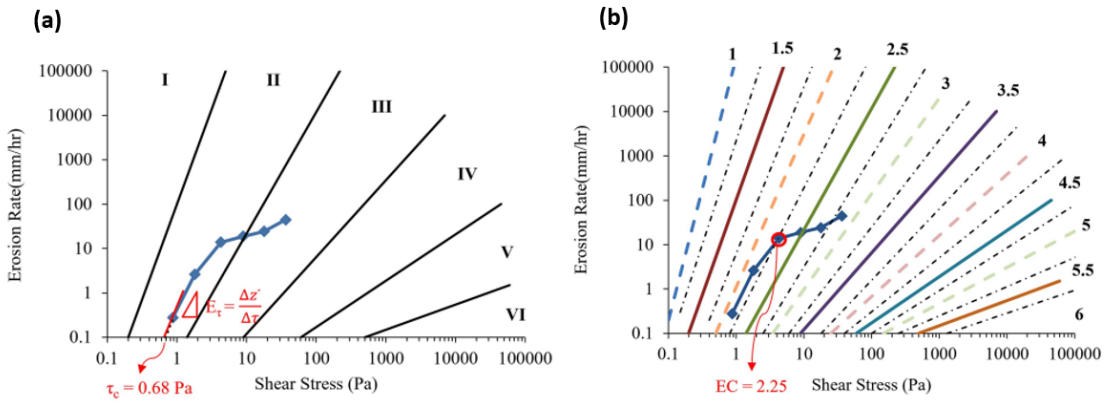

Figure I.12: Example of determination from the erosion curve of (a) : the critical erosion stress τ_{cr} and the initial soil erosion rate E_τ, (b) : the erosion category EC; Shaffi et al. 2023 [224], Where from the erosion categories (EC), the soils are classified as follows, I(1) : Very High Erodibility, II (2): High Erodibility, III(3): Medium Erodibility, IV (4): Low Erodibility, V (5): Very Low Erodibility and VI (6) : Non Erosive

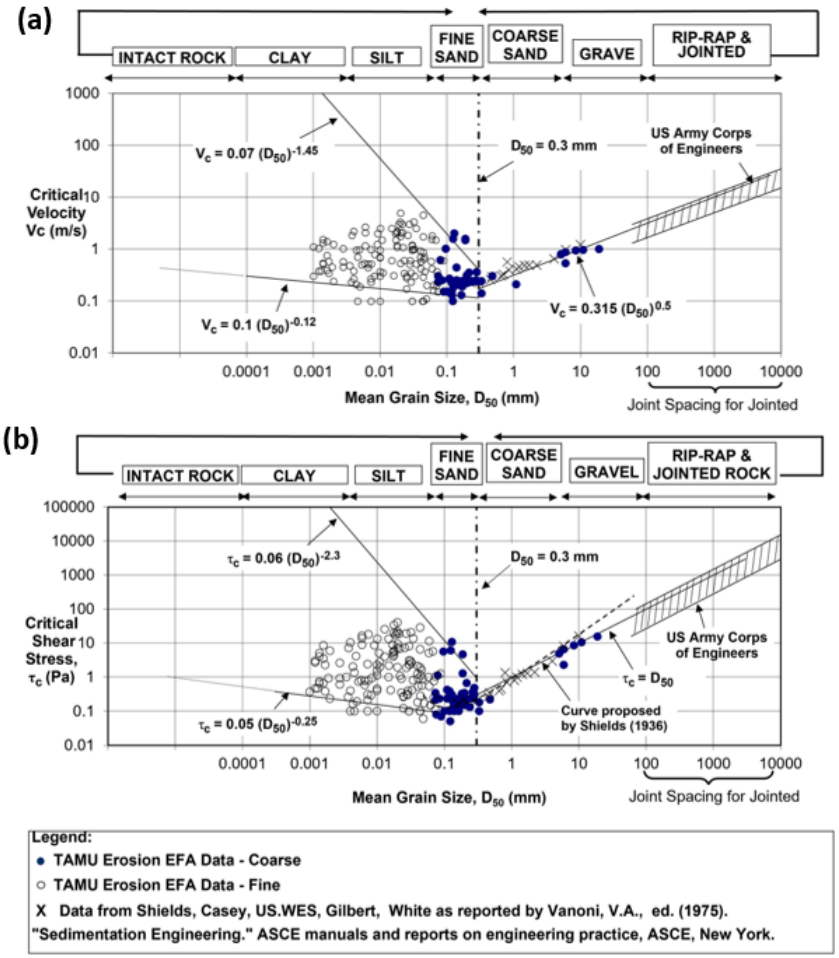

Figure I.13: Correlation between mean particle size D_{50} and (a) : the critical velocity v_{cr}, (b) : the critical shear stress τ_{cr}; Shaffi et al. 2023 [224]

An extensive study on the development of theoretical correlation equations to predict the aforementioned erosion elements from the basic geotechnical properties of a soil, without the need for costly multiple erosion tests are presented in [54, 222, 224]. Using the median diameter d_{50} to define critical erosion values for purely or partially cohesive sediments raises a number of difficulties (see Figure I.13 above). Shaffii et al. 2023 [224] addressed these challenges by finding equations to predict aforementioned erosive parameters based on a range of geotechnical parameters, not solely reliant on d_{50}.

I.6 SEDIMENT TRANSPORT LAWS

A classic way of quantifying sediment load transport is as a function of the excess of bottom stress over threshold stress.

For cohesionless soil, the Einstein parameter 1950 (Φ) is used to switch from dimensional to adimensional transport (Equation I.4) [91].

$$\Phi = \frac{Q_s}{\sqrt{(s-1)gd_{50}^3}} \tag{I.4}$$

Where, Q_s is the erosion flux (m^2/s), s is the relative density of the sediment, g is the acceleration of gravity (m/s^2) and d_{50} is the median diameter of the grain (m).
The formulation proposed by Meyer-Peter and Müller 1948 [170] (Equation I.5) is commonly used with different values for coefficients m and n depending on the value of the Shields number (θ) (Table I.1). The additional stress induced by sedimentary structures is not taken into account in this case.

$$\Phi = m(\theta - \theta_c)^n \tag{I.5}$$

where m and n are dimensionless coefficients (Table I.1) and θ_c is the critical Shields number.

Reference	m	n	Validity domain
Meyer-Peter and Muller 1948 [170]	8	3/2	θ <0.2
Fernandez Luque and van Beek 1976 [100]	5.7	3/2	θ <0.1
Nnadi and Wilson 1992 [185]	12	3/2	θ >1
Ribberink 1998 [212]	11	1.65	0.03 < θ <7.7

Table I.1: Values of coefficients m and n defined by some authors for Equation I.5

For cohesive soil, the most common transport law is that of Partheniades et al. 1965 [196] given by the following (Equation I.6):

$$E = \begin{cases} M\left(\frac{\tau}{\tau_c} - 1\right) & \text{If } \tau > \tau_c \\ 0 & \text{else} \end{cases} \tag{I.6}$$

Where E is the Erosion flux ($kg/m^2/s$), M is the Erosion rate ($kg/m^2/s$), τ is the bottom shear stress (Pa) and τ_c is the critical shear stress (Pa).

I.7 PIER SCOUR IN COHESIONLESS BED

In last decades, numerous laboratory studies on pier scour in cohesionless soil have been carried out [39, 86, 150, 166, 211, 230, 266]. The upstream part of the scour hole was commonly described by an inverted cone frustum [150, 160, 166, 168, 171, 252]. Yanmaz and Altinbilek. 1991 [266] utilized the inverted cone model to approximately determine the scour hole volume. They discovered through experimentations that the sizes of the scour holes in each of the three coordinate axes were linearly correlated. Liu et al. 2019 [158] observed that the different dimensions of geometric parameters (depth, width, upstream extent, plan area, and volume) in the scour hole follow a logarithmic law with a corresponding power law rate of change. The plane shape of the upstream section of the scour hole is characterized by following an ellipse (Figure I.14). There is a region within the scour hole where the bed slope angle surpasses the angle of soil repose and the remaining area of the scour hole far away from the pier had lower slopes.

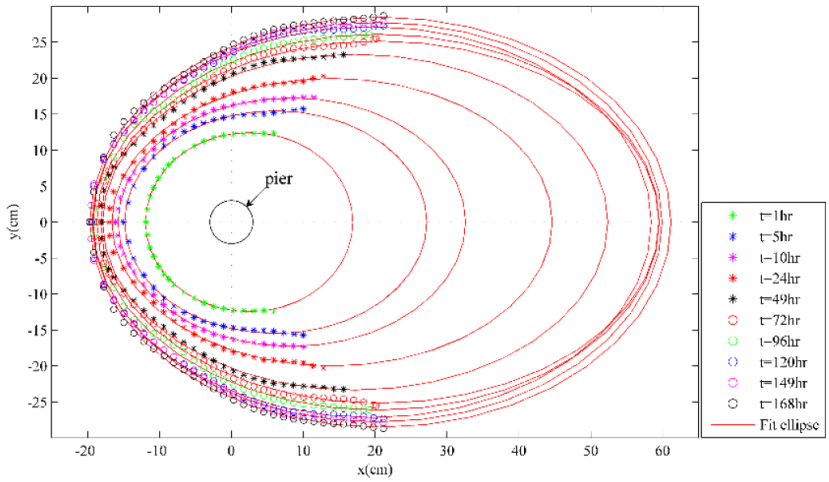

Figure I.14: Elliptical plane shape of the upstream part of the scour hole; Liu et al. 2019 [158]

Some studies observed at the upstream longitudinal section the presence of various inclinations [78, 157, 252] (Figure I.6 and Figure I.15(a)). In the longitudinal section, the upstream slope of the scour hole is steeper than the downstream slope (Figure I.15(a)) [244]. The longitudinal upstream angle exceeds the natural angle of repose of bed sediment, also termed friction angle [6]. The slope of the scour hole at the downstream of the pier was around the half of the angle of repose of the sediment $\pm$ 2° [118]. However, in other studies, the observed side slopes were approximately equal to the sediment angle of repose [150, 273] (Figure I.15(b)). McGovern et al. 2014 [165] observed reduced mean slope angles (11–12°) from their tidal scour studies compared to unidirectional flow, implying larger overall scour extents. Bouratsis et al. 2017 [32] reported that the average slope of the scour hole function of azimuth angle can be approximated by a sine function.

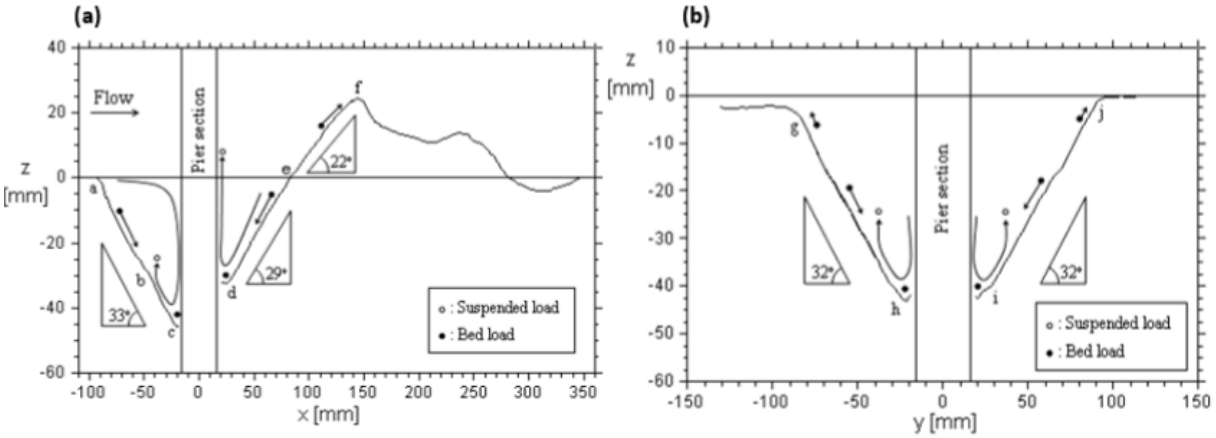

Figure I.15: Scour hole profile in cohesionless bed (a): longitudinal section; (b): transversal section; Umeda et al. 2008 [252]

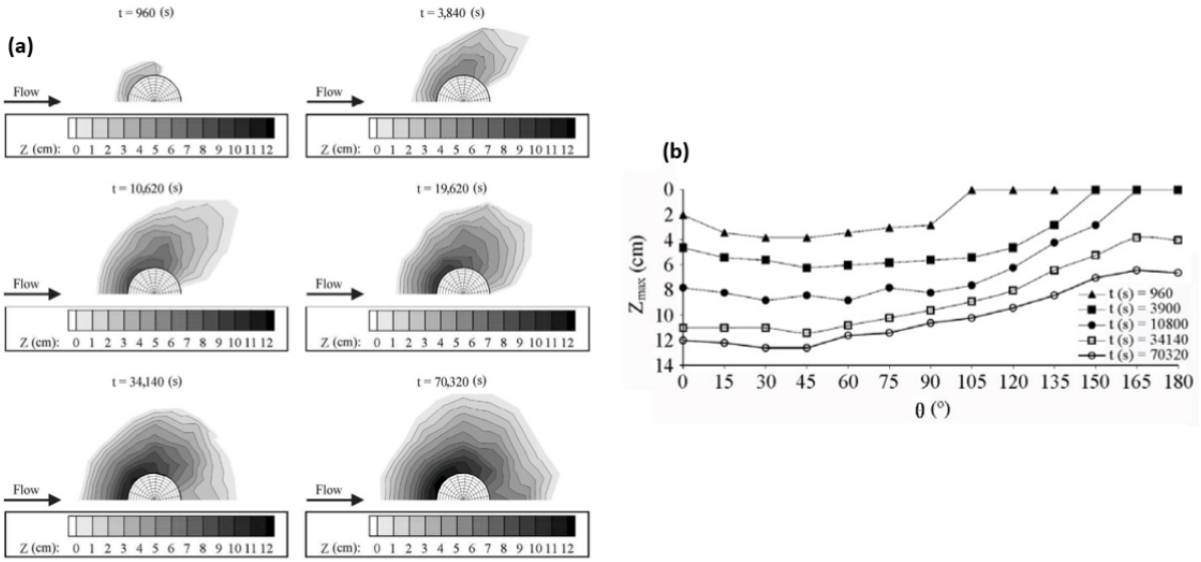

Figure I.16: Dynamic evolution of the scour hole morphology in sand bed, (a):contour plot of the scour hole topography, (b): Scour depth function of azimuth angle; Link et al. 2008 [157]

Temporal pier scour experiment in clear water were conducted in gravel (d50= 3.25 mm) by [89], medium sand (d50 = 0.26 mm) by [157] and fine sand (d50= 0.139 mm) by [252]. These studies revealed that the scour initiates at the side of the pier, then propagates upstream of the pier (Figure I.16). The maximum final scour depth was observed at the front of the pier (Figure I.16). The non dimensional scoured volume and the non-dimensional maximum scour depth at the azimuthal half-plane at the front is correlated following a parabola [89, 157]. The shape of the mound is similar to a crescent [252] (Figure I.17 (a)).

The classical scour pattern was principally formed by a scour hole (erosion zone), and a single mound (deposition zone) (Figure I.17 (a)). [143] identified a scour pattern *rabbit ear* in the vicinity of an submerged cylinder in clear water condition (Figure I.17 (b)). This pattern was characterized by two side-by-side symmetrical elongated holes without a mound behind the cylinder. They were formed due to wake vortices at lower velocities and with longer duration of formation than the classic scour pattern induced by horseshoe vortex. An extended zone of pits and mounds of sediment forming downstream of the cylinder were observed by [219] for immersed cylinder (Figure I.17 (c)) and by [16] for emerged cylinder (Figure I.17 (d)). [251] distinguished a number of scour regimes based on the observed scour hole and ripple pattern around a cylinder exposed to waves.

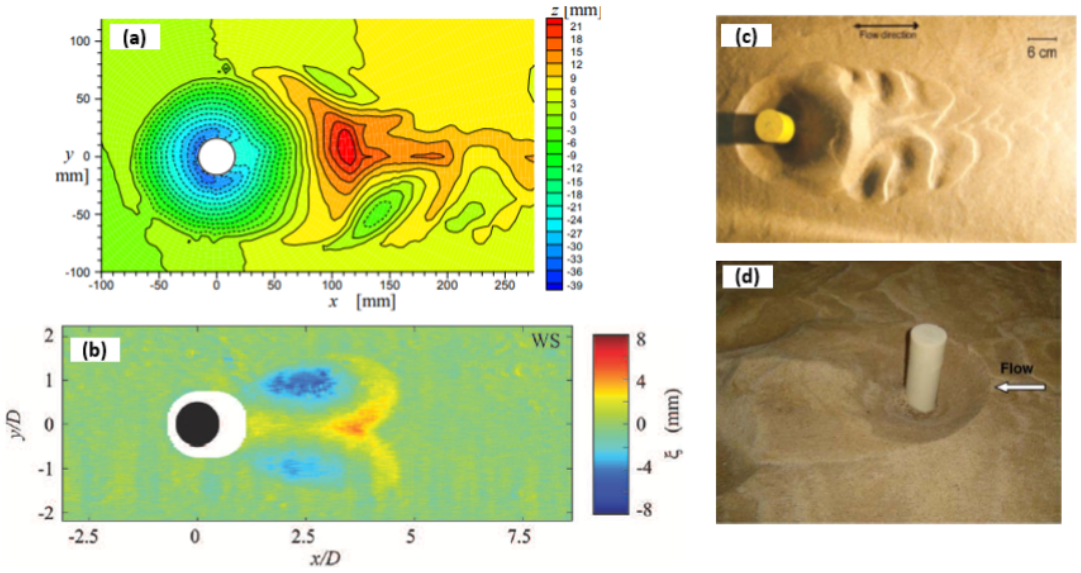

Figure I.17: Scour hole pattern; (a): classical scour hole pattern; Umeda et al. 2008 [252], (b): rabbit ear pattern; Lachausée et al. 2018 [143], (c): Succession of sedimentary patterns downstream of a cylinder; Sarkar et al. 2016 [219], (d): Scour hole pattern in live bed scour; Zhao et al. 2010 [273]

A widely used formula I.7 for the maximum scour depth evolution in literature was proposed by [242]. This equation has an exponential form and has been used by various researchers e.g.[16, 119, 199].

$$S_t = S_0\left(1 - e^{-t/T}\right) \tag{I.7}$$

Where, S_0(m) is the equilibrium scour depth, T is the time-scale of scour.

$$T = \frac{b^2}{\left(g(s-1)d_{50}^3\right)^{1/2}} T^* \tag{I.8}$$

Where, T^* is non dimensional time scale of scour.

$$T^* = \frac{1}{2000}\frac{\delta}{b}\theta^{-2,2} \tag{I.9}$$

Where, δ is the boundary layer thickness, θ is the Shields number, b is the pier diameter, s is the relative density of the sediment grain (2.65), g is the acceleration of gravity 9.81 m/s^2, d_{50} is the medium sand diameter.

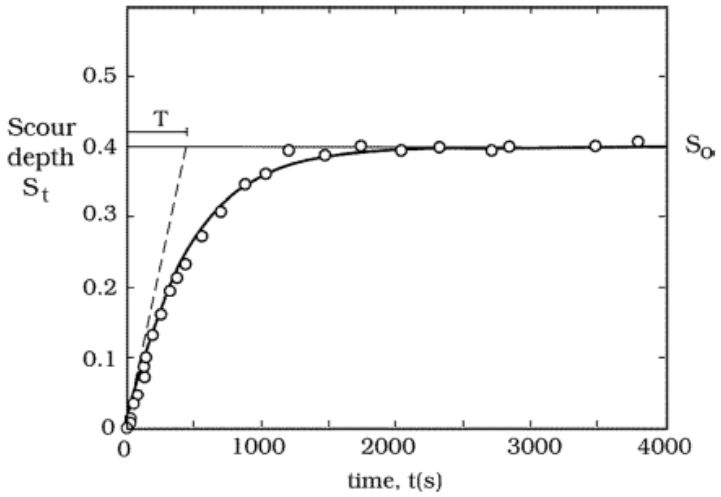

Figure I.18: Exponential law for scour depth over time with determination of the time scale; Petersen et al., 2012 [199]

Relatively few authors used the hyperbolic law defined later (equation IV.2 in section I.9) for cohesionless bed [56, 274]. Zhao et al. 2012 [274] concluded that the hyperbolic law fitted better the experimental data than the exponential law for live bed scour experiments around square pier in sand bed.

I.8 PIER SCOUR IN COHESIVE BED

Compared to cohesionless beds, few studies have been devoted to local scour in cohesive beds. The difficulties come from the complexity of preparing and handling this particular type of sediment. Cohesive soils have stickiness and require attention to additional parameters. Some researchers investigated the impact of sediment cohesion on local scour around piers. They conducted studies under steady currents [13, 66, 80, 82, 122, 128, 133, 173, 221], waves [85], and varying sequential flow events [163]. Typically, non-cohesive soil, mainly sand, was used, excepted [122, 133] studies which used fine gravel or a mixture of fine gravel and fine sand in similar proportions. The cohesive soil content varied among the studies, including a combination of sand, silt, and clay particles [66, 80, 82, 87, 173], and cohesive soil with a similar fraction of silt and clay particles [128]. Some authors focused on cohesive materials (clayey soil), without doing mixtures, which was either collected from the field [156, 163, 173, 181, 209] or commercially available [56, 112, 153, 249]. A summary of the most relevant studies is presented here.

Molinas and Hosny. 1999 [173] investigated the local scour around a vertical cylindrical pier founded in a mixture of non-cohesive and cohesive soils ($4\% \leq Pc \leq 40\%$), unsaturated and

saturated cohesive soils. The cohesive soil used in this study was a natural cohesive soil with medium plasticity with montmorillonite as dominant clay mineral. They found that increasing cohesive soil content in a mixture, reduced the scour depth, the scour volume and the deposition in the wake region of the pier and increased the side scour slope. Increasing the percentage of cohesive soil in the montmorillonite combinations up to 30% can minimize scour by up to 40%. When the clay content exceeds 30%, other factors such as initial water content, degree of saturation and compaction start influencing the pier scour.

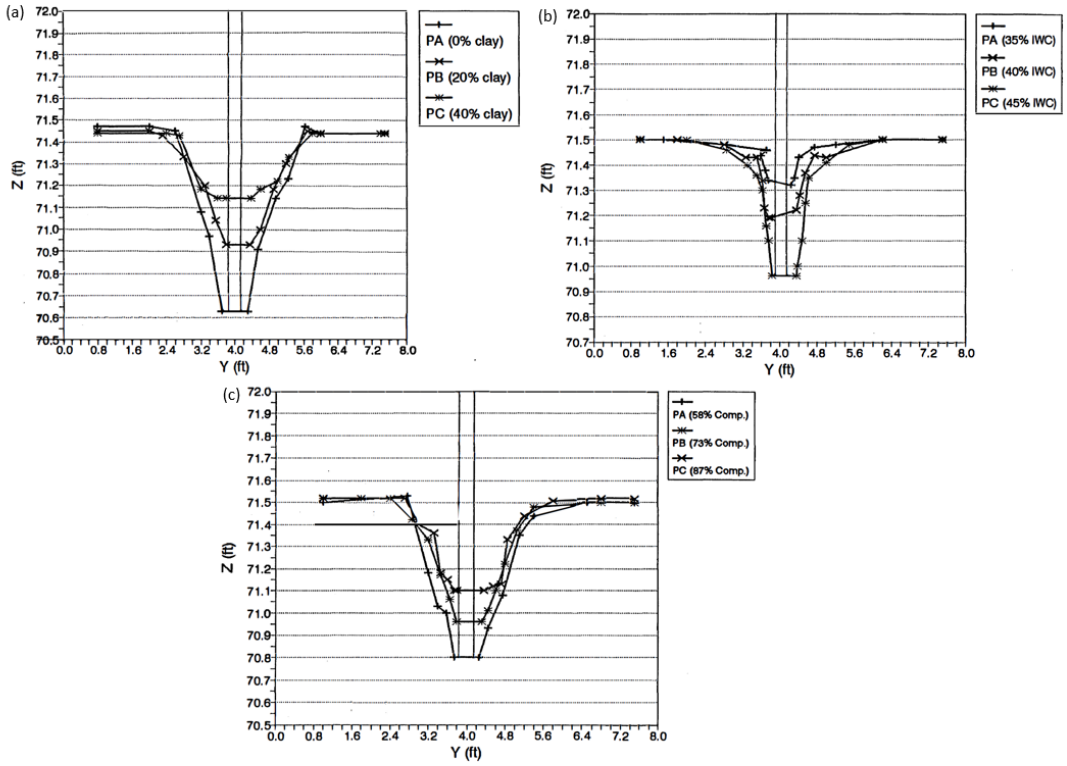

Figure I.19: Transversal scour hole profiles (a) : effect of clay content in cohesive mixtures at Fr= 0.307-0.33, initial water content (IWC) = 10-12% at the same energy of compaction; (b): effect of initial water content (IWC) in saturated cohesive soils at Fr=0.367-0.445, Comp=86-95%; (c): effect of degree of compaction (Comp) in unsaturated cohesive soils at Fr=0.336-0.369, IWC=20%; where Fr is the froude number; Molinas and Honsy 1999 [173]

Figure I.19 shows examples of results where PA, PB and PC are three pier three widely separated piers prepared in three separated recess areas at different initial conditions. Scour holes were found to be conical in shape for mixtures soils and unsaturated cohesive soil at low compactions. However, the shape of the scour hole was more likely to be cylindrical with steeper side slopes in saturated cohesive soil with low water content and unsaturated cohesive soil with high degree of compaction.

Flume tests were conducted at Texas A & M University, USA, on local pier scour for cohesive soils by [112, 138, 153, 249]. The experiments were made on two types of sand (d_{50}= 0.6 and 0.14 mm) and three types of cohesive soil beds: low plasticity porcelain (25% clay, 75% silt), high plasticity bentonite (65% clay, 35% silt) and medium plasticity armstone (45% clay, 30% silt, 25% sand). These series of flume tests constitute a very significant effort over many years, because installing the clay beds would take approximately 1 month and each experiment lasted at least one another month. Gudavalli. 1997 [112] and Ting et al. 2001 [249] presented results of tests carried out on single cylindrical pier with various diameters in steady current at deep water conditions. Ting et al. 2001 [249] observed that the maximum scour depth and the shape of the scour hole mainly depend on pier reynolds number Re (Figure I.20). The scour depths on the nose and the wake regions of the pier were similar at lower Re values; nevertheless, scour depths on the wake region were greater than noise region at higher Re values. Under the same flow and structure geometry conditions, they observed much slower scouring rate in clay compared to that of sand. A comparison between the equilibrium scour depths calculated using the HEC-18 (Hydraulic Engineering Circular) empirical equation which assessed for sand bed and those derived by fitting a hyperbola to the experimental data was shown in Figure I.21. This figure demonstrates that, similar maximum equilibrium scour depths in clay were typically within 30% of scour in sand that contradict Molinas and Hosny 1999 [173] finding that cohesive material in sandy soil reduces the scour depth. This explains their proposition of an empirical equation for maximum local scour depth that does not consider the geotechnical properties (see equation in Table I.2). Kwak. 2000 [138] studied the effects of multi-floods and layered soils. Li. 2002 [153] studied the effect of water depth, pier spacing, pier shape and attack angle. Oh. 2009 [190] collected and re-analyzed all flume results conducted in Texas A & M University from 1997 to 2002. He applied dimensional analysis and proposed an empirical equation to estimate maximum equilibrium scour depth including the soil properties.

Ansari et al. 2002 [13] conducted flume experiments with a mixture of sand and clay (10% $\leq$ Pc $\leq$ 60%). The clay used had the illite as dominant clay mineral. It was observed that the scour started always at the sides of the pier. For Pc $\leq$ 40%, in unsaturated condition, the final deepest scour depth was located at the upstream of the pier. Nevertheless, in saturated condition, the final maximum scour depth was at the side of the pier. For Pc $\geq$ 50%, the final maximum scour depth was observed at the side of the pier with negligible scour depth upstream of the pier. They found lower or even higher maximum scour depths for cohesive soils compared to non-cohesive soils depending on the initial moisture content, as shown in Figure I.22. Ansari. 2003 [11] made a discussion on [249] findings based on the results of the experimental program provided by

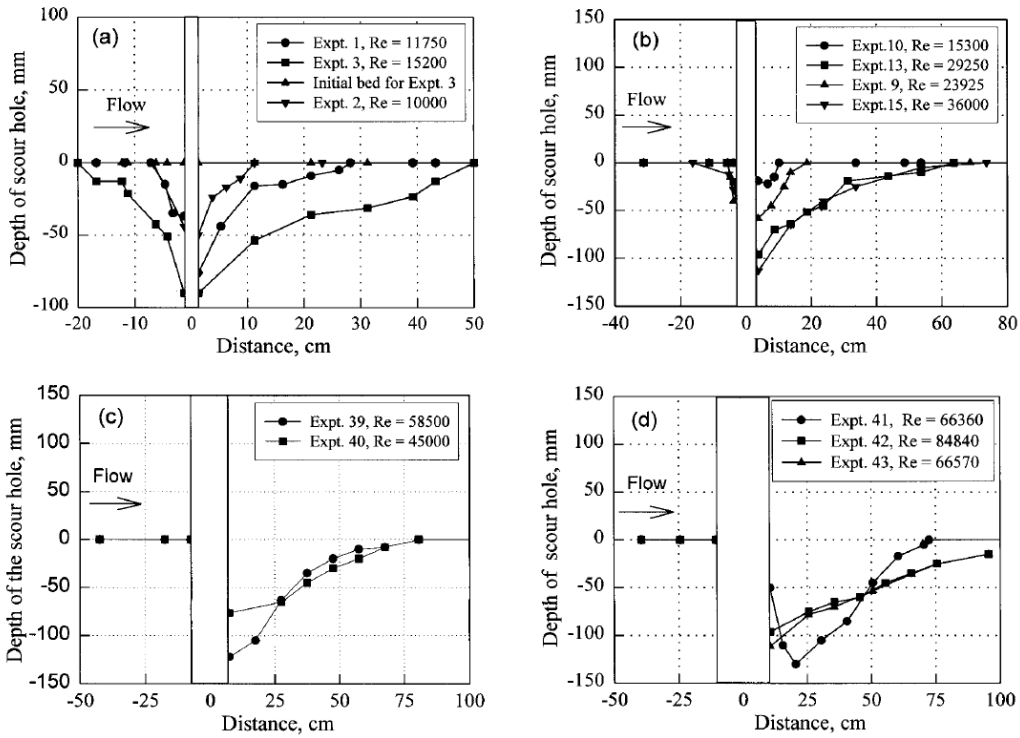

Figure I.20: Longitudinal Profiles of the final scour holes in Porcelain Clay for different pier diameters (a) b=25 mm, (b) b=75 mm, (c) b=150 mm and (d) b=210 mm, where Re is the pier reynolds number; Ting et al. 2001 [249]

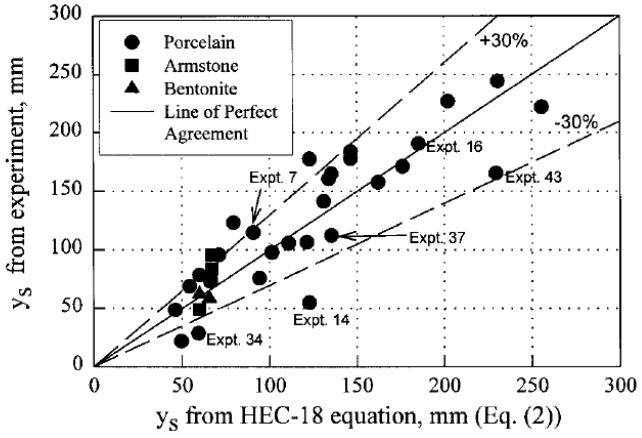

Figure I.21: Comparison between extrapolated equilibrium scour depth and the HEC-18 prediction in clay; Ting et al. 2001 [249]

[10, 12, 13]). They emphasised that other parameters, including clay content added in cohesive sediments, the plasticity index, initial moisture content, dry density, etc., also affect the shape of the scour hole in addition to the pier Reynolds number ReD. Figure I.23 illustrates different shapes of scour around a circular pier in cohesive sediments. In Figure I.23 legend, ReD is the pier Reynolds number, b is the width of the pier, V is the mean velocity approach flow, h is the

water depth, Pc is the clay content in cohesive mixture, PI is the plasticity index, W is the initial moisture content, W_* is the initial moisture content at saturation, which found approximately equal to liquid limit LL, γ_d is the dry unit weight of sediment, γ_w is the unit weight of water. It was clear that all of these factors have a considerable impact on the geometry of the scour hole for a constant pier Reynolds number ReD. Regarding [249] conclusion that clay exhibits lower scour rate than sand, Ansari [11] points out that in the case of cohesive sediments, depending on the initial moisture conditions, the rate of scour around a pier can be slower or faster than that occurring around the same pier if it was founded in cohesionless sediments for the same flow conditions (Figure I.22).

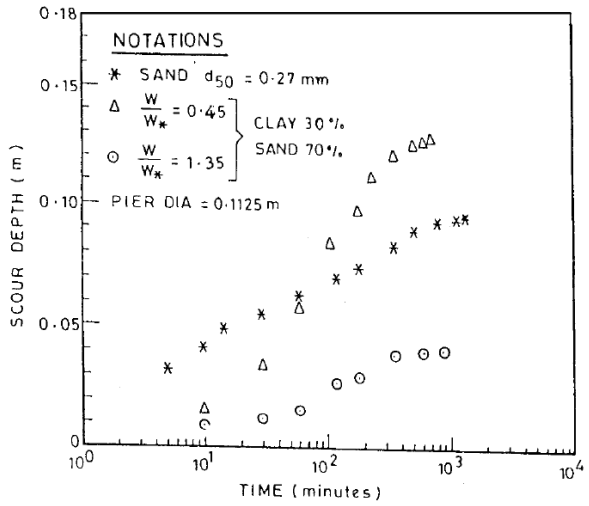

Figure I.22: Temporal evolution of scour depth around circular pier; Ansari 2002 [13]

Rambabu et al. 2003 [209] conducted laboratory testing program on piers in field normally consolidated soft silty clay soil of medium plasticity (9% sand, 47% silt, 44% clay) having consisteny index 0.27 in saturated condition. Similar study accomplished by [181] using three types of site cohesive soils having also sand, silt and clay particles in different proportions (type 1: 21% sand, 27% silt, 52% clay; type 2: 30% sand, 29% silt, 41% clay; type 3: 41% sand, 25% silt, 34% clay) with a consistency index between 0.19 and 0.3 in unsaturated condition. In [181, 209] researches, the ultimate scour depths were estimated using the theoretical hyperbolic fitting model as suggested by [56, 249]), based on the measurements over a short period (4 hours).[209] Rambabu et al. 2003 suggested formula between the maximum scour depth and non-dimensional parameters that combine the Froude number, Reynolds number, and soil strength parameter (critical shear stress and undrained shear strength) (see Table I.2). Najafzadeh and Barani. 2014 [181] proposed relationship between the ultimate scour depth and Froude number, flow depth,

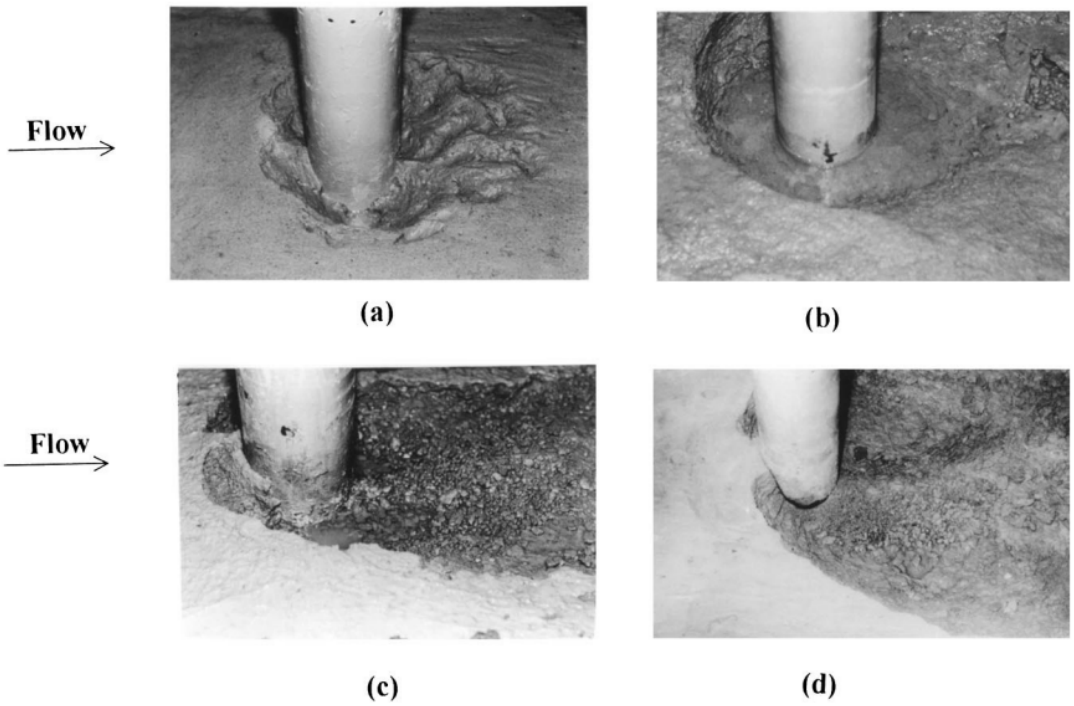

Figure I.23: Photographs of scour patterns examples around a circular pier in cohesive sediments for ReD= 50625, b= 0.1125 m, V=0.45 m/s and h=0.15 m; (a): Pc = 20%, PI=Non Plastic, W/W_*=1.1, γ_d/γ_w=1.62; (b): Pc=40%, PI=7% , W/W_*=0.61, γ_d/γ_w=1.76; (c) : Pc=50%, PI=9%, W/W_*=0.75, γ_d/γ_w=1.71; (d) :Pc=60%, PI=13%, W/W_*=0.25, γ_d/γ_w=1.66; Ansari 2003 [11]

clay content, undrained shear strength and unit weight of soil (see Table I.2).

Kho et al. 2004 [128] investigated scour depth around a cylinder using a mixture of three types of soils: synthetic-supreme kaolinite (silt), Grade E kaolinite (clay) and fine sand. In all experiments, the silt and clay content were equal. Each one of this content varied from 0% to 50% in order to construct soils with Pc=0% (100% sand) to 100% (50% silt+50%clay). The minimum flow velocity chosen was higher than the threshold velocity of the sand. They indicated an increase in equilibrium scour depth with the increase in clay content. This might be due to the scour hole being filled with sand during the high-flow live bed scour. They reported that the increase of the cohesive content results in an increase in the side slope, a reduction in the width and volume of the scour hole upstream of the pier. The critical percentage of cohesive soil at which the erosion behavior change was Pc=20%. From this value, the final maximum scour depth was observed to be the same on both sides and even in the wake's of the pier.

Data on local scour around pier for clay–sand mixed cohesive sediment beds were reported by [65–67, 80, 82, 83] at Bengal Engineering and Science University, Shibpur, India. The cohesive clay materials used in the experiments were primary artificial kaolinite clay. Some tests were also made using river cohesive clay sediment.

Debnath and Chaudhuri. 2010 a [82] presented results on mixtures with clay content in the range of 20-100% and water content in the range of 20-45.92%. They addressed the obvious question on the inconsistent observations from previous research on the impact of cohesion on the maximum scour depth reported by [13, 128, 173]. They suggested that for initial water content less than 24%, the maximum scour depth decreased as the clay percentage increased. From an initial water content greater than 27%, the scouring depth curve as function of clay percentage exhibits an inflection point with scour depth decreasing up to Pc 50-70% and then increasing. The initial water content in the clay-sand mixture affects the percentage of clay that corresponds to the point of inflection. They also argued the validity of [249] observations on the dependency of the scour hole shape on the Reynolds number ReD. They identified that the combination of the resistance bed shear stress and the bed shear stress caused by the flow has the strong influence in describing the shape of the scour hole and whether the upstream or downstream part of the pier has more scour depth. The scouring process began at the sides of the cylinder and then gradually moved downstream for all studied cases. For relatively low flow bed shear stress, scouring occurred upstream of the pier at a much slower rate compared to downstream, and the maximum equilibrium scour depth at the upstream was less than that of the downstream. For relatively intermediate range of the flow bed shear stress, scouring occurred simultaneously at the upstream and downstream at comparable rates, and the maximum equilibrium scour depth at the upstream was similar to that of the downstream. For relatively high range of the flow bed shear stress, the scouring rate at the upstream of the pier was faster than downstream, and the maximum equilibrium scour depth was greater at the upstream compared to the downstream. In addition, the transverse profiles were compared at different clay contents for velocity range 78.98–82.73 cm/s. It was observed that sharp cones were formed for clay contents between 50% and 85% (Figures I.24 b, c, and d), while the profiles were not sharply conical for 35% and 100% clay contents (Figures I.24 a and e), showing some curvature instead.

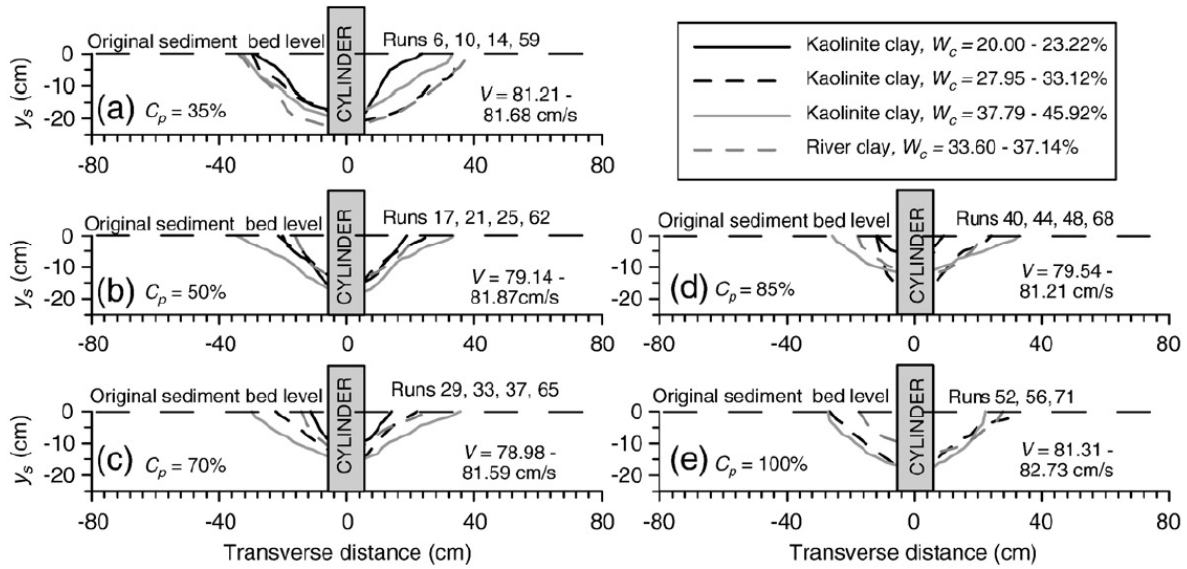

Figure I.24: Transversal Profile of the equilibrium scour hole for runs in a velocity range 78.98–82.73 cm/s, for different clay content and initial water content; Debnath and Chaudhuri 2010 a [82]

Debnath and Chaudhuri. 2012 [83] discussed the mechanism of scouring and the time variation for round-nosed, square and rectangular pier shapes compared to circular. They introduced the "characteristic heart shape" for the scour hole at equilibrium in the case of the square and rectangular pier at low velocity range. Similar observation of scour depth function of clay content for initial water content greater than 27 % as reported in [82] for circular pier is founded in case of square, rectangular and round-nosed pier shape (Figure I.25). Furthermore, the variation of scour in the longitudinal extend and in the transversal extent as function of the clay content shows similar trend of variation than the scour depth as function of the clay content for square, rectangular, round-nosed and circular pier (Figure I.26).

Chaudhuri and Debnath. 2013 [65] reported observations on the initiation and temporal development of the scouring process around circular and square piers. The photographs in Figure I.27 depict the profiles of the scour hole surfaces, which were captured from various angles using a camera placed within the pier during the experimental runs. The images reveal that the surface of the scour hole is rough and present undulation in all directions for both the square and circular pier.

Chaudhuri et al. 2018 [67] documented the impact of contraction ratio within a contracted channel on the scour around circular and square pier embedded in the mixed bed of cohesive sediment.

Chaudhuri et al. 2022 [66] observed for circular pier that best-fit exponential curves satisfactory present the variation of the dimensionless scour volume function of the clay content for three range of threshold dimensionless velocity (0.99-1.1, 0.87-0.92 and 0.78-0.85) (Figure I.28 (a),(b)

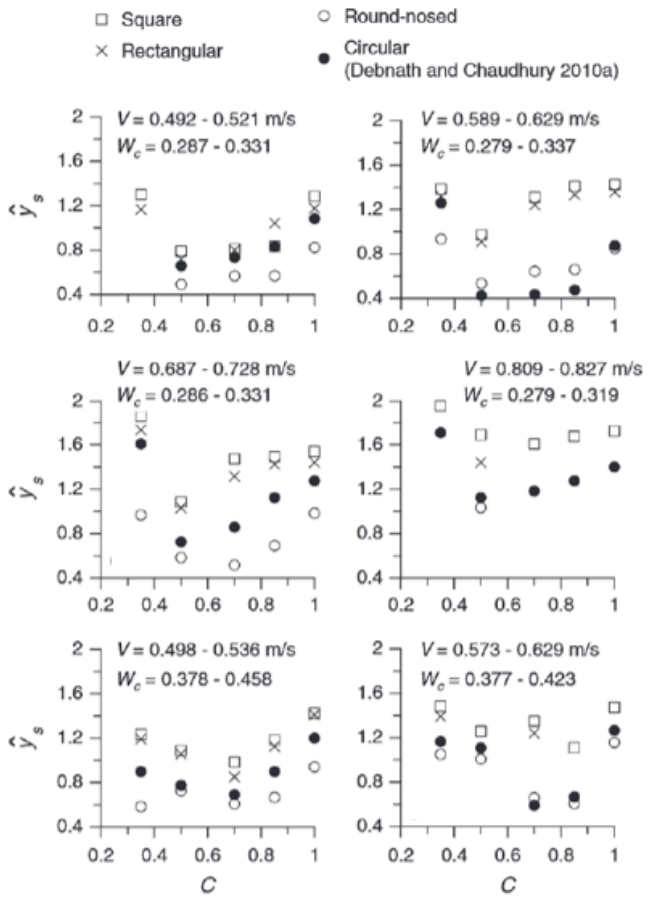

Figure I.25: Comparison of scour depth versus pier diameter ($\hat{y_s}$) as a function of kaolinite clay percentage in clay–sand (C) for different initial water content (W_c) and flow velocity (V) for $Wc \geq 27.9\%$; Debnath and Chaudhuri 2012 [83]

and (c)). The dimensional scour volume function of the dimensional equilibrium scour depth was similarly shown to have a single exponential equation (Figure I.28 (d)). The proposed equations were satisfactorily consistent with the experimental data provided by [173] (Figure I.28 (a),(b), (c) and (e)). They also found that the increase in the grain size of the sand used in the cohesive mixture results in greater reduction of the equilibrium scour hole volume as function of cohesive content Pc.

Muzzammil et al. 2015 [177] utilized the gene express programming (GEP), an evolving artificial intelligence (AI) tool, to develop a predictive equation for scour depth at a pier located in cohesive soil. The researchers employed laboratory data from [80] for their analysis. The findings revealed that GEP outperformed a nonlinear regression-based formula in accurately predicting scour depth at piers situated in cohesive beds.

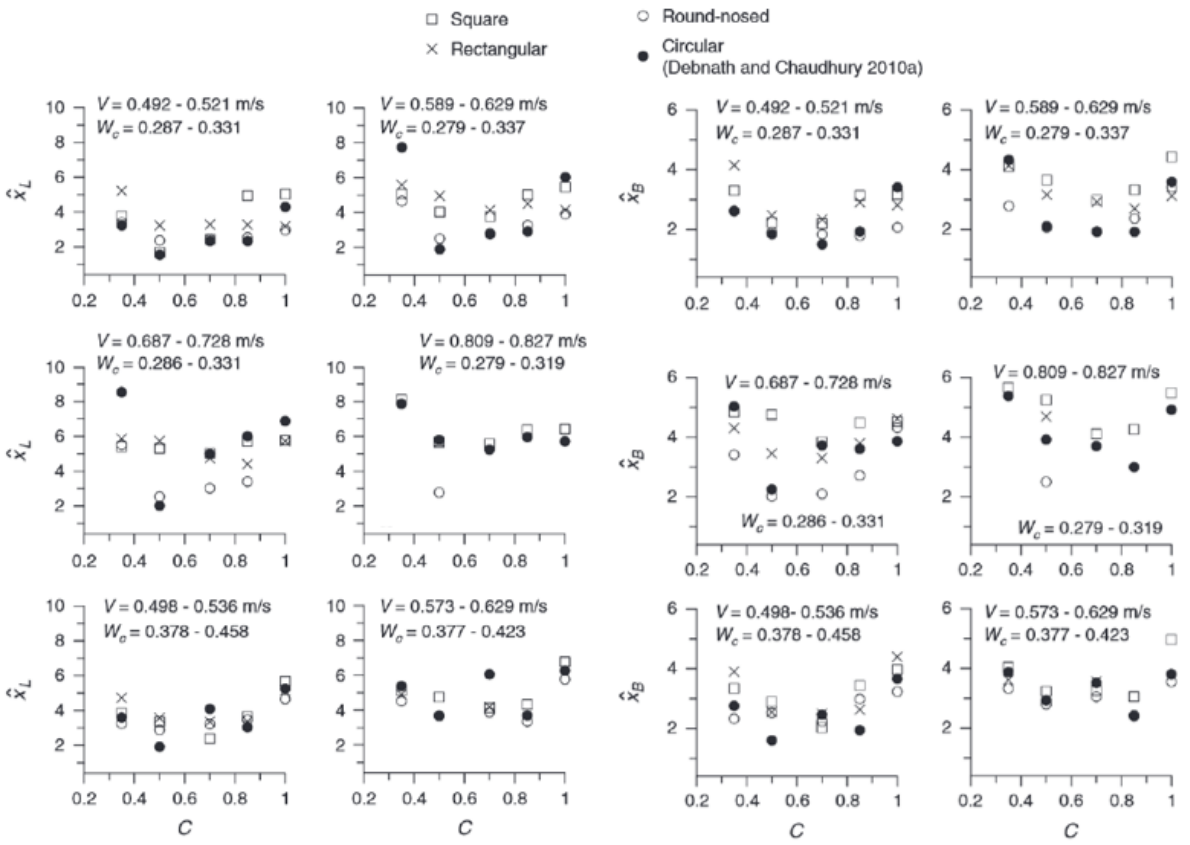

Figure I.26: Comparison of scour longitudinal extend versus pier diameter ($\hat{x_L}$) and scour transversal extend versus pier diameter ($\hat{x_B}$) as a function of kaolinite clay percentage in clay–sand (C) for different initial water content (W_c) and flow velocity (V) for $Wc \geq 27.9\%$; Debnath and Chaudhuri 2012 [83]

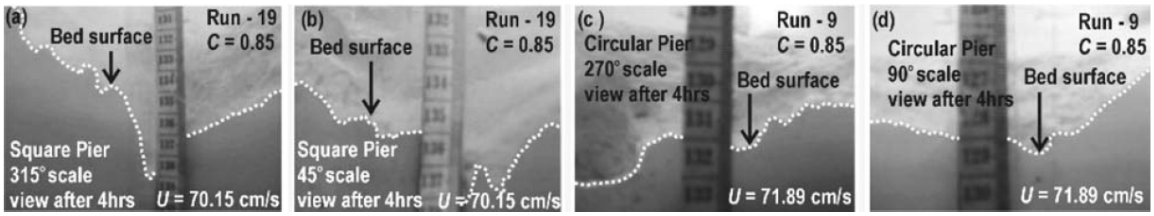

Figure I.27: Evolution of bed surface (a),(b) : around rectangular pier and (c),(d): circular pier, as captured by a camera at the locations of maximum scouring 4 hours after initiation; Chaudhuri et al. 2013 [65]

Dey et al. 2011 [87] studied the scouring process around vertical piers under waves using various clay-sand mixture ratios as the bed sediments. They stated that the depth of scouring decreased as the clay content in the clay-sand mixture bed increased. An interesting observation from the study is that the reduction in scour depth is nearly the same for clay proportion Pc in the sand-clay mixture equal to 30% and 100%. This suggests that the sand-clay mixture behaves

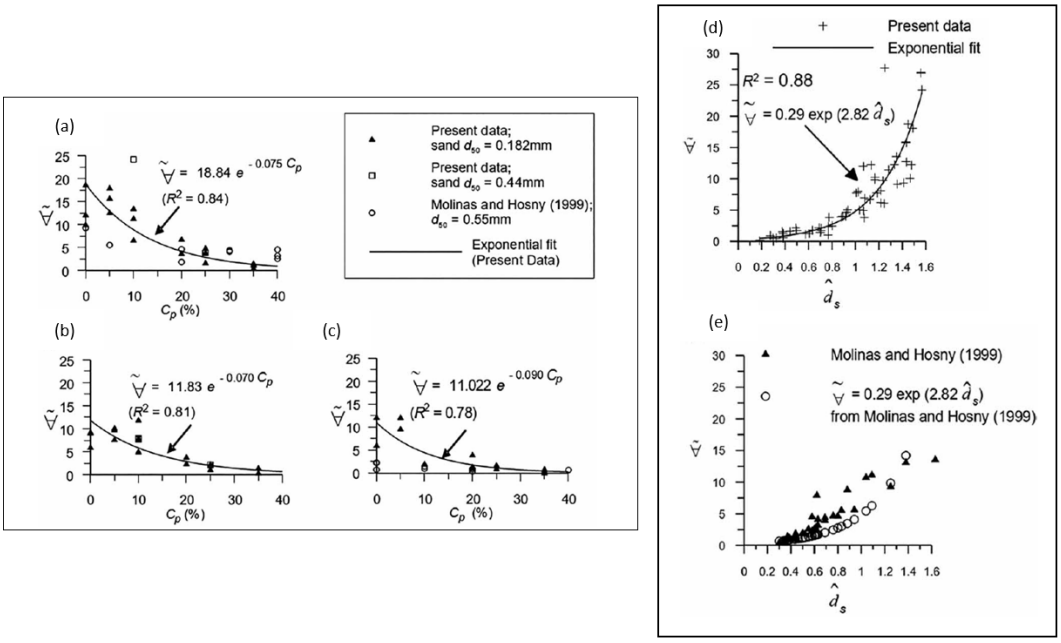

Figure I.28: Dimensionless equilibrium scour volume $\tilde{\forall}$ function of the percentage of cohesive content Cp in the mixture for three different threshold dimensionless velocity ranges: (a) $\hat{V}$=0.99-1.10, (b) $\hat{V}$=0.87-0.92, and (c) $\hat{V}$=0.78-0.85, Dimensionless equilibrium scour volume $\tilde{\forall}$ function of dimensionless scour depth $\hat{d}_s$ (d) Chaudhari et al. 2022 [66] data , (e): Molinas and Hosny 1999 [173] data; Chaudhari et al. 2022 [66]

like a clay alone in terms of scour depth when the clay proportion reaches 30%.

Link et al. 2013 [156] investigated the effect of bed compaction around circular pier on natural cohesive bed containing 72% sand. They observed that within a range of compaction energy applied (E=0-2.713 J/cm^3), the maximum scour depth was found to be between 10% to 58% of that which occurred in sand, with maximum scour depth occurring in the wake zone. Figure I.29 illustrates how the ratio of the maximum depth of scouring in cohesive soil to the maximum depth of scouring in sand (Z (cohesive bed)/Z (sand)) changes with respect to the ratio of the initial water content to the optimal water content for molding (W/Wop), at different levels of applied compaction energy to the optimum proctor energy (E/Eop). For a given compaction energy, the maximum depth of scouring decreases as the water content increases up to (W/Wop=2.5). This is because the clay particles tend to form fluffy masses that gradually disperse as the water content rises. when the water content (Wc) exceeds a value of 2.5 times the optimal water content (Wop), the maximum scour depth starts to increase again. At this point, the sediment matrix behaves like a fluid mud and gradually transforms into a liquid state.

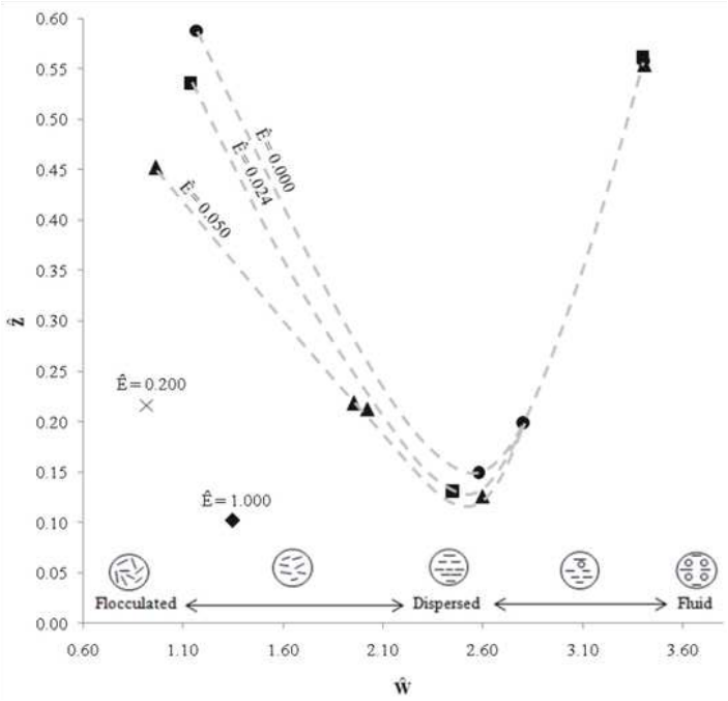

Figure I.29: Variation of the scour depth ratio (Z (cohesive bed)/Z (sand)) with dimensionless compaction energy (E/Eop) and molding water content (W/Wop); Link et al. 2013 [156]

Schindler et al. 2016 [221] focused to see how clay's physical cohesiveness within a cohesionless matrix affects scour development. The following six substrata were investigated: sand and five combinations of sand-Polywhite E clay (Pc ranging from 2.5 to 15%). The flow condition chosen were the nearest threshold velocity for sand alone. The results reveal that physical cohesion reduces the overall rate, extent and maximum depth of scour around monopiers. The scour morphology became increasingly irregular due to modification in erosion mode with an increase in slope steepness. A clay fraction of 10% was enough to reduce the equilibrium scour depth to the half and the excavated area by 75%.

Kothyari et al. 2014 [133] and Jain et al. 2021 [122] carried out laboratory experiments on scour in cohesive soils containing gravel. Two types of sediment mixtures were used: fine gravel was mixed with varied proportions of clay (Pc) and fine gravel and fine sand present in equal proportion by weight were mixed with varied proportions of clay (Pc). Kothyari et al. 2014 [133] focused on measuring the depth of scour only in the wake region of bridge piers. They used mobile beds with clay content (Pc) ranging from 20% to 60%. Experimental runs conducted using cohesive sediments ranged in duration from 3.42 hours to 15.67 hours. Jain et al. 2021 [122] aimed to evaluate the scour depth changes over time at both the wake and sides regions, over runs lasting 16 to 40 hours. The range of clay content (Pc) used in their study was from

10% to 50%. The results of [122, 133] revealed that a significant different scour hole shape from those in cohesionless soil was observed for a clay fraction ≥20 %. In cohesionless sediments, maximum scour depth occurs nearly always at the upstream of the pier, whereas mainly scour occurred in the wake zone of piers in cohesive sediments. Furthermore, a low to nul depth was recorded at the upstream of the pier in some cohesive sediment's situations (Figure I.30 (b)). Kothyari et al. 2014 [133] mentioned that for certain sediment's combinations, the scoured zone stretched downstream of the pier in the shape of a narrow but long strip (Figure I.30 (a)). Jain et al. 2021 [122] observed that the initiation of the scour in the case of cohesionless sediment from the sides of the pier immediately after starting the run. The scour hole then gradually extended to the noise of the pier where the maximum equilibrium scour depth was observed. The scour in the trials with cohesive sediment combinations initiated at the sides of the pier where flow separation occurred and typically continued there until it reached its maximum depth at the equilibrium stage. From experiments done by [122, 133]), a significant influence on the scour depth by the unconfined compressive strength and the clay fraction is noticed. As the unconfined compressive strength and clay fraction rise, the depth of scour decreased.

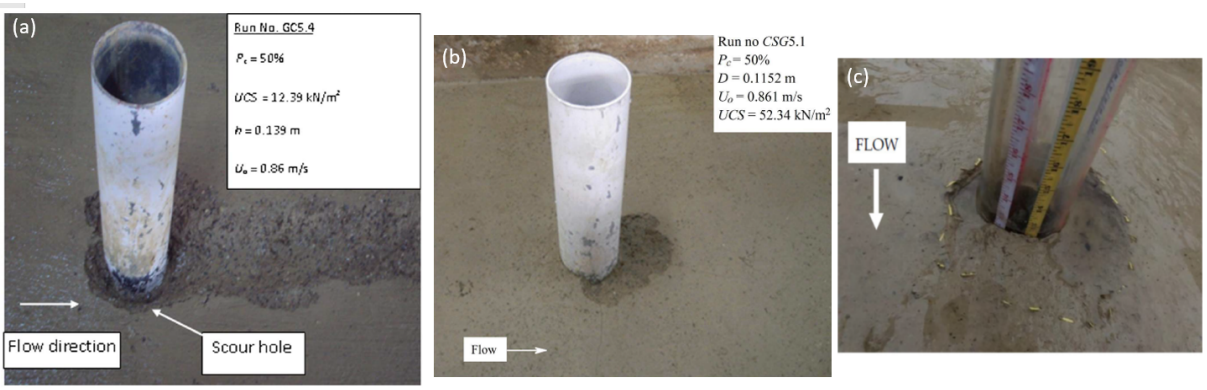

Figure I.30: Scour pattern (a): in Clay-Gravel mixture Kothyari et al. 2014 [133], (b): in Clay-Sand-Gravel mixture Jain et al. 2021 [122]; (c): in natural cohesive soil, U= 0.801 m/s, IWC=38% Malhader et al. 2021 [163]

Mahalder et al. 2021 [163] explored scour hole development around cylinder in natural cohesive sediment (3% sand, 72% silt, 25% clay) subjected to multiple flow events using different flow sequences. For all experiments, the flow shear strength and the Reynold number ReD were high. The observed scour hole in the wake zone had a larger lateral and transverse extent than other sides of the cylinder (Figure I.30 (c)). Rather than deepening at the same location, scour holes were seen down-cutting and spreading over time. The finding of this investigation regarding the scour hole propagation differed from those published by [82] and were more coherent with observations made by [249]. However, the scour depths at the pier's nose were greater than scour

depths at the wake zone with maximum scour depth at the sides of the pier. Depending on the soil bulk density, the maximum scour depths for the Low-Medium- High and High-Medium-Low flow sequences were similar. Scour rates were shown to be influenced by the bulk density and the initial flow velocity.

I.9 EMPIRICAL EQUATIONS FOR SCOUR DEPTH PREDICTION

When designing a bridge, accurately prediction of the maximum depth of scour in advance is crucial. This prediction helps determine the appropriate depth of the foundations and prevents instability of the structure. To achieve this, since the 1950s researchers have developed several empirical equations based on data obtained from model flumes or on-site structures. These equations consider three types of parameters (geotechnical, hydraulic, and structural) in different ways.

The general form of these equations can be described as follows:

$$Z_s = f\left(\begin{array}{c}\text{hydraulic parameters } (\rho_w, V, h, g, \nu),\\ \text{geotechnical parameters } (d_{50}, \sigma_g, \rho_s, V_c r),\\ \text{structural parameters } (b, K_i), \text{time}(t).\end{array}\right) \tag{I.10}$$

Where ρ_w representing the density of water (kg/m³), V the approaching velocity (m/s), h the water depth (m), g the gravitational constant (9.81 m/s²), ν the fluid viscosity (Pa·s), d50 the mean diameter of grains (m), σg the grain dispersion (-), ρs the sediment density (kg/m³), Vc the critical velocity (m/s), b the pier diameter (m), Ki the shape and angle of attack correction factors (-), and t the time (s).

Prediction methods in uniform and non-uniform cohesionless soils under clear water and live bed regimes were founded in several studies [14, 39, 94, 106, 168, 225, 229, 230]. These formulas were proposed based on laboratory data or/and site data in the colorado State University (CSU), an empirical formulation was recommended in the Hydraulic Engineering Circular 18 (HEC-18) manuel [14]. It was given by the following equation:

$$Z_s = 2K_1K_2K_3K_4K_w hFr^{0,43}\left(\frac{b}{h}\right)^{0,65} \tag{I.11}$$

Where, K_1, K_2, K_3, K_4, K_w are the correction factor for pier nose, angle of attack of flow, bed condition, size of bed material and shallow water respectively. Fr is the Froude number directly upstream of the pier $(V/(gh)^{1/2})$.

Reference	Empirical Relationship	Limitation
[173]	$\frac{Zcs}{b} = 18.9\left(\frac{Fr}{1+Pc}\right)^2$ $\theta_s = 1.422 + 0.06 \times Pc$ $B = 2 \times b + 2 \times \alpha_s \times Zcs$	For mixture soils Fr = 0.18-0.33; Pc$\leq$ 31%
	$\frac{Zcs}{b} = 0.9(\mathrm{IWC})^{-\frac{2}{3}}\mathrm{Fr}^{3/2}(\ \mathrm{Comp.}\ )^{-2}$	For cohesive soils IWC=0.15-0.5; Fr=0.18-0.51; Comp.= 0.58-1
[112]	$\mathrm{Z_{cs}} = 0.00018 Re_b^{0.635}$	–
[249]	$\mathrm{Z_{cs}} = 0.00012 Re_b^{0.682}$	–
[13]	$\frac{\mathrm{Z_{cs}}}{\mathrm{Z_s}} = 1.51\left(\frac{IWC}{IWC_*}\right)^{0.35}\left(\frac{C_*}{\emptyset_*}\right)^{0.2}$	PI=0
	$\frac{\mathrm{Z_{cs}}}{\mathrm{Z_s}} = \frac{6.02-10.82\left(\frac{IWC}{IWC_*}\right)+5.41\left(\frac{IWC}{IWC_*}\right)^2}{\left(\frac{C_*}{\emptyset_*}\right)^{0.2}}$	PI $\geq$ 4
[209]	$\frac{Z_{cS}}{b} = 0.124(Fr \times \mathrm{Reb} \times \left(\frac{\tau_{cr}}{\mathrm{VS}}\right))^{0.236}$	Fr=0.08-0.18; Reb=$10^4 - 3.6 \times 10^4$; τ_{cr}/VS=0.026-0.104
[128]	$\mathrm{Z_{cs}} = 0.0044\,\mathrm{Re_b}^{1.0234}(1 + \mathrm{Pc}/100)^{0.5}$ $\theta_s = 0.3205C + 30.84$ $B = Zcs/\tan\theta_s$	For mixture soils
[82]	$\frac{Zcs}{b} = 2.05\mathrm{Fr}_{(\mathrm{pier})}{}^{1.72}\mathrm{Pc}^{-1.29}\mathrm{VS}^{-0.37}$	IWC =20%-23.22%; Pc=20%-85%
	$\frac{Zcs}{b} = 3.64 Fr_{(pier)}^{0.22} Pc^{-1.01}\mathrm{VS}^{-0.69}$	IWC =27.95%-33.55%; Pc=20%-50%
	$\frac{Zcs}{b} = 20.52 Fr_{(pier)}^{1.28} P^{0.19}\mathrm{VS}^{-0.89}$	IWC =27.95%-33.55%; Pc=50%-100%
	$\frac{ZcS}{b} = 3.32 Fr_{(pier)}^{0.72} Pc^{-0.62} IWC^{0.36}\mathrm{VS}^{-0.29}$	IWC =33.60%-45.92%; Pc=20%-70%
	$\frac{ZcS}{b} = 8 Fr_{(pier)}^{0.62} Pc^{0.58} IWC^{1.24}\mathrm{VS}^{-0.19}$	IWC =33.60%-45.92%; Pc=70%-100%
[80]	$\frac{Zcs}{b} = 8.2 Fr_{(pier)}^{0.79} Pc^{-0.28} IWC^{0.15}\mathrm{VS}^{-0.38}$ $\frac{B}{b} = 22.77 Fr^{0.57} Pc^{-0.19} IWC^{0.2}\mathrm{VS}^{-0.26}$	IWC$\leq$ 40%; Pc$\leq$ 40%; V/Vcr(sand)=0.78-1.65
[181]	$\frac{Z_{cS}}{h} = 55565.05\left(\frac{VS}{\gamma_s \times h}\right)^{0.83} Pc^{-2.179}\mathrm{Fr}^{2.306}$	–
[177]	$\frac{Zcs}{b} = 0.656 + 2Fr_{(pier)} - 3Pc + IWC + \frac{1}{VS}$	IWC$\leq$ 40%; Pc$\leq$ 40%; V/Vcr(sand)=0.78-1.65
[133]	$\frac{\mathrm{Zcs(wake)}}{\mathrm{Zs}} = \frac{1}{[(1+PC)^{5.24}]\left[(1+UCS_*)^{0.42}\right](t_*^{-0.24})}$	For clay-gravel mixtures Pc=20%-60%
	$\frac{\mathrm{Zcs(wake)}}{\mathrm{Zs}} = \frac{1}{[(1+PC)^{5.98}]\left[(1+UCS_*)^{0.69}\right](t_*^{-0.42})}$	For clay-sand-gravel mixtures Pc=20%-60%
[122]	$\frac{\mathrm{Zcs(side)}}{\mathrm{Zs}} = 0.0102\left[(1+\mathrm{Pc})^{-9.7657}(1+UCS_*)^{-0.0914}(t_*)^{0.3385}\right]$ $\frac{\mathrm{Zcs(wake)}}{\mathrm{Zs}} = 0.004\left[(1+\mathrm{Pc})^{-3.577}(1+UCS_*)^{-0.238}(t_*)^{0.342}\right]$	For clay-gravel mixtures and clay-sand-gravel mixtures Pc=10%-20%
	$\frac{\mathrm{Zcs(side)}}{\mathrm{Zs}} = 0.0003\left[(1+\mathrm{Pc})^{-9.5363}(1+UCS_*)^{-0.3789}(t_*)^{0.6566}\right]$ $\frac{\mathrm{Zcs(wake)}}{\mathrm{Zs}} = 0.00001\left[(1+\mathrm{Pc})^{-8.715}(1+UCS_*)^{-0.232}(t_*)^{0.7513}\right]$	For clay-gravel mixtures and clay-sand-gravel mixtures Pc=30%-50%

Table I.2: Equilibrium pier scour predictive equations for Cohesive Sediment (see the nomenclature list page xx, xxi); In [13] empirical equations : $C_* = \frac{P_c \times C_u}{(\gamma_s - \gamma_w)d_{50}}$ and $\emptyset_* = \frac{P_c \tan(\emptyset c) + (1-P_c)\tan(\emptyset s)}{\tan(\emptyset s)}$; In [133] and [122] empirical equations : $UCS_* = \frac{UCS}{(\gamma_S - \gamma_W)d_{50}}$ and $t_* = t\left(\frac{\mathrm{Vcr}}{d_{50}}\right)$; The V_{cr} was estimated using the expression given by [124] in [209] equation and given by [107] in [133] and [122] equations

In some countries (such as France and Germany), predicting the scour depth in cohesive soil is still a problem in bridge foundation design [42]. In engineering companies, scour depth estimation methods used are those proposed for cohesionless bed, such the CSU equation. Concerning the proposed equation for cohesive bed, some researchers didn't take into account the significance of the properties of the cohesive bed [112, 249], while some others related it to cohesive soil properties [13, 80, 82, 122, 128, 132, 173, 177, 181, 190, 209]. Former predictions align with non-cohesive soil equations, while latter predictions decrease with higher clay percentage. Table I.2 above provides some of existing predictive equations of equilibrium scour depth in cohesive soil. Some equation for the prediction of side slope and the width of the scour hole were also presented. Particular attention was paid to the range of validity of the equations.

Briaud et al (1999 and 2005) [47, 56] developed a procedure known as the SRICOS (Scour Rate In COhesive Soils) method, recently introduced in HEC-18, for predicting scour in cohesive soils. It takes account of time-dependent scour in silts and clays, and requires EFA erosion tests on soil samples. This method generally results in shallower scour depths, which can translate into savings in bridge construction. This prediction method retains the essential variables introduced in previous methods and adds the crucial influence of soil erosion characteristics. keeps these essential variables while also adding the crucial influence of soil erosion characteristics. This prediction approach was relevant to the three types of scour: pier scour, contraction scour and abutment scour.

For a uniform soil layer and a constant flow velocity, the curve describing the scour depth Z versus time t used was well approximated by a hyperbola [41, 45, 55, 56, 112, 249] (Figure I.31).

$$Z_{max}(t) = \frac{t}{\frac{1}{\dot{Z}_i} + \frac{t}{Zeq}} \tag{I.12}$$

$Z_{max}(t)$ is the deepest scour depth observed at time t; Z_{max} is the deepest final scour depth reached at the end of an experiment which is run during a specific duration; $\dot{Z}_i$ is the initial scour rate, or the slope of the tangent line at the origin of the hyperbolic curve (Figure I.31); Zeq is the asymptotic value of the hyperbola or the deepest scour depth at the equilibrium state reached when a constant velocity is applied for infinite time (Figure I.31).
This method predict the equilibrium scour depth Zeq as well as the final scour depth Z_{max}.

In the NCHRP report 24-15, the SRICOS-EFA method was extended to the case of complex piers [48]. Complex piers refers to piers with different shapes, flow attack angles, side spacings

between piers and at any water depth. In the following, the predictive equations applicable in case of complex piers scour founded in uniform layer of soil and subjected to a constant velocity were presented in details.

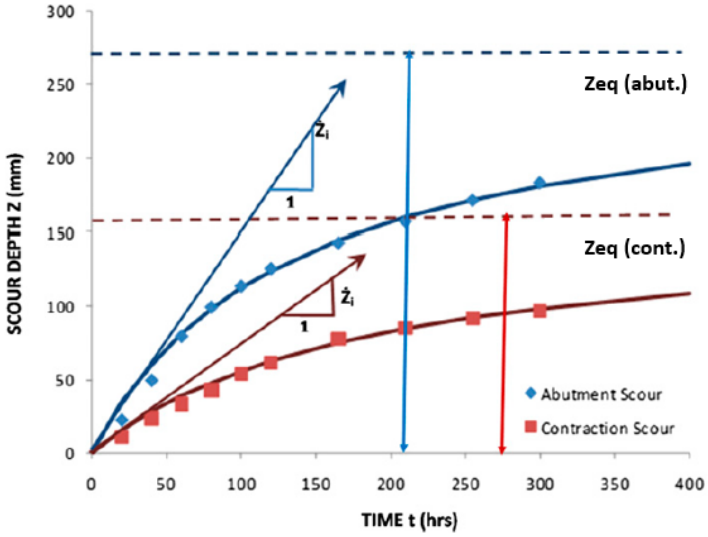

Figure I.31: Scour depth function of time curve for an example of abutment and contraction scour experiment (Briaud et al. 2015 (a) [41])

For the prediction of Z_{max}, the initial erosion rate $\dot{Z}_i$ is required. This represents the initial rate of erosion at the beginning of the scour hole development. The $\dot{Z}_i$ was determined by reading the erosion rate that corresponds to the calculated maximum initial shear stress $\tau_{\max}$(pier) in the erosion rate $\dot{Z}_i$ function of shear stress τ curve obtained using the EFA test. The $\tau_{\max}$ (pier) represents the initial maximum shear stress caused by the flow around a cylinder at the water-soil interface during the early stage of scour hole formation.
An equation to estimate the value of $\tau_{\max}$ (pier) was given by [189] as follows:

$$\tau_{\max(\text{pier})} = kw \times ksh \times ksk \times ksp \times 0.094 \times \rho_w \times \mathrm{V}^2 \times \left(\frac{1}{\log(Reb)} - \frac{1}{10}\right) \tag{I.13}$$

Where, kw, ksh, ksk and ksp are the influence factor for water depth, pier shape, attack angle and pier spacing respectively; ρ_w is the unit weight of water; V is the mean-depth velocity at the location of the pier if the pier was not there; Reb is the pier Reynolds number based on the width of the pier b ($Reb = Vb/\nu$), ν is the kinematic water viscosity ($\nu = 10^{-6}$ at temperature $20°C$). The expression on the right side of the equation, without considering the influencing factors, was derived for a circular pier in deep water $h/b' > 1.43$ by Wei et al. 1997 [260], where h is the water depth and b' is the projected width of the pier in the direction perpendicular to the flow direction. They conducted numerical simulations using CHEN4D (Computerized Hydraulic

ENgineering in 4Dimensions) software, which was developed by [69], for varying values of pier diameter and water velocity. Figure I.32 (a) presents the visualization of the location where the maximum shear stress was observed. The results of the simulations illustrating the relationship between the normalized maximum shear stress and Reynolds number were presented on Figure I.32 (b). If the maximum shear stress τ_{max} exceeds the critical shear stress of the tested soil τ_{cr}, it leads to the initiation of scour. The shear stress at the bottom of the hole τ_{bot} decreases as the scour hole deepens around the cylindrical pier. Figure I.32 (c) illustrates the profile of the shear stress at the bottom of the scour hole τ_{bot} as a function of the depth of the scour hole. The soil stops scouring and the scour hole reaches the final depth Z_{max} when τ_{bot} equals τ_{cr}. Using a parametric study through the basis of CHEN4D simulations by [189].

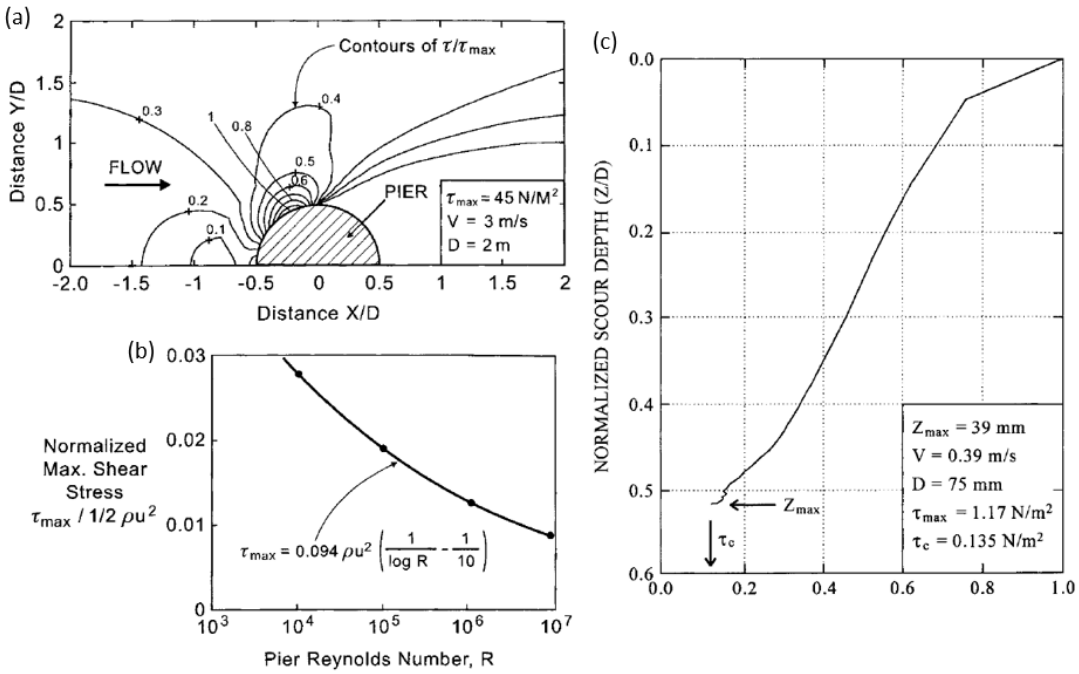

Figure I.32: Maximum shear stress around cylindrical pier τ_{max}(pier); Briaud et al. 1999 [56] (data from Wei et al. 1997 [260]) (a) Contour plot showing the distribution of shear stress; (b) Relationship between the maximum shear stress and Reynolds Number; (c) variation in shear stress at the scour hole's bottom function of its depth

The equation I.14 of Z_{eq}(pier) was developed on the basis of 47 large-scale laboratory flume tests performed on three types of clay and two types of sand by [112, 138, 153], followed by a dimensional analysis done by [190].

$$\frac{Zeq(pier)}{b'} = 2.2 \times Kw \times Ksh \times Ka \times Ksp \times (2.6 \times \mathrm{Fr}(pier) - \mathrm{Frc}(\text{ pier }))^{0.7} \tag{I.14}$$

$$\mathrm{Fr}(pier) = \frac{V}{\sqrt{gb'}};\ \mathrm{Frc}(pier) = \frac{V_{cr}}{\sqrt{gb'}};\ b' = b\left(\cos\theta + \frac{L}{b}\cdot\sin\theta\right)$$

The influence factors for water depth, pier shape, aspect ratio of a rectangular pier and pier spacing were Kw, Ksh, Ka and Ksp respectively. Using the projected width b' instead of b, the aspect ratio influence factor Ka was eliminated. In the formula of b', L corresponds to the length of the pier (m) and θ is the attack angle, the angle between the flow direction and the longitudinal axis of the pier. The critical velocity Vc, characterizing the resistance of the soil, in the equation I.14 was measured using the Erosion Function Apparatus (EFA) [55]. The suitability of equation I.14 for various soil types, including sands, can be implicated from the use of the Vcr reflecting the soil parameters [40, 190].

Notes that the equations of τ_{max} and Z_{eq} for contraction and abutment scour in case of constant velocity and uniform soil layer were differents than pier scour and were presented in [41, 42].

This method was extended by creating robust algorithms to accumulate the scour depths of a sequence of flood velocities and a layered soils system by [45]. These contributions enable the engineer to make the predictions of the maximum scour depth in any complexes scenari in laboratories and field. A distinction between S-SRICOS (Simplified-SRICOS) and E-SRICOS (Extended-SRICOS) was identified. The simplified version of this method required only manual calculations and can be used for preliminary design purposes, as it is fast. This method used an equivalent time t_e for a constant design velocity v_{max} history. The equivalent time t_e is the time needed for the design velocity in the hydrograph to produce the same scour depth as that produced by the full hydrograph. The expression of te was function of the hydrograph duration t_{hydro}, design hydrograph velocity v_{max} and initial erosion rate Z_i. The design velocity was selected usually from the 100 year flood or the 500 year flood. In addition, the simplified method was based on the creation of a single equivalent erosion function which was the average erosion functions over the anticipated scour depth. On the other hand, the extend version required the use of the complete hydrograph using a computer program, SRICOS-EFA ,or, TAMU-scour (which was software in the window environment). This program was developed to automate all the calculations for all types of scour in addition to the sum of various types of scour [46, 140]. The output of the program is the scour depth versus time curve over the period of the hydrograph. Erodibility data involved in the soil stratigraphy was needed. Soil sample, which was collected in shelby tube from the site, should be tested in the EFA. In addition, the flow hydrograph recorded from nearby gauge station or from the internet, such as USGS website, should be transformed to velocity hydrograph (velocity function of time) using the HEC-RAS program [59]. This transformation was performed with knowledge of the cross section geometry

of the river, channel slope and roughness (Manning coefficient).

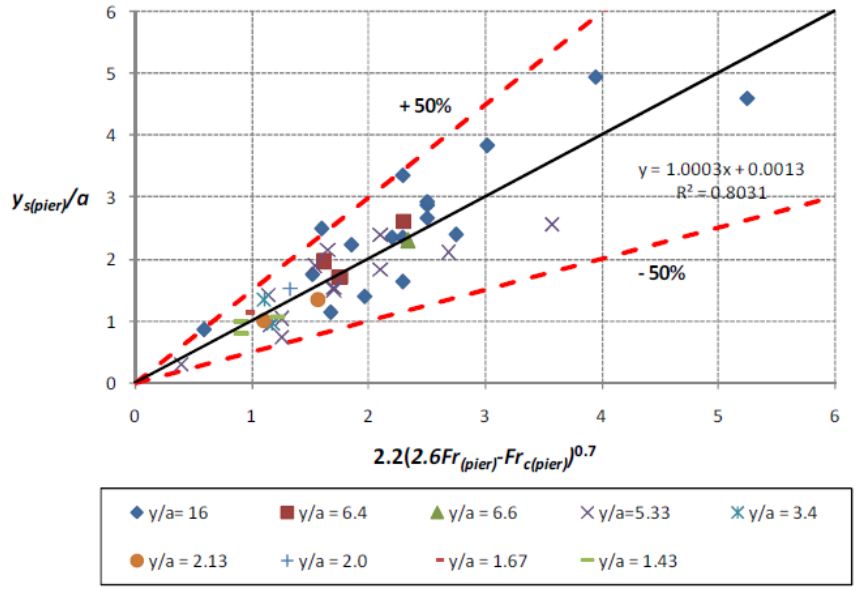

Figure I.33: Prediction versus flume measurement for circular pier scour in deep water condition; a is the pier diameter D, ys(pier) is the equilibrium scour depth Zeq(pier), y is the approach water depth flow hw; Oh 2009 [190]

This predictive method of the scour depths was evaluated by comparison with laboratory flume tests [120, 190] and field pier scour observations [106, 115, 139, 148, 239, 250]. Figure I.33 compares the results of the flume tests at TAMU with the prediction equation I.14 for circular pier in deep water condition, without the infuence factors and where b' in the equation is the diameter of the pier b. All experiment findings are almost in agreement with the prediction method affected by a factor of safety of 1.5 [190]. Hassan et al. 2020 [120] compared flume measurements of scour depths around two-in line (tandem) circular piers founded in a clay-sand bed with TAMU-scour method. They observed that the predictive method overestimates the depths of scour at both the upstream and downstream piers. The overestimation of the scour depths may be attributed for the following reasons. In the critical pier Froude number, the critical velocity for sand fraction thresholds in the clay-sand bed soil was used, and was not the value measured on a mixture sample using the EFA test. In addition the value of spacing used was the spacing in the line parallel to the flow, and was not the side by side spacing. The field measurements databases available in [106, 148] were used to evaluate the accuracy of this method. These databases were primarily associated with coarse-grained soils. The majority of the measured field data was kept on the safe side when the prediction values were multiplied by a factor of 1.5, effectively converting the prediction approach into a design method. The predicted

versus measured plots show that there was larger scatter for full-scale observations compared to laboratory investigations. Some of the explanations suggested for this increased scatter include the lack of site-specific information on soil erodibility and the unreliability of the velocity linked to the scour depth readings. This method was also used for evaluating the scour depths in field studies in cohesive soils by various authors [45, 115, 139, 239, 250].

In addition, a framework for the probabilistic design and risk assessment of scour-exposed bridge foundations was provided by this approach. It allowed the development of a curve for the probability of exceedance of the predicted scour depth [29, 35, 43]. It allowed to make modification on the resistance factors in the probabilistic formulation LRFD bridge design specifications using AASHTO [1] guidelines [49]. This was done to provide the same target reliability index and probability of failure while accounting for the scour depth, its bias,and its uncertainty. In 2012, this method was incorporated in the HEC-18 manual (5th edition) [14] and was called HEC-18 Clay [28, 49, 51, 267].

SYNTHESIS

In last decades, significant efforts have been achieved in laboratory-based bridge scour research, aiming to comprehend its physical mechanisms and control factors. Flume studies has been conducted extensively on the scour around circular bridge pier on cohesionless bed e.g. [16, 86, 167, 211, 230]. However, many natural alluvial channels consist of cohesive materials or a mixture of cohesionless and cohesive sediments [132]. Comparatively, limited researches on local scour around cylinder on cohesive beds have been reported.

Previous studies either investigated the influence of cohesion on local scour around piers using cohesive (clayey) soil [155, 163, 181, 209, 249] or non-cohesive and cohesive sediment mixture [13, 66, 122, 173]. Non-cohesive soil, mainly sand, was commonly used, excepted [122, 133], who included gravel. Cohesive soil, a clay composed of sand, silt, and clay particles, was used by [66, 87, 173]. The cohesive soil used in the prior flume tests was collected from field [155, 163, 173, 181, 209] or was commercially available [56, 249]. Molinas and Hosny. 1999 [173] reported high local scour resistance in saturated cohesive soil with low water content and in unsaturated cohesive soil with high compaction. Ting et al. 2001 [249] observed that scour depths in the nose and wake regions of the pier were similar when pier Reynolds number ReD was low (10000-15200); nevertheless, scour depths in the wake region were greater than in the nose zone when ReD values were higher (15300-84840). Debnath et al. 2010 a [82] argued that

the findings of [249] may not be universally applicable. They identified that the combination of bed shear stress caused by flow and bed shear stress strength determines whether the upstream or downstream portion of the pier has a greater scour depth. Recently, Mahalder et al. 2021 [163] deviated from the statement of [82] and were more consistent with [249]. To cover the spectrum of cohesive sediment sizes and sediment combinations found in river bed, it is important to examine the scouring phenomenon and measure the geometric characteristics of holes formed around bridge piers in soil beds with varying mixtures of sand and fines. This study maintains consistent proportions of these components while altering the specific type of fines. The primary focus of this thesis is to assess how changes in the type of fines content influence both the geometry of the scour hole and the temporal progression of scour processes around circular piers, a question not addressed in previous studies.

In certain countries, as France and Germany, there remains a challenge in predicting scour depth for bridge foundation design, especially in cohesive soil conditions [42]. In engineering companies, scour depth estimation methods primarily rely on equations designed for non-cohesive beds, such as the CSU equation. This can lead to an overestimated depth causing unnecessary increase in construction costs. Based on flume studies of pier scour in cohesive sediments e.g. [122, 173, 181], various empirical formulas were proposed to estimate the maximum scour depth as a function of sediment properties, flow parameters and pier shape. The more general one was the SRICOS-EFA method (also known as TAMU-SCOUR) developed by Briaud [41, 42, 56]. It has the advantage compared to others of being time dependent and takes into consideration the soil erosion characteristics measured by the erodimeter “Erosion Function Apparatus” (EFA). Oh. 2009 [190] suggested that the SRICOS method should be affected by a factor of safety 1.5. In this study, the maximum scour depth over time obtained experimentally is compared to the SRICOS-EFA prediction approach.

A wide range of measurement techniques has been used for the monitoring of pier scour in laboratory scale. These include traditional methods like gauges [147, 191] or scales [82, 266], as well as more advanced approaches like acoustic sensors [16, 216], photogrammetry [17, 31], laser technology (laser distance sensors [90, 156], profilometer laser technique [143] and scanner laser [162, 234]). The scanner in previous studies e.g. [162, 234] was commonly used after the drainage of the water in the flume. In this thesis, we investigate the potential of using 3D Laser Scanner to capture the dynamic topographic bed deformation induced by the pier scouring process continuously in a laboratory flume experiment.

Chapter II :

Experimental set-ups and methods

INTRODUCTION

The aim of this chapter is to present the experimental set-ups as well as the different measurement methods used in our study.
The sediments and their main geotechnical properties are presented. The experimental flume test model design, set-up choices, assessments, modifications and protocols are described. The measurement methods implemented to obtain information about the hydraulic conditions and those applied to monitor the soil bed during the scour process are described. The erosion function apparatus (EFA) used to quantify the erodibility of all tested soils is presented.

II.1 MATERIALS

During the scour experiments, the test section of the flume was filled with soil modeling the river bed. Different types of soils were used, exhibiting different geotechnical characteristics. The different types of sediments used are summarized in Figure II.1 : medium sand (Hostun Sand HN 1/2.5), fine sand (Fontainebleau Sand NE34), natural Silt and Kaolinite Proclay Clay. The Fontainebleau Sand NE34 was provided by Sibelco. The silt was collected from the top layer of the eastern area of Paris (France). The Kaolinite Proclay Clay was provided by IMERYS Ceramics.
The typical medium sand having a well known behaviour in clear water scouring regime around a circular pier, according to the literature, is used during the first flume tests. These tests were performed in order to validate the performance of the developed topographic measurement method developed for this concern.
Then, to better understand the effect of cohesive soil type on local scour around a pier, an issue not addressed in previous studies, two types of cohesive soil (silt, Kaolinite clay) were mixed

with 85% fine sand. The cohesive soil mixed with 85% sand was composed successively of 15% silt, 10% silt and 5% clay, 7.5% silt and 7.5% clay, 5% silt and 10% clay and finally 15% clay.

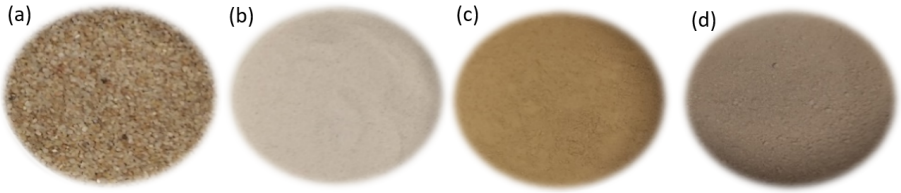

Figure II.1: Original sediments used, (a): Hostun Sand HN1/2.5, (b): Fontainebleau Sand NE34, (c): Natural Silt, (d): Kaolinite Proclay

A multistage procedure was carried out to transform the silt collected from field into fine sieved laboratory soil ((Figure II.2)).

1. The original silt is passed through the sieve #40 (400 µm opening). Then, the fraction of silt obtained is re-passed by the sieve #170 (80 µm opening) using the wet method sieving. After passing the silt through each sieve, the silt is rested for 24 hours to settle and then the excess of water is removed. This step takes in total 4 days to be accomplished.

2. The silt is dried in the oven at 105 °C for 24 h. The dry silt was in form of large thick plate.

3. Finally, the silt goes through two stages of crushing with different opening sizes (2 mm then 0.4 mm) in a jaw crusher.

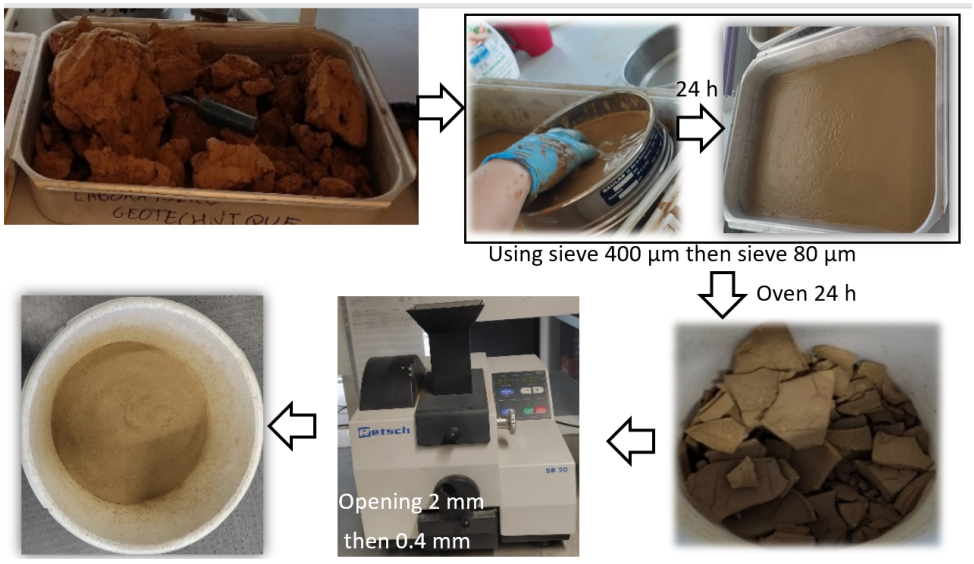

Figure II.2: Different steps of silt preparation

II.2 GEOTECHNICAL PROPERTIES OF TESTED SOILS

Figure II.3 shows the different devices used to study the geotechnical properties of the soils used, according to the experimental procedures described by the French Standards Association (AFNOR).

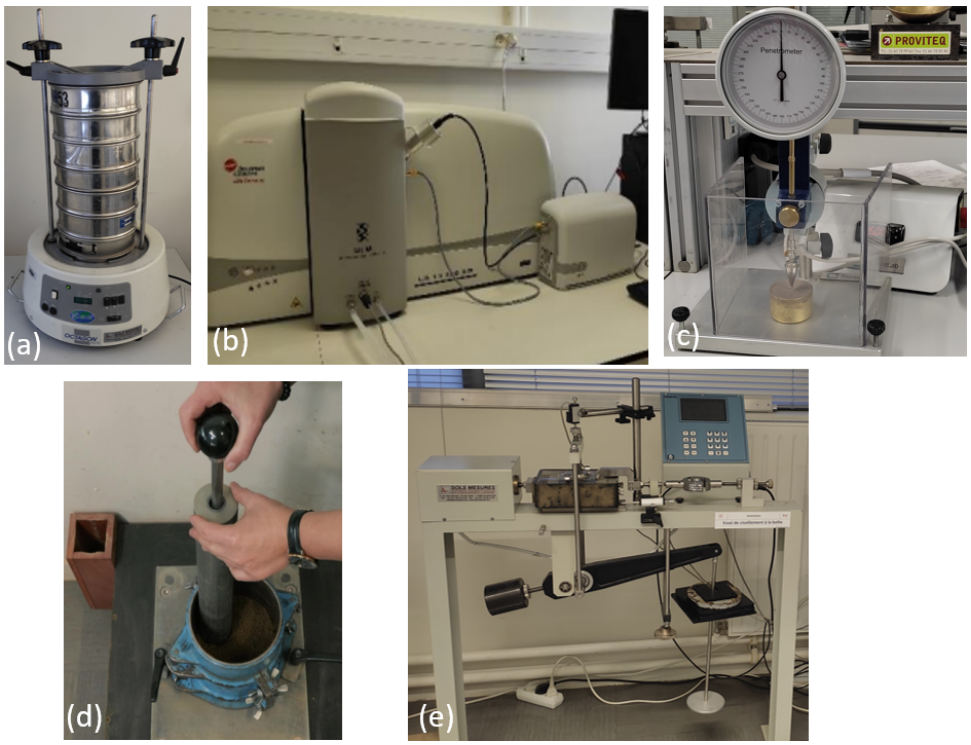

Figure II.3: Geotechnical characterization devices, (a): sieve apparatus, (b): laser diffraction device, (c): cone penetrometer, (d): standard normal Proctor test and (e): direct shear test

The particle size distribution curves of the medium sand, the two cohesive materials and the fine sand with the five made mixtures are presented in Figure II.4. The sieve method (Figure II.3(a)) was used for the granular medium sand HN 1/2.5 and laser diffraction method (Figure II.3(b)) for the fine soils. The main characteristic parameters obtained from the particle size distribution curves are summarized in Table II.1. The d_i is the sediment diameter for which i% of the sediment material is finer by weight. The median d_{50} gives an indication of the average coarseness of the sediment. The σ_g which represents the geometric standard deviation of Soulsby [236] is a dispersion index which is widely used in the sedimentology. If $\sigma_g^2 < 2$ the granulometry is considered as well sorted and as widely dispersed if $\sigma_g^2 > 16$. The granulometry of the two pure sands are thus considered as well sorted and of other soils includes a dispersion. In particular the 85% fine sand mixed to 15% clay has a widely dispersed granulometry.

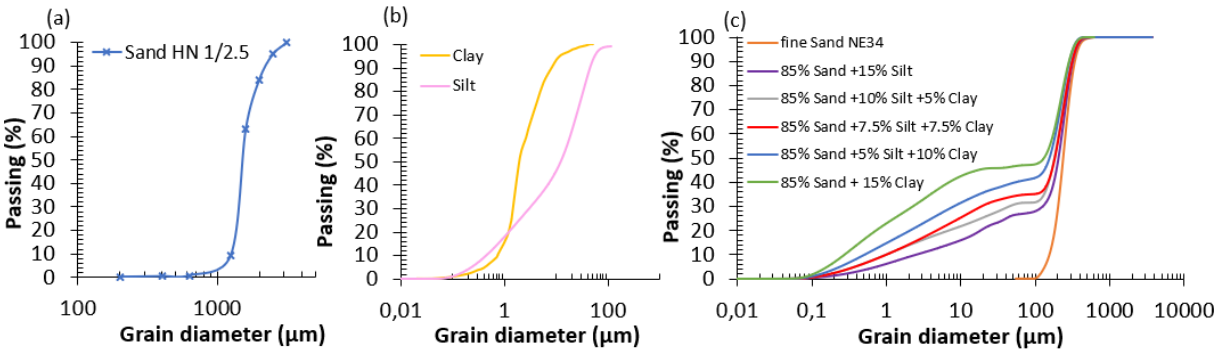

Figure II.4: Particle size distribution curves, (a): medium sand, (b): cohesive soils used, (c): the fine sand with the made mixture

	Sand HN1/2.5	**Sand NE34**	**Silt**	**Clay**	**M1**	**M2**	**M3**	**M4**	**M5**
Sand particle $d > 63\ \mu m\ (\%)$	100	100	2	0	73	69	65,3	59,5	53
Silt particle $2\ \mu m < d < 63\ \mu m\ (\%)$	0	0	73	50	18	17	18,7	20,5	19
Clay particle $d < 2\ \mu m\ (\%)$	0	0	25	50	9	14	16	20	28
Medium diameter $d_{50}(\mu m)$	1700	210	12	2	195	180	175	150	120
Geometric standard deviation $\sigma_g=(\frac{d_{84}}{d_{16}})^{0,5}$	1.2	1.3	6.7	2.6	4.9	9.4	10.5	14.1	22.4

Table II.1: Parameters determined from the particle size distribution curves where M1: 85% Sand +15% Silt, M2: 85% Sand +10% Silt +5% Clay, M3: 85% Sand +7.5% Silt +7.5% Clay, M4: 85% Sand +5% Silt +10% Clay and M5: 85% Sand +15% Clay

Concerning the Atterberg limits tests, soil samples should consist of material passing the sieve # 40 (400 μm opening). The liquid limit (WL) was measured by the cone penetrometer method (Figure II.3 (c)) and the plastic limit (WP) by the roller method. According to the plasticity chart of Casagrande, the soil can be classified as function of the plasticity index (IP) and the liquid limit (WL). The results displayed in the Table II.2 below indicated that the clay has high plasticity, the silt has low plasticity and the other soils are non-plastic.

Standard normal Proctor tests (Figure II.3 (d)) were performed on all the mixture soils tested in the flume. The results indicated that the optimum dry unit weight and the optimum water

	Liquid Limit $WL(\%)$	**Plastic Limit** $WP(\%)$	**Plasticity Index** IP **(%)**
Clay	55	31	24
Silt	34.9	23.7	11.2
100 % Sand	6.0	NP	NP
85 % Sand +15 % Silt	19.0	NP	NP
85 % Sand +10 % Silt+5 % Clay	19.5	NP	NP
85 % Sand +7.5 % Silt+7.5 % Clay	20	NP	NP
85 % Sand +5 % Silt+10 % Clay	21.5	NP	NP
85 % Sand +15 % Clay	23.0	NP	NP

Table II.2: Atterberg Limits test results. NP: Non-Plastic

content for the mixture soils is around 1890-1980 kg/m3 and 8.5-10% respectively (Figure II.5). In literature, [156, 173] noted that as compaction levels increase, scour depth tends to decrease. Furthermore, studies by [80, 82, 181] observed a reduction in scour depth as the initial water content of the cohesive bed rises. In our experiments, the compaction level and the initial water content were fixed. The initial water content was fixed to 5% (±1%) which was sufficient to slightly humidify all soils matrix. The 5% (±1%) water content gives a minimum dry volumetric mass equals to 95% the optimum dry volumetric mass of the tested soil according to the Proctor tests results. When applying the proposed methodology of soil preparation in the flume, which will be described in section II.3.5.3, it was not possible to have higher water content value because the soil, having some cohesion in presence of high percentage of water, sticks to the plate used for compaction purpose. In order to confirm the uniformity of compaction, for all tested fine soils at three different location in the flume test section, the dry density was measured using core cutter method. The range of average values obtained was 1650-1800 kg/m3, which correspond to a relative constant degree of compaction in the range of 83-95% of the optimum Proctor of all tested mixture soils (Figure II.5). The range of average values of the dry densities chosen was close to the values that can be found on real sites being in the order of magnitude (1300-2040 kg/m3) [45]. The bed was reconstructed at these areas before the experiment began.

Direct shear tests (Figure II.3 (e)) in Drained Consolidated conditions were achieved in order to provide the shear strength parameters for all tested soils. A 6 cm diameter circular metal box is used for the tests. Firstly, the sample is prepared under geotechnical conditions similar to those of the flume test. After placing the specimen in the shear box, it was saturated during 1 hour. The consolidation of the sample was maintained 1 h which was sufficient to ensure that no more vertical settlement is observed. Samples were tested through several vertical stresses from 100 to

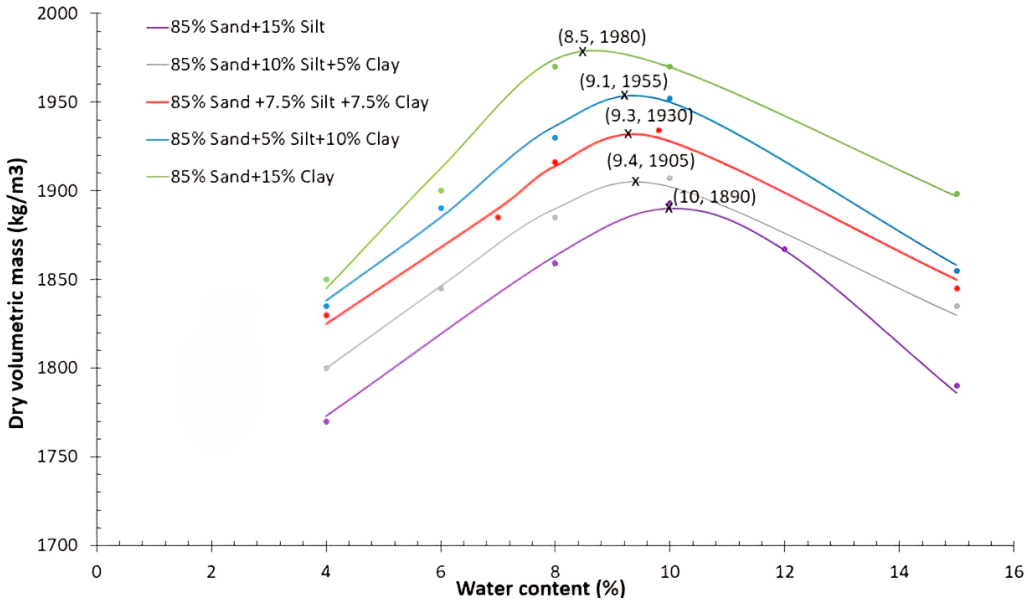

Figure II.5: Standard Proctor test results

300 kPa with an increment of 50 kPa. After the consolidation step, the soil sample is sheared with a control strain rate of 0.01 mm/min. This low strain rate is chosen to achieve the best reliable results with a high precision. The applied lateral load (shear stress) is continuously recorded during the test with a rate of 1 measurement each 10 seconds. The shear test was stopped when the horizontal displacement reached i.e. 12% of the diameter of the specimen, 7.2 mm for a total duration of 12 hours.

Figure II.6 illustrates the results obtained for all fine soils of maximum shear stress as function of the normal stress.

According to Mohr-Coulomb failure criterion, the line that represents the failure envelop can be expressed as follow:

$$\tau = C + tan(\Phi)\sigma \tag{II.1}$$

Where τ, σ, C and Φ are the shear stress, normal stress, cohesion and internal friction angle respectively.

The linear fitting of Mohr-Coulomb curve is plotted to derive the values of cohesion and internal friction angle for all the soils.

Table II.3 provides a summary of cohesion and internal friction angles obtained for all tested soils.

The findings indicate that as the fines content is increased, the soil will have more cohesion whereas the friction angle is reduced. It can be noted that Kaolinite exhibits a more pronounced cohesive effect than silt. The pure sands (medium and fine) have non-cohesion with high internal friction angle.

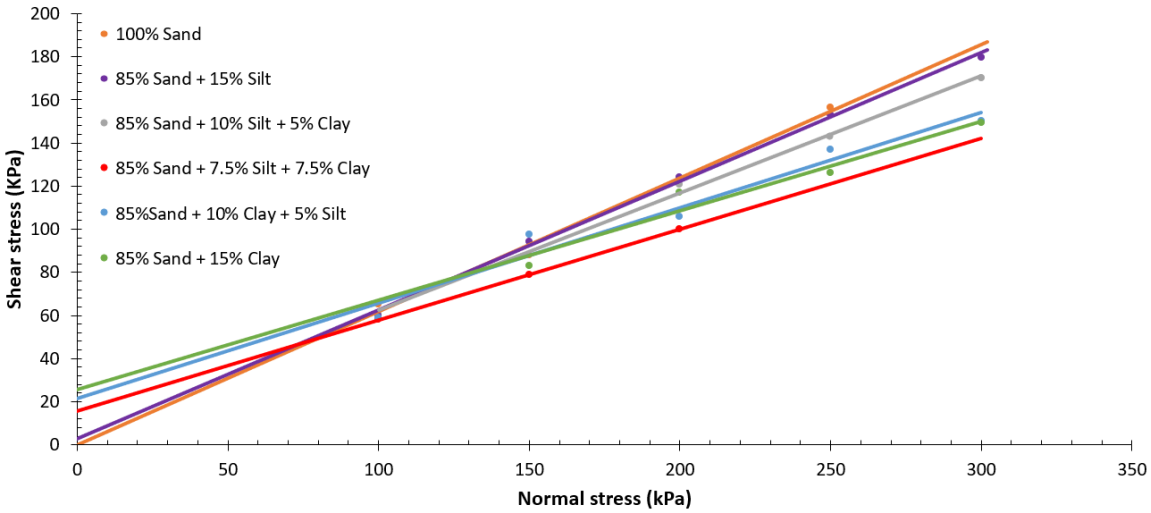

Figure II.6: Mohr-Coulomb Failure envelop for the fine soils

	Sand HN1/2.5	Sand NE34	M1	M2	M3	M4	M5
Cohesion (kPa)	0	0	2.8	8.2	15.9	21.4	25.5
Angle of internal friction (°)	35	31.7	30.8	28.5	22.8	23.8	22.5

Table II.3: Cohesion and angle of internal friction results, where M1: 85% Sand +15% Silt, M2: 85% Sand +10% Silt +5% Clay, M3: 85% Sand +7.5% Silt +7.5% Clay, M4: 85% Sand +5% Silt +10% Clay and M5: 85% Sand +15% Clay

II.3 HYDRAULIC FLUME

II.3.1 *Description*

In research, the hydraulic flume was used largely to observe and analyze the scour phenomenon at the laboratory scale [80, 156, 181]. In this study, the main experiments are conducted in the recirculating rectangular hydraulic flume of ESTP whose 3D view is illustrated on Figure II.7. Water flows from the entrance element through a flow rectifier consisting of two perforated sheet metal plates. The rectifier reduces the turbulence and creates a more linear flow [175]. Above this rectifier, a damping plate floats on the surface of the water preventing water from spraying upwards. The central section element where the measurements occurred, consists of several plate elements installed next to each other. The flow measuring section is rectangular with 410 mm wide, 500 mm deep with a central useful length of 10 m. The total length of the flume is 13 m. There is a system to adjust the inclination of the flume in a range of -0.5% and +2.5% with a graduation of 0.1%. The walls of the flume are made of glass in order to allow the visualization of the experiments carried out by using optical sensors. The horizontal position of the accessories

installed may be read on horizontal graduated scales above and below the glass wall. Threaded bores are located at the bottom of the central section of the flume, spaced by 0.25 m apart. In the outlet element, a rotate tail gate is installed to regulate the water level by a hand wheel. It consists of two plates: the top plate is removed and the bottom one is installed. The water must rise above the crest height of the gate. A sediment trap is located at 1.6 m from the gate in the opposite direction of the water flow. The centrifugal pump with three-phase motor is fixed to the ground by means of a base plate. A shut-off valve is installed on the back flow side of the pump. The flow rate is automatically regulated by a frequency converter for the flow velocity control. It can provide a minimum flow rate of 15 m^3/h and a maximum of 130 m^3/h. A flow meter is installed at the level of the re-circulation pipe between the water pump and the inlet element. The measured flow rate is displayed on the control panel as the real flow rate value and can be adjusted by the operator to the desired target value. Float switches are placed in the intlet and outlet elements. When the water level reaches a height of 450 mm, the power supply is interrupted to prevent water overflow. In the 3D view above, only two water tanks are illustrated to simplify the representation but, in the reality, there are five water tanks in the used flume which are connected to each other. Being connected to each other, the filling/evacuation of one tank (generally the primary tank) with water allows the filling/evacuation of all five tanks with water in a homogeneous way. Each tank has a length of 2 m, a width of 1 m and a height of 0.79 m and a capacity of water volume around 1 100 L. A metallic walkway gallery is located on the side of the flume to facilitate the achievement of experiments.

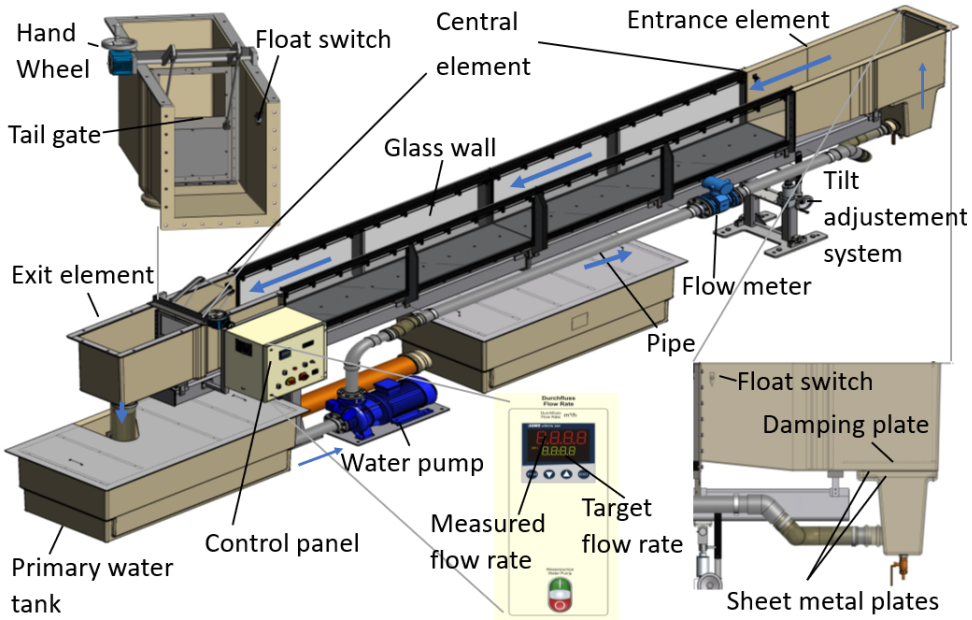

Figure II.7: A 3D view of the Hydraulic Flume of the ESTP Paris (not at scale), the direction of the flow is indicated by blue arrows

II.3.2 *Physical scour model implemented*

A simplified overview of the physical scour model implemented in the flume is illustrated in Figure II.8. A recess area extending 1 m in length and 0.062 m in depth was installed at 6.6 m from the entrance of the flume. To contain the soil, a false bottom floor made of PVC (Poly Vinyl Chloride), with the same height of the recess area, was installed upstream and downstream. The false bottom allows a uniform small roughness along the whole flume corresponding to hydraulic smooth condition. The upstream part measured 5 m in length (1 m per plate) with the first plate including a slope of 20°. The downstream part is formed by two plates, the first plate of 0.6 m length is adjacent to the soil sample and the second one of 2 m length containing a gradual slope of (2%)°. The various plates of false bottom are put next to each other and are screwed to the stainless-steel bottom of the flume. Silicones are put along the connection between the different plates of false bottom and between the plates of false bottom and the flume wall to avoid any leakage (Figure II.9 (b)).

Concerning the choice of the pier, it was observed by [241] that hydro-dynamically smooth external surface of the pier has a beneficial effect on the scouring process. PVC piers are fairly smooth and have therefore been used as model piers in current scour studies. A hollow PVC cylinder with chamfer at the bottom was firstly tested. The installation after the preparation of the soil of this type of cylinder had a significant impact on the initial soil's surface in contact with the pier and it was difficult to maintain the cylinder's verticality (Figure II.9 (a)). This led us to use a filled cylindrical PVC pier which was positioned vertically at the center of the soil section before the soil preparation. A threaded rod is added at the bottom of this pier and is used to screwing it to the bottom of the flume. The Figure II.9 (b) shows a zoom in of this cylinder configuration chosen. Two plastic wires are used to connect this cylinder to the right and left sides of the flume to prevent its vibration. This cylinder, used to model the pier of the bridge, was 0.032 m in diameter, 1 m in length. The model's pier diameter to flume width ratio (0.078) was below the limit of 1/6 to prevent the effect of flow constriction [261]. For circular piers section, the reported extent of scour depth is 1 to 2.5 times the diameter [95, 244]. In our tests, for the experimental conditions considered, the depth of the pit where the soil was placed, around 2 times the diameter of the pier, was observed to be sufficient to allow the full development of the maximum scour depth observed. A significant rise in erosion thresholds over a salinity gradient has been reported by [237]. In our case, the water used is tap water with a relatively low salinity, and is therefore considered to have a negligible effect.

In the following sections, we will discuss in details all the measuring instruments (Level Gauge, Vectrino and 3D Scanner) that were purchased, developed and used for the first time in ESTP laboratory.

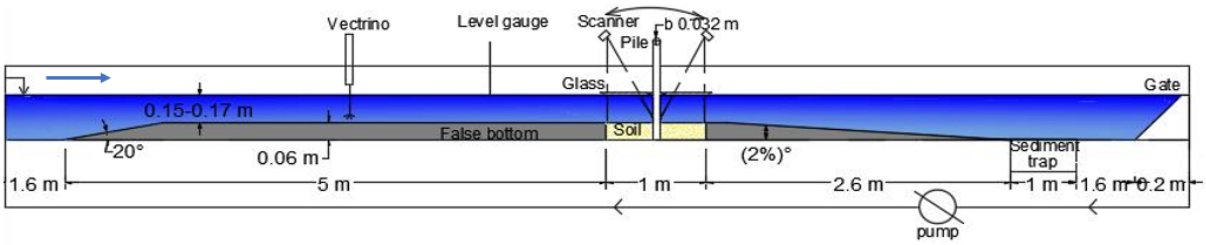

Figure II.8: Flume set-up scheme (not at scale), the direction of the flow is indicated by blue arrows

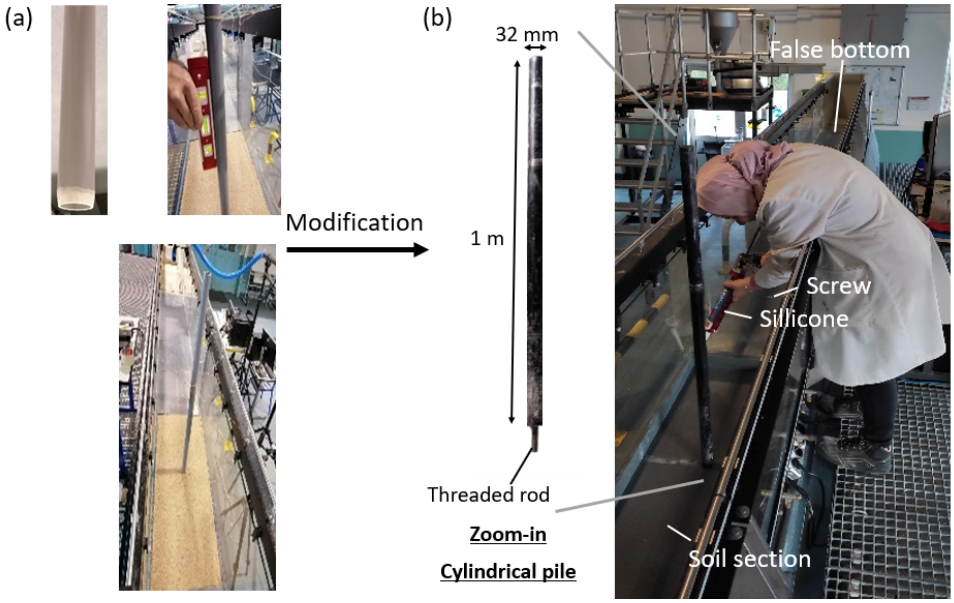

Figure II.9: Photograph of the physical scour model (a): test on hollow cylinder, (b): filled cylinder and false bottom installation

II.3.3 *Water depth measurement: Manual Level Gauge*

A manual level gauge is used to measure the depth of the flow with an uncertainty of measurement around ±0.5 mm in the flume (Figure II.10). It consists of a rod ending by a contact point. The rod can be moved vertically. The contact point is designed in such a way that when it touches the water surface, it forms a meniscus. A depth flow display scale is located on the top of the level gauge, with a range from 0 to 500 mm and a 1 mm graduation. The position of the zero scale is set before taking the measurements. It is adjusted to have a zero displayed depth value when the point of the rod is in contact with the false bottom of the flume. It's mounted on a

mobile support and can be used over the entire length and width of the test section. The water depth measurement was done always at 1.5 m from the upstream edge of the soil section in the opposite direction of the flow, where the water flow was undisturbed. The flow depth is always maintained constant during the entire duration of the test.

Figure II.10: Manual Level Gauge

II.3.4 *Velocity measurement: Acoustic Doppler Velocimetry*

II.3.4.1 *Description*

The velocity profiles over the false bottom were measured using an Acoustic Doppler Velocity Profiler (ADVP) called Nortek Vectrino Profiler. The vectrino profiler is a profiling version of a vectrino which was primarily developed for laboratory measurement.

Figure II.11 gives an overview of the main components of this device. It is composed of a pressure housing, probe and measuring head. The measuring head comprises central transmitter surrounded by four receivers which inclined 30°towards the center. It is a bistatic system as the emitter and the receiver are physically separated. These mechanical components were combined with an acquisition software “Multi-Instrument Data Acquisition System (MIDAS)” which is used to configure the instrument, collect, display in real time and save data [186].

The processing of the device is based on pulse-coherent technique [187]. In fact, the central transmitter sends two continuous pulses with a time lag which propagate and are backscattered

by the seed particle in suspension. The doppler effect induces a phase shift which is recorded by each receiver. A temperature sensor is embedded in the probe so the speed of sound can be correctly determined. The Vectrino Profiler uses this phase shifts and the speed of sound to estimate the velocity of beam receiver, as shown below (Equation II.2).

$$Vbeam = \frac{\Delta\phi C}{4\pi f \Delta t} \tag{II.2}$$

Where, $\Delta\phi$, C, f and Δt are phase difference, speed of sound, transmitted frequency and time difference between two consecutive pulses.

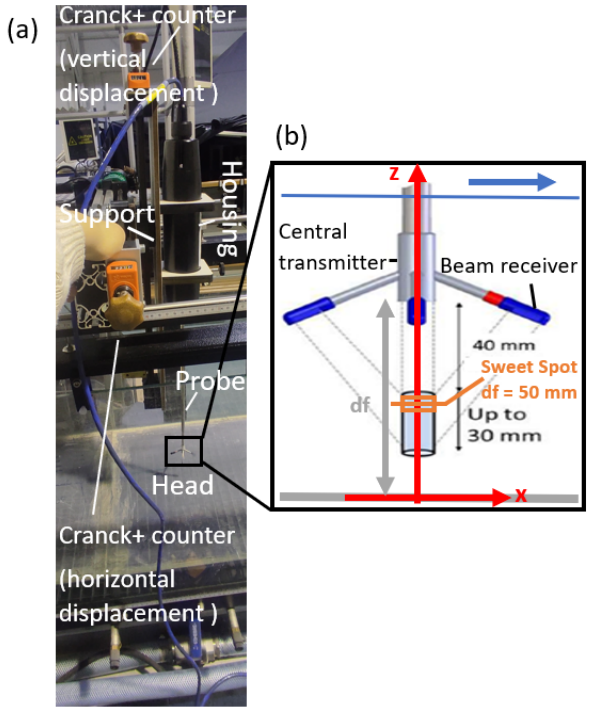

Figure II.11: Nortek Vectrino Profiler, (a): Installation of the Vectrino on the flume, (b): notation and sampling volume after [187], the direction of the flow is indicated by blue arrows

The manufacturer performs a calibration of the probe geometry, which is used to determine the transformation coefficient from beam coordinates to XYZ coordinates. Receivers 1 and 3 are used to estimate the horizontal component in the x direction, u, and the first vertical component in the z direction, w1. Receivers 2 and 4 are used to estimate the horizontal component in the y direction, v, and the second vertical component in the z direction, w2.

The accuracy of the velocity measurement provided by the manufacturer is "± 0.5% of the measured value ± 1 mm s^{-1}" [188]. The vertical spatial resolution of the device can be adjusted between 1 and 4 mm. The velocity data acquisition frequency can be chosen between 1 and 100

Hz.

The elevation of the bottom floor relative to the central transmitter (df) is also obtained by the recording of a simple echo. When the transmited pulse hits the bottom, a strong echo is produced. The bottom check data are sampled and can be taken at a rate between 1 and 10 Hz. The measurements of velocity and bottom floor position are performed simultaneously. The ADVP provides up to 30 mm length of the velocity profile between 40 and 70 mm from the transmitter.

The constant transformation matrix determined by the manufacturer is ineffective when applied to the entire velocity profile. Indeed, the geometry of the probe causes a decrease in signal quality (signal-to-noise ratio, amplitude and signal correlation) on either side of the point of maximum quality, located 50 mm from the transmitter and following a parabolic profile shape. At 50 mm, the 4 beams show a maximum overlap, creating an area called the "sweet-spot" (Figure II.11). Within a range of 10 mm around this maximum beam correlation point, the mean velocity values indicated no variation compared with other measurement technique such as the standard acoustic doppler velocimetry (ADV) [34] and the particle image velocimetry (PIV) [141, 218]. Above and below this area, the doppler noise and signal decorrelation increase, resulting in a bias with an underestimation of the mean velocity up to 10% [34]. [213] recently proposed a new data acquisition methodology that reduces measurement uncertainty. They obtained 25 mm of vertical velocity profile by tracking five 10 mm profiles corresponding to the best range in the sweet spot region with an overlapping portion of around 5 mm between the profiles.

In our measurement, the support used was proposed and designed to allow vertical and horizontal displacement of the vectrino by means of screw-nut system (Figure II.11). The screws have 10 mm diameter with 2mm pitch which means that a turn of the screw corresponds to a displacement of 2mm horizontally and vertically. A crank and a counter were provided on each axis to permit the displacement and the visualization of the displacement value simultaneously. The instrument was oriented vertically so that the leg with a red ribbon referring to beam 1 was oriented in the same direction as the water flow. The head of the instrument must be completely immersed in water during measurements. The head of the instrument is too sensitive. It was necessary to handle the Vectrino Profiler with great care avoiding shocks. A very small modification in the orientation of one of the receivers distorted the results. The results were expressed assuming that the bottom corresponds to the zero altitude (Z=0 m).

II.3.4.2 *Experimental procedure and methodology for data acquisition*

First, the flow was seeded with hollow glass microspheres (Spherical 110P8), recommended by the manufacturer. The microspheres have a median diameter of 10 µm and a density of (1.10± 0.05) gcm^{-3} very close to that of water. The Vectrino Profiler was configured with the maximum frequency of the velocity measurement (100 Hz) and the maximum frequency of bottom elevation (10 Hz) coupled with the optimum spatial resolution (1 mm). The chosen algorithm is the maximum ping algorithm, since smooth hydraulic conditions are respected. The parameters are chosen based on standards in the instrument manual. We check that the seeding is enough by making Vectrino measurement in the flume while we add the seeding material. The signal to noise ratio (SNR) and signal correlation increase with the addition of seeding material. We add seedings until, for all instantaneous data, the signal to noise ratio (SNR) of each receiver is greater than 20 dB along the profile and the signal correlation for each beam is also greater than 90%. These values were used according to the standards recommended by the manufacturer. Water quality plays a very important role in the measurements. It was observed during measurements that the presence of limestone in the water can greatly reduce the amount of seeding required.Our measurements were made along a 30 mm elevation while lowering the instrument around 15 mm towards the bottom. This allowed to have an overlapping of around 50 % in the common elevation zones. Finally, the data was processed using Matlab and the velocity value at each altitude in the velocity profile is time averaged.

Figure II.12 shows an example of results obtained in the axial direction, noted 1, for the vectrino profiler at an axial distance from the initial slope of the false bottom dx equal to 4.8 *m* at a flow rate Q = 65 m^3/h and a water depth h = 14.8 *cm*. Each color in the Figures II.12 (a),(b),(c),(d) and (e) corresponds to one measurement at a specific elevation of the bottom floor relative to the central transmitter (df) with a recording duration of 1 minute, corresponding to the average of 6 000 instantaneous measurements.
The results show that the parameters describing the quality of the signal (amplitude, signal-to-noise ratio and correlation) have in most cases the same parabolic shapes with a maximum at the sweet spot 50 mm from the transducer. The corresponding standard deviation has also a parabolic shape with inverted curvature. This means that the best quality of the signal depends on the distance from the transducer head and was located in the zone of maximum amplitude, signal-to-noise ratio and correlation, which was at 50 mm from the transducer. Above and below this sweet area, the doppler noise and signal decorrelation increase due to the decreasing overlap of the individual beams.

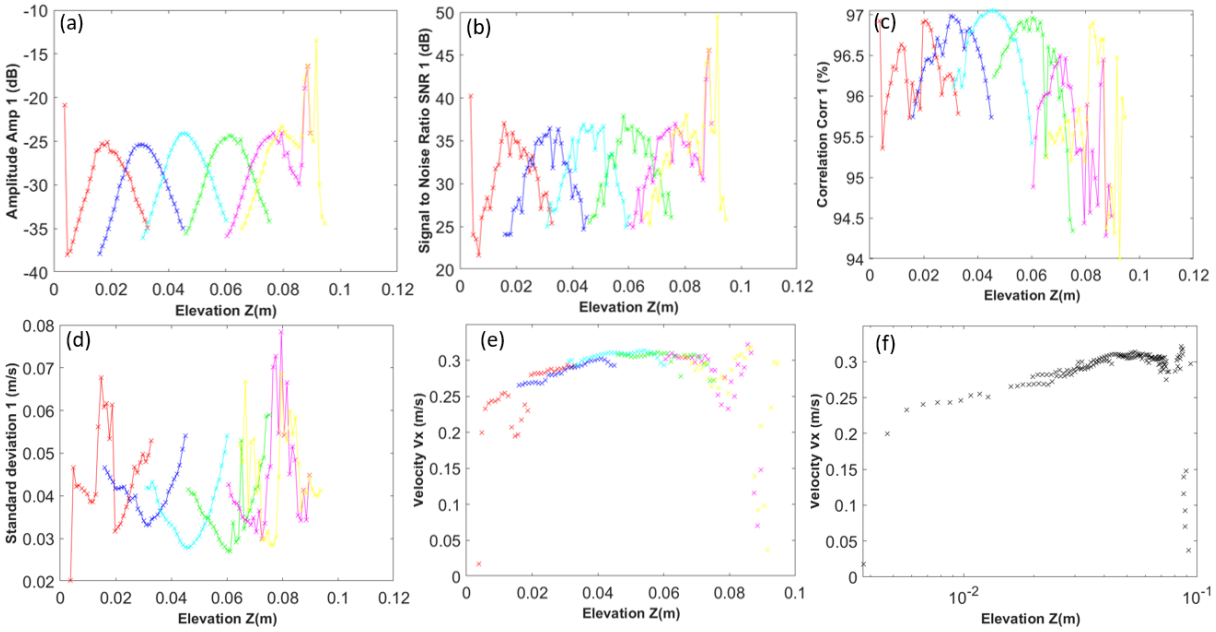

Figure II.12: Vertical profiles in the axial direction of the : (a) amplitude, (b) signal to noise ratio, (c) correlation, (d) standard deviation and (e) velocity before filtration in arithmetic scale, (f) : velocity after filtration in semi-logarithmic scale, at an axial distance with respect to the initial slope of the false bottom dx equal to 4.8 m at a flow discharge Q 65 m3/h and a water depth h 14.8 cm.

Some anomalies appear in the measurements, creating aberrant points especially for the profiles at the extremities, the closest to the false bottom (in red) and closest to the free water surface (in magenta and yellow). We noticed that these aberrant points correspond to a discrepancy in the quality of the signal, visualized as a discontinuity in the parabolic shape. Concerning the closest profile to the false bottom, these anomalies may be due to the acoustic interference. This phenomenon can occur if the current pulse is interfered with by reflections from the previous pulse(s), creating an area called “weak spot”. The interference region depends on the type of material in contact with the water interface and is estimated to be between 1.7 and 5 mm (± 0.5mm) above the bottom by [130]. On the other hand, concerning the profiles closest to the free surface of the water, these anomalies may be explained by the higher influence of the probe on the flow close to the free surface, affecting the measurement flow velocity zone.

To reduce the number of outliers in the measurements, a filtration of data has been performed. This filtering consists in removing all the measurements having a standard deviation higher than 20% of the measured value. Figure II.12 (f) shows the final result after grouping all the data of the six average flow velocity measurements at the different elevations from the bottom and filtering them in a semi-logarithmic scale. All measurements leading to the final profile are performed under the same hydraulic conditions.

Due to instrument displacement uncertainty ($\pm$0.1 mm), points in the overlap area had slightly

different elevations. The velocity measurement uncertainty in the Vectrino Profiler varied with transmitter position, which caused minor oscillations in the profile. In smooth flow, the profile consists of a millimetric viscous layer near the sediment-water interface, followed by a centimetric turbulent layer with a logarithmic velocity profile. Despite the measurement disturbances related to the displacement of the instrument, these results provided a satisfactory velocity profile.

In the following, all the results shown are realized by following this acquisition methodology. A general tendency to a continuity in the measured vertical profiles of axial velocity is clearly observed in all the obtained results.

II.3.4.3 *Hydraulic conditions of the performed scour flume tests*

The hydraulic conditions of the performed scour flume tests are summarized in Table II.4 which give the main values of the dimensional and adimensional parameters.

Hydraulic condition	**Soil type**	**Q** m^3/h	**h** cm	**V** m/s	**Vc** m/s			**Re**	**Fr**	**ReD**	**V/Vc**
					Theoretical	**Flume experiment**	**Erodimeter experiment**				
1	Medium sand	65	15	0.29	0.48	0.41 ($\pm$ 0.005)	_	42920	0.24	9280	0.7
2	Fine sand	65	17	0.26	0.27	0.22 ($\pm$ 0.008)	0.24	44200	0.20	8320	1.08
	M1				-	-	0.25				1.04
	M2				-	-	0.4				0.65
	M3				-	-	0.45				0.57
	M4				-	-	0.5				0.52
	M5				-	-	0.62				0.42

Table II.4: Hydraulic conditions of the performed scour flume tests; Where M1: 85% Sand +15% Silt, M2: 85% Sand +10% Silt +5% Clay, M3: 85% Sand +7.5% Silt +7.5% Clay, M4: 85% Sand +5% Silt +10% Clay and M5: 85% Sand +15% Clay

The conditions 1 and 2 describe the hydraulic conditions for tests on medium sand and fine soils respectively. The water discharge Q, the water depth h and the depth averaged flow velocity V are maintained at a constant values during the experiments. The flow regime of performed tests was turbulent since the Reynold's number values based on water depth were Re=42920 and Re=44200 respectively [235]. The Froude number Fr values of 0.24 and 0.2 indicate subcritical hydraulic conditions. The Reynold number based on the diameter of the cylinder ReD= 9280 and ReD= 8320 point out a laminar boundary layer separation and a completely turbulent wake region [105].

The average critical velocity of the initiation of the bed movement was determined using three methods : theoretical, carrying out flume tests without piers and erodimeter tests under the same

geotechnical conditions as those described above. The erodimeter results on the fine soils and the methodology used to determine the critical velocity Vc were detailed in Chapter IV.

The theoretical method which is based in the following equations has a limitation, being only applicable for the pure sandy soils. [236] proposed the relation II.3 to determine the critical Shields number (θ_{cr}) for the incipient motion from the dimensionless sedimentological diameter (D_*).

$$\theta_c = \frac{0,3}{1+1,2D_*} + 0,055\left[1-\exp\left(-0,02D_*\right)\right] \tag{II.3}$$

Where,

$$D_* = \left[\frac{g(s-1)}{\nu^2}\right]^{1/3} d_{50} \tag{II.4}$$

where, g is the acceleration of gravity, ν is the kinematic viscosity of water, s=ρ_s/ρ_w with, s, ρ_s and ρ_w are the relative density of the sediment, the volumetric mass of the sediment and the volumetric mass of the water respectively.

The Shields parameter θ is defined by the relation II.5 :

$$\theta = \frac{\tau_0}{\rho_w(s-1)gd_{50}} \tag{II.5}$$

Where, τ_0 is the bed shear stress.

Using the equations II.3 and II.5, for the present tests on sand, it is possible to estimate the critical Shields number θ_c = 0.037 (medium sand) and θ_c= 0.046 (fine sand), the critical value of shear velocity at the bed $u_{*c} = \sqrt{\tau_{0c}/\rho_w}$, u_{*c}= 0.032 (medium sand) and u_{*c}= 0.0125 (fine sand) and the corresponding critical bed shear stress τ_{0c} = 1.029 Pa (medium sand) and τ_{0c} = 0.157 Pa (fine sand).

The value of the Reynolds number is defined by $Re_* = u_* k_s/\nu$, where $k_s = 2.5d_{50}$ is the roughness length of the bed [184], where d_{50} is the mean size of sediment. The Re_*= 136.39 for medium sand lies in the hydraulically rough since $Re_* > 70$ [235]. The Re_* = 6.58 for fine sand is in the transition region since $5 < Re_* < 70$ [235].

In the hydraulic rough regime, the length scale z_0 in the log-law velocity distribution can be estimated by the equation II.6 [235] and the flow velocity (V) is given by the equation II.7 [235]:

$$z_0 = \frac{k_s}{30} \tag{II.6}$$

$$V = 2.5u_* \ln\left(\frac{11h}{30z_0}\right) \tag{II.7}$$

In the transition hydraulic regime, the length scale z_0 in the log-law velocity distribution can be estimated by the equation II.8[235] and the flow velocity (V) is given by II.9 [235]:

$$z_0 = \frac{k_s}{30}\left[1 - \exp\left(-\frac{u_* k_s}{27\nu}\right)\right] + \frac{\nu}{9u_*} \tag{II.8}$$

$$V = 2.5u_* \ln\left(\frac{h}{2.72 z_0}\right) \tag{II.9}$$

Using equations II.3, II.6 and II.7, the depth-average velocity for incipient motion is estimated to 0.48 m/s for the medium sand. Using equations II.3, II.8 and II.9, the depth-average velocity for incipient motion is estimated to 0.27 m/s for fine sand.

The flume experiments without pier were carried for pure sandy soils (medium and fine sand). For this type of experiment, we start by preparing a flat bed and saturate it by applying the methodology described in section II.3.5.3. For the bed compaction, a plate without a hole in the middle is used. At the beginning of the experiments, a low flow velocity (0.1 m/s) is set. We opted to measure the threshold visually, by gradually increasing flow velocity in steps of 8 mm/s until at least three grains were observed to move around one minute, as previously done by [143]. A stronger mobilization of the grains are observed by slightly increasing the approach velocity from threshold value. The test without flume on medium sand and fine sand were repeated three times. The average values of the critical velocity from the three tests is 0.41 m/s for the medium sand and 0.22 m/s for the fine sand.

The values obtained by the three methods in the case of pure sand are very close showing the validity of the three methods, with a standard deviation of 0.02 m/s. This justifies the fact that one of these methods can be done alone to determine the value of the threshold value. The measurements recorded with the EFA erodimeter, which will later be used for the scour depth estimation method (in Chapter IV), were selected for the campaign on fine soils.

For pier scour tests, a flow intensity V/Vcr greater than 1 indicates a live bed water scour condition for fine sand and for the mixture 1 (85% fine sand + 15% silt). A V/Vcr intensity below 1 indicates a clear water scour condition for all other soil configurations. The critical velocity values used in the computation of the flow intensity come from flume non-pier measurements for medium sandy soils and from EFA testing for all other configurations of soil.

II.3.4.4 *Results*

In order to characterize the flow in the experimental flume, various measurements of the velocity profiles far from the pier are performed for the two hydraulic configurations of the scouring tests performed during my thesis work. The measurements are taken in the presence of the pier, by putting a smooth surface plate made of PVC flush with the false bottom, instead of the soil bed in the recess area. The position of the measurements of the different profiles are far enough from the cylinder pier to avoid the disturbance as shown in Figure II.13. Lateral profiles at E and F are performed 10 cm from the center width of the flume at an axial distance with respect to the initial slope of the false bottom dx 4.8 m. The other profiles A, B ,C and D are performed at the longitudinal axis of channel (center width of the flume) at an axial distance from the initial slope of the false bottom dx = 2 m, 3.3 m, 4.3 m and 4.8 m respectively (Figure II.13). The flow direction is in the direction from A to D.

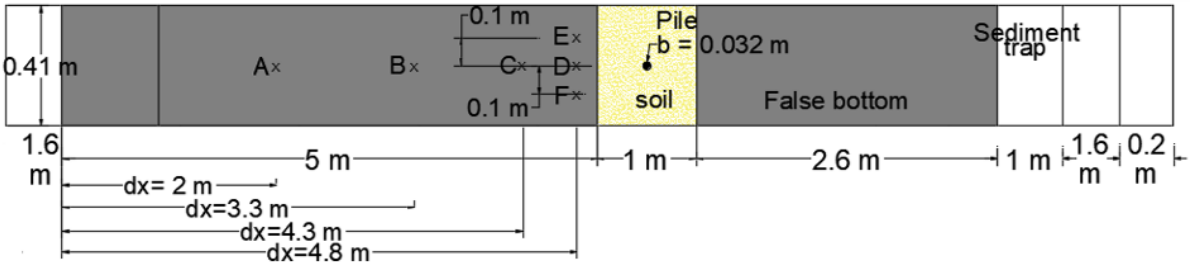

Figure II.13: Top view flume scheme showing the position of the indexes from A to F

Evolution of the velocity profiles as function of the axial distance

Figure II.14 shows the evolution of the mean velocity profiles in the longitudinal axis of the flume as a function of the distance to the initial slope of the false bottom (dx) for the two hydraulic configurations. The dotted lines represent the best logarithmic fit with the experimental data between an elevation (Z) 0.005 m and 0.05 m.

The average velocity profiles reach a state of near-constant coefficient in the logarithmic variation zone at a distance downstream of the initial slope of the false bottom. For the two hydraulic conditions considered, this distance is approximately 4.3 meters.

The velocity profile in turbulent flow can be written as a logarithmic law as stated by [235] :

$$\frac{V(z)}{u_*} = \frac{1}{K} \ln\left(\frac{z}{z_0}\right) \tag{II.10}$$

Where V is the horizontal component of flow velocity, u_* the friction velocity at the bottom, K the von karman constant, usually believed to be constant (0.4) and z_0 is a Nikuradse roughness length scale. It is important to note that the water turbidity may affect the Von Karman constant.

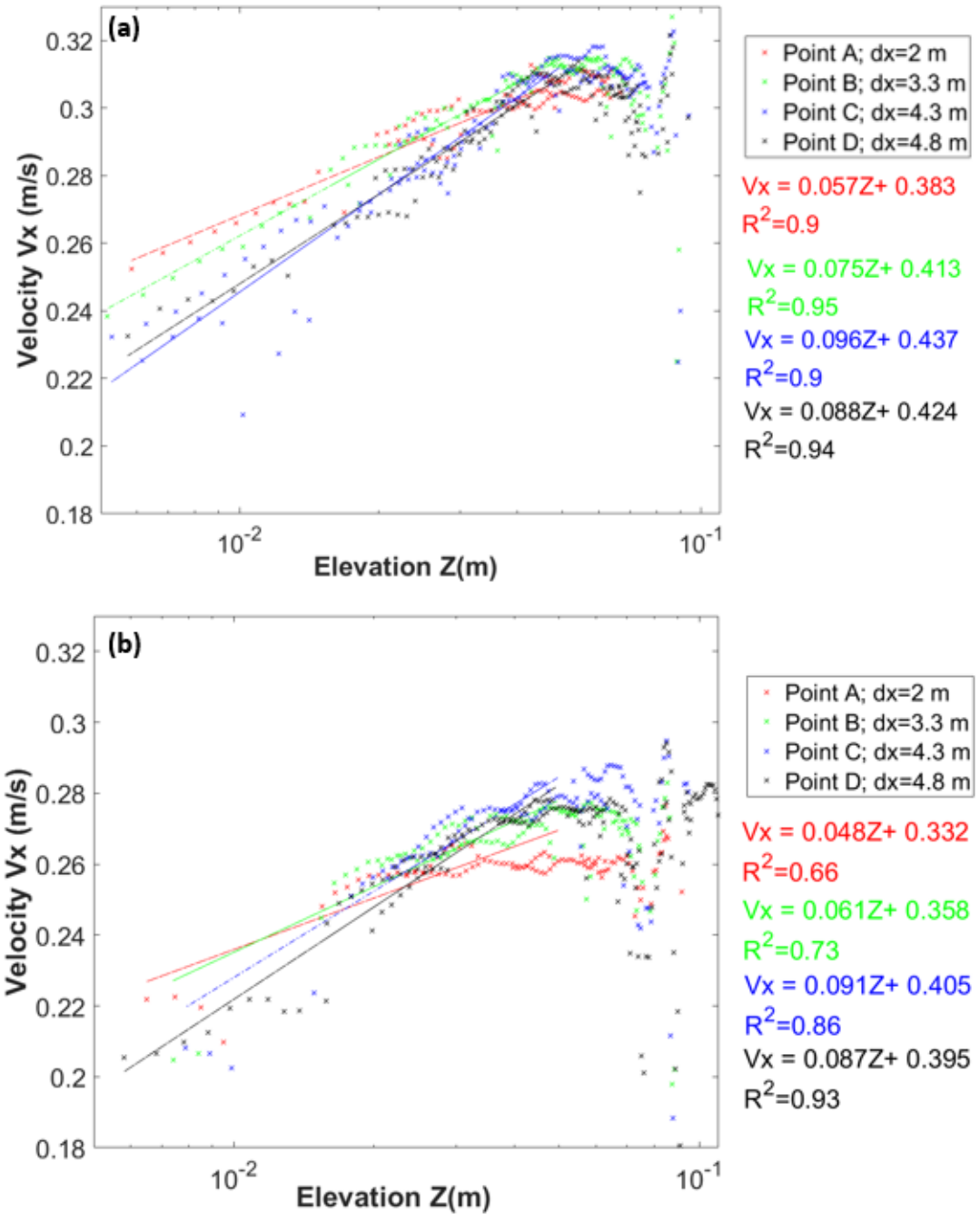

Figure II.14: Evolution of the mean velocity profiles in the longitudinal axis of the flume as a function of the axial distance with respect to the initial slope of the false bottom (dx), (a) : hydraulic condition 1 (with medium sand) (b) : hydraulic condition 2 (with fine soils)

According to [102], the determination of the affine fit equation of the velocity profile in the logarithmic variation zone, in a semi-logarithmic graph, enables the values of u_* and z_0 to be estimated. The slope of this linear relationship, represented by u_*/K provides the value of u_*. Additionally, z_0, which is the null velocity elevation, is determined as the point where the log-layer intersects the z-axis. This intersection point corresponds to the elevation (Z) that returns a zero velocity value in the fitting linear relationship.
The thickness of the sub-viscous layer δ_v just above the bottom is estimated by [159]:

$$\delta_v = 11,6\frac{\nu}{u_*} \tag{II.11}$$

Where ν is the kinematic viscosity of the water.

Frictional forces are represented by the shear stress at the bottom.

$$\tau_* = \rho u_*^2 \tag{II.12}$$

Where, ρ is the volumetric mass density of the water (1000 kg/m^3).

Table II.5 summarizes the values obtained for the flow parameters (u_*, z_0, δ_v and τ_*) from measurements at the different positions and for the two hydraulic tested configurations while using the equations II.10, II.11 and II.12.

Measurements were made on top of a PVC plate with a smooth surface, which justifies the existence of a hydraulic smooth flow condition.
Under hydraulic smooth flow condition, the average depth flow velocity across the water depth can be expressed as:

$$V = \frac{u_*}{K}\ln\left(3.31\frac{u_* h}{\nu}\right) \tag{II.13}$$

In the case of an average depth flow velocity V = 0.29 m/s and a water depth h = 0.15 m, the friction velocity u_* is approximately 0.0337 m/s using the equation II.13, which is close to the value obtained from measurement (u_* = 0.0352 m/s). Similarly, for an average depth flow velocity V = 0.26 m/s and a water depth h = 0.17 m, the friction velocity u_* is approximately 0.0301 m/s using the equation II.13, which is close to the value obtained from measurement (u_* = 0.0348 m/s).

Position	Flow parameter	Hydraulic condition	
		1 (with medium sand)	2 (with fine soils)
A	$u_*(m/s)$	0.0228	0.0192
	$Z_0(mm)$	0.00019	0.00012
	$\delta_v(mm)$	0.5	0.6
	$\tau_*(Pa)$	0.520	0.369
B	$u_*(m/s)$	0.0300	0.0244
	$Z_0(mm)$	0.0031	0.0013
	$\delta_v(mm)$	0.4	0.5
	$\tau_*(Pa)$	0.900	0.595
C	$u_*(m/s)$	0.0384	0.0364
	$Z_0(mm)$	0.0283	0.0350
	$\delta_v(mm)$	0.3	0.318
	$\tau_*(Pa)$	1.475	1.325
D	$u_*(m/s)$	0.0352	0.0348
	$Z_0(mm)$	0.0152	0.0288
	$\delta_v(mm)$	0.3	0.3
	$\tau_*(Pa)$	1.239	1.211

Table II.5: Flow parameters estimated at different locations in the axial distance along the flume for the tested hydraulic configurations; u_*, Z_0, δ and τ_* represent the friction velocity at the bottom, length scale, thickness of the subviscous layer and friction shear stress at the bottom respectively

The established velocity profile, measured at position D in the two hydraulic configurations, are discretized at 1 mm intervals along the Z-axis after removing outliers from the measurements. The discretization process assumes that there is a velocity of 0 m/s at Z=0 m and a constant velocity between Z=0.011 m and the elevation corresponding to the surface of the water. To calculate the average velocity over a the water depth, the data within that interval is used, which yields a value of 0.29 m/s and 0.26 m/s for condition 1 and 2 respectively. These velocities are equal to the calculated values from the imposed flow rate by the pump divided by the measured water depth.

Effect of the Plexiglas plate

Velocity measurements at the downstream distance from the initial slope of the false bottom dx= 4.8 m are taken in the presence and absence of the Plexiglas plate on the water surface under the recess area as shown in Figures II.8 and II.18 (b), once upstream and again downstream of the pier. These measurements are carried out for hydraulic condition 2 at the center of the flume

(position D) and results are illustrated in Figure II.15. The comparison of the three profiles shows no significant differences, indicating that the influence of Plexiglas plate on the flow is negligible. Thus, in the presence of the plate in the upstream and downstream positions of the pier, the flow is well established with always the same logarithmic layer for the profile.

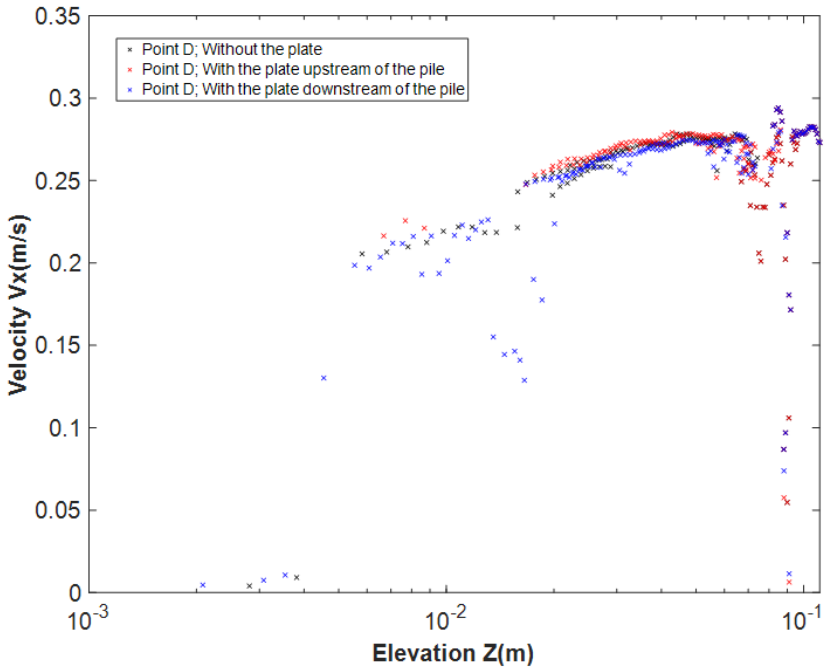

Figure II.15: Effect of the Plexiglas plate on the vertical profile of the mean velocity measured at position D with the hydraulic condition 2 (with fine soils)

Effect of the flume edge

The effect of the flume edge was studied at dx=4.8 m. The results are shown in the Figure II.16. The points at left and right of the flume are defined with respect to the flow direction. It is important to note that we found that there is an asymmetry in the flow. Indeed, we observed a higher velocity on the left side by about 20% and 13% than the right velocity values for conditions 1 and 2 respectively. This was unexpected and may be the reason of some unexpected asymmetry in the scour hole topography measurement.

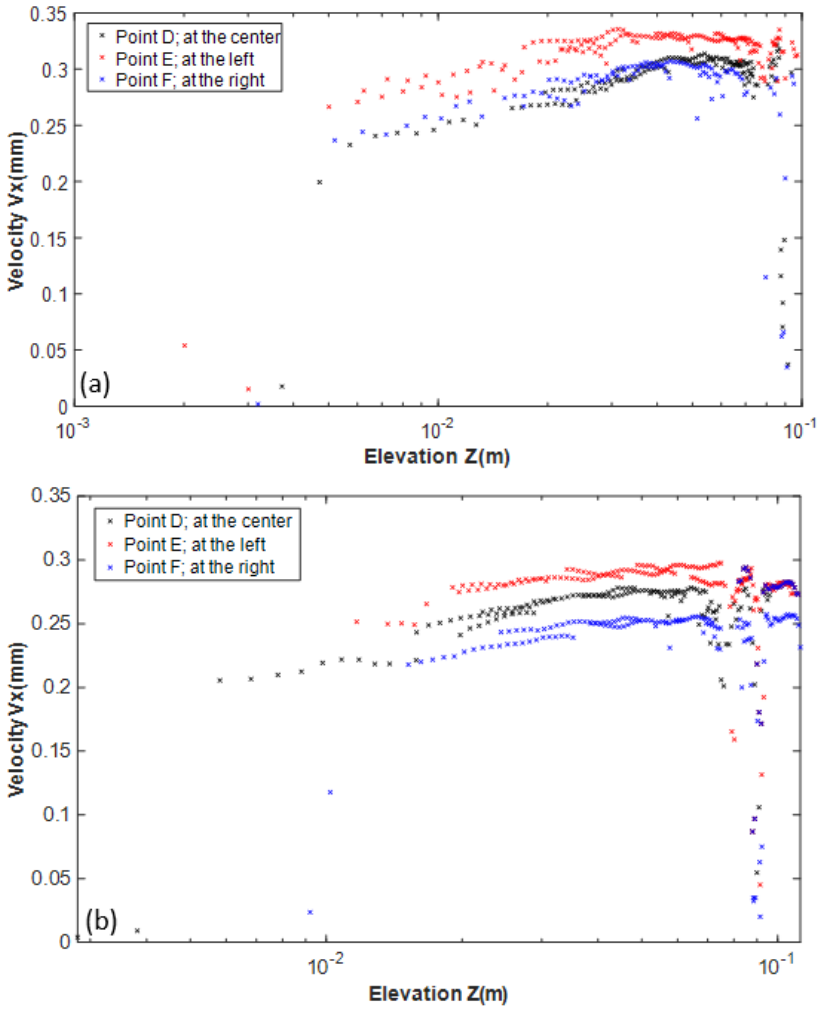

Figure II.16: Effect of the flume edge on the vertical profile of the mean velocity (a): hydraulic condition 1 (with medium sand), (b): hydraulic condition 2 (with fine soils)

II.3.5 *Bed topography measurement: 3D Scanner Laser*

II.3.5.1 *Description*

The photoneo scanner, type Phoxi 3D scanner size S, involves a camera and a laser class 3R pattern projector with a signal wavelength in the red spectrum (about 639 nm) (Figure II.17 (a)). The scanning volume has trapezoidal shape located at a range distance from the device of 384-520 mm with an optimum scanning distance at 442 mm (Figure II.17 (b)). The scanning area at focus distance is 360 × 286 mm. The scanning time provided by the device is in the range 250-2250 ms. According to the manufacturer, this technique's key advantages are its capacity to attain a high level of spatial accuracy (0.05 mm) and temporal accuracy (250 ms). The coordinate system is located at the center projection pinhole of the camera. The measuring

principle is based on sophisticated 3D surface imaging technology using structured light (Figure II.17 (c)). Multiple light planes were emitted by the projector to cover the complete scanned scene in form of patterns. The surface's geometric shape distorts structural light pattern. A unique intensity code is assigned to every projection column. Using various structural light principles and algorithms, a correspondence between this intensity and the camera pixel was determined. The 3D dimensional coordinates are then computed for the corresponding point on the scene using the triangulation plane theory, knowing the distance between the laser source and the camera (230 mm) allowing the automatic reconstruction of the 3D object shape.

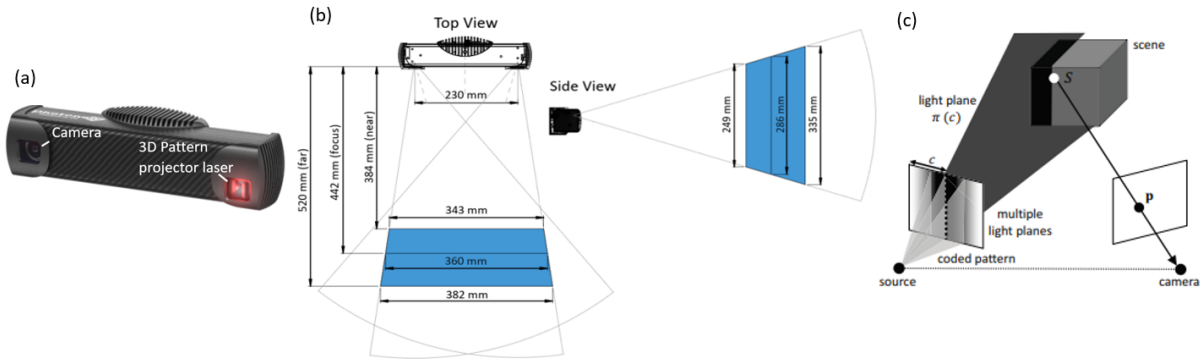

Figure II.17: PhoXi 3D Scanner S, (a): main components, (b): Scanning volume, (c): Structural light 3D imaging principle [114]

II.3.5.2 *3D scanner Installation*

Preliminary tests at various orientations of the scanner positioned on the side of the glass wall flume were carried out. The results revealed that in this scanner position it was not possible to access the topography of the scour area. The scour hole appears as an empty data region. The presence of this blind area may be explained by the fact that in this position the incident pattern cannot have a high inclination with respect to the normal at the glass wall. As a consequence, the flat bed surface hides from the laser scanner the scour hole as seen in the (Figure II.18 (a)). The incident pattern sheet may be blocked by the presence of a transition in the depth zone preventing the visibility of scour hole data by the scanner. The size of this region depends strongly on the slope of the scour hole and the scour depth on the side of the pier, the greater the slope and the depth, the more difficult it is to detect this zone. The clouds illustrated in this figure were obtained when the pier had a white outer surface.

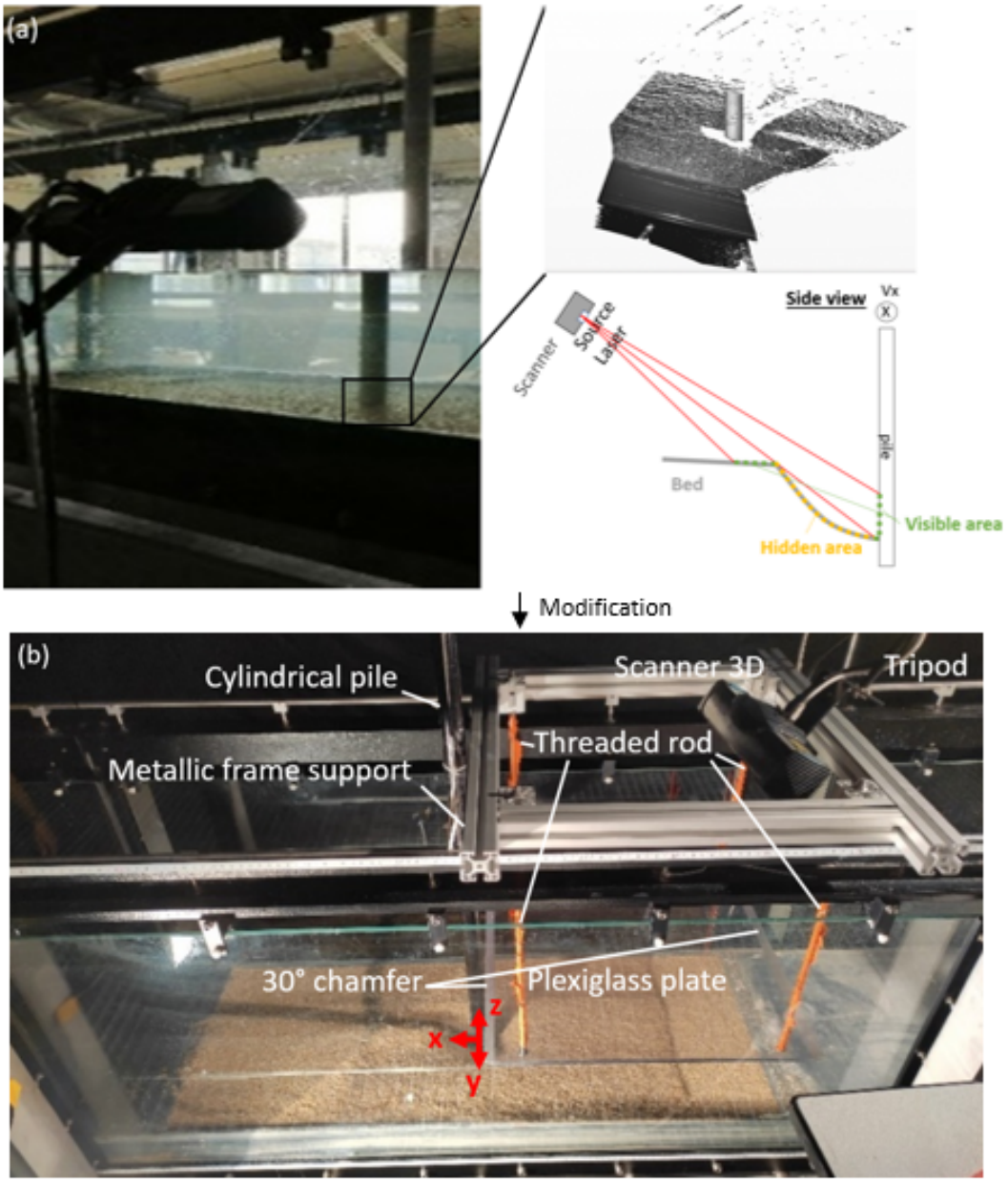

Figure II.18: 3D scanner positioning, (a): scanner located at the side of the flume, (b): scanner located above the water surface

To solve this problem, the scanner position was modified and positioned above the water surface (Figure II.18 (b)). As the laser sheet illuminated a scan area that measured around 360 by 286 mm, the single complete underwater test was composed of two similar separated experiments, focusing the scanner to the upstream and downstream of the pier respectively while placing a Plexiglas plate at the water surface. At these locations, the incident pattern can have high slope with respect to the normal at the Plexiglas plate preventing the blind area to appear. The Plexiglas plate has 1 cm thickness, 0.5 m in the length and span the entire width of the flume. It was fixed

to a metallic frame support which was placed on the banks of the flume, by four threaded rods. On each of these threaded rods, there are nuts on both sides of the metal support. These nuts are used to adjust the vertical position of the Plexiglas plate so that its internal interface coincides with the water surface desired. The plate is attached to the flume banks, hence, cannot respond to water level change, and pressured condition exist beneath the plate. Two 30° chamfer were at either end of the plate to aid in directing flow underneath and prevent the flow over top. The shadow is lessened at these two stations, and the laser reflection caused by the pier is stopped by coloring it by black permanent marker, and the pier is not appeared in the input scanner data which facilitates the data treatment. The acquisition of a full half-plane (180° view per test) of the scour hole with the presence of the highest number of cloud points surrounding the pier is then made feasible by the 3D scanner. The data acquisition methodology developed and its validation will be presented in chapter III.

II.3.5.3 *Soil and flume setting before test running*

Preparation of bed sample

Figure II.19 shows the steps of the mixture preparation. Powdered fine sand and fines content (silt or/and clay) were thoroughly mixed by hand in dry weight then with the water content using accurate proportions. The sediments were mixed thoroughly again in a concrete mixer machine for a sufficient time (around 30 min) to ensure homogeneity. To prepare the required 50 kg of soil mixture for a single test, we individually prepared 10 kg of material five times. The mixture then was then placed in buckets, with closed covers, to rest during minimum three days.

Figure II.19: Mixture preparation

The prepared mixture was then filled in the test section, where the cylinder has been fixed centrally and vertically. Regarding the method of compaction of cohesive soils in flume tests, various methods are reported in the literature. Dynamic compaction for sediments having hard, semisolid and plastic consistencies using cylindrical roller was done by [122, 132] and using hammer while controlling the number of blows by [13]. Kneading method using tamper was made on delivered block of soft clay by [112, 153]. The applied method in our tests is described as follow. The sediment is compacted in the test section in three different layers each having approximate thickness of 2 cm. Each layer is compacted using a standard Proctor hammer which has a 2.45 kg weight and from a drop height of 30.5 cm, with the presence of a grid plate placed at the soil surface. The plate is 0.5 m long and 0.4 m wide. It has a semicircular hole at one of its central edges. Two plates are required in order to fit into the total soil section area (shown in Figure II.20). Each plate is divided to identical rectangular portions to form a grid. Before proceeding with the experiments, preliminary tests were carried out by changing the order of blows between the grids on the plate, before finally proposing an order that would maintain a horizontal ground surface. Approximately eighty blows evenly distributed over the entire surface of the plate are applied in each layer. Each layer's top surface is roughened in order to ensure that the various layers would bound to one another. Furthermore, using a wooden template, the bed surface is planned from the working section's upstream to its downstream end. Figure II.20 illustrate photographs of the procedure described previously in the case of the fine sand.

Figure II.20: Procedure for placing the soil in the flume

Water filling procedure

To avoid initial scour not desired, some precautions are proposed and taken while filling the flume. For the first tests done on the medium sand, the methodology applied is described in Figure II.21. After placing the medium sand in the flume test section, the two plates used for the compaction purpose are placed on the soil surface. Weights are placed along the surface of the plates with symmetrical longitudinal and transversal distribution around the cylinder. The flume is then filled with water at a very low flow rate, 15 m^3/h, in presence of the plates and the weights until the initial water depth reaches the desired value. Then the weights and plates are gently removed consecutively without disturbing the surface of the bed. The bed was kept under water initially during 1h before running the test. Owing to the medium size distribution of this soil, 1 h was sufficient to saturate the bed.

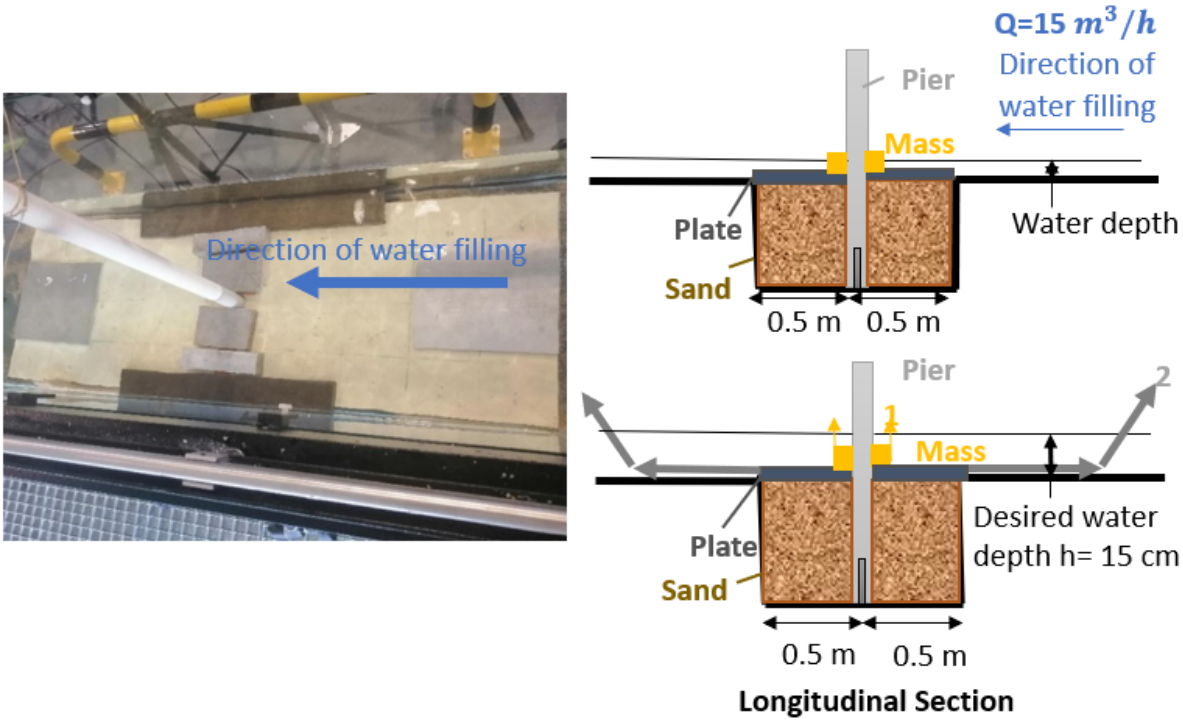

Figure II.21: Water filling procedure for medium sand, (a): photograph taken during the water filling step, (b): Illustration of the applied methodology

Unfortunately, this procedure is not applicable in the case of fine cohesive soils since they stick to the surface of the plates in the presence of water. For this reason, another type of procedure is applied (Figure II.22 (a)).

First, two inflatable balloons are used to plug the outlet of the hydraulic flume which is inclined by +2.5%. In parallel to this, the pipe of the flume on the back flow side of the pump must be

closed by means of the shut-off valve plugging the inlet of the flume.
After that, the filling of clear and clean water is done through a garden hose connected to an exterior tap and set down in the outlet element of the flume. The use of the garden hose and the inclination of the flume help slowing down the water velocity during the water filling step.
Once the surface of water arrives and attains around 5 cm of depth at the flume entrance, the flume is gently reclined in the opposite direction by around - 0.1% every 15 minutes until the slope of the zero flume is reached. This step must be done slowly in order to avoid generating waves that could disturb the initial soil surface.
To ensure a good flow initiation at the beginning of the experiment, the level of water in the flume, prior running the test, should be fixed to the initial water depth of the experiment and the amount of water in the tanks must be evacuated to around 5 cm below the medium height of each tank. The evacuation is done by placing a submersible drainage pump at the bottom of the tank and connecting to an exit hose. Failing to evacuate a significant amount of water from the tanks will cause them to overflow.
Following this, all fine soils were kept under water overnight 12-16 hours, allowing the saturation phase of the bed. The non-cohesive and cohesive matrices acquired then cohesive bounding that was closer to the field conditions [84].
The next day, the pump started with a very low flow rate of 15 m^3/h at the beginning of the test, the channel pipe is opened and the balloons are successively deflated. With a water height of about 17 cm, this very low flow rate does not cause any erosion for all the soils used.

Figure II.22 (b) illustrates a photograph of the fine sand surface in its initial condition before running the test and after following the water filling procedure described previously.

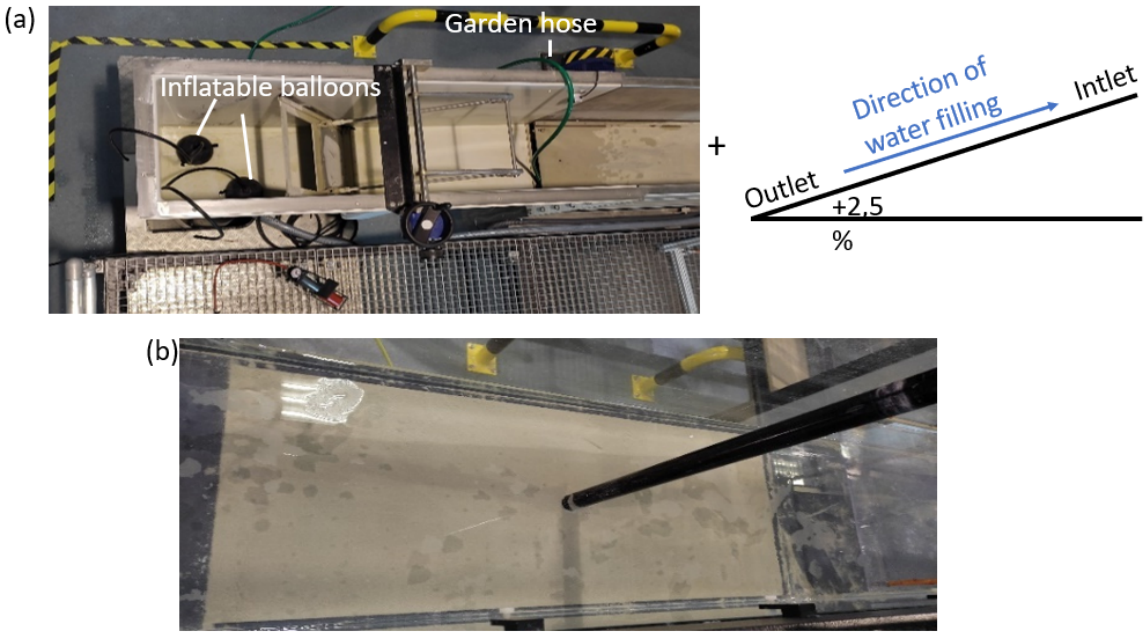

Figure II.22: Water filling procedure for all fine soils, (a): explanation of the methodology applied, (b): the surface of the sand NE34 after water filling and before running the test

II.3.6 *Experimental program for flume tests*

Table II.6 presents a summary of the experimental program for flume tests carried out during this PhD research. In total, there are 18 flume tests: 5 preliminary tests on medium sand and 13 tests on fine soils. The pier scour tests (in presence of the pier) were conducted during 360 min. Two similar tests were always carried out, one dedicated to the upstream side of the pier and the other to the downstream side.

Test	Pier	Plate	Medium Sand (%)	Fine Sand (%)	Silt (%)	Clay (%)	Pier Side scanned	V (m/s)	h (m)
1*	X	O	100	–	–	–	–	–	–
2*	O						Upstream	0.29	0.15
3*							Downstream		
4		X					Upstream		
5							Downstream		
6*	X	O	–	100	0	0	–	–	–
7	O						Upstream	0.26	0.17
8							Downstream		
9				85	15	0	Upstream		
10							Downstream		
11					10	5	Upstream		
12							Downstream		
13					7.5	7.5	Upstream		
14							Downstream		
15					5	10	Upstream		
16							Downstream		
17					0	15	Upstream		
18							Downstream		

Table II.6: Summary of the experimental flume test program, where 'X' indicates absence, 'O' indicates presence, and '*' indicates tests that were repeated three times, V is the flow velocity and h is the water depth

Five preliminary tests were conducted on medium sand to validate the measurement technique of the 3D Scanner Laser. The first test, corresponds to non-pier flume test (Test 1 in Table II.6). This test aimed to determine the critical velocity of the sand (Vc). The subsequent four tests, named Tests 2, 3, 4, and 5 in Table II.6, were carried out with a pier in clear water scour regime (V/Vc=0.7), with a flow velocity V (0.29 m/s) and a water depth h (0.15 m). Tests 2 and 3 involved continuous monitoring over a 360 min, which was possible in presence of the Plexiglas plate. These tests were repeated three times to demonstrate the repeatability of results. Tests 4 and 5, conducted without the Plexiglas plate, aimed to show whether the presence of the Plexiglas plate had any influence on the topography of pier scour.

Thirteen tests on pier scour on fine soils were conducted. We started by carrying out a flume test on fine sand without pier (Test 6 in Table II.6) to determine the critical erosion velocity for the reference fine sand (Vc). Then, 12 pier scour tests were performed on the different tested fine soils. We maintained consistent flow velocity V of 0.26 m/s and water depth h of 0.17 m for

all these tests. To establish a reference test for comparison, we carried out Test 7 and Test 8 in Table II.6 on pure sand. Following these initial tests, we focused on the effect of progressively increasing the percentage of clay compared to silt within the percentage of fines in the soil mixtures on the scour process. This investigation spanned from Test 9 to Test 18 in Table II.6. We aimed to compare the behavior of soil starting with a 15%silt mixture (Test 9, 10) and then gradually increasing the clay content within the sand-silt-clay mixture in subsequent tests.

II.4 EROSION FUNCTION APPARATUS (EFA)

II.4.1 *Description*

The Erosion Function Apparatus (EFA) was conceived by Jean-Louis Briaud in 1991, designed in 1992 and realized in 1993 mainly to characterize the erosive properties of all types of soils (natural and artificial), ranging from clay to gravel, and from soft soils to soft rocks [55]. More precisely, it measures the erosion function, which relates the hydraulic shear stress τ applied to the water-soil interface to the soil erosion rate $\dot{z}$. Used in conjunction with the SRICOS (Scour Rate In COhesive Soils) method, the EFA can provide accurate scour depth prediction [56].

Figure II.23 shows photographs of the main components and the test section of the erodimeter and a conceptional diagram of the soil erosion sample. The erodimeter consists of a closed rectangular cross section conduit in which a flow circulates in close cycle. A water tank at the back with a capacity of 700 L connected to a pump supplies the erodimeter with water. The soil sample is placed in an ASTM standard Shelby tube of external and internal diameters 76.2 mm (3 pouces) and 73 mm respectively. The turn hand wheel is used to set the Shelby tube through a circular opening at the bottom of the rectangular cross sectional pipe which is 101.6 mm width, 50.8 mm height, 1.22 m long and has at one end flow straightener. A pump drives the water throught the pipe. The flow is regulated manually by means of a valve. Average water velocity ranges from 0.1 m/s to 6 m/s. Plexiglas windows at the top and side of the flow channel provide a visual check on the thickness of eroded soil. The device is equipped with a flow meter and temperature sensors.
These measuring devices are connected to a computer which, through the control software, allows to have an instantaneous reading of the flow velocity and the temperature as well as to record them. In this way, flow velocity and temperature averages for the duration of the test are calculated from instantaneous recording values.

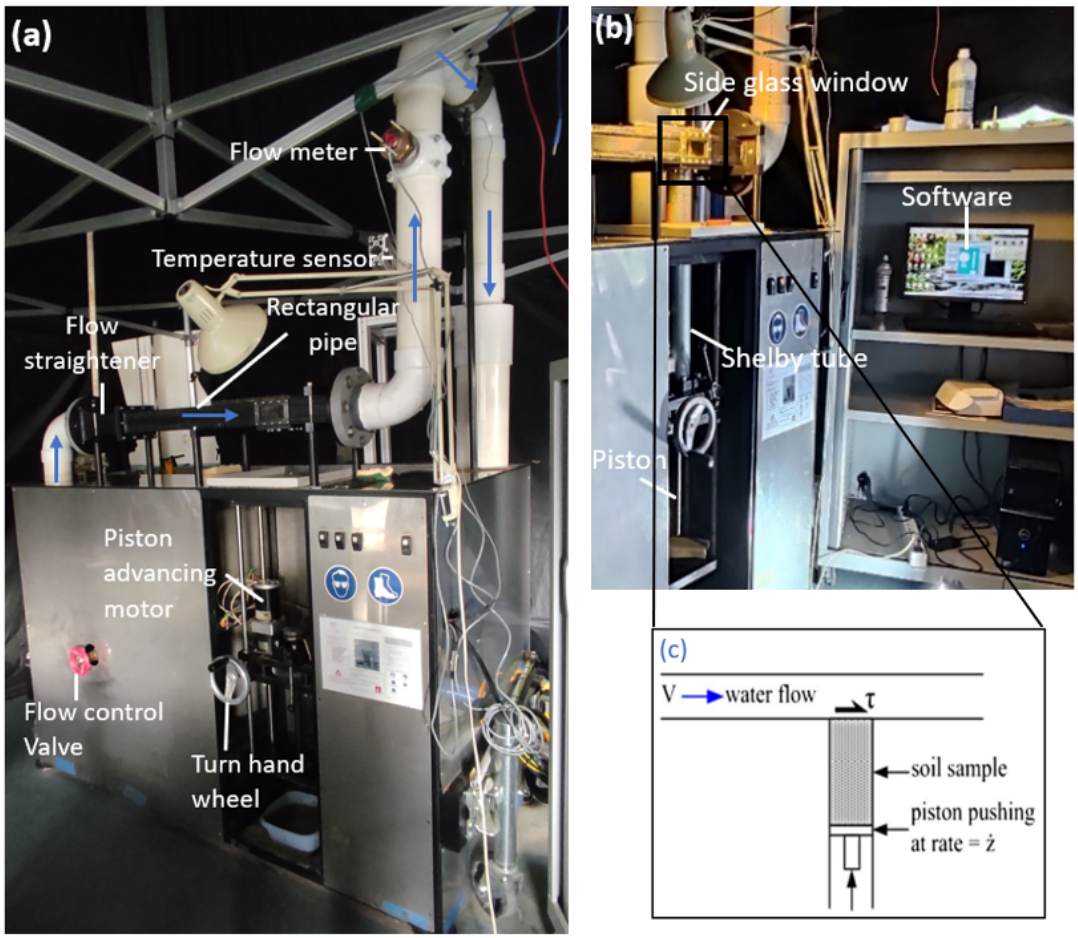

Figure II.23: Erodimeter Erosion Function Apparatus (EFA), (a): overview, (b): test section, (c): conceptional diagram of soil erosion sample [50], the direction of the flow is indicated by blue arrows

Below the measuring section there is a platform with a piston allows moving up the sample. During the test, the number of times the sample was pushed by 1 mm was indicated to obtain the total eroded height. This is a visual inspection test that depends on the operator. For this reason, it is better to have the same person to carry out the tests. The relative error on the erosion rate and the shear stress parameters measured by the EFA reported by [55] is about 10%.

II.4.2 *Sample preparation*

The Shelby tube is used to collect soil from site as well as to prepare the sample of soil in the laboratory. The latter case was done in our work by compacting the material inside the tube (Figure II.24).

The Shelby tube should be well cleaned by water from the inside and outside before preparing the soil. A cylinder was installed at the bottom part of the Shelby tube to reduce the time of

pushing the soil sample in the erodimeter. The total length of the sample chosen for all the tests performed was fixed to 15 cm. The soil sample was uniformly compacted in 3 layers of 5 cm length. Blows were done until obtaining the 5 cm of length for each layer. To make sure that the different layers would bound to each other, the top surface of each layer was roughened. In our measurements, 7 cm of space at the top of the cylinder remains. The dry volumetric mass and initial water content of the prepared tested soils in the Shelby tube for EFA tests were fixed to the same values as those for flume tests.

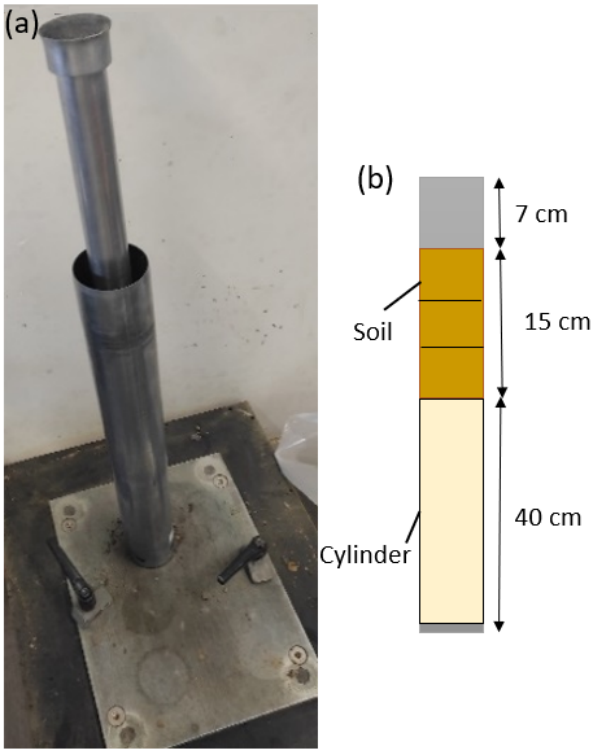

Figure II.24: Soil sample preparation, (a): during the compaction, (b): illustration of the soil in the Shelby tube

II.4.3 *Experimental procedure*

A complete test consist in considering several flow velocities and quantifying for each of these velocities the rate of erosion produced.

The EFA general procedure test is as follow:

1. Sampling Shelby tube is installed on the piston platform.

2. The soil sample is pushed by the piston and trimmed at the top of the sampling tube using a thin metal plate to flush with the edge of the sampling tube.

3. The sampling tube is installed into the rectangular pipe and an initial low water velocity (say 0.1 m/s) is achieved in the flume during 1 h to saturate the soil.

4. The pump is stopped, the tube is taken out, the surface of soil sample is trimmed to be again flush with the edge of the sampling tube and the sampling tube is installed again into the rectangular pipe.

5. The water flow is applied over the sample at a chosen velocity and the soil sample is pushed into the flow by 1 mm when necessary during the erosion process to maintain its level at the bottom of the pipe until a 50 mm height of soil is eroded or 30 min test time is reached, whichever comes first. The erosion rate is then calculated by dividing the total eroded soil height by the time.

6. Steps 4 and 5 are repeated with higher values of velocity (at least 6 value of velocities).

We start with low velocities and increase them progressively in order to be able to determine the critical value that corresponds to the iniation of the erosion.

II.4.4 *Data processing*

Once 6 velocities have been tested, the scour rate ($\dot{Z}(mm/h)$) versus velocity (V (m/s)) curve is obtained then converted to scour rate ($\dot{Z}(mm/h)$) versus shear stress ($\tau(Pa)$) curve or erodibility function.
The bottom shear stress imposed by the water on the soil (τ) is calculated from the average flow velocity (V) in the closed channel section by applying the Darcy-Weisbach law [57] given by:

$$\tau = \frac{1}{8} f \rho V^2 \tag{II.14}$$

Where, f is the friction coefficient and ρ is the volumetric mass density of the water ($1000\, kg/m^3$).

The friction coefficient (f) is obtained from Moody diagram [174] (Figure II.25). It is function of the number of Reynolds (Re) and the relative pipe roughness (ε/D) for the flow.

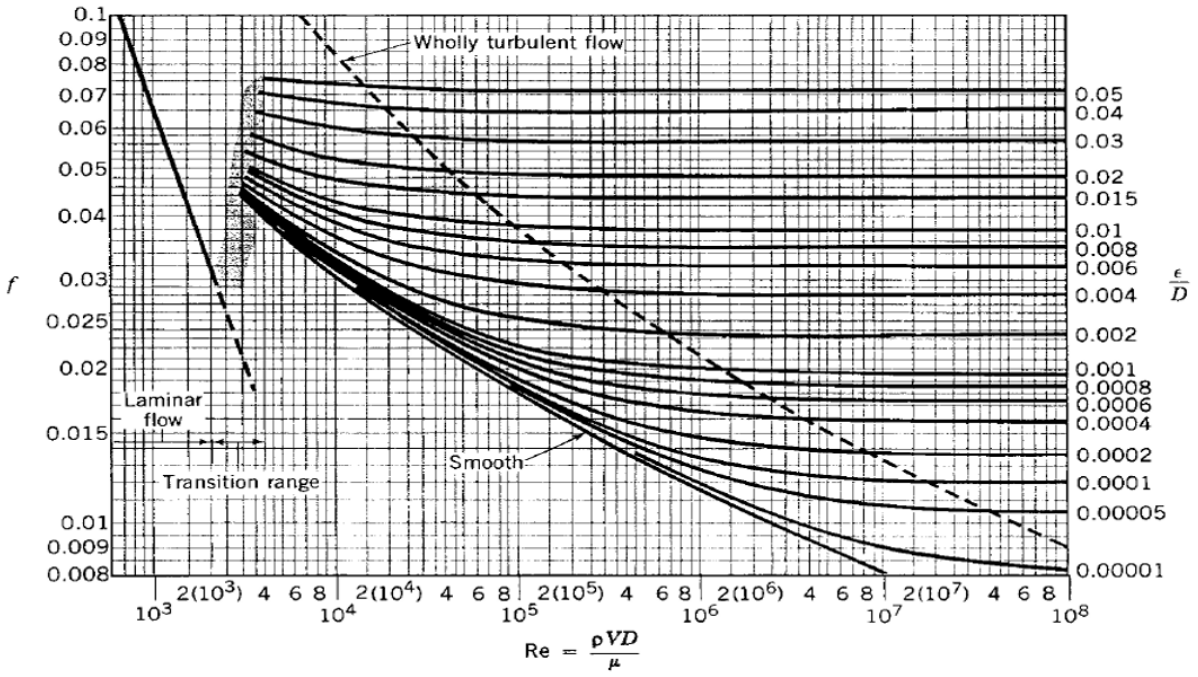

Figure II.25: Moody Chart [55]

An alternative to using the Moody diagram is to solve the equations:

- For laminar flow regime: $f = \dfrac{64}{Re}$
- For transition and turbulent regime (Colebrook equation): $\dfrac{1}{\sqrt{f}} = -2\log_{10}\left(\dfrac{2.51}{Re\sqrt{f}} + \dfrac{\varepsilon/D}{3.7}\right)$

The parameters that should be calculated to determine the friction coefficient are listed and defined as follow:

- The hydraulic diameter is equal to the diameter of a circular pipe when $D = \dfrac{4A}{P}$, where A and P are the wet cross-sectional area and perimeter respectively. For a pipe with a rectangular cross section

$$D = \frac{2ab}{(a+b)} \tag{II.15}$$

  Where a and b represents the width and the height of the pipe respectively.

- The Reynolds number (Re) is calculated assuming that the characteristic length is the equivalent diameter of the pipe (D).

$$Re = \frac{VD}{\nu} \tag{II.16}$$

  Where ν is the kinematic viscosity of water determined as function of water temperature.

- The relative roughness (ε/D) represents the the roughness elements' average height on the pipe surface (ε) on the equivalent diameter of the pipe (D). The roughness elements' average height on the pipe surface (ε) is estimated the half of the medium particle diameter of the soil studied (d_{50}). The use of the factor 0.5 come from the assumption that the top half of the particle protrudes into the flow and the bottom half is embedded in the soil mass.

$$\varepsilon/D = 0.5\, d_{50}/D \tag{II.17}$$

SYNTHESIS

This chapter covers in details the soil selection, experimental facilities, sample preparation and testing technique.The results to better understand the geotechnical and hydraulic conditions of the performed tests are presented. The instruments used are described, their advantages and limitations are specified.

Chapter III :

Development of a novel 3D Scanner Laser Technique for Continuous Monitoring of Pier Scour Topography : Validation and Preliminary tests

INTRODUCTION

This chapter focuses on the measurement validity of a 3D Scanner Laser Technique to continuously monitor the local scour around a pier. First, the proposed data processing methodology was shown in details, with all the softwares used. Next, the results of preliminary flume tests on local scour carried out on medium sand in clear water (considered as benchmark test) were presented. The repeatability of the tests was examined. Finally, the effect of the glass plate maintained on the water surface and water evacuation on the scour topography were studied.

III.1 STRATEGY FOR PROCESSING THE DATA

The Phoxi 3D scanner was purchased from R&D Vision. As a part of my thesis, a systematic strategy for the processing of data acquired by this scanner was developed. This methodology was structured into four main steps (Figure III.1): Data acquisition, Calibration, Post-treatment and Representation. Each of these steps was driven by dedicated software tools : Phoxi-Control, Scilab, Cloud Compare and Matlab, respectively. The primary software used in each step was shown in Figure III.1. In the following sections, a comprehensive details of these steps will be provided.

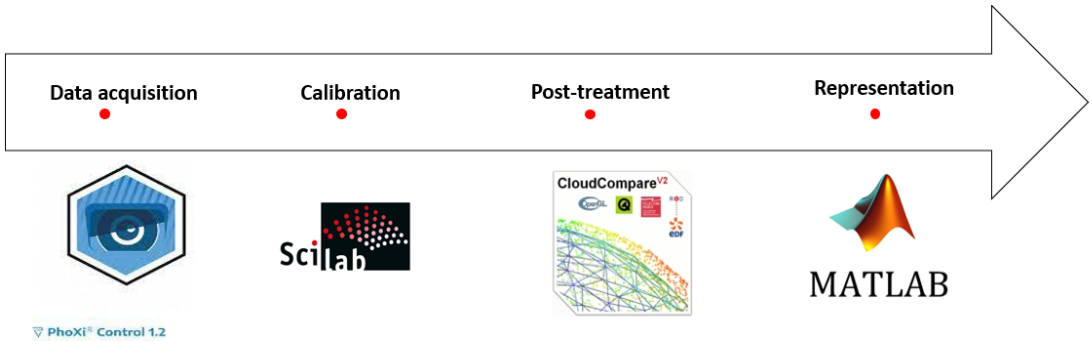

Figure III.1: Methodology used for data processing

III.1.1 *Data acquisition*

The laser scanner was connected through the data acquisition software Phoxi Control to obtain the 3D scans around the pier. Suitable acquisition parameters were chosen in our measurements.By default, the laser power was set to 4095 μWatt, and the exposure time was configured at 20.48 milliseconds. In our measurements, these specific parameter values do not lead to overexposure or camera saturation. The shutter multiply, number of repetitions of a pattern (1) and scan multiply, number of repetitions of a scan (1) parameters provided a good density of original cloud data (up to 1.3 million 3D points). As the scour in sand is a rapid process especially at the beginning of the experiments, the frequency rate of acquisition was set to 0.5 Hz for the first 5 minutes (1 scan per 02 seconds) and then to 0.0033 Hz (1 scan per 5 minutes) for the rest of the experiment. An acquisition method with limited impact of ambient light was also chosen. An automatic triggering of scans was set up with a fixed frame rate and an automatic saving of scanned clouds in ". ply" extension. An example of 3D point cloud, bed around vertical circular pier, obtained using the Phoxi Control software was shown in Figure III.2. In terms of acquisition, the main advantages of this instrument are the rapid acquisition and the ability to give a representation with millions of 3D points.

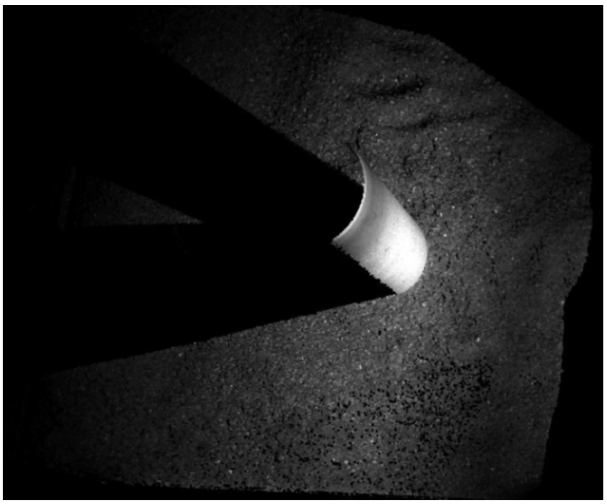

Figure III.2: Typical 3D point cloud in the data acquisition software Phoxi Control

III.1.2 *Calibration*

The calibration described in the following is necessary and valid only for one position of the laser scanner, so the operator should pay attention that the device is well fixed without any movement (example: vibration) during the test running. These corrections were applied to all the data clouds acquired by the instrument.

III.1.2.1 *Refraction correction*

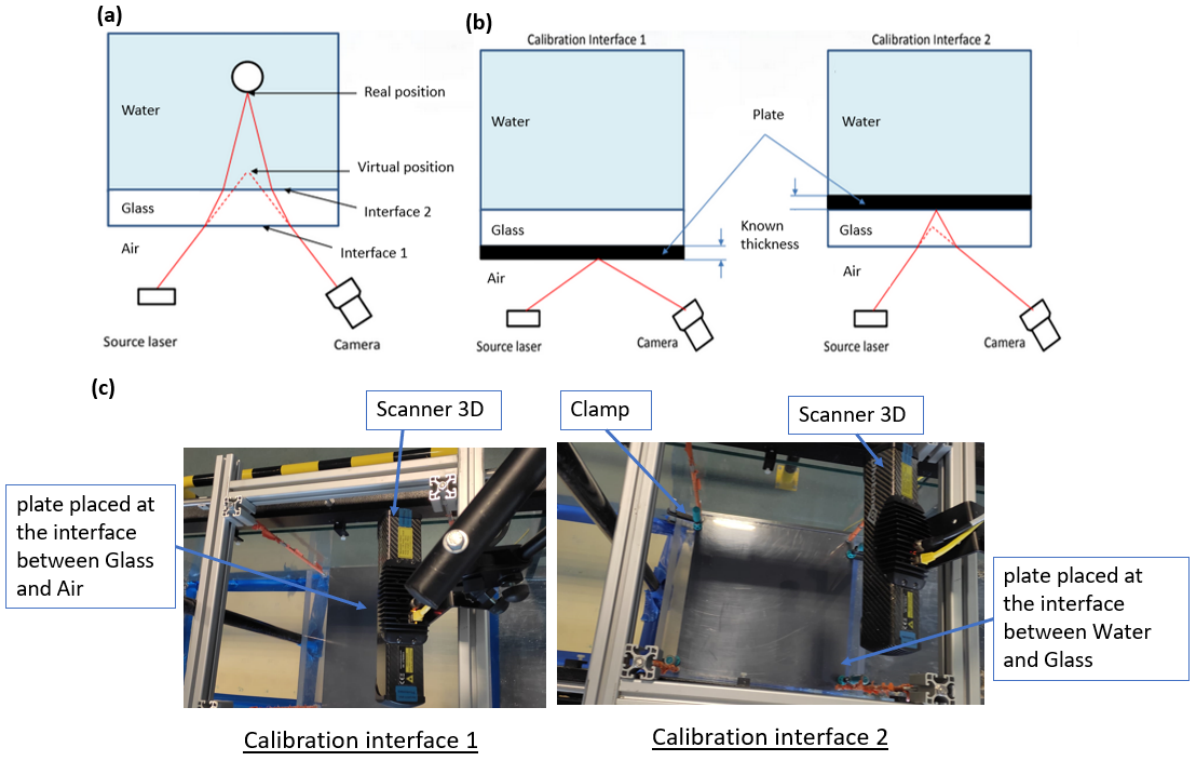

Figure III.3: Refraction correction, (a): scheme showing the consequence of refraction of light ray, (b): scheme showing the steps of calibration, (c): application of the procedure in our measurements

The refraction of light at the interface between two different materials modifies the trajectory of light rays (Figure III.3 (a)) and therefore measured elevations. A correction algorithm in Scilab software to account for the refraction of the light was developed by the R&D Vision and offered with the scanner 3D. The application of this correction algorithm necessitated the determination of the position of the interface 1 (between air and glass) and interface 2 (between glass and water) in function of the position of the camera and the laser device (Figure III.3 (b), (c)). Clamps were used to fix the plate at the interface 2. Two scans of a plate reference, object of known thickness at the two different positions, should be done for each test. To prevent the formation of air bubbles, this step was always performed in empty flume before each test. Having the point clouds from both interfaces in ".ply" extension, the Scilab code was runned after all the data for the scour hole topography were acquired (in ".ply" extension). This process enabled the correction of each acquired scan, resulting in a corresponding corrected scan (in ".ply" extension).

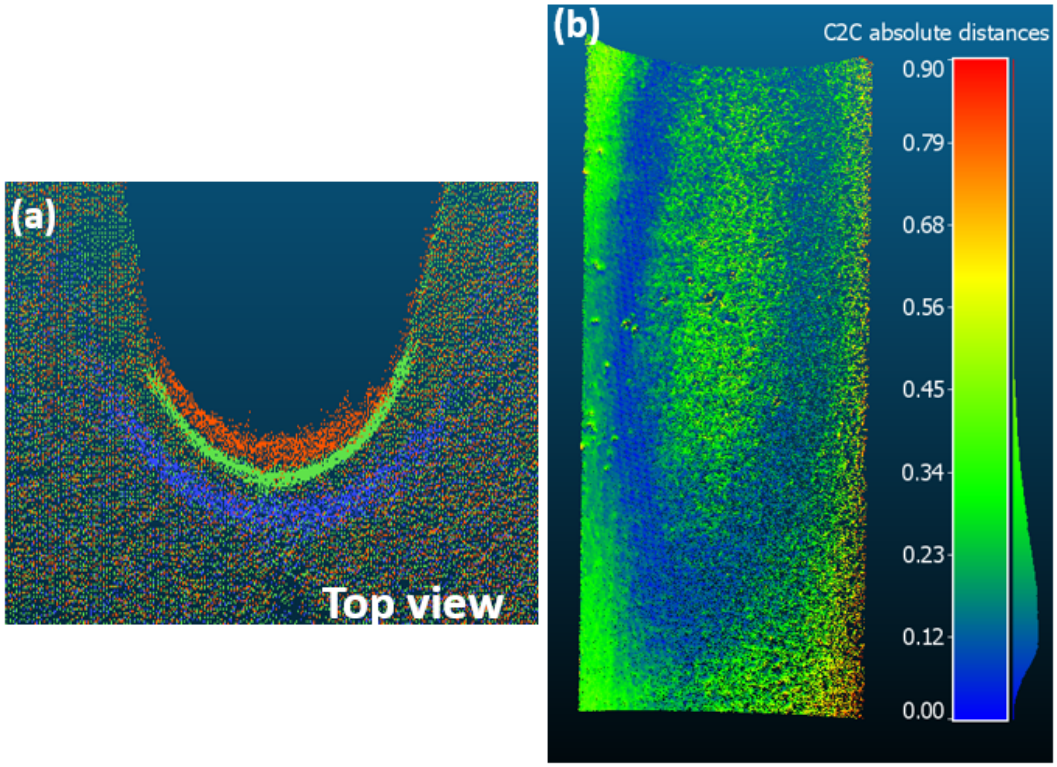

Figure III.4: Comparison between the three clouds resulting of scanning a white circular pier visualized using Cloud Compare;(a): Top view visualisation; Green : Without water and glass; Blue : With water and glass (before correction); Red : With water and glass (after correction), (b):C2C absolute distances between the cylinder after the correction and the cylinder in the air medium

To visualize the importance of this correction step, an application in case of the PVC smooth cylinder obstacle (b=32mm) was done (Figure III.4). The cylinder was scanned before being painted black (originally white) as part of our physical pier scour model test, with the scanner positioned in the upstream section, focusing on the pier. The green, blue and red surfaces refer respectively to scanned cylinder without water and glass, with water and glass before correction and with water and glass after correction visualized in Cloud compare software (Figure III.4(a)). It was observed that the surface of the cylinder scanned in the presence of water and glass before correction was not at all a circle, which means that refraction can have the effect of modifying completely the shape of the scanned object. The application of the correction gave back a near cylinder even if its relative spatial placement was not exactly the same. The amount of refraction depends mostly on the incident angle in water medium and therefore varies with the change in position of the scanner. The refraction correction applied to the underwater scene allows us to restore the accurate geometry without distortion, but it does not place the elements in their exact

correct spatial position relative to reality.

The data sheet for the Photoneo sensor specifies an error margin of 0.05 mm [201]. This error is in the air medium. The R&D Vision supplier of the 3D scanner instrumentation states that directly evaluating the measurement error of Photoneo for an object submerged in water is challenging due to non-linear deformations caused by refraction. Even after running the code correction in Scilab, it's not possible to achieve perfect correction. Therefore, to assess Photoneo's error in a water medium, it's essential to calculate the relative deformation of the object after correction in comparison to the object scanned without water. From the measurements presented for the cylinder case, this error was quantified as follows. First, to minimize the relative positioning error of the two point clouds, the cloud compare's "clouds registration" tool was used. Then, the distance of one cloud to the other was estimated using the Cloud compare's "C2C (Cloud to Cloud) absolute distance" tool for each point of a reference cloud (Green cloud in the air medium (Figure III.4(a))) in relation to a second point cloud (Red cloud in the water medium after correction (Figure III.4(a))). The definition of the "C2C tool" was shown in Appendix. The distribution of the C2C absolute distance along the submerged length of the cylinder was shown in Figure III.4 (b). The highest difference was observed on the edges because in this region, the density of the cloud is the lowest. The average of the error distribution obtained was equal to 0.11 mm. It is important to note that the 0.11 mm does not correspond directly to the residual refraction error. It was considered the mean error that corresponds to Photoneo sensor error in water and after applying the correction code. The observed value is the range of the measurement uncertainty given by the Photoneo, 0.1-0.2 mm. The 0.2 mm given by the Photoneo corresponds to scanner positions too far from the scene being scanned, which was not in our case study. The error was quantified in static water case, without flow. Some additional errors were caused by the turbidity of the water (shown in chapter IV), the high flow velocity, the presence of waves on the water surface and the reflection characteristics of the surface (the color of the surface) being scanned and the presence of a light spot.

III.1.2.2 *Reference change*

The XYZ coordinates were used to identify the location of each point in a point cloud. Photoneo 3D Sensor was configured to generate point cloud within the camera coordinate space (R) (Figure III.5). The origin of the reference R is the center of the camera sensor. The camera sensor is inclined at 15.45° with respect to the sensor's body [275]. In the camera space R, the X-axis points to the device's right side and the Y-axis points below the device [275]. The depth at which the object was observed by the scanner was determined by the Z-axis [275]. The Z-axis aims to

the scene perpendicular to the XY camera sensor plane [275]. The device offers the capability to convert the point cloud into any user-defined coordinate space. However, the refraction code was developed in the camera space coordinate system. For this reason, it was required that the acquisition by the scanner was done using the camera's reference, subsequently applying the necessary of light refraction correction, and finally the step of the reference change.

An algorithm for changing the camera space coordinate system to a local space coordinate system centered on the pier (R') (as shown in Figure III.5) was added to the Scilab code existing for the refraction correction. The algorithm was based on the following points:

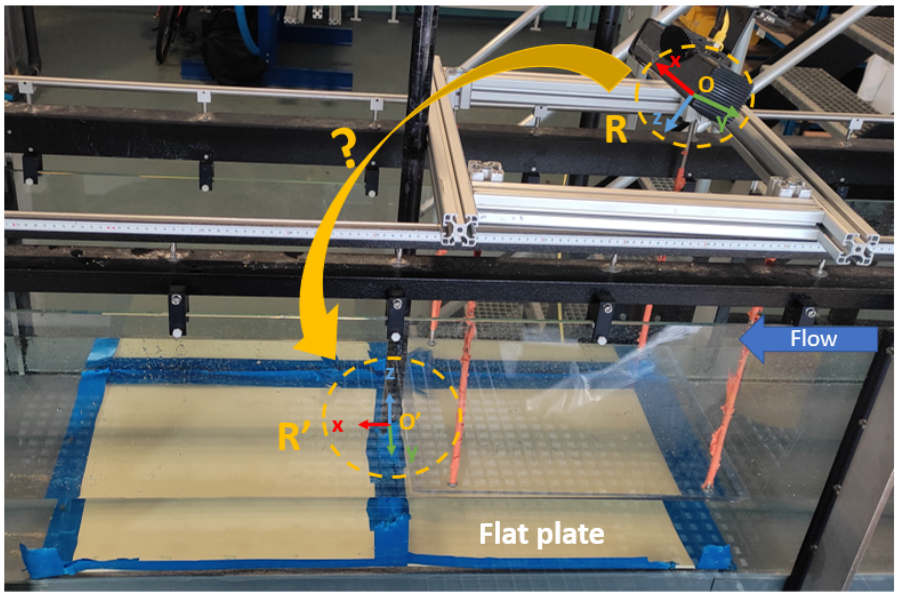

Figure III.5: Reference change from the camera space coordinate system (R) to the local space coordinate system centered at the pier (R'); The X-axis, Y-axis and Z-axis is red, green and blue axis respectively; O is the origin of R being the center of the camera, O' is the origin of R' being the center of the pier; The blue arrow refers to the flow direction

- The mean plane (P) of the point cloud in the reference R was established using the least square method. The equation of the mean plane was denoted as (P): z = ax + by + c. A function F was defined as the sum of squared differences between z_i and $(ax_i + by_i + c)$ for each data point P_i : $\mathrm{F} = \sum_{\mathrm{i}} (\mathrm{z_i} - \mathrm{ax_i} - \mathrm{by_i} - \mathrm{c})^2$
  The coefficients a, b and c of the plane correspond to the minimum of the function F. This implies that the values of a, b, and c can be determined by solving a system of three equations being the derivatives of the function F equals to zeros. $\begin{cases} \frac{\partial \mathrm{F}}{\partial \mathrm{a}} = 0 \\ \frac{\partial \mathrm{F}}{\partial \mathrm{b}} = 0 \\ \frac{\partial \mathrm{F}}{\partial \mathrm{c}} = 0 \end{cases}$

Developing these equations gives : $\begin{bmatrix} \sum_i x_i^2 & \sum_i x_i y_i & \sum_i x_i \\ \sum_i x_i y_i & \sum_i y_i^2 & \sum_i y_i \\ \sum_i x_i & \sum_i y_i & \sum_i 1 \end{bmatrix} \begin{bmatrix} a \\ b \\ c \end{bmatrix} = \begin{bmatrix} \sum_i x_i z_i \\ \sum_i y_i z_i \\ \sum_i z_i \end{bmatrix}$

- Once the coefficients were determined, the coordinates of the unit normal vector on this plane were calculated in the space coordinate system (R) as follows :
$\vec{n} = \left(\mathrm{a}/\sqrt{a^2+b^2+1},\ \mathrm{b}/\sqrt{a^2+b^2+1}, -1/\sqrt{a^2+b^2+1} \right)$

- The rotation angles γ and α for the rotation matrices around the z-axis (Rz) and the x-axis (Rx) respectively were computed using the following formulas: $\gamma = \arctan(n(x)/n(y))$ and $\alpha = \arctan(nyz(y)/nyz(z))$ (Figure III.6). The nyz is the component of vector $\vec{n}$ in the (yz) plane. The rotation matrice R=Rx*Rz allows the transformation of the unit normal vector $\vec{n}$ (n(x),n(y),n(z)) into (0,0,1).
The matrices Rx and Ry were defined by :
$Rx = \begin{bmatrix} 1 & 0 & 0 \\ 0 & \cos(\alpha) & -\sin(\alpha) \\ 0 & \sin(\alpha) & \cos(\alpha) \end{bmatrix}$ and $Rz = \begin{bmatrix} \cos(\gamma) & -\sin(\gamma) & 0 \\ \sin(\gamma) & \cos(\gamma) & 0 \\ 0 & 0 & 1 \end{bmatrix}$

- The coordinate of the center of the cylinder O' (xo',yo',zo') was used to determine the translation matrix $\mathrm{T} = \begin{bmatrix} -xo' \\ -yo' \\ -zo' \end{bmatrix}$

- Once, the rotation and translation matrix were specified. The transformation of the reference was applied to the points in the cloud as follows. P_i' and P_i refer to the point in the cloud after the reference change and before the reference change respectively.
$P_i' = P_i \times \mathrm{Rx} \times \mathrm{Rz} + \mathrm{T}$
$$\begin{bmatrix} x' \\ y' \\ z' \end{bmatrix} = \begin{bmatrix} 1 & 0 & 0 \\ 0 & \cos(\alpha) & -\sin(\alpha) \\ 0 & \sin(\alpha) & \cos(\alpha) \end{bmatrix} \begin{bmatrix} \cos(\gamma) & -\sin(\gamma) & 0 \\ \sin(\gamma) & \cos(\gamma) & 0 \\ 0 & 0 & 1 \end{bmatrix} \begin{bmatrix} x \\ y \\ z \end{bmatrix} + \begin{bmatrix} -x'o \\ -y'o \\ -z'o \end{bmatrix}$$

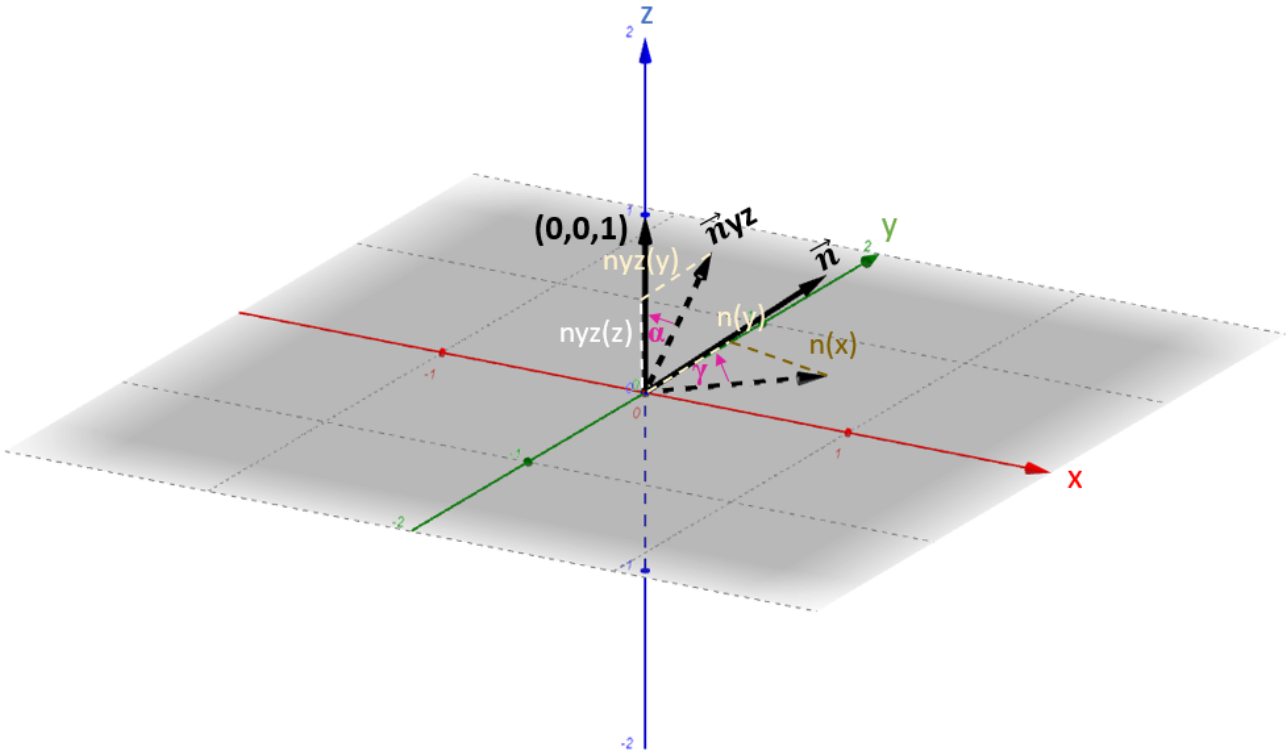

Figure III.6: Rotation angles, γ is the angle used in the rotation matrix Rz and α is the angle used in the rotation matrix Rx; n(x) and n(y) are the components of the unit vector n along the x and y axes, respectively, nyz is the component of vector n in the (yz) plane, nyz(y) and nyz(z) are the components of the vector nyz along the y and z axes, respectively

The outcomes of a practical application example within a smooth PVC flat plate configuration (see Figure III.5) were illustrated in Figure III.7. The blue, green, and red surfaces correspond to the initial scan, the scan post-translation, and the scan after both translation and rotation, respectively. Despite scanning a flat plate, the resulting point cloud doesn't form a perfect plane. Variations from the mean plane were observed in the point cloud, reflecting the uncertainty in the measurement of the 3D laser scanner. The maximum deviation was observed at the edges of the acquisition zone. The presence of this slight curvature is probably due to the sphericity of the fisheye lenses.

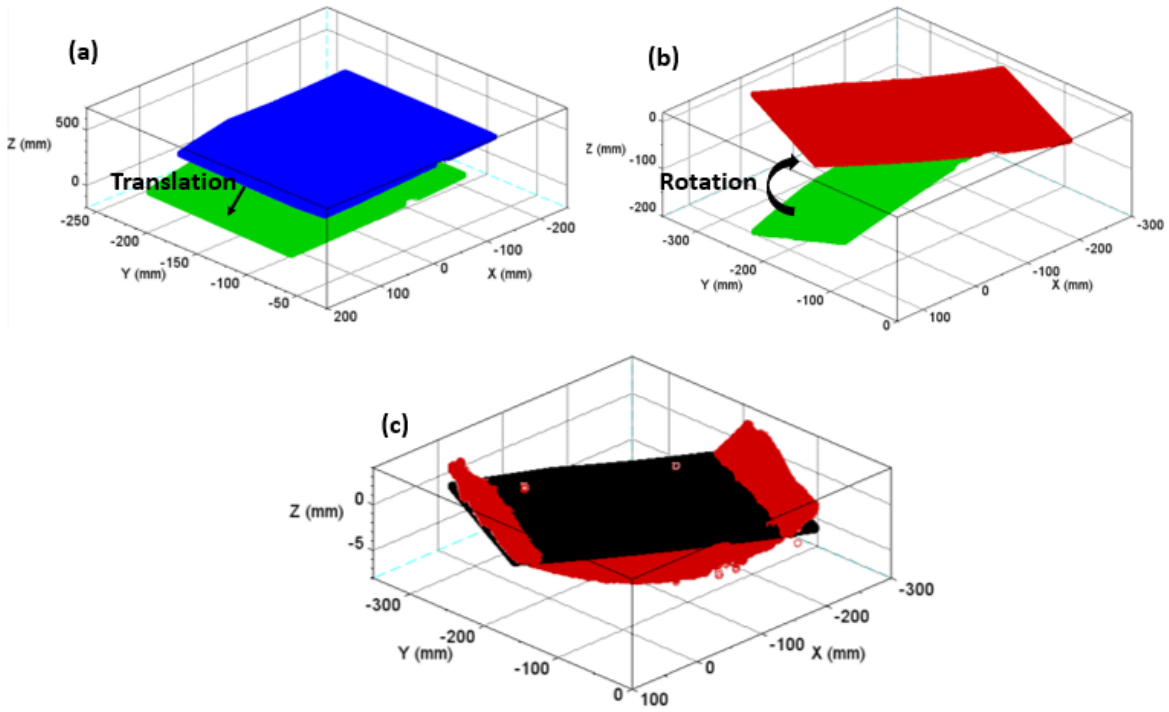

Figure III.7: Results of the reference change applied to an horizontal flat plate using Scilab software, (a): Clouds before and after the application of the translation, (b): (a): Clouds before and after the application of the rotation, (c): Clouds after the reference change (translation + rotation) with the corresponding mean plane (black plane)

III.1.3 *Post treatment*

The post treatment step including cloud cleaning and relative rasterization was performed using Cloud Compare. This software was created by Girardeau-montaut 2006 [108]. It was selected due to its compatibility with ".ply" file formats, its open-source nature, and its extensive utilization in post-treatment of laser scanner acquired clouds by many authors [145, 206, 238, 265].

III.1.3.1 *Cloud cleaning*

The data acquired by the laser scanner always contain scatter points and noises (Figure III.8 (a)). Their presence do not allow a correct interpretation of the object details. Scatter points are points that do not belong to the target object “bed surface”. In our model, the pier was colored in black which permits the elimination of all the points related to the pier. The noise is the result of the divergence of the laser beam. The cloud was cleaned manually using the Cloud Compare software by removing all the scatter points and reducing the noise as much as possible (Figure III.8 (b)).

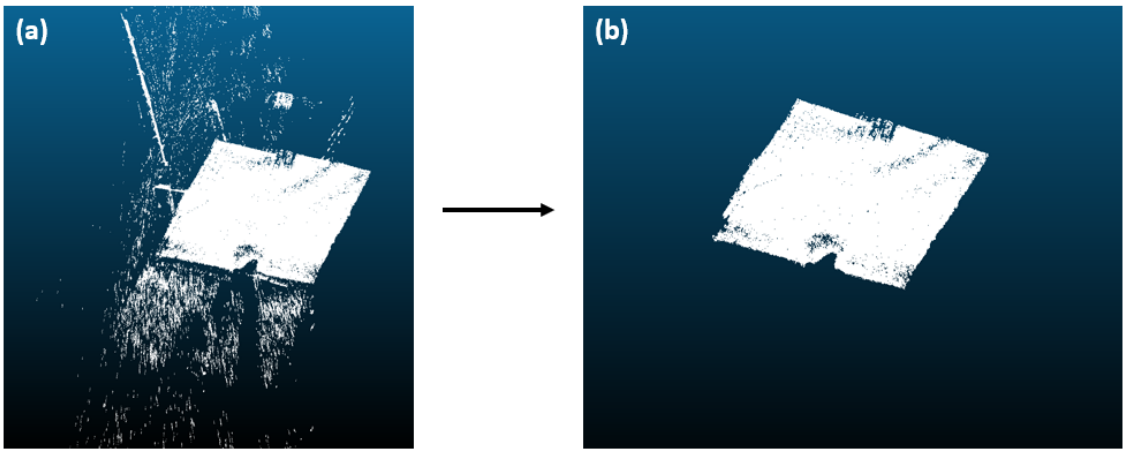

Figure III.8: Cloud cleaning step using Cloud Compare; (a): Cloud before the cleaning step, (b): Cloud after the cleaning step

III.1.3.2 *Relative rasterization*

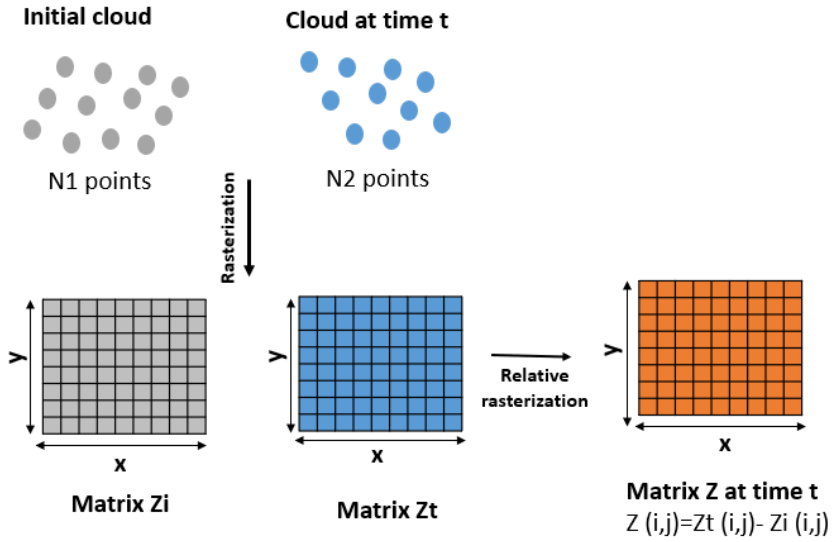

Figure III.9: Relative Rasterization; Where N1 and N2 are the number of points in initial cloud and the cloud at time t, Zi, Zt are the matrices of the elevation for the initial cloud and the cloud at time t, Z is the relative elevation for the cloud at time t, the index i and j refer to the column and line in each matrix

A relative rasterization with the reference cloud, which is always the initial state of the soil, was adapted. Figure III.9 provides a visual representation to enhance the understanding of this step. This choice was due to several reasons:

- The number of points among the different clouds exhibits variations.

- The point density within a single scan is non-uniform, diminishing as the distance from the scanner increases.
- The scan of a flat plate reveals a vertical deviation from a perfectly flat plane.

Each 3D cloud was transformed into a matrix of altitude Z (in ".txt" extension), with the lines and columns corresponding respectively to x and y coordinates. The digital elevation model was created with a fixed horizontal grid resolution of 1×1 mm. The data at time t is the difference between the Z matrix at time t and the Z matrix at the initial time, from the scan of the bed before the erosion (Figure III.9). This step was manually performed for each cloud within Cloud Compare using the "Relative rasterization" tools, specifying the parameters : center, dimensions (width, length) and size of the grid. The previously mentioned parameters were taken constant for every cloud in each specific test.

III.1.4 *Representation*

Once the Z matrices were well defined, Matlab software was used to represent the data. To enhance result quality and achieve a precise digital elevation model, a code for linear interpolation was written in Matlab to replace missing data points (the white area in Figure III.10 (a)) by numbers obtained by linear interpolation (as shown in Figure III.10 (b)). The results were presented using Matlab software in different representation forms (counter map plot, section profiles, scour depth function of azimuth angle, etc.) as shown in following section III.2.

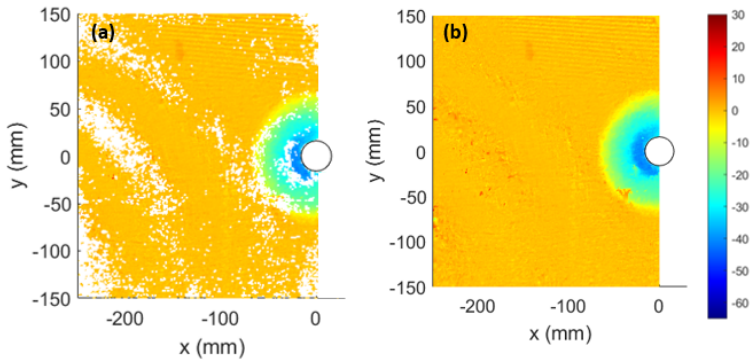

Figure III.10: Results of the linear interpolation applied on a 3D cloud using MATLAB, (a): Cloud points before the interpolation, (b): Cloud points after the interpolation

III.2 RESULTS AND DISCUSSION

III.2.1 *Pier scour on medium sand using 3D Laser Scanner*

III.2.1.1 *Spatio-temporal evolution of the scouring process*

Figure III.11 shows the contour maps of the relative elevation ΔZ from data collected during both upstream and downstream tests at different time intervals, including 2 min, 3 min, 15 min, 30 min, 120 min, 240 min, and 360 min.The general pattern of the local scour observed was distinguished by: the scour hole around the pier and a single dune. The presence of this dune induced the formation of a small hole behind it which marked the sedimentary patterns downstream of the cylinder (Figure III.11 (f),(g)). During the scour development, the shape of the scour hole remained nearly constant and nearly symmetric with respect to the flow direction. The scour pattern observed was consistent with the classical scour hole pattern observed on cohesionless bed in clear water scour regime in the literature (e.g. [219, 252]). The artefact in the contour maps representation was caused by the presence of the light spot near the measurement zone. The contraction of the main flow due to the presence of the pier upstream accelerated the flow, sweeping then ejecting the eroded sediment from the scour hole to the downstream side. Those sediments were deposited downstream the pier and formed the dune which increased progressively in height and reached finally a maximum value close to 0.8 times the pier diameter. Since the scour process was in progress, the sediment in the dune was always in movement by the wake vortices to far downstream of the pier until the equilibrium state was reached. The periodic shedding of von Karman wake vortices made the transportation of the sediments quasi-periodic.

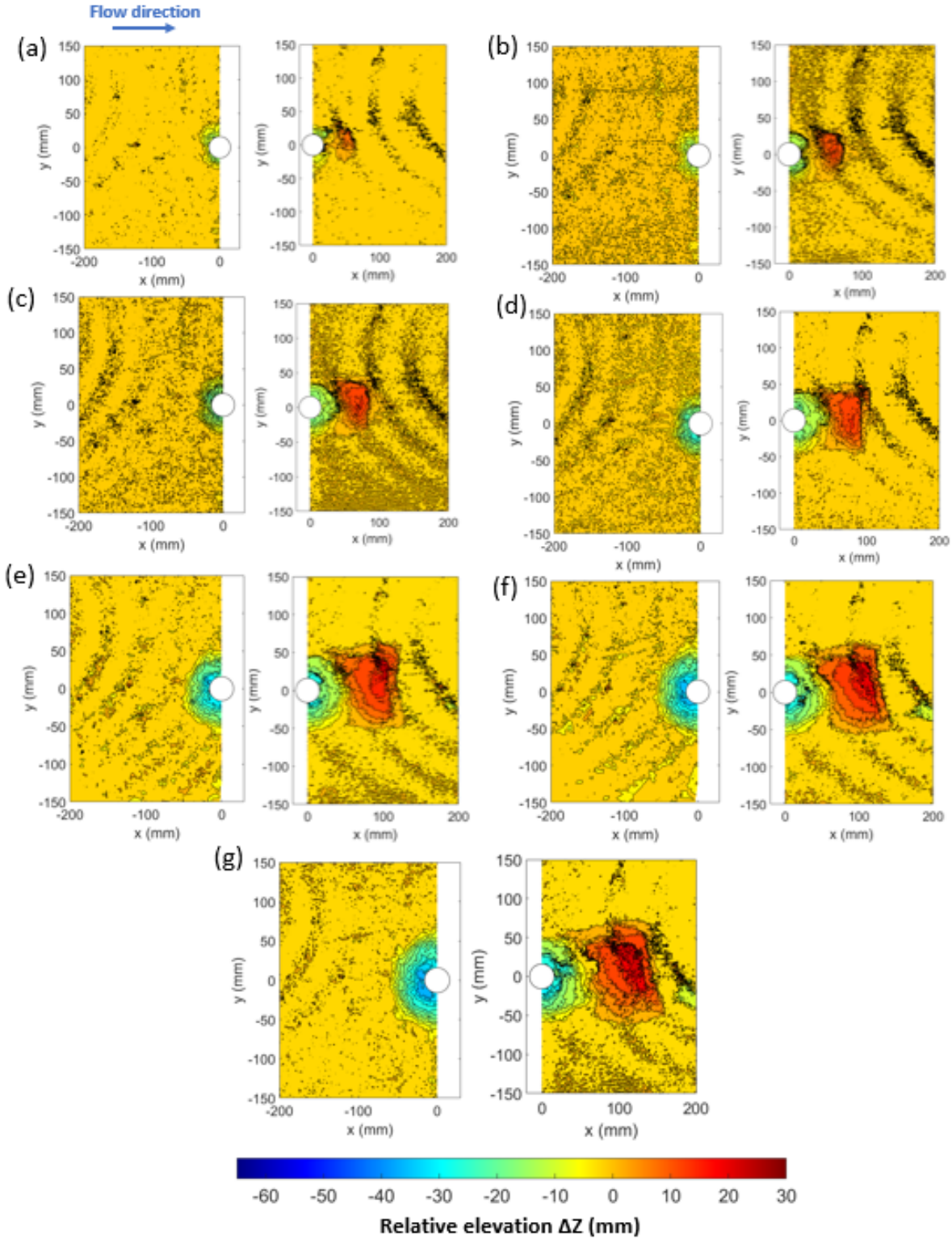

Figure III.11: Contour maps of the relative elevation ΔZ (mm) at various instants during the experiments (a):2 min, (b):3 min, (c):15 min, (d):30 min, (e):120 min, (f):240 min, (g):360 min; the blue arrow corresponds to the flow direction being from the left to the right

Figure III.12 illustrates the scour depth function of the azimuth angles upstream α_u and downstream α_d of the pier at various instants (1 min, 2 min, 3 min, 15 min, 30 min, 120 min and 360 min). The upstream azimuth angle α_u was determined by measuring the angle clockwise from the horizontal axis in the opposite direction of the flow. The downstream azimuth angle α_d was determined by measuring the angle counterclockwise from the horizontal axis in the direction of the flow. The scour hole started at the sides of the pier, where depressions were formed at 01 min (Figure III.12 (a)). The scour depths at 2 min and 3 min was larger on the sides than the front of the pier (Figure III.11 (a), (b) and Figure III.12 (a)). This was in accordance with the initial shear stress distribution around a pier reported in the literature (e.g. [217, 260]). Then, the scoured region enlarged to cover all the area surrounding the cylinder after 15 minutes (Figure III.11 (c)and Figure III.12 (a)). It was observed that the maximum depth at the upstream region was close to the maximum depth at the side of the pier at this stage. Then the scour hole continued progressively to extend and deepen and the maximum final scour depth at the front of the pier became deeper than that at the side region at the end of the experiment (Figure III.11 (f),(g) and Figure III.12 (a)). Whereas, the scour at the downstream region was always the smallest one (Figure III.11 and Figure III.12 (b)). These findings were in agreement with previous studies in literature (e.g. [154, 252]).

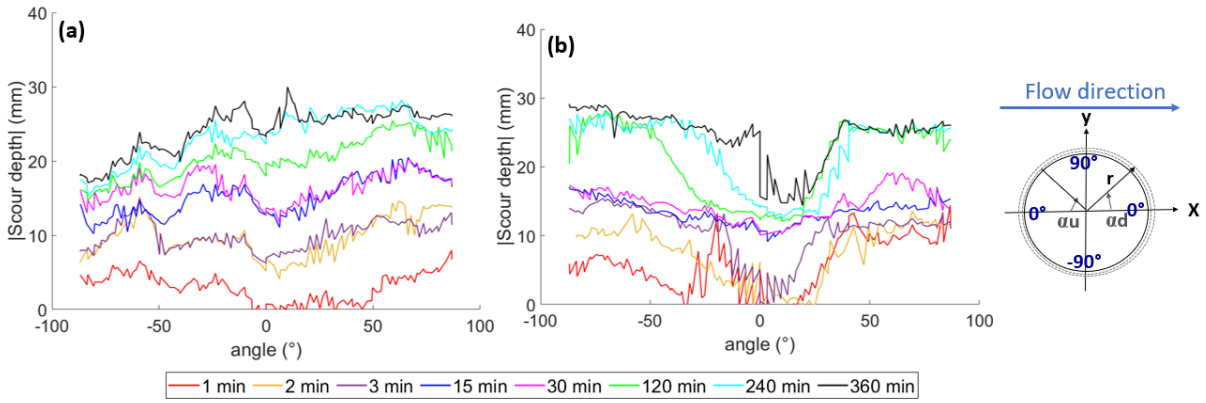

Figure III.12: Temporal variation of the scour depth as function of the azimuth angle at radial coordinate r=18 mm (2 mm from the pier surface); (a) :for the upstream part, (b): for the downstream part; the scheme illustrates the orientation of the azimuth angle for the upstream test α_u and the downstream test α_d

III.2.1.2 *Temporal variation of the scour hole profile*

Figures III.13 and III.14 represent the temporal variation of the longitudinal scour profiles and the transversal scour profiles respectively. In these figures, the upstream part of the profile is on

the left side, while the downstream part of the profile is on the right side.

In longitudinal and transversal sections, the existence of a flat bottom region near the cylinder was identified quantitatively using the scanner 3D and visually. Obtaining topographical measurements in this area was hindered by the presence of the pier, which posed limitations across various instrumentation methods. This constraint was noted in studies by [143] utilizing profilometer laser technique, [203] employing photogrammetry and echosounder profiling, and [154] using a laser distance sensor.

The slope of the best fit straight line for each scour hole profile without the flattened portions was determined. The values of these slopes are almost constant during the part of test from 15 min to 360 min. From the values obtained for the various instants, the mean values were calculated. For the longitudinal profile at the upstream part, two slopes were recognized from 15 min data record. The α_{l1} represents the slope of the upstream section nearest to the pier, α_{l2} represents the slope of the upstream section farther from the pier, and α_l denotes the slope of the entire upstream section. The presence of two slopes in the upstream of the pier suggested the action of the system of horseshoe vortex as reported by [78]. This system has the most important contribution in the deformation of the bed during scour mechanism in cohesionless bed. The values obtained for the time average longitudinal slope at the upstream part are as follows: α_{l1}= 52.66°, α_{l2}= 38.94° and α_l= 41.15°. The natural angle of repose of the sand HN 1/2.5, which is similar to the friction angle measured by the direct shear test was shown in Table II.3 (equals to 35°). The observed scour slopes at the upstream part exceeds the natural angle of respose of sediment particles which was consistent with the prior findings in various studies (e.g. [6, 85, 158]). According to [85], the average scour hole slope in this region is about 10%-15% sharper than the natural angle of repose of sediment particles. The obtained average slope $\alpha_l = 41.15°$ was around 15% sharper than the natural angle of repose of Sand HN1/2.5 particles. If the measurement was made after water was paused or was drained out, the sediment will settle under gravity, then in this case the slope in this region will be equal to the natural angle of repose of the soil as obtained by [166, 266].

Therefore, at the longitudinal downstream part the time average slope of the scour hole (α_{l1}) reaches around 23.75°, beside a time average slope (α_{l2}) 17.68° at the dune. Sediment continuously slides upward on the upper slope of the dune, and downwards on the lower slope of the scour hole. The observed value was consistent with the observation of [118], being around half of the angle of repose of the sediment + 2°. The wake vortices picked the downward sliding

sediments and transported them as bed load to the upward part. Some sediments passed through the dune, while others fed continuously and were deposited at the mount.

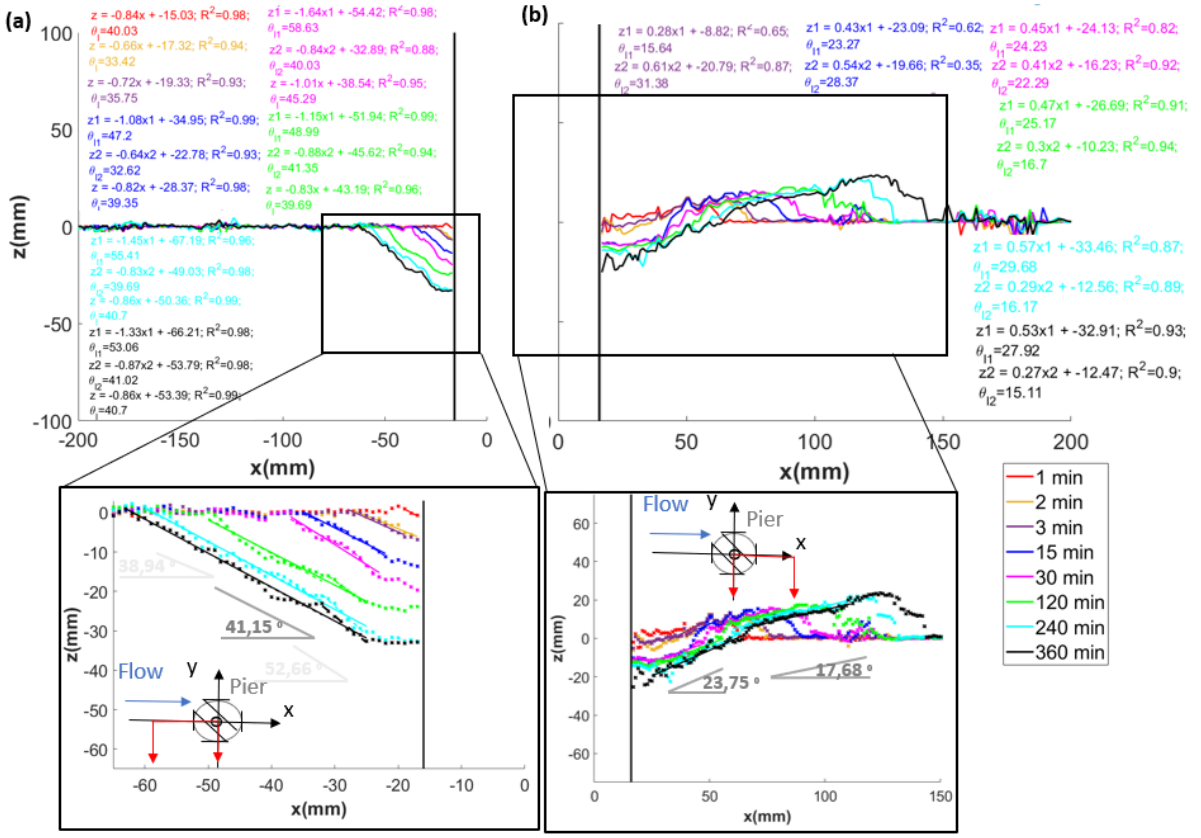

Figure III.13: Temporal variation of the longitudinal scour profiles; (a): upstream of the pier, (b): downstream of the pier; the schemes illustrate the corresponding cross section in red color for each cases

On the other hand, for the central transversal profiles, α_{sl} and α_{sr} are the side slopes at the left of the pier with respect to the flow (for y < 0) and at the right of the pier with respect to the flow (for y > 0). The side slope α_s is the average of the time average α_{sl} and the time average α_{sr}. The α_s was measured around 31.83° for the upstream test against 32.67° for the downstream test. These values were close to the friction angle of the sand HN1/2.5. This was in agreement with the literature (e.g.[150, 273]).

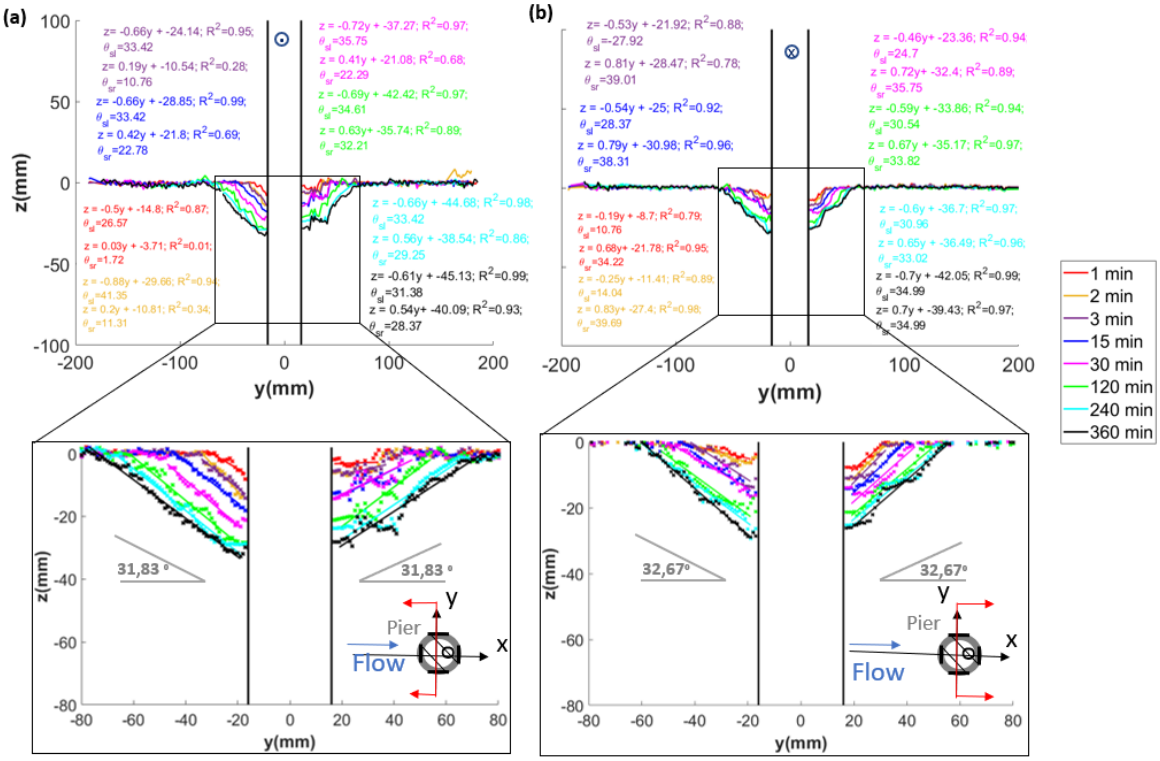

Figure III.14: Temporal variation of the transversal scour profiles; (a): upstream of the pier, (b): downstream of the pier; the schemes illustrate the corresponding cross section in red color for each cases

III.2.1.3 *Temporal variation of maximum scour depth*

The point having the maximum depth was identified based on experimental measurements obtained at the end of the tests, corresponding to the 360 minutes. This determination was made for both upstream and downstream test campaigns. The point with the greatest depth value, from either campaign, was selected. The radial coordinate (r) of this point measures 19 mm (at 3mm from the pier face), and it was positioned at an azimuth angle upstream of the pier of $\alpha_u = 7°$. The position of the deepest scour depth in the medium sand was at the front of the pier having α_u close to 0°. This was consistent with findings from earlier studies on cohesionless bed in clear water scour regime [92, 96, 268].

The temporal variation of non dimensional scour depth at the point of the final maximum scour depth previously determined was presented in Fig. III.15. In the initial stage of the scour process, scour depth increased very rapidly. It attained above 60% of the final scour depth at the first 30 min, then increased more slowly to reach finally at 240 min an asymptotic final state. The final scour depth measured was 1.1 times the diameter of the pile used, in accordance with the values reported in the literature [96, 164, 217]. The best trend curves for the exponential and

hyperbolic laws were determined from the measured data. These two laws were selected being commonly used in the literature [16, 56, 119, 199, 242, 249, 274] for the temporal evolution of the maximum scour depth. The regression coefficients obtained were of the order of 0.9, showing that these equations describe well the temporal evolution of the maximum scour depth.

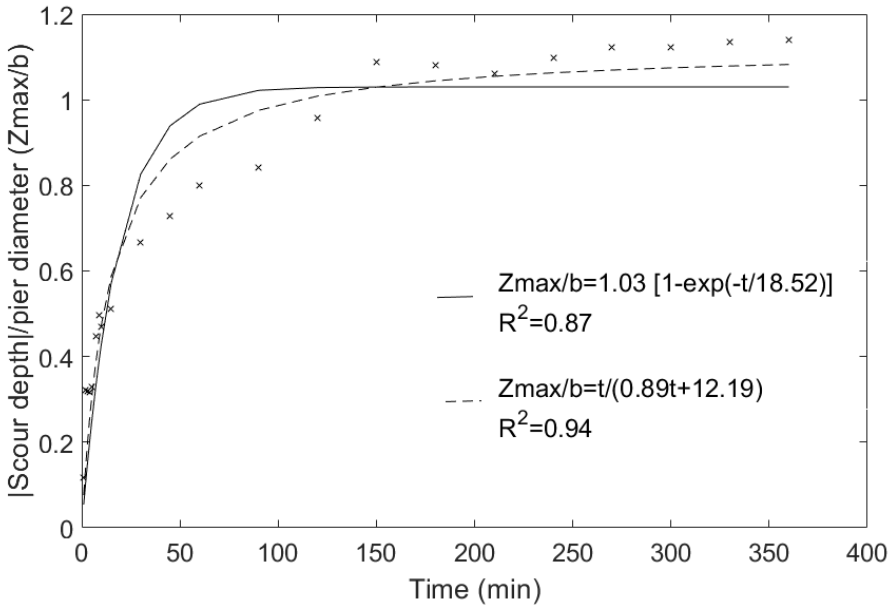

Figure III.15: Temporal evolution of maximum scour depth, (x): experimental data, (-): exponential fitting curve, (- -): hyperbolic fitting curve

III.2.1.4 *Repeatability of the tests*

The experimental procedure raises the issue of test repeatability, since a full geometry of the scour hole will result from two experiments. The quantification of the error due to test repeatability was done based on a total of six tests: three tests upstream of the pier and three tests downstream of the pier.

For each point P within the data set, the mean depth $Z_{p(average)}$ and the standard deviation σ_p were calculated. The punctual mean depth $Z_{p(average)}$ were determined by averaging the depths $Z_{p(i)}$ from each of the three tests, denoted by the index (i) ranging from 1 to 3. The punctual standard deviation for each data point was computed using the formula $\sigma_P = \frac{\Sigma\left(Z_{p(\,\mathrm{i}\,)} - Z_{p(\,\mathrm{average}\,)}\right)^2}{n-1}$, where n equals the number of tests, which is 3.

Figure III.16 illustrates the spatial distribution of the $Z_{p(average)}$ and σ_p across the measured zones at 15 min, 60 min, 240 min and 360 min. The figure on the left represents the results obtained when the scanner is focused on the upstream part, while the figures on the right represent

the results when the scanner is focused on the downstream part for each respective time. These results show that the punctual standard deviation was less than 5 mm on the most surfaces. Therefore, the standard deviation (σ) was the average of all punctual standard deviations (σ_p) for data points where $Z_{p(average)}$ exceeds 0.11 mm or falls below -0.11 mm. Repeatability was checked for different times (2, 5, 10, 15, 30, 45, and 60 minutes, followed by every 30 minutes up to 360 min). The resulting value of σ was found to be within the 0.5-1.12 mm range, which was considered acceptable.

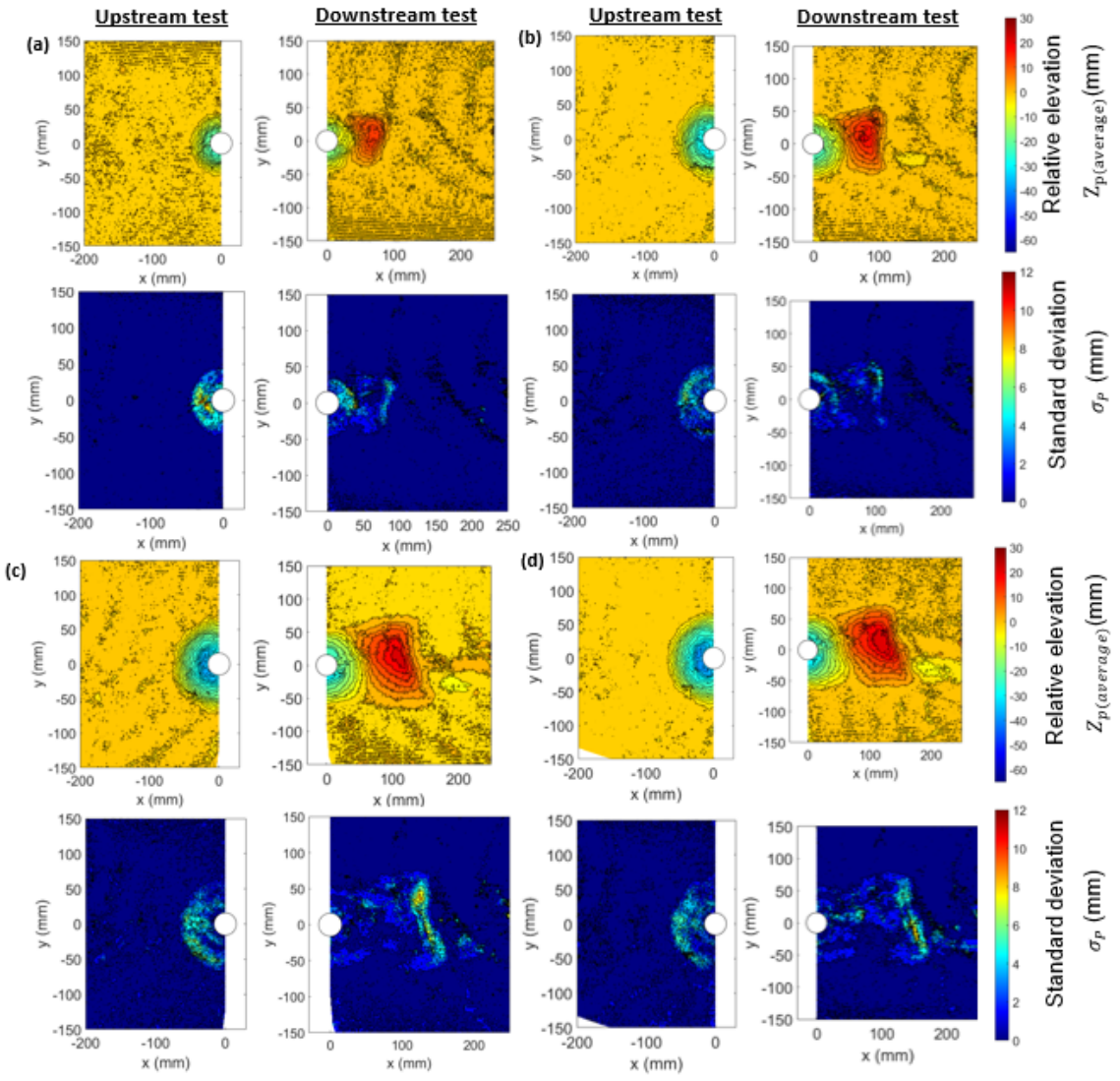

Figure III.16: The spatial distribution of the punctual mean depth $Z_{p(average)}$ and the punctual standard deviation σ_p from three tests upstream and three tests downstream of the pier at (a):15 min, (b): 60 min, (c): 240 min and (d):360 min; the flow direction is from the left to the right

III.2.1.5 *Effect of Plexiglas plate on pier scour topography*

Two tests were conducted without the Plexiglas plate covering the water surface. In the first test, the scanner focused on the upstream part of the pier, while in the second test, it focused on the downstream part of the pier. For each test, initially, the Plexiglas plate was placed on the water surface to enable calibration and capture an initial scan before any soil erosion occurred. Subsequently, the Plexiglas plate was removed, and the test was running for a duration of 360 minutes. At the end of the 6-hour test run, the Plexiglas plate was carefully replaced on the water surface and the topography of the scour was scanned. These tests were conducted using Hostun sand HN1/2.5 under a water depth of 15 cm (as indicated in Table II.6 and Table II.4). According to [254, 263], as the water depth beneath the ice cover decreases, the maximum velocity was increased, and its location was shifted downward simultaneously. This resulted in increasing the effect of the ice cover on the pier scour. So, this particular condition was chosen due to its lower water depth compared to the other test scenario performed in hydraulic condition 2 under a water depth of 17 cm (Table II.6 and Table II.4).

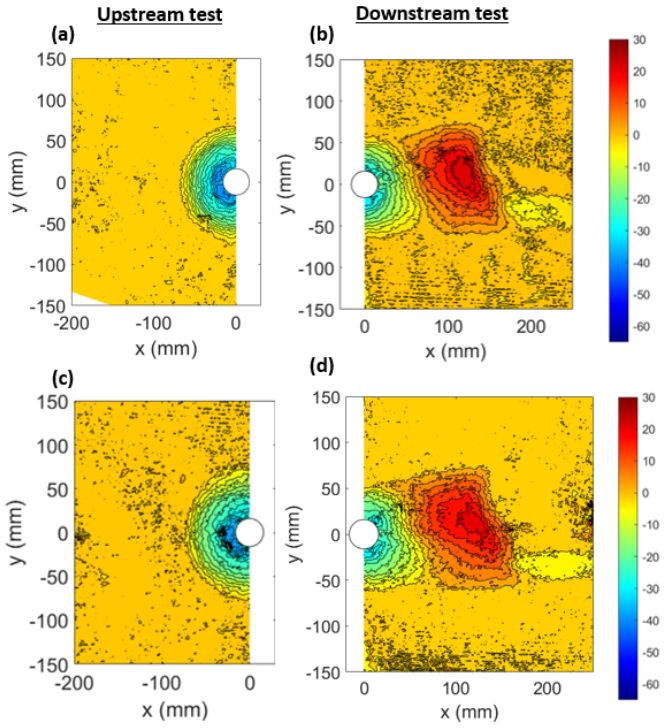

Figure III.17: Contour maps of the scour topography at 360 min for upstream and downstream tests, (a),(b): with the Plexiglas plate $Z_{(average)}$ from three tests, (c),(d): without the Plexiglas plate; where (a),(c):from upstream test and (b),(d): from downstream test, the flow direction is from the left to the right

Figure III.17 above shows a comparison of the contour maps of the scour topography at the end of tests (360 min) for tests with and without the Plexiglas plate. The figures at the left side refers to the results from the upstream tests and those on the right refers to results from the downstream tests. For tests with the Plexiglas plate, the values taken are those of the average relative elevation $Z_{p(average)}$ from the three tests as previously described in the section III.2.1.4. The contours with and without plate obtained were similar.

For a better view of the results, Figure III.18 presents a comparison of longitudinal and transversal profiles with and without the Plexiglas plate. The figures on the left pertain to the results obtained from the upstream tests, while those on the right side correspond to the results derived from the downstream tests. The red curve represents the punctual average scour depth $Z_{p(average)}$, which is the result of three tests. The corresponding error bar indicates the corresponding punctual standard deviation σ_p. The longitudinal and transverse profiles without the plate lie within the error bar zone determined for the test with the plate.

These results confirm that the Plexiglas plate has negligible effect on the topography of the scour hole. The observed results contradicts the observations reported by [234, 254, 263] that the presence of an ice cover surrounding the bridge pier amplify the pier scour. The Froude number in our study, which is less than 0.24, explain why the plate did not influence pier scour [143].

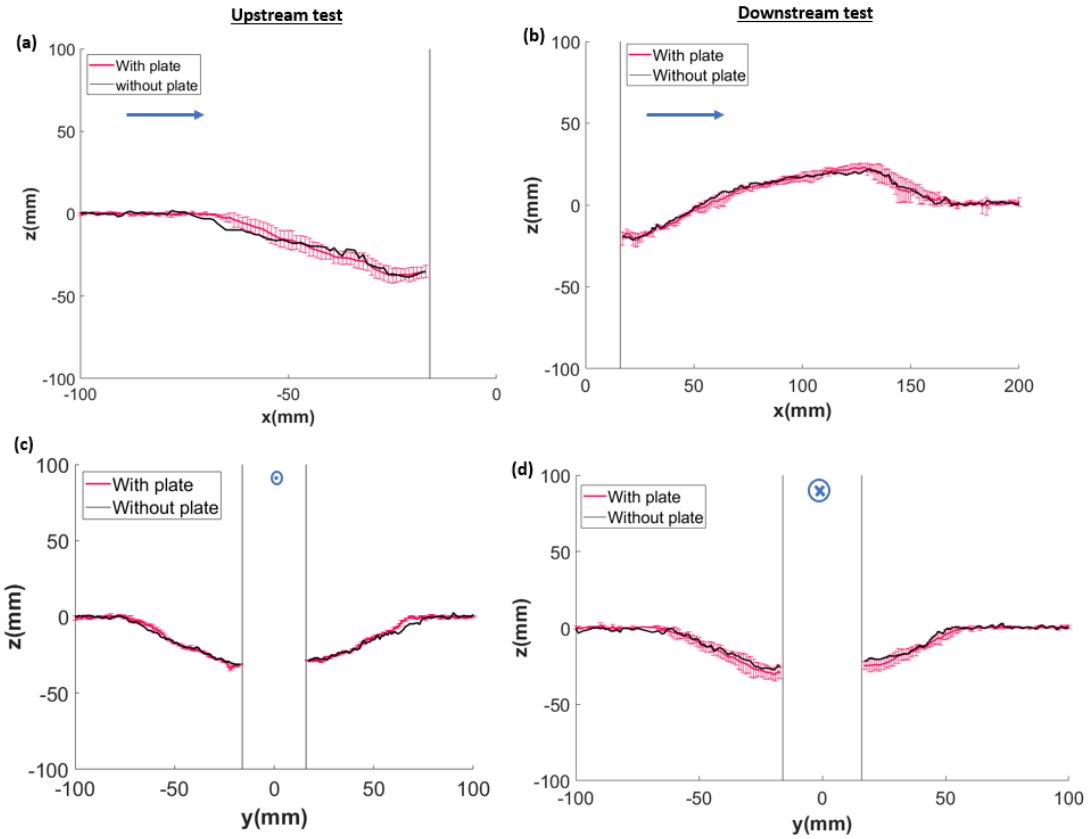

Figure III.18: Comparison of the scour hole profiles with and without the Plexiglas plate at 360 min; (a),(b):for the longitudinal section and (c),(d): for the transversal section; where (a),(c): from upstream test and (b),(d): from downstream test; The blue arrows refers to the flow direction

III.2.2 *Effect of water evacuation on pier scour topography*

Acquiring scans under water requires a calibration process specific to the laser scanner's position. Given the constraint of only one scanner device available, obtaining a complete scan of the entire scour hole area under water was not feasible. A practical solution involves draining water, conducting scans on each side, and then merging the two scan portions. The effect of water evacuation on the geometric shape of the scour pit was studied for this purpose. To make evacuation as slow as possible, we've tilted the channel by (-0.5%) and kept the tail gate located at the exit element of the channel vertical during the draining.

Figure III.19 compares longitudinal and transversal scour profiles before and after water evacuation at the end of the upstream test (at 360 min). This comparison was conducted for two mixtures: 85% sand+15% clay and 85% sand+10% clay+5% Silt. These two mixtures were selected from our tested soils based on their erosion resistance. The mixture 85% sand+15% clay,

demonstrated the highest critical shear stress and critical velocity, followed by the mixture 85% sand+10% clay+5% Silt (as shown in Table II.4). Despite the precautions taken to slow down the water evacuation, the results show that the evacuation has an effect on the scour hole geometry (Figure III.19). Water drainage leads to sediment deposition in the scour hole, reducing scour depths. This effect was more significant in the 85% sand+10% clay+5% Silt mixture, compared to the 85% sand+15% clay mixture. This was expected because the mixture 85% sand + 15% clay is more resistant to erosion than 85% sand+ 10% clay+ 5% Silt. This clarifies the reason that in our tests collecting data post-water evacuation was not an appropriate method. Therefore, it was not feasible to capture the complete scour hole using the 3D scanner for a single test. It is important to note that likely the procedure already described will be feasible for soils more resistant to erosion than our tested beds.

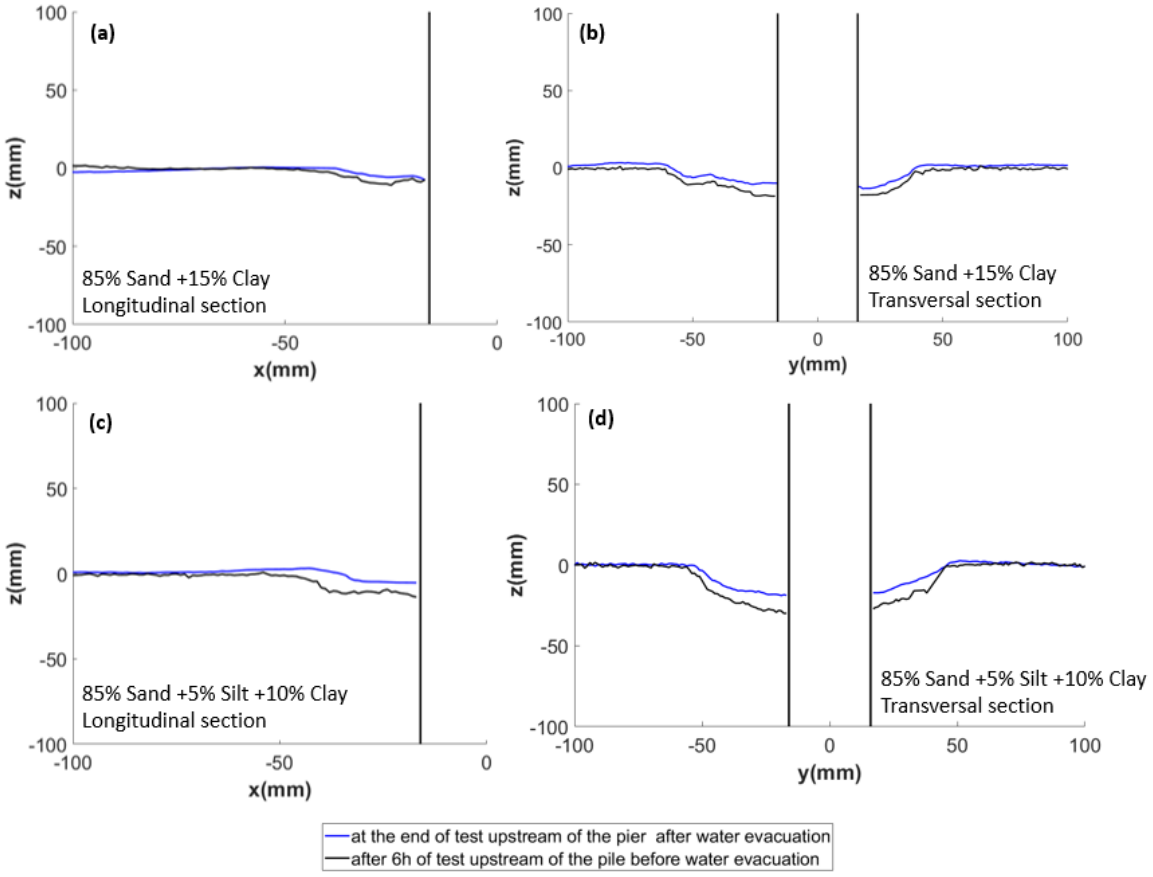

Figure III.19: Comparison of scour profiles at the end of the upstream test (at 360 min) before and after water evacuation; on (a),(b): 85% sand+15% clay and (c),(d):85% sand+10% clay+5% Silt; where (a),(c): longitudinal profile, (b),(d): transversal profile

SYNTHESIS

The capability of a terrestrial laser scanner to dynamically measure the bed elevation change during the physical scour mechanism in laboratory setups was demonstrated. A suitable procedure was presented as a set of actions for calibrate, treat the acquired data in order to make operational the device and obtain a correct 3D digital elevation data of the shaped scour hole with the highest spatial accuracy. All observed preliminary results on medium sand are in agreement with previous studies. Repeatability tests showed a temporal standard deviation within accepted range 0.5-1.12 mm. The presented work provides an experimental database for numerical simulation of medium granular sediment scour models. Such measurement approach provides appreciated advancements in monitoring the development of the scour hole around a pier. The discussed methodology is rapid, automatic and allows temporal scour measurement with high level of spatial accuracy. In addition, it allows the measurement without the necessity to drain the water. However, limitations were related to the crucial position choice due to the shadow formed by the presence of object and the limited dimensions of acquisition zone. Some environmental (turbidity, waves) can also affect the original data acquisition and then can prevent the possibility of measurement. It was observed that the Plexiglas plate maintained on the water surface has negligible effect on the recorded topography of the scour hole. However, a deformation of the scour hole topography was caused by the water evacuation. From that observation, measurements were achieved in water presence in the flume.

Chapter IV :

Experimental Investigation of Pier Scour in Cohesive Soils

INTRODUCTION

This chapter presents the results from experimental investigation of the pier scour in cohesive soils. The erosive parameters of the investigated soils are first determined. Then, the flume tests measurements on the scouring process are presented. They focus mainly on the effect of changing the type of fines content on the geometry of the scour hole and the temporal propagation of scour process. In addition, the study compares the maximum scour depth over time obtained experimentally to the SRICOS-EFA prediction approach. Other empirical relationships are also evaluated. Further, the temporal variation of the plane scour hole dimensions and volumes is reported.

IV.1 EROSION FUNCTION APPARATUS MESUREMENTS : QUANTIFICATION OF SOIL'S ERODIBILITY

The erosion properties of the tested soils are obtained using the Erosion Function Apparatus (EFA). Tests results for scour rate ($\dot{Z}$) function of shear stress (τ) and also scour rate ($\dot{Z}$) function of flow velocity (V) are shown in Figure IV.1 in linear scales and in Figure IV.2 in logarithmic scale. The relative error of measurement of the erosion rate, shear stress and flow velocity in our results is taken 10% as previously reported by [55]. This relative error is represented by error bars for each measurement point on the figures IV.1 and IV.2. The values of the erosive parameters like, the critical shear stress τ_c, the critical velocity Vc, the initial slope of erosion rate vs shear stress curve Si_τ, the initial slope of erosion rate vs velocity curve Si_V and the Erosion Category EC for the tested soils are summarized in Table IV.1.

The method used to determine these erosive parameters is described below.

- Data for erosion rate vs shear stress and erosion rate vs velocity are fitted to best curves taking all points providing an erosion rate greater than 0.1 mm/h [54]. The choice of an arbitrarily low erosion rate of 0.1 mm/h is justified by the fact that 0.1 mm/h is practically the same as 0 mm/h. Fitting curves from measurements for all tested soils are observed to be linear (Figure IV.1). The linear fitting was observed in previous studies using the erosion function apparatus [55], as well as using other erosion tests such as the hole erosion test [20, 116].

- The critical shear stress and the critical velocity represent the threshold values at which erosion is initiated and correspond to the extrapolation of the linear erosion function trend to the horizontal axis as previously reported by [24, 256]. An example of the position of critical shear stress for mixture M5 (green curve) is illustrated in Figure IV.1 (a).

- Using results from different soils, [44] established the erosion category (EC) of soils presented by linear limits on the logarithmic scale chart plots of erosion rate versus shear stress or flow velocity. The representative value for EC is determined as the location of median point of the erosion curve on the defined boundaries in erosion rate versus shear stress in the logarithmic chart [54], as shown in Figure I.12 (b) in Chapter I.

- The initial erodibility (S_i) is represented by the slope of the erosion curve when erosion is initiated [54]. It indicates the rate at which the soil erodes at the critical shear stress or critical flow velocity. When the curve is linear, S_i is its slope. For each tested soil, the Si is calculated separately for the shear stress plot, named Si_τ, and for the flow velocity plot, named Si_V [54].

As depicted in Figure IV.2, the erosion characteristics of fine sand and the M1 mixture (85% sand and 15% silt) fall within the classification of "Very High Erodibility I". The erosion category of the M2 mixture (85% sand, 10% silt, and 5% clay), M3 (85% sand + 7.5 % silt + 7.5 % clay) , M4 (85% sand + 5 % silt + 10 % clay) and M5 (85% sand + 15 % clay) are classified as "High Erodibility II". It is observed that adding cohesive fines to fine sand results on an increase of critical shear stress τ_c, critical velocity Vc and an improvement of erosion category EC (Table IV.1). Simultaneously, it causes a decrease in the initial slope of the erosion curve Si_τ and Si_V (Table IV.1). Furthermore, it is observed that the clay has a greater influence than silt on the erodibility behaviour of the soil. These observations are consistent with previous studies on fine grained soils that indicated that a decrease in the d_{50} parameter makes the soil more resistant to erosion [75, 223]. The erosion properties observed for a natural sand tested at the Erosion Function Apparatus (EFA) by Briaud are as follow: Critical shear stress $\tau_{cr} = 0.22$ Pa, Initial slope (shear plot) $Si_\tau = 1163.22\ mm/h/N/m^2$, Critical velocity Vc=0.25 m/s, Initial slope

(velocity plot) $Si_V = 2480.40\ mm/h/m/s$ and Erosion Category EC=1 [53]. It is noted that the values of erosion parameters observed for our sand exhibit a similar order of magnitude.

The flow intensity values are presented in the Table IV.2. The flow intensity was defined as the ratio between the flow velocity V (0.26 m/s) and the critical velocity V_c for each soil.

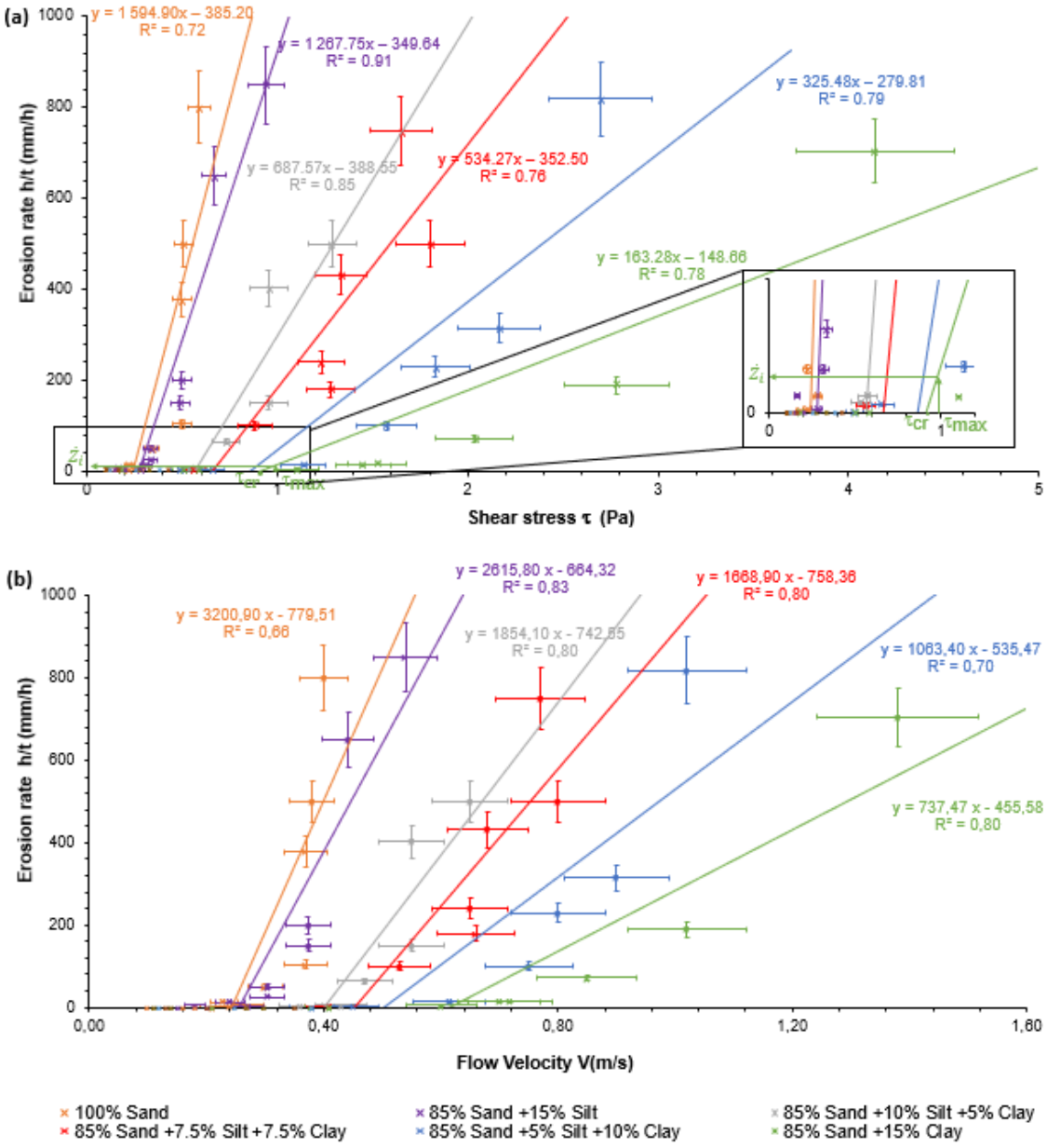

Figure IV.1: EFA results for the different soils using linear scales, (a) erosion rate as a function of shear stress, (b) erosion rate as a function of flow velocity

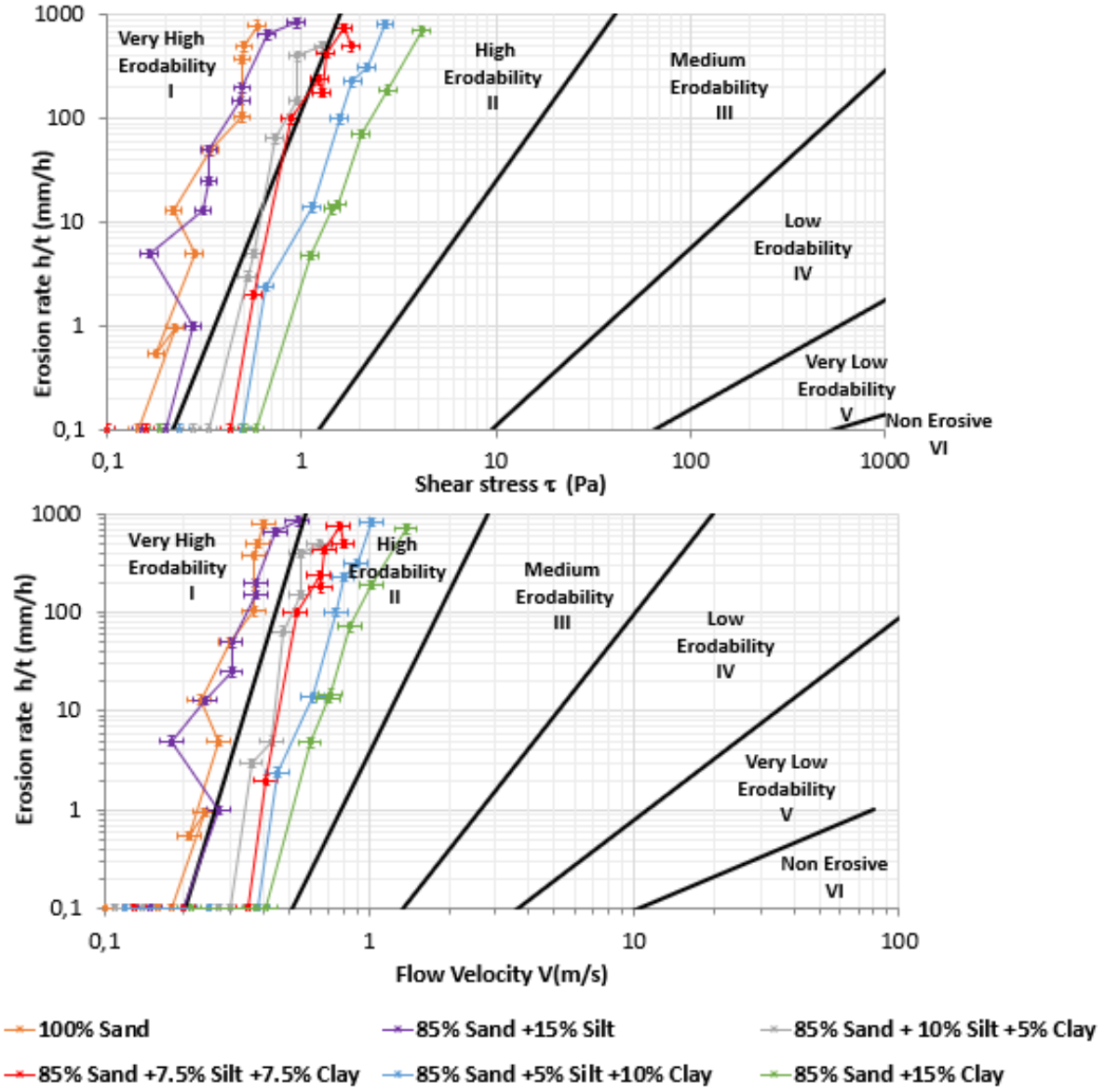

Figure IV.2: EFA results for the different soils using logarithmic scales, (a) erosion rate as a function of shear stress, (b) erosion rate as a function of flow velocity

	Sand	M1	M2	M3	M4	M5
Critical shear stress τ_c (Pa)	0.24	0.28	0.56	0.66	0.86	0.91
Initial slope (shear plot) Si_τ (mm/h/N/m^2)	1594.90	1267.75	687.57	534.27	325.48	163.28
Critical Velocity V_c (m/s)	0.24	0.25	0.40	0.45	0.50	0.62
Initial slope (velocity plot) Si_V (mm/h/m/s)	3200.94	2615.84	1854.13	1668.94	1063.44	737.50
Erosion Category EC	1.25	1.30	1.50	1.60	1.70	1.80
Erosion Classification	Very High Erodibility I			High Erodibility II		

Table IV.1: Erosive characterization of tested soils, where M1: 85% Sand +15% Silt, M2: 85% Sand +10% Silt +5% Clay, M3: 85% Sand +7.5% Silt +7.5% Clay, M4: 85% Sand +5% Silt +10% Clay and M5: 85% Sand +15% Clay

	Sand	M1	M2	M3	M4	M5
Flow intensity $\frac{V}{V_{cr}}$	1.08	1.04	0.65	0.57	0.52	0.42

Table IV.2: Flow intensity for the conducted flume tests on the different soils, V is the flow velocity 0.26 m/s and V_{cr} is the critical velocity determined by the Erosion Function Apparatus,, where M1: 85% Sand +15% Silt, M2: 85% Sand +10% Silt +5% Clay, M3: 85% Sand +7.5% Silt +7.5% Clay, M4: 85% Sand +5% Silt +10% Clay and M5: 85% Sand +15% Clay

The critical bottom velocity (u_*) and critical Shields number (θ_c) were determined based on the critical shear stress values (τ_c) for the different tested soils (Table IV.3).

	Sand	M1	M2	M3	M4	M5
Critical bottom friction velocity u_{*c} (m/s)	0.015	0.017	0.024	0.026	0.029	0.030
Critical Shields number θ_c	0.046*	0.03**	0.025**	0.022**	0.024**	0.027**

Table IV.3: Critical bottom friction velocity u_{*c} and critical shields number θ_c for the different tested soils; * : using equation of Soulsby 1997 [236]; ** : using the diagram θ_c as function of Re_* proposed by Ternat et al. 2008 [247] considering that the porosity n is equal to 0.62-0.67

IV.2 FLUME TESTS : SCOURING PROCESS MEASUREMENT

IV.2.1 *Scour evolve and deposition pattern*

IV.2.1.1 *Quantitative approach: data processing using Scanner 3D*

Figure IV.3 illustrates a visual representation of the changes in the scour and deposition patterns with time around the circular pier founded in the different tested soils. The results obtained from upstream and downstream campaign tests are shown at the left and right sides respectively and are displayed by contour plots. The plots present the results of the tests at only six specific intervals, 4, 10, 30, 45, 240 and 360 minutes.

For mixture M1 (85% Sand +15% silt), because of involved turbidity, the scanner is unable to identify the soil bed from 120 min for the upstream test and 45 min for the downstream test, hence, the 240 and 360 min cloud data are not accessible (Figure IV.3 (b)). The presence of a relatively large amount of silt makes the water turbid, preventing data acquisition by the 3D scanner used.

Live bed scour regime is observed for pure sand and M1 soil mixture, with erosion far from the circular pier after 30 to 45 minutes (Figure IV.3 (a), (b)). It is noted that ripples develop and move in the direction of flow. When the ripple reaches the front edge of the scour hole, it crumbles and falls down into the scour hole. However, the other soil mixtures transitioned to a clear water scour regime (Figure IV.3 (c), (d), (e), (f)). These observations are consistent with the flow intensity values obtained in Table IV.2.

Once the scouring process is initiated around a pier, a single dune forms behind the hole and gradually moves downstream over time. The size of the dune varies with the soil type, decreasing as the soil becomes more cohesive. For the M5 mixture (85% sand +15% clay), this dune is almost non visible downstream of the pier (Figure IV.3 (f)).
In addition, it is also observed that there is a significant decrease in the size of the scour hole as the soil cohesion increases. This finding aligns with the outcomes in reviewed literature [66, 80, 173]. This reduction depends on the type of the cohesive material content.

It is clear from the observed results that Kaolinite Proclay clay has stronger effect than silt. The silt particles (mainly made of quartz) are larger and have less specific surface area than clay particles, so they are less likely to stick together and form cohesive bonds. The specific surface area of a soil particle refers to the total surface area per unit mass of that particle. It is often expressed in square meters per gram (m^2/g).

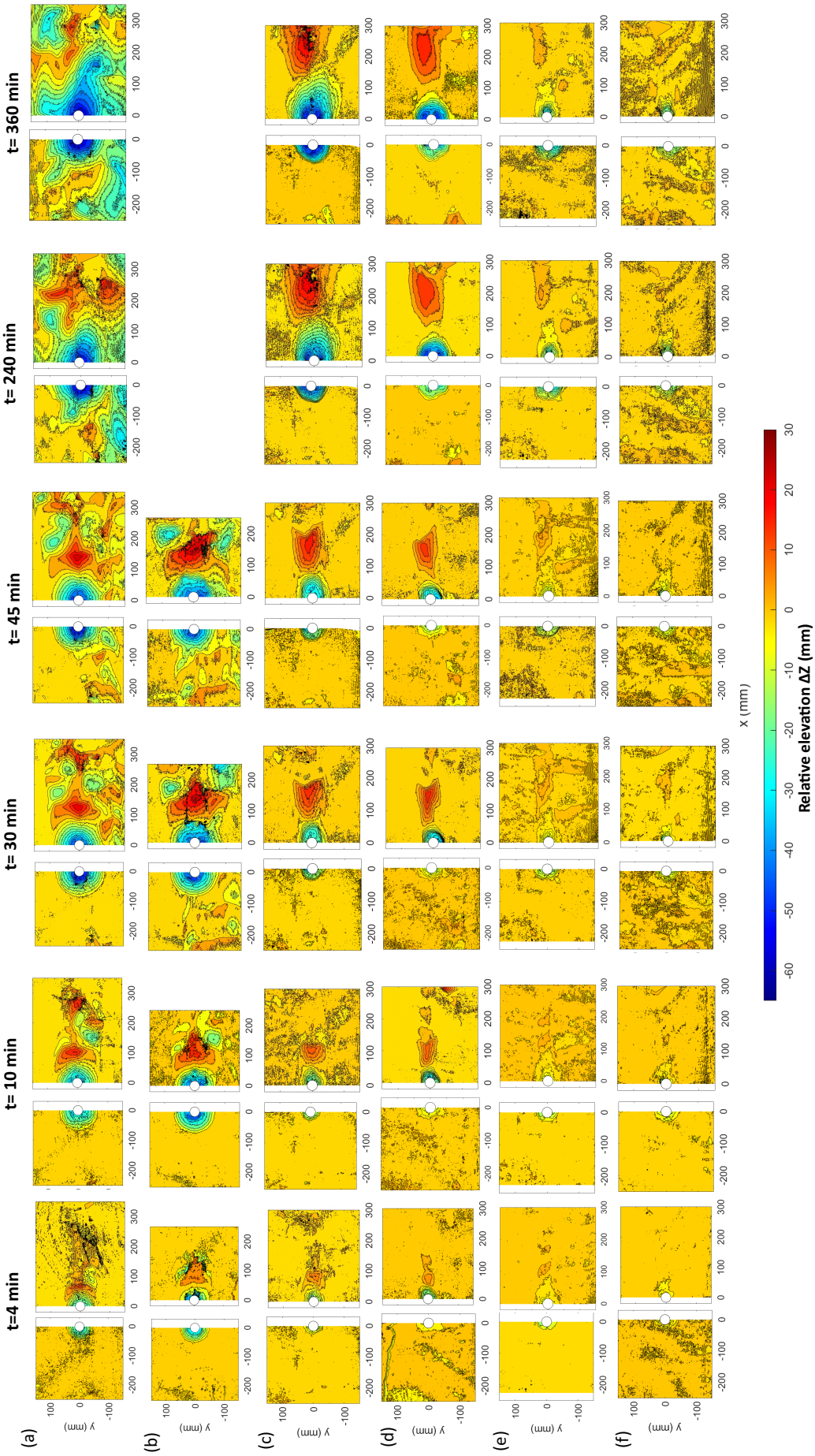

Figure IV.3: Temporal evolution of the scour and deposition topography (a): 100% sand, (b): 85% sand+15% silt, (c): 85% sand +10% silt +5% clay, (d): 85% sand +7.5% silt +7.5% clay, (e): 85% sand +5% silt +10% clay and (f): 85% sand +15% clay, the direction of the flow is from left to right

IV.2.1.2 *Qualitative approach : visual observation*

Photographs capturing the scour pit during both upstream and downstream tests are presented in Figures IV.4 and IV.5 respectively.

It is noticed that a trend to change in the scouring behavior of the soil is observed from a clay percentage between 7.5 and 10. Indeed, the shape of scour hole changes from 7.5% clay (mixture M3) in the upstream campaign test (Figure IV.4 (c)-(d)) against 10% clay (mixture M4) in the downstream campaign test (Figure IV.5 (d)-(e)). This may be related to the shear strength of a mixture of clay, silt, and sand that depends on the proportion of each component in the network structure [172]. The results obtained from the direct shear tests conducted on tested used soils, including friction angle ϕ and cohesion C, are presented in Table II.3 in Chapter II. These findings demonstrate that the addition of cohesive particles to sand sediment produces a drop in the angle of internal friction and a rapid increase in cohesion. This observation suggests that some of the added clay and silt is trapped between sand particles. As the cohesive fines content increases, the cohesion also increases, reflecting an increase in compactness and degree of void filling.

The main characteristics of the scour hole shape identified visually and assigned to cohesive soils are:
i) A flattened area upstream of the pier.
ii) A pier wake zone where scour hole propagation is most pronounced. Compared to the other sides of the circular pier, the lateral and transverse sides extent and the depth are larger.
The above characteristics are noticed in all mixtures with a clay content greater or equal to 7.5% for upstream campaign tests (Figure IV.4 (d),(e) and (f)) and 10% for downstream campaign tests (Figure IV.5 (e) and (f)).

In the results from scanner data, like those presented in Figure IV.3, characteristic ii) for the scour hole shape assigned to cohesive bed for mixtures M4 (85% sand + 5 % silt + 10 % clay) and M5 (85% sand + 15 % clay) are unclear and cannot be reliably identified due to the non perfect repeatability between the trials done on the same soil with similar experimental conditions, focusing the scanner once on the upstream part and a second time on the downstream part. Test repeatability is difficult to achieve in the case of cohesive soils due to the complexities involved in the manual compaction procedure not ensuring that the density of the prepared soils is perfectly uniform and constant. Despite the efforts made to minimize the error, we observe an influence of this parameter on the scouring process.

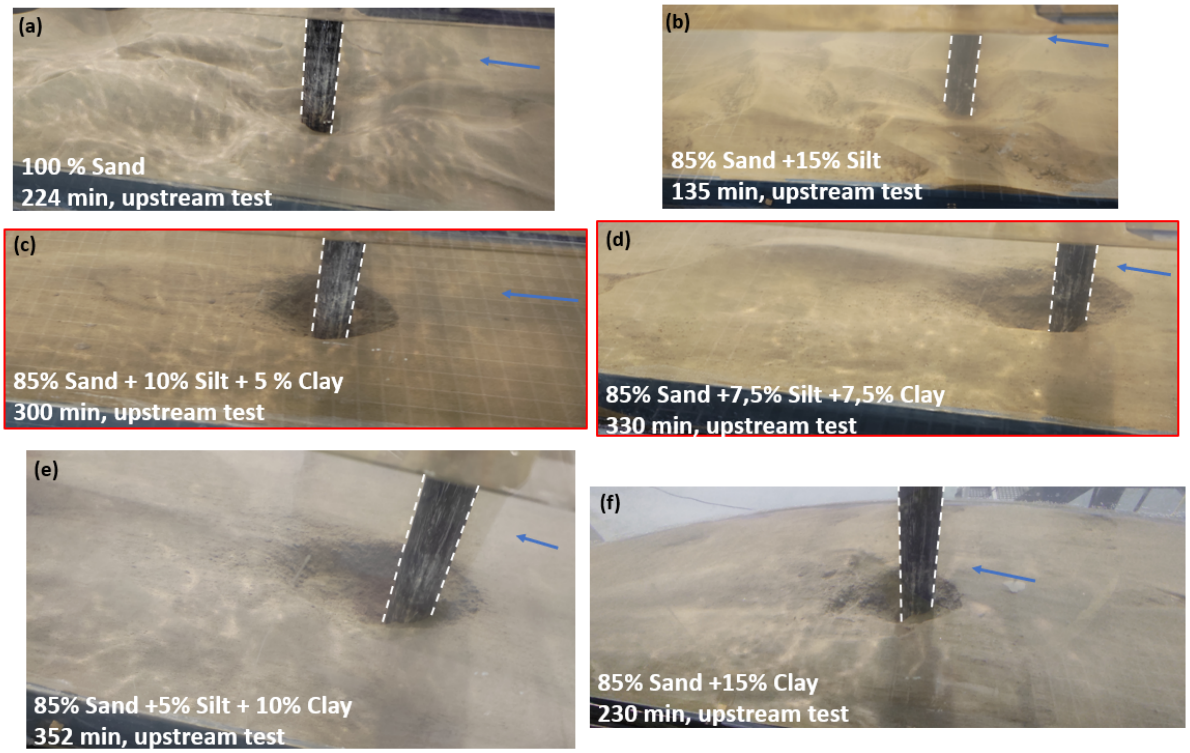

Figure IV.4: Photographs (not at the same scale) showing the transition in the scour behaviour from non cohesive to cohesive soil for upstream campaign tests; the dashed lines refer to pier walls and the blue arrows to the flow direction; It should be noted that the photographs are taken from different positions and are not at the same scale

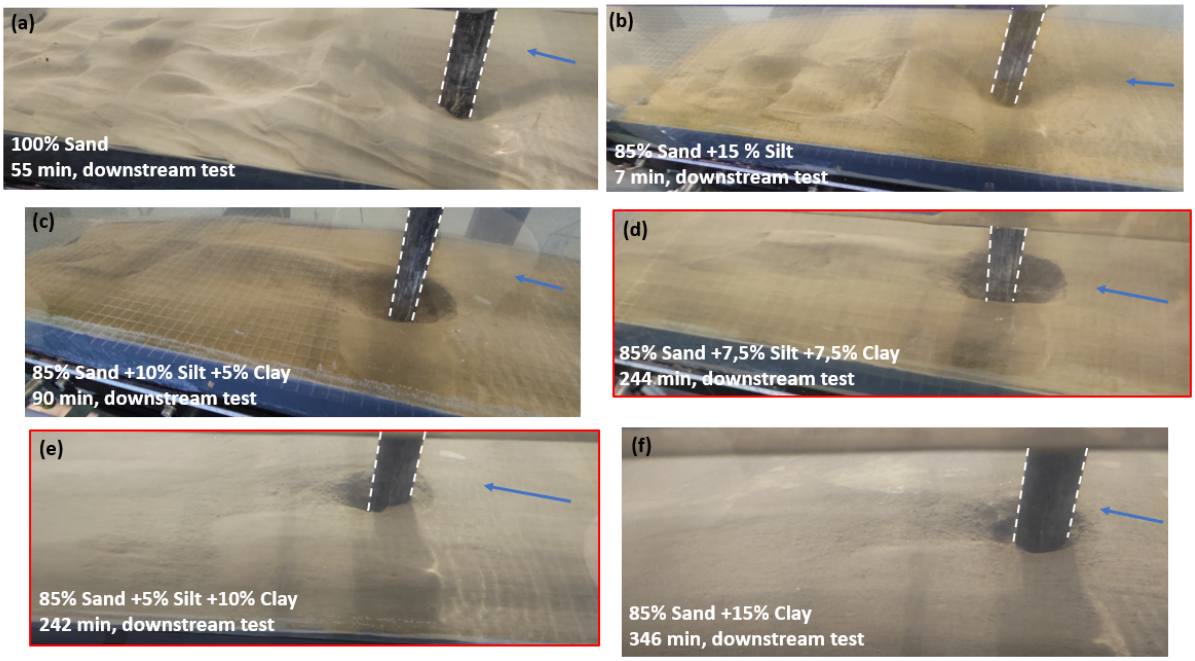

Figure IV.5: Photographs showing the transition in the scour behaviour from non cohesive to cohesive soil for downstream campaign tests; the dashed lines refer to pier walls and the blue arrows to the flow direction; It should be noted that the photographs are taken from different positions and are not at the same scale

Table IV.4 shows a comparison of observed scour propagation around circular pier from present study, Ting et al. 2001 [249], Debnath and Chaudhuri. 2010 (a) [82] and Mahalder et al. 2021 [163]. For each study, the type of tested soil, the Pier Reynolds number Re_b and the maximum bed shear stress τ_{max} are provided. Re_b is the Reynolds number based on the diameter of the pier b, $Re_b = Vb/\nu$, where V is the average depth velocity and ν is the kinematic water viscosity. τ_{max} represents the maximum bed shear stress induced by the flow around a circular pier at the beginning of the test, prior to the development of the scour hole. The location, where τ_{max} was observed, is illustrated in Figure I.32 (a) in Chapter I. The values of τ_{max} in Table IV.4 are estimated using equation IV.1, given by [260], as previously done by Debnath and Chaudhuri. 2010 [82] and Mahalder et al. 2021 [163].

$$\tau_{\max(\text{ pier})} = 0.094 \times \rho \times \mathrm{V}^2 \times \left(\frac{1}{\log(Re_b)} - \frac{1}{10} \right) \tag{IV.1}$$

Where, ρ is the unit weight of water; V is the average depth velocity at the location of the pier if the pier was not there; Reb is the pier Reynolds number based on the diameter of the cylinder b, as follows $Reb = Vb/\nu$, ν is the kinematic water viscosity.

According to Ting et al. 2001 [249], at lower pier Reynolds number Re_b values (Re_b= 10 000 - 15 200), the scour on the upstream and the downstream sides of the pier were similar; however, at

higher pier Reynolds number Re_b values (Re_b= 15 300 - 84 840), the scour on the upstream side was less than the scour on the downstream side (Table IV.4). However, Debnath and Chaudhuri. 2010 (a) [82] raised concerns regarding the validity of Ting et al. 2001 [249] observation on the scour propagation. They argued that the differences in scour on the upstream and downstream sides of a pier may not be attributed to pier Reynolds number Re_b values, as suggested by Ting et al. 2001 [249]. They attributed the change in the scour propagation in cohesive beds to the value of τ_{max} (Table IV.4): Low range of τ_{max} (2.54-3.03 N/m^2) lead to less upstream scouring, potentially with no scouring observed upstream in extreme cases. In the intermediate range of τ_{max} (3.29-5.09 N/m^2), similar scour was observed at the upstream and downstream sides of the pier. In cases of high τ_{max} values (5.91-6.44 N/m^2), scour progresses at the front of the pier more than at the wake region of the pier. It is important to note, that for different cohesive beds, the low, intermediate, and high range of τ_{max} quantitatively depend on the bed shear resistance. The critical shear stress of Porcelain clay, measured by Briaud et al. 1999 [56] using the Erosion Function Apparatus (EFA), which is also used in Ting et al. 2001 [249] study, is 0.5 N/m^2. The trend in the scour propagation in the study by Ting et al. 2001 [249] based on the values of τ_{max} and the bed shear resistance as suggested by Debnath and Chaudhuri. 2010 (a) [82] works also well.

Recently, Mahalder et al. 2021 [163] findings deviated from the results reported by Debnath and Chaudhuri 2010 (a) [82]. Mini-jet tests were performed in situ on a flume soil sample to estimate the critical shear stress. The critical shear stress obtained are in a range of 2.1-3.86 N/m^2. The calculated τ_{max} values were high (6.38-9.76 N/m^2), however, the scour were found to propagate predominantly towards the downstream side of the circular pier (Table IV.4). The results from this study are more in agreement with the observation of Ting et al. 2001 [249], since the values of pier Reynolds number Re_b were high being in a range of 66 000 - 98 000.

The observations from this present study are not in agreement with findings presented by Ting et al. 2001 [249] on the influence of the pier Reynolds number Re_b on the scour hole propagation. The results are rather consistent with the outcomes reported by Debnath and Chaudhuri. 2010 (a) [82]. In this study, Re_b is relatively small (8 320), but the scour propagation in the nose and wake of the pier are not similar (Table IV.4). The τ_{max} ($0.98N/m^2$) is slightly higher than the critical stress of mixtures M3 (85% Sand +7.5 % Silt +7.5 % Clay), M4 (85% Sand +5 % Silt +10 % Clay) and M5 (85% Sand +15% Clay) measured using the EFA, which are in a range of 0.66-0.91 N/m^2 (see Table IV.1). This bed shear stress τ_{max} was thus insufficient resulting in

scour depth at downstream side greater than upstream side.

Similar erosion pattern was observed by [249] in case of Porcelain clay at Reb = 15 300 - 36 000, by [13, 82] in case of clay-sand mixtures and by [133] in case of clay-fine sand-fine gravel and clay-fine gravel mixtures.

Reference	**Soil type**	Re_b	$\tau_{max}(N/m^2)$	**Observation on scour propagation around circular pier**
[249]	Porcelain Clay	10 000-15 200	2.26-4.83	upstream side = downstream side
		15 300-36 000	0.54-2.59	upstream side <downstream side
		45 000-84 840	0.97-1.57	upstream side <downstream side (No scour at upstream side)
[82]	Sand-Clay Mixture made in laboratory	15 923-17 507	2.54-3.03	upstream side <downstream side
		18 339-23 289	3.29-5.09	upstream side = downstream side
		25 273-26 474	5.91-6.44	upstream side >downstream side
[163]	Natural cohesive soil	66 000-98 000	6.38-9.76	upstream side <downstream side
Present Study	Mixture made in laboratory	8 320	0.98	upstream side <downstream side

Table IV.4: Comparison of the scour propagation around a circular pier from present study and observations from Ting et al. 2001 [249], Debnath and Chaudhuri. 2010 (a) [82] and Mahalder et al. 2021 [163]; Where, Re_b is the pier Reynolds number and τ_{max} is the maximum bed shear stress

IV.2.2 *Temporal variation of the scour depth as a function of the azimuthal direction*

The variation of the scour depth versus the azimuth angle upstream (αu) and downstream (αd) the pier is presented in Figure IV.6. The upstream azimuth angle (αu) is determined by measuring the angle from the horizontal axis in the opposite direction of the flow with positive value in the clockwise direction. The downstream azimuth angle (αd) is determined by measuring the angle from the horizontal axis in the direction of the flow with positive value in the counterclockwise direction. The region of interest corresponds to all the points with radial coordinates (r) between 17 and 19 mm, located at a distance between 1 to 3 mm from the outer surface of the circular pier. The results are shown for seven specific times (2, 4, 10, 30, 45, 240 and 360 minutes). Results from the upstream campaign tests are displayed on the left side of Figure IV.6, while those from the downstream campaign tests are on the right side.

The results indicate that local scour started at the pier sides. The deepest point at 2 min is observed around αu between 30° and 70° from both sides of the pier's horizontal symmetry axis for pure sand (Figure IV.6 (a)). This is consistent with the shear stress distribution caused by the horseshoe vortex around the pier observed in rigid beds [217]. The deepest point at 2 min is found to become at $\alpha u = \pm 90°$ for all mixtures with clay content $\geq 7.5\%$ (Figure IV.6 (d), (e), (f)). This finding is in accordance with the results of pier scour flume tests in cohesive soils reported by previous studies [13, 80, 122, 163].

During the scour process, it is observed that the scouring propagates around the entire circumference of the pier for all the soils. The scour depths in the upstream part are relatively similar for pure sand and mixtures with clay percentage $< 7.5\%$ (Figure IV.6 (a), (b), (c)). In these cases, the upstream portion of the scour hole has the shape most commonly described by different researchers [160, 168, 171].This shape is an inverted cone frustum and is observed for circular piers founded in non-cohesive bed. In sandy bed, it is observed that after the scour initiation, a horseshoe-shaped vortex develops upstream of the pier. In the case of cohesive soil, the depths of the scour on the upstream sides are always greater than that on the nose of the pier (Figure IV.6 (d), (e), (f)). The results also suggest that there is a tendency from 30 min for greater scour depth to occur in the central wake region compared to the downstream sides for cohesive soils with clay content $\geq 10\%$ (Figure IV.6 (e), (f)). This can be attributed to the absence of sediment deposition in the wake zone and may be related to the von Karmanvortex behind the pier. This vortex may act as the dominant flow component in the scour process for these cases.

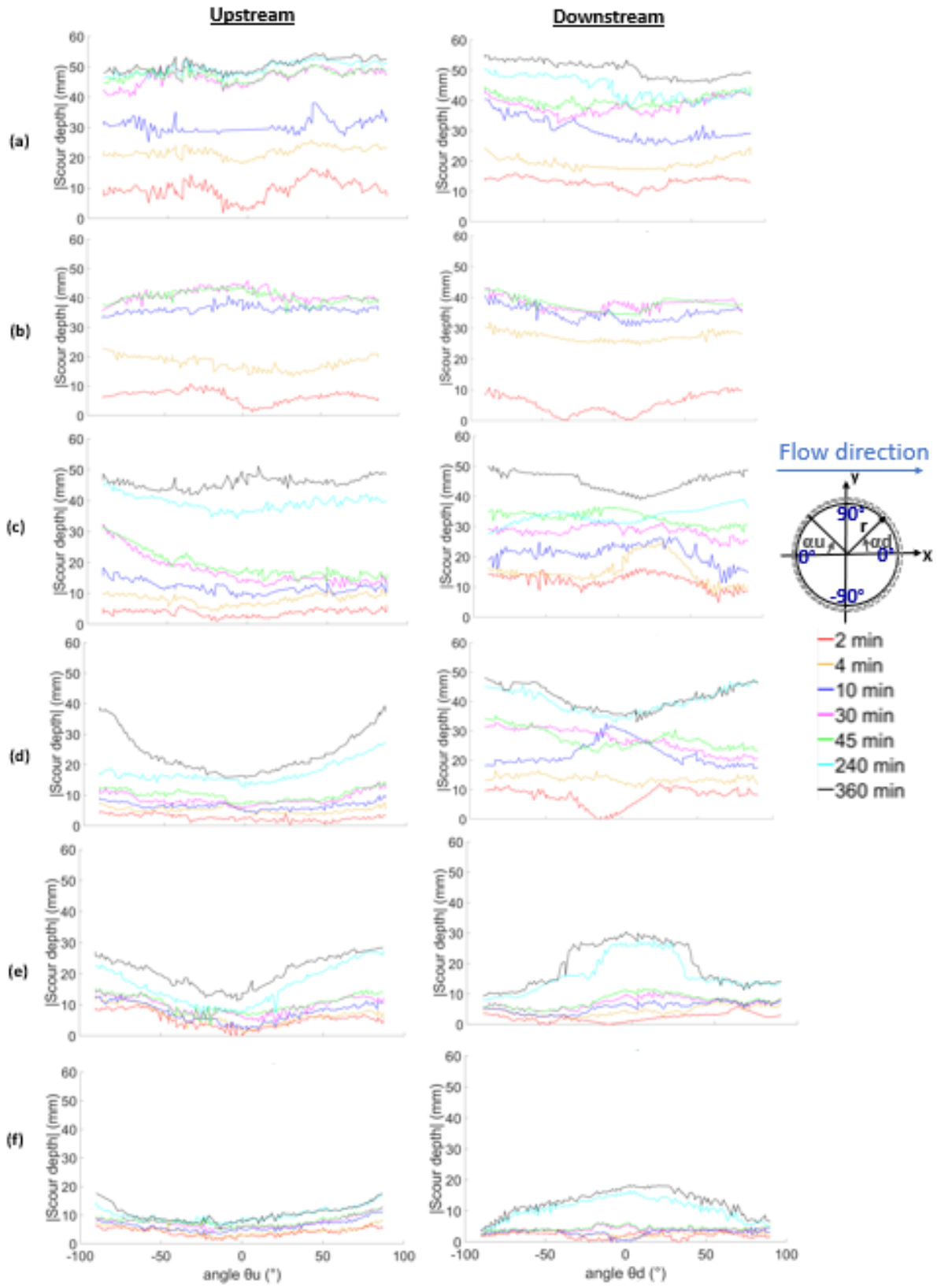

Figure IV.6: Scour depth as a function of azimuth angle upstream (α_u) and downstream (α_d) for points at radial coordinate r between 17 mm and 19 mm, (a): 100% sand, (b): 85% sand+15% silt, (c): 85% sand +10% silt +5% clay, (d): 85% sand +7.5% silt +7.5% clay, (e): 85% sand +5% silt +10% clay and (f): 85% sand +15% clay, the scheme illustrates the corresponding value of the azimuth angle for the upstream and the downstream part

IV.2.3 *Scour hole profiles*

IV.2.3.1 *Scour hole function of the type of soil*

Figure IV.7 shows the longitudinal and transversal cross-section views of scour hole profiles for all tested soils after 360 minutes. The duration 360 minutes is selected according to the predicted maximum scour depth (using SRICOS) which falls within the range of 82.90% to 99.17% of its corresponding equilibrium value (Table IV.7). The left side of the figure shows the test results from the upstream tests campaign, while the right side shows the test results from the downstream campaign.

This figure provides additional information on the shape and size of the scour hole. It can be seen that the measured hole profiles do not have perfect symmetry for all soils. This may be due to the non-perfect symmetry in the flow as previously mentioned in II.3.4.4 in Chapter II. It was observed that the shape of the scour hole is influenced by the presence of fine particles. Some irregularities in the scour hole shape especially upstream of the pier are observed for mixtures M3, M4 and M5 with clay content $\geq 7.5\%$. These irregularities correspond to a discontinuity in the scour hole slope due to the presence of a flattened portion of soil with undulations away from the pier. For these tests, it was consistently observed that erosion occurs through different modes. The scouring mechanism in cohesive soil exhibits the form of chuck and aggregate erosion mode at the beginning of the experiment then evolves to particle erosion mode. The existence of these modes of erosion explains the irregularity of the scour morphology observed.

To the best of our knowledge, no studies have been conducted to explore the hydrodynamics around a pile in cohesive soil. Chaudhari et al. 2013 [65] proposed hypotheses on changes in flow characteristics around a pier founded in a mixture of 15% fine sand and 85% kaolinite clay, compared with pure sand. The present findings further extended the assumptions, which are reported in the following, by considering them applicable to the case of cohesive soil mixture containing lower proportion of fine particles. It is possible that grow and spread of flow structures like down flow and horseshoe vortex during the formation of the scour hole do not proceed in the order that is typically seen in a sand bed. It is probable that the rough surface do not allow to a fully development of the horseshoe vortex system. The horseshoe vortex system is primarily responsible of developing the maximum depth of the scour hole at the front of a pier in a sand bed. Then, a change in this flow component probably significantly influence the resulted shape of the scour hole. The greater scour depth at the upstream part observed at the side of the pier compared to the nose of the pier for M3, M4 and M5 (as shown in the Figure IV.6 (d),(e) and (f))

is probably attributed to the concentration of horseshoe flow structures responsible of eroding bed material on the sides of the pier throughout the entire duration of the experiments.

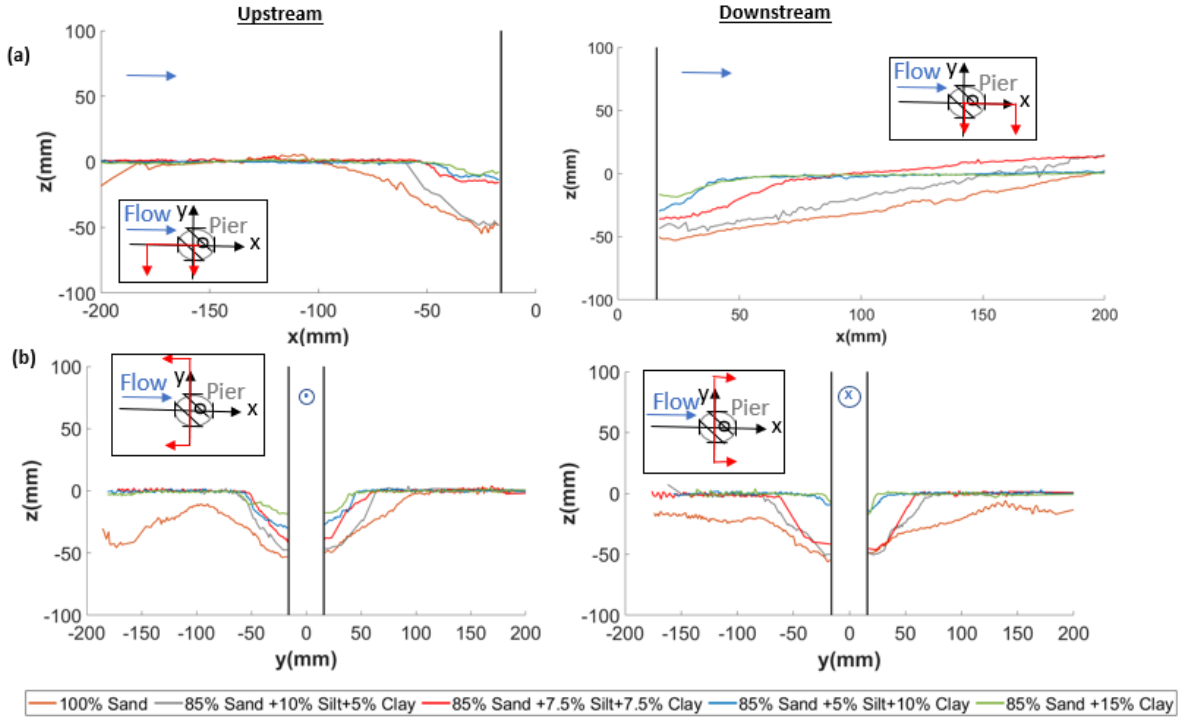

Figure IV.7: Measured scour profiles at the end of each experiment (360 min) for the different soils, (a): Longitudinal sections, (b): Transversal sections; the schemes illustrate the corresponding cross section in red color for each cases

The slope of each scour hole profile is calculated by determining the slope of the best-fitting straight line without the flattened areas. For the lateral slope, an average value is estimated by taking the average of the left and right slopes. α_{lu}, α_{su}, α_{ld}, α_{sd} represent respectively the upstream longitudinal slope, the average side upstream slope, the downstream longitudinal slope and the average side downstream slope. The flattened areas for the upstream tests are considerable for mixtures M3, M4, and M5. This results in a smaller zone that is utilized to calculate the slopes in the upstream part of the pier. Figure IV.8 shows these different slopes of the scour hole at the end of the tests (360 minutes) versus different types of soil.

For 100% sand, the values of the slopes obtained are as follows: $\alpha_{lu} = 36°$, $\alpha_{su} = 32°$, $\alpha_{ld} = 16°$ and $\alpha_{sd} = 29°$. These values are consistent with the results reported by [6, 154, 244, 252, 273]. The longitudinal upstream angle exceeds the natural angle of repose of bed sediment [6]. Link et al. 2008 [154] attributed this shape to the action of the system of horseshoe vortex. The longitudinal downstream angle is lower than the natural angle of repose [244]. The values

on the sides (α_{su} and α_{sd}) are close to the natural angle of repose according to [273]. The natural angle of repose of the used sand is basically equal to the internal friction angle measured by the direct shear test (31°).

For the pure sand and the mixture M2, the slopes decreased from the upstream to the downstream. The value of α_{lu} is greater than that of α_{su} and α_{sd}, which is in turn greater than α_{ld}. For mixtures M3, M4 and M5, α_{lu} becomes lower than α_{su}, however α_{ld} is always lower than α_{sd} except for M4 mixture. The reduction in α_{lu} compared to α_{su} can likely be attributed to the action of horseshoe-shaped flow structures. These flow structures, may be, located alongside the piers rather than at the front (as in the case of sandy soils) at 360 minutes.

A similar variation of α_{lu} and α_{su}, as well as of α_{ld} and α_{sd}, depending on the soil type, are observed. In fact, for α_{lu} (Figure IV.7 (a)) and α_{su} (Figure IV.7 (b)), the increase of cohesion increase the slope angles, till a mixture involving 7.5% clay (Figure IV.8). Then, from mixture M3 ($\geq$ 7.5%), as the clay content increases, a tendency to a decrease in their values are observed (Figure IV.8). This reduction can be explained by the decrease in horseshoe vortex action upstream of the pier as the percentage of clay in the soil increases. On the other hand, a tendency to an increase in α_{ld} (Figure IV.7 (a)) and α_{sd} (Figure IV.7 (b)) are observed as the clay content added to the sand matrix increases (Figure IV.8). The increase in the side slopes is in accordance with the findings reported by [13, 128, 173, 221]. A probable explanation is an increase in the action of Bénard von-Karman structures, which can lead to an increase in slope steepness in the downstream part of the pier.

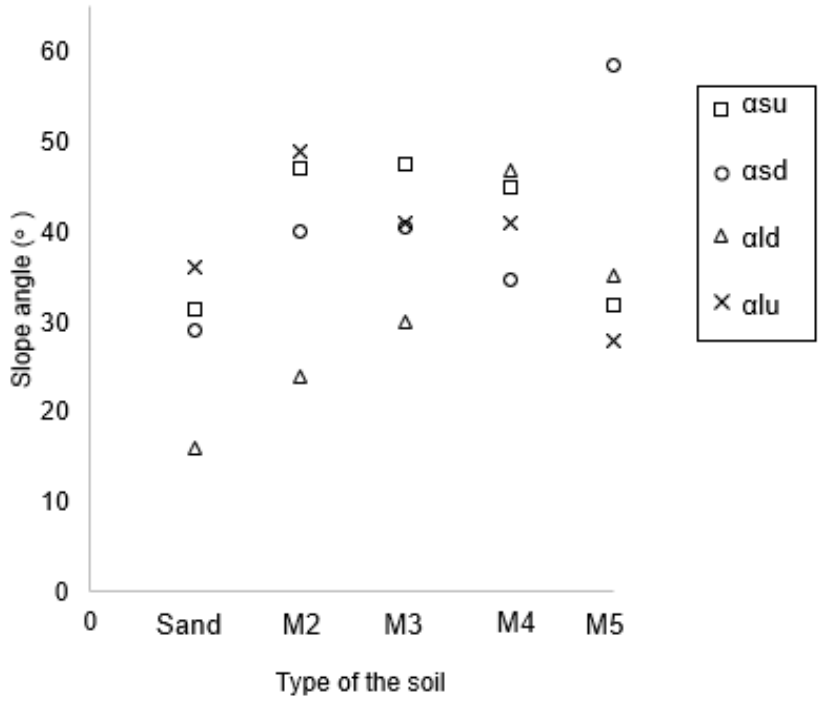

Figure IV.8: Slope of the scour hole at the end of the tests (360 min) as a function of the type of the soil; α_{lu}, α_{su},α_{ld}, α_{sd} are the longitudinal slope upstream, the average side slope upstream, the longitudinal slope downstream and the average side slope downstream respectively and M2,M3, M4 and M5 are 85% sand +10 % silt +5 % clay, 85% sand +7.5 % silt +7.5 % clay, 85% sand +5 % silt +10 % clay and 85% sand +15 % clay respectively

IV.2.3.2 *Temporal variation of the scour hole profiles*

Figures IV.9 and IV.10 present longitudinal and transverse sections obtained through measurements for both upstream and downstream tests at distinct time intervals: 2, 4, 10, 30, 45, 240, and 360 minutes, covering all soil conditions. The corresponding slope angles for these profiles are depicted in Figure IV.11.

For pure sand and the M1 mixture, the conical shape of the cross-sections is always constant over time test (Fig. IV.10 (a), (b), (g), (h)). The slope angles on the sides are also quite constants from 10 min for sand and 30 min for M1 mixture. The slopes are in the order 29°-32° (Fig. IV.11 (a),(b)), which are close to the internal friction angle measured by the direct shear test, 31° for sand and 30.8° for M1 mixture. In the upstream longitudinal sections, we observe the emergence of two distinct slopes for the sand at around 30 minutes and for the M1 mixture at around 4 minutes (Figure IV.9 (a), (b)). The slope closer to the pier is notably steeper than the one farther away. The values depicted in the Figure IV.11 (a) and (b) are those across the overall upstream lengths, considered as average upstream longitudinal slopes. A reduction in this slope occurs at 10, 45 and 240 minutes. This decline at 10 minutes corresponds to the time just

before the appearance of the two distinct slopes. This shift can be attributed to changes in the horseshoe vortex system, from one single primary vortex to two primary vortexes as previously reported by [78]. The decrease in slope value at 45 minutes and 240 minutes is associated with the elongation of the upstream length, L_u, resulting from the merging of the scour hole with an eroded pit situated away from the upstream pier (Figure IV.3 (a)). The recorded α_{lu} values range are $34-36°$ for the sand bed at 4, 30 and 360 minutes and for the M1 mixture, and $22-23°$ for the sand bed at 10, 45 and 240 minutes (Figure IV.11). The α_{ld} value remains within the range of $30-31°$ for the sand between 10 and 45 minutes, subsequently declining to a range of $16-20°$ at 240 and 360 minutes (Figure IV.11 (a)). This reduction can be attributed to the elongation of the downstream pit length (Figure IV.3 (a)). In the case of the M1 mixture, the water turbidity of the water primarily impacted the acquisition of the scanner influencing the central downstream section, thereby the observed αld values (Figure IV.9 (h) and IV.11 (b)).

Over time, the upstream pit's shape remained relatively consistent across different soil types. It transitioned from a conical form to a concave shape with a distinct curvature in the case of the M2 mixture containing 5% clay (Figure IV.9 (c)). Subsequently, for the M3, M4, and M5 mixtures, the pit's shape evolved into a flatter configuration, featuring a prominent horizontal segment (Figure IV.9 (d),(e) and (f)). The flattened segment is discernible from the test start and progressively expands in magnitude as time advances. This observation indicates that upstream erosion of the pier is predominantly oriented horizontally rather than vertically. The reasons underlying this observation remain elusive so far. A plausible physical interpretation for this phenomenon could be associated with a combination of factors, encompassing the dimensions, numbers, intensity, and spatial arrangement of horseshoe vortices. It is conceivable that the vortex present in this specific region exhibits an exceptional largeness, coupled with a reduced strength in comparison to instances involving exclusively fine sand. This particular distinction may contribute significantly to a marked decrease in the extent of vertical bed erosion. When considering the longitudinal slope upstream over the entire length, the calculated values appear remarkably low. This is primarily due to the relatively limited extent of the sloped portion in comparison to the horizontal segment. The calculated angle, derived from the sloped section excluding the flattened segment, demonstrates a gradual increasing as function of time for the M3 and M4 mixtures. This progressive increase correlates with the increase in the proportion of flattened bed to the overall length. For M5 mixture, the slope angle α_{lu} is always in the order 28-33° (Figure IV.11 (f)). Regarding the longitudinal and transversal sections at the downstream parts, a notable increase in the slopes α_{ld} and α_{sd} is observed over time, in the cases of the M4 and M5 mixtures (Figure IV.11 (e), (f)). The shape of the scour pit on the

downstream transversal cross-section tends to change from conical to concave with a steeper slope as the percentage of clay gradually increases (Figure IV.10), coherent with the finding from [173]. This increase in slope values is attributed to a more pronounced erosion rate occurring vertically as opposed to horizontally. Similarly, for the α_{su} parameter across all mixtures containing clay (M2, M3, M4, and M5), a prevailing trend towards an increase over time is discernible. Mixtures contaning Kaolinite clay have cohesive properties, which means that their particles are more likely to stick together. However, over time, continuous water flow can weaken these cohesive bonds, leading to particle detachment. This detachment can gradually steepen the side slopes. However, no clear trends for α_{ld} and α_{sd} are noticed for the M2 and M3 mixtures.

To gain a more comprehensive understanding of the intricacies at the topographical level, the prospect of conducting hydrodynamic measurements during the experiments presents itself as a promising approach perspective. Such measurements could provide invaluable insights into the dynamic interaction between fluid forces and bed morphology, shedding light on the mechanisms driving the observed erosion patterns.

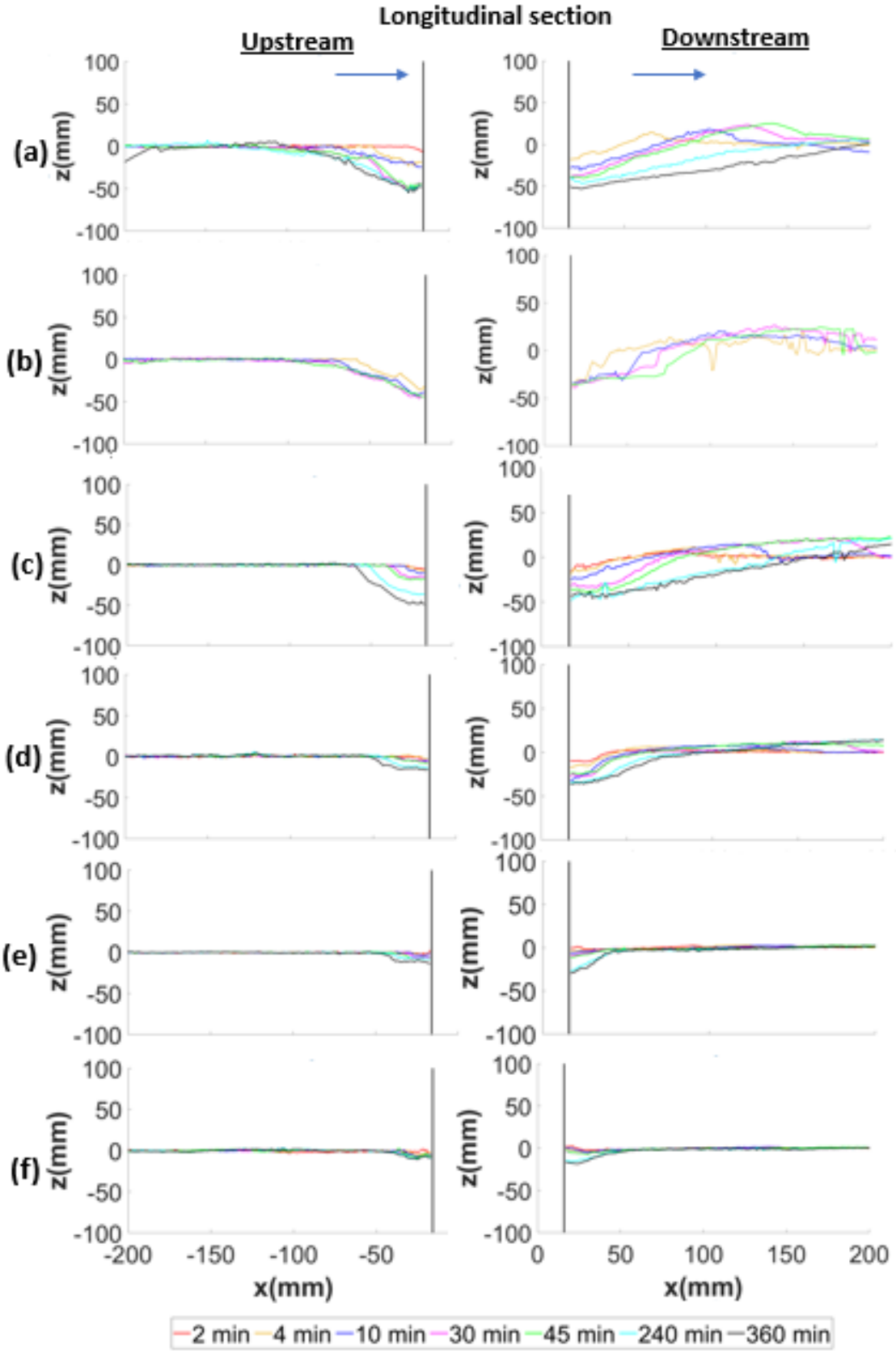

Figure IV.9: Temporal evolution of longitudinal sections for upstream and downstream tests, (a): 100% sand, (b): M1 mixture (85% sand+15% silt), (c): M2 mixture (85% sand +10% silt +5% clay), (d): M3 mixture (85% sand +7.5% silt +7.5% clay), (e): M4 mixture (85% sand +5% silt +10% clay) and (f): M5 mixture (85% sand +15% clay)

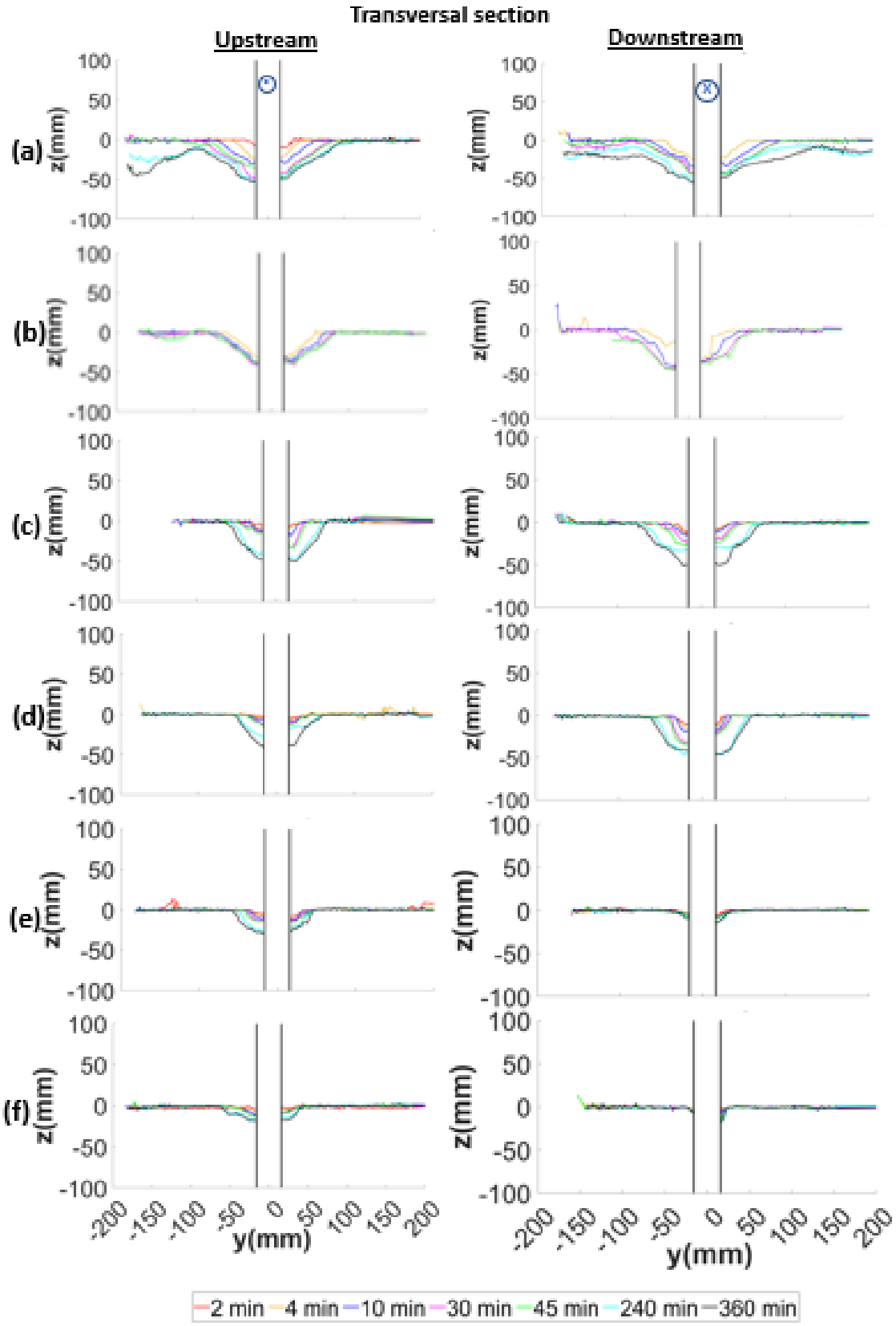

Figure IV.10: Temporal evolution of longitudinal sections for upstream and downstream tests, (a): 100% sand, (b): M1 mixture (85% sand+15% silt), (c): M2 mixture (85% sand +10% silt +5% clay), (d): M3 mixture (85% sand +7.5% silt +7.5% clay), (e): M4 mixture (85% sand +5% silt +10% clay) and (f): M5 mixture (85% sand +15% clay)

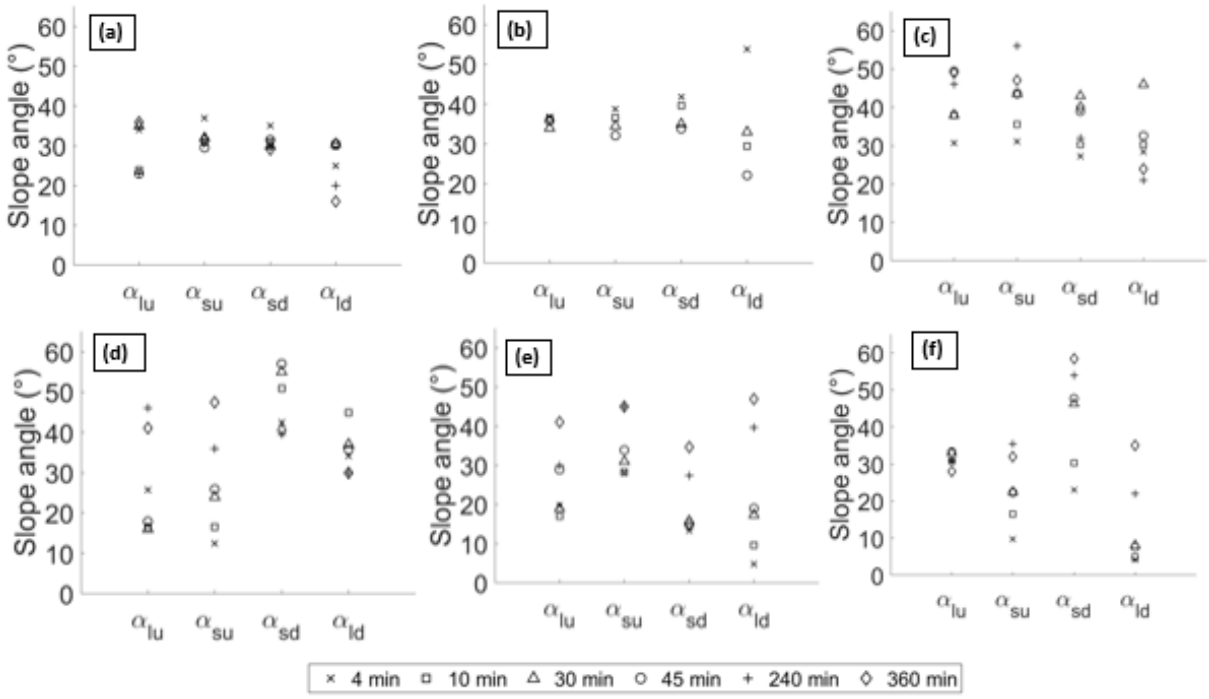

Figure IV.11: Slope angles within the scour hole; (a): 100% sand, (b): M1 mixture (85% sand+15% silt), (c): M2 mixture (85% sand +10% silt +5% clay), (d): M3 mixture (85% sand +7.5% silt +7.5% clay), (e): M4 mixture (85% sand +5% silt +10% clay) and (f): M5 mixture (85% sand +15% clay); α_{lu}, α_{su},α_{ld}, α_{sd} are the longitudinal slope upstream, average side slope upstream, longitudinal slope downstream and average side slope downstream respectively

IV.2.4 *Maximum scour depth*

IV.2.4.1 *Comparing flume measurements and SRICOS prediction*

Measurements of the temporal evolution of maximum scour depth are compared to those estimated using the SRICOS-EFA method (Figure IV.12).

The main parameters in the SRICOS-EFA method are the maximum depth of the scour hole at the equilibrium state (Z_{eq}) and the initial scour rate ($\dot{Z}_i$). The time-scale T is defined by $\frac{Z_{eq}}{\dot{Z}_i}$. The deepest scour depth observed at a specific time, $Z_{max}(t)$, was given by the following hyperbolic expression [249]

$$Z_{max}(t) = \frac{t}{\frac{t}{Zeq} + \frac{1}{\dot{Z}_i}} = Zeq \times \frac{t}{t+T} \tag{IV.2}$$

The maximum scour depth at the equilibrium state (Z_{eq}) was given by the following relationship [190]

$$\frac{Zeq}{b} = 2.2 \times (2.6 \times \mathrm{Fr}(pier) - \mathrm{Frc}(\text{ pier }))^{0.7} \tag{IV.3}$$

Where, Fr$(pier)$ is the pier Froude number based on flow velocity V and pier diameter b, as follows Fr$(pier) = \frac{V}{\sqrt{gb}}$; Frc$(pier)$ is the pier Froude number based on critical velocity Vc and pier diameter b, as follows Frc$(pier) = \frac{V_c}{\sqrt{gb}}$.
The choice of the Froude number in the equation of Oh 2009 [190] remains questionable. We note that the Shields number might offer a more appropriate parameter for sediment transport, in particular pier scour depth estimation.
In our tests, the critical velocity Vc for each soil used in the calculation is measured using the Erosion Function Apparatus (EFA) [55] (values in Table IV.1). It was noted that there is a safety factor of 1.5 recommended to increase the maximum scour depth predicted using equation IV.3 [190]. Hassan et al. 2020 [120] compared flume measurements of scour depths around two-in line (tandem) circular piers founded in a clay-sand bed with the SRICOS-EFA method. In their study, the EFA test was not performed on the tested soil. They observed that this predictive method overestimates the depths of scour at both the upstream and downstream piers. The overestimation of the scour depths may be attributed to the critical velocity of the sand fraction in the clay-sand bed soil which was used in the critical pier Froude number.
The initial scour rate $\dot{Z}i$ is the scour rate corresponding to the maximum initial shear stress τ_{max}(pier) in the EFA curve. An example of $\dot{Z}i$ determination for the mixture M5 (green erosion curve) is shown in Figure IV.1. τ_{max}(pier) represents the maximum shear stress caused by the flow around the circular pier at the beginning of the test before the scour hole formation. An equation was proposed to estimate the value of τ_{max}(pier), which was given by [260] (Equation IV.1). The equations for Z_{eq} and τ_{max}(pier) described in this chapter are suitable for circular pier in deep water with a constant flow velocity. These equations are used in this study, which was conducted in deep water condition, h/b = 5.3 $>$ 1.43, where h is the water depth and b is the pier diameter.

On the other hand, from experimental measurements, the position of the point having the maximum depth is determined for each type of soil at the end of the tests (at 360 minutes). This was done where data is collected for both the upstream and downstream test campaigns. The largest value obtained between the two test campaigns is chosen. The radial coordinates of these points with the corresponding value of the maximum scour depth are provided in the Table IV.5. Concerning the mixture M1, the last good acquisition is obtained at 120 minutes for the upstream tests and 45 min for the downstream test and were assumed as the later one instead of 360 min. Since for both tests on pure sand, the upstream scour depth was visually greater than the downstream one, we retained the position of point having the maximum value taken from the upstream test at 120 min. The positions of maximum scour depth are not always at the pier

surface (R=16 mm) and vary between the radial coordinate r = 16 mm and r = 25 mm. As clay content increased, the position of deepest scour moved from the pier front, having α_u near 0°, to the pier downstream with α_d between 64° and 0°. The position of the deepest scour depth in non-cohesive soils is coherent with the previous studies in live bed scour [273] and clear water scour [92, 96, 268].

	Sand	**M1***	**M2**	**M3**	**M4**	**M5**
Radial coordinate r (mm)	25	17	17	23	16	16
Azimuth angle usptream α_u (°)	- 2.29	-3.37	-6.71	_	_	_
Azimuth angle downstream α_d (°)	_	_	_	+63.54	+7.13	+21.80
Maximum scour depth Z_{max} **(mm)**	58.06	50.10	51.19	48.08	30.58	18.19

Table IV.5: Position of the maximum scour depth for tested soils, where M1: 85% Sand +15% Silt, M2: 85% Sand +10% Silt +5% Clay, M3: 85% Sand +7.5% Silt +7.5% Clay, M4: 85% Sand +5% Silt +10% Clay and M5: 85% Sand +15% Clay
*: *value observed at 120 min instead of 360 min*

Figure IV.12 (a) shows the temporal evolution of the maximum scour depth for each soil at the points previously determined. The best fit hyperbolic law models from the experimental data are compared to the hyperbolic model predicted using SRICOS-EFA method. The equations of the hyperbolic functions from measurements and SRICOS-EFA method are summarized in Table IV.6. The hyperbolic curves obtained from experimental measurements for all the soils exhibit a minimum regression coefficient R^2 exceeding 0.9, signifying a strong degree of fit. From the hyperbolic equations, the $\dot{Z}i$ and Z_{eq} are determined. The values obtained are also summarized in the Table IV.6. In the predicted hyperbolic law on M5 mixture, the definitions of the parameters $\dot{Z}i$ and Z_{eq} are presented. $\dot{Z}i$ is the tangent line's initial slope, while Z_{eq} is the asymptote of the hyperbolic curve. The relative error on Z_{eq} (4%) is calculated applying the logarithmic differentiation method. The relative error of the flow velocity measurement in the flume is considered negligible in the calculation. The relative error on $\dot{Z}i$ is considered 10%, equal to the relative error of Erosion Function Apparatus measurement of $\dot{Z}$ [55]. This allows to draw the limits of the error as a filling area (Figure IV.12 (a)). A progressive decrease in the initial scour rate with increasing soil cohesion is well observed using SRICOS-EFA method. The results from flume tests show that the initial scour rate of soils can be classified based on the type of the tested soils. The sand and the mixture M1 (85 % sand + 15% silt) exhibit relatively

high value of $\dot{Z}i$ in the order 10-25.5 mm/min. On the other hand, other soil mixtures have lower $\dot{Z}i$ values in the range of 0.3-2.5 mm/min. Hence, the two methods show that the variation in the initial scour rate is in the same trend. The results also indicate that higher cohesion results in a longer time required to reach equilibrium state for maximum scour depth. The time intervals span between 1.81 and 100.11 minutes for measurements, and 3.01 to 73.74 minutes for the SRICOS-EFA prediction method (Table IV.7). The maximum scour depth attained at 360 minutes corresponds to a range of 78.3% to 99.50% and 82.9% to 99.17% of the equilibrium state for measurements and the SRICOS-EFA prediction method, respectively (Table IV.7). It is also noticeable that considerable oscillations in the function of scour depth versus time are observed for 100% Sand and mixture M1 (Figure IV.12 (a)). This variation is believed to be caused by the mitigation of the sand ripples within the flume. The results displayed in Figure IV.12 (b) indicate a good comparison for the equilibrium scour depth (Z_{eq}). The relative error between the two approaches is estimated to be less than $\pm$ 25%. This observed value falls within the range of $\pm$ 50% as reported by [190]. As cohesion increases, the maximum equilibrium value of scour depth decreases. This observation corroborates with results reported in prior research studies [87, 122, 173, 209]. The reduction obtained for the maximum scour depth in the cohesive mixtures compared to the reference case (pure sand) is on the order of 8.5-68.5% for the measurement versus 1.5-76.5% for the SRICOS prediction method (Table IV.6).

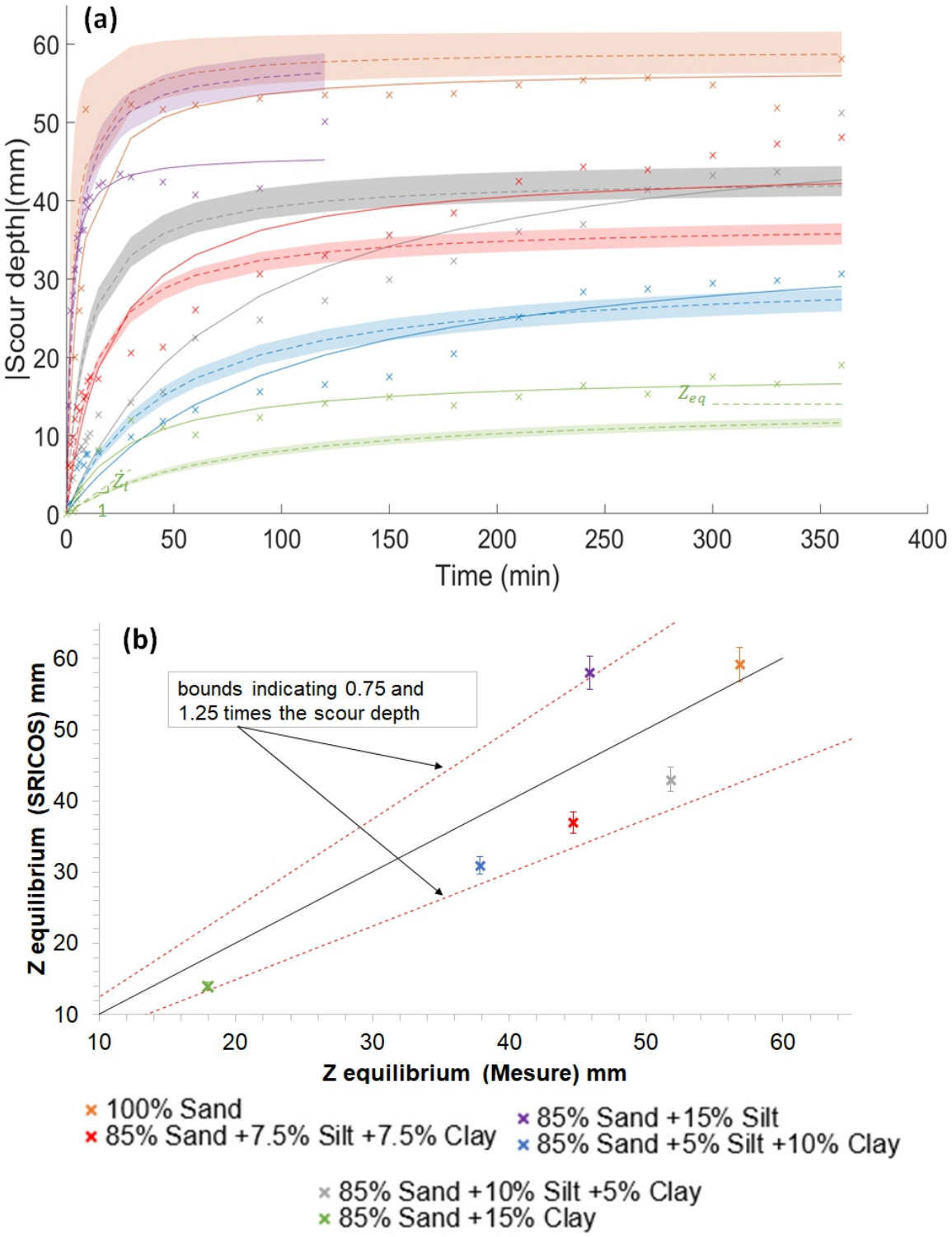

Figure IV.12: Comparison of the maximum scour depth between measurement from flume tests and prediction using SRICOS-EFA method, (a): temporal evolution of the maximum final scour depth, (x): experimental data, (-): hyperbolic best fit with the experimental data, (- -): hyperbolic law predicted using SRICOS-EFA method with error bounds as fill area, (b): Predicted versus measured equilibrium scour depth

	Mesure				SRICOS			
	$Z_{max}(t)$ mm	$\dot{Z}_i$ mm/min	Zeq mm	Reduction factor Zeq $(1-\frac{Zeq}{(Zeq)sand})\times 100$	$Z_{max}(t)$ mm	$\dot{Z}_i$ mm/min	Zeq mm	Reduction factor Zeq $(1-\frac{Zeq}{(Zeq)sand})\times 100$
Sand	$\frac{t}{0.0975+0.0176\times t}$ $R^2=0.92$	10.26	56.82	–	$\frac{t}{0.0509+0.0169\times t}$	19.65	59.17	–
M1 *	$\frac{t}{0.0395+0.0218\times t}$ $R^2=0.97$	25.36	45.87	19.27	$\frac{t}{0.0672+0.0172\times t}$	14.88	58.14	1.74
M2	$\frac{t}{1.4950+0.0193\times t}$ $R^2=0.94$	0.67	51.81	8.82	$\frac{t}{0.2103+0.0230\times t}$	4.76	43.48	26.52
M3	$\frac{t}{0.4712+0.0224\times t}$ $R^2=0.90$	2.12	44.64	21.44	$\frac{t}{0.3510+0.0270\times t}$	2.85	37.04	37.24
M4	$\frac{t}{2.6810+0.0270\times t}$ $R^2=0.92$	0.37	37.04	34.81	$\frac{t}{1.5310+0.0323\times t}$	0.65	30.96	47.68
M5	$\frac{t}{1.6610+0.0557\times t}$ $R^2=0.96$	0.60	17.95	68.41	$\frac{t}{5.2940+0.0714\times t}$	0.19	14.01	76.32

Table IV.6: Comparison of the maximum scour depth $Z_{max}(t)$, initial scour rate $\dot{Zi}$ and equilibrium scour depth Z_{eq} between measurement from flume and prediction using SRICOS-EFA method, R^2 is the regression coefficient

*: *extrapolation from data measurements based on an upstream test lasting 120 min and a downstream test lasting 45 min instead of 360 min*

	Mesure		SRICOS	
	Time-scale (min) $T=\frac{Zeq}{Zi}$	Maximum scour depth development at 360 min (%) $\frac{Z_{max}(360min)}{Zeq}\times 100$	Time-scale (min) $T=\frac{Zeq}{Zi}$	Maximum scour depth development at 360 min (%) $\frac{Z_{max}(360min)}{Zeq}\times 100$
Sand	5.54	98.51	3.01	99.17
M1 *	1.81	99.50	3.91	98.93
M2	77.33	82.30	9.13	97.52
M3	21.06	94.49	12.99	96.51
M4	100.11	78.37	47.63	88.36
M5	29.92	92.37	73.74	82.90

Table IV.7: Comparison of the time-scale T and the percentage of the scour depth development at 360 min between measurement from flume tests and prediction using SRICOS-EFA method

*: *extrapolation from data measurements based on an upstream test lasting 120 min and a downstream test lasting 45 min instead of 360 min*

IV.2.4.2 *Comparison with other empirical relationships*

A comparison of selected empirical methods of the maximum equilibrium scour depths from the literature for the tested soils with measurements is done. The histogram in Figure IV.13 (a) shows the values of the depths predicted and those from flume measurements, taken as the asymptotic value of the best fit hyperbolic evolution law, as a function of the soil type. Figure IV.13 (b) shows the predicted equilibrium scour depth by the different prediction methods selected as a

function of the equilibrium measured scour depth for all tested soils.

With regard to the choice of the empirical methods used, the HEC-18 Sand equation (equation I.11 in Chapter I) is chosen being widely used in the literature, while the other equations being proposed for coherent soils, or for sand-clay mixtures. The equations by Gudavalli 1997 [112], Ting et al. 2001 [249], Molinas and Hosny 1999 [173], Rambabu et al. 2003 [209], Debnath and Chaudhuri. 2010 (a) [82], Debnath and Chaudhuri. 2010 (b) [80], Muzzamil et al. 2015 [177], Najafzadeh and Barani. 2014 [181] are all given in Table I.2 in Chapter I.

In Figure IV.13, the equation Molinas and Hosny 1999 [173], noted as Equation 1, is the first equation listed for reference [173] in Table I.2 in Chapter I intended for use in mixed soil. The equation Molinas and Hosny 1999 [173] Equation 2 is the second equation listed for reference [173] in Table I.2 in Chapter I designed for cohesive soil. The equation referred to as Debnath and Chaudhuri. 2010 (a) [82] - Equation 1 is the first equation listed for reference [82] in Table I.2 within Chapter I. The equation by Oh 2009 [190] refers to the equation IV.3 used in SRICOS-EFA method.

In the predictive equations used, the cohesive soil percentage (Pc) in the soil mixtures in the equations derived from the references [80, 82, 173, 177, 181], is considered equivalent to the proportion of Kaolinite clay within the mixture. Our calculations assume that the silt has a negligible impact on the scour depth. In the equations derived from Debnath and Chaudhuri. 2010 and Rambabu et al. 2003 references [80, 82, 209], the undrained shear strengths were measured by field miniature vane shear tests. Muzzamil et al. 2015 [177] have used the data of Debnath and Chaudhuri. 2010 (b) [80] study. However, Najafzadeh and Barani. 2014 [181] have measured the undrained shear strength using direct shear tests. In our calculations, the value of the undrained shear strength taken in the equations of [80, 82, 177, 181, 209] are those measured by the direct shear test.

The depths computed using the HEC-18 sand by Arneson et al. 2012 [14], equation by Gudavalli 1997 [112], and equation by Ting et al. 2001 [249], exhibit remarkably close values. Their equations, which do not take into consideration the soil properties, result in consistent values regardless of variations in soil types. This differs from the observed measurements. We point out that in some situations, these equations can overestimate the scour depth. The overestimation observed is high for M4 and M5 mixtures with a multiplying factor to the measured values in the order of 2-3.2. This observation contradicts the Ting et al. 2001 [249] findings on Porcelain,

Armstone and Bentonite clays showing that the observed scour depths were in the 30% of those predicted by the HEC-18 Sand equation (Figure I.21 in Chapter I).

The scour depths calculated by the equations of Molinas and Hosny. 1999 [173] (Equation 1 and 2), Rambabu et al. 2003 [209], Debnath and Chaudhuri. 2010 (a) [82] (Equation 1), Debnath and Chaudhuri. 2010 (b) [80] and Muzzamil et al. 2015 [177] show for the most cases an underestimation compared to the values observed experimentally. The factors to be multiplied by the depth values measured for the equations of Molinas and Hosny 1999 [173] and Rambabu et al. 2003 [209] are in the order of 0.25-0.42, those from Debnath and Chaudhuri. [80, 82] and Muzzamil et al. [177] are in the order of 0.003-0.3. The Debnath and Chaudhuri. [80, 82] and Muzzamil et al. [177] equations show the smallest prediction values. The empirical formula presented by Najafzadeh and Barani. 2014 [181] yields values ranging from 565.84 to 2 417.57 mm for the mixture M2,M3, M4 and M5, which significantly differ in magnitude from our measured values. In the interest of providing a more comprehensive representation of the results, they are excluded from the Figure IV.13.

The formulated empirical equations are derived through regression analysis of flume results under varying experimental conditions from our conducted tests. This can account for the observed disparities. The differences in values are also due to the variability of the parameters taken into account in the various equations as shown in Table I.2 in Chapter I, the scale effect, the experimental conditions and set-ups which are not the same in all studies. It is important to note that [228] compared the values derived from 22 equations proposed for sandy bed in case of clear water scour on two types of sand and also obtained a wide dispersion of results. In addition, [36, 257] reported that, formulas for scour depth prediction, mainly derived from experimental laboratory tests, have a number of limitations.

The outcomes indicate that these empirical equations are not universal methods and can not provide a right applicability across all experimental scenarios. These equations only clarify the variability of pier scour with cohesive properties and can not be envisioned for a general application. All the equations proposed for the cohesive soils and including the soil properties by [80, 82, 173, 177, 209], estimated lower maximum scour depth as the HEC-18 sand Arneson et al. 2012 [14], Gudavalli 1997 [112], Ting et al. 2001 [249] equations. Interestingly, the results showed that the Oh 2009 [190] equation, used in the SRICOS-EFA method, provides the best estimation values compared to all the other prediction equations evaluated for all the tested soils.

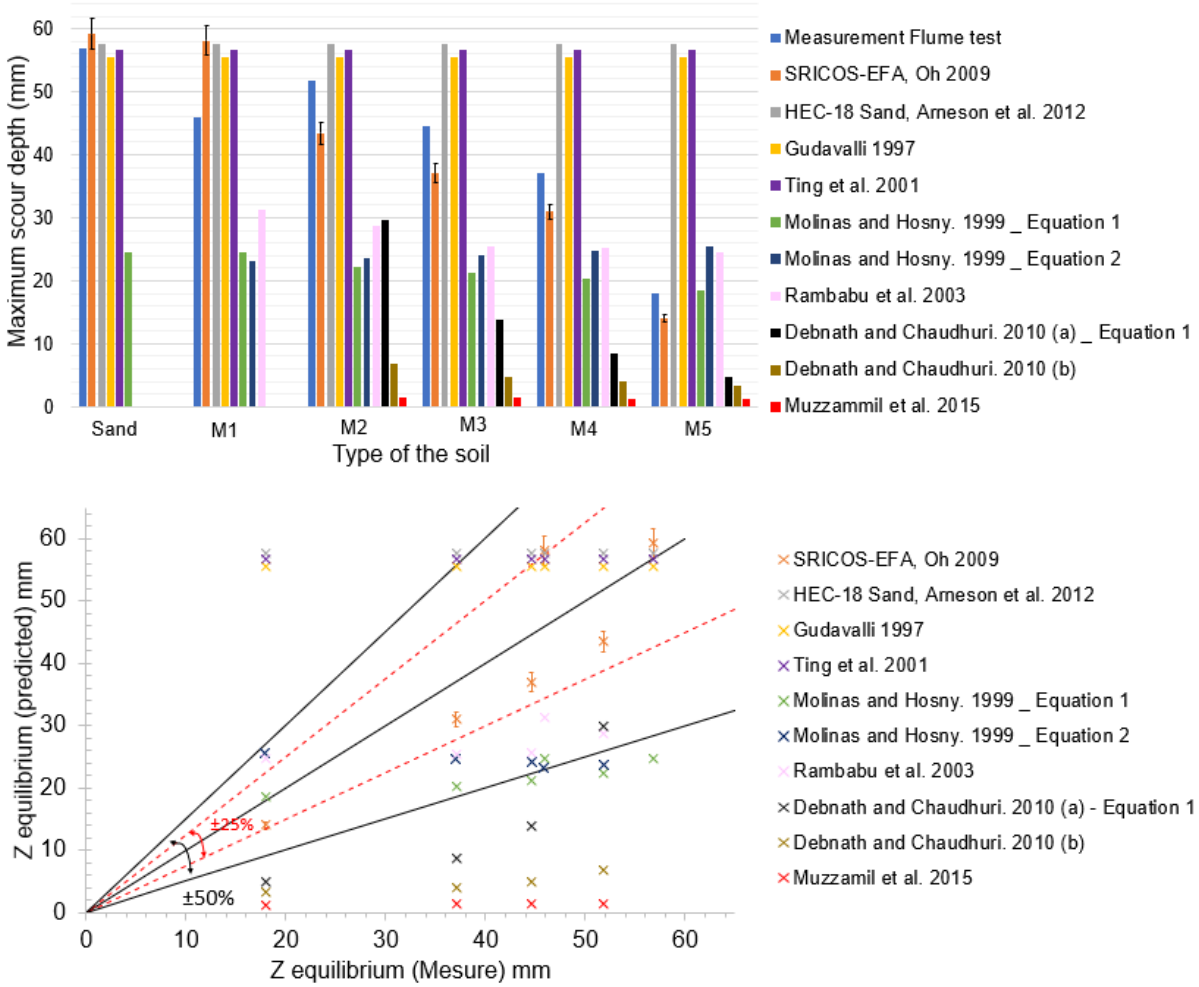

Figure IV.13: Comparison of equilibrium maximum scour depth between measurements from flume using the hyperbolic law and calculated using some selected empirical formulas in the literature, (a) : histogram of maximum scour depth function of the type of the soil, (b): Predicted scour depth function of measured scour depth, (- -) : bounds indicating 0.75 and 1.25 times the scour depth, (-) : bounds indicating 0.5 and 1.5 times the scour depth; where M1: 85% Sand +15% Silt, M2: 85% Sand +10% Silt +5% Clay, M3: 85% Sand +7.5% Silt +7.5% Clay, M4: 85% Sand +5% Silt +10% Clay and M5: 85% Sand +15% Clay

IV.2.4.3 *Effect of clay content on the maximum scour depth*

Figure IV.14 shows the non-dimensional equilibrium scour depth Zeq/b versus the percentage clay in the tested soils obtained from the present data, compared to those in Debnath and Chaudhuri. 2010 (b) [80] and Molinas and Hosny 1999 [173]. For present study, two values of the non-dimensional equilibrium scour depth for percentage of clay Pc=0 were provided, one obtained in pure sand and the other in the mixture M1 (85% sand +15 % silt).

The majority of the values closely align with those reported by Debnath and Chaudhuri. 2010 [80], and they significantly surpass the values documented by Molinas and Hosny in 1999 [173] for similar clay percentage. In our study and Debnath and Chaudhuri. 2010 [80] study, the clay mineral is Kaolinite, whereas Molinas and Hosny. 1999 [173] used montmorillonite, which is the primary clay mineral in Bentonite [210]. Montmorillonite has larger specific surface area and cation exchange capacity than kaolinite, which suggests that the cohesive forces are more active [208].

Ting et al. 2001 [249] conducted flume experiments around circular piers on various types of clay, including Porcelain or Kaolin, Armstone, and bentonite. The non-dimensional scour depths were similar for the same velocity on the different clay mineral. Debnath and Chaudhuri. 2010 (b) [80] found that, for similar clay percentages, the non-dimensional scour depth values reported by Molinas and Hosny 1999 [173] were lower than those in their own study. Debnath and Chaudhuri. 2010 (b) [80] attributed this difference to the lower initial water content IWC (0.1) values used by Molinas and Hosny [173] compared to the IWC in their own study (0.2–0.4) rather than to the difference in the clay mineral types. By increasing the IWC, the contact forces between particles became weak leading to the decrease of cohesion [204].

In our study, the IWC (0.05) is lower than that used by Molinas and Hosny 1999 [173] and Debnath and Chaudhuri. 2010 (b) [80] studies, shows scour depths close to Debnath and Chaudhuri. 2010 (b) [80] values. The clay mineral used in our study and in Debnath and Chaudhuri. 2010 (b) study [80] is the Kaolinite clay. The clay mineral used by Molinas and Hosny 1999 [173] is the montmorillonite clay. The results show that the difference in the non-dimensional scour depth values by Molinas and Hosny. 1999 [173] and Debnath et al 2010. (b) [80] for clay percentage Pc ≤ 0.1 could be attributed to the different types of clay minerals rather than the initial water content. For a clay proportion of 15%, the effect of initial water content may become predominant. Conducting experiments involving increased clay proportions can serve as a perspective to asses this item.

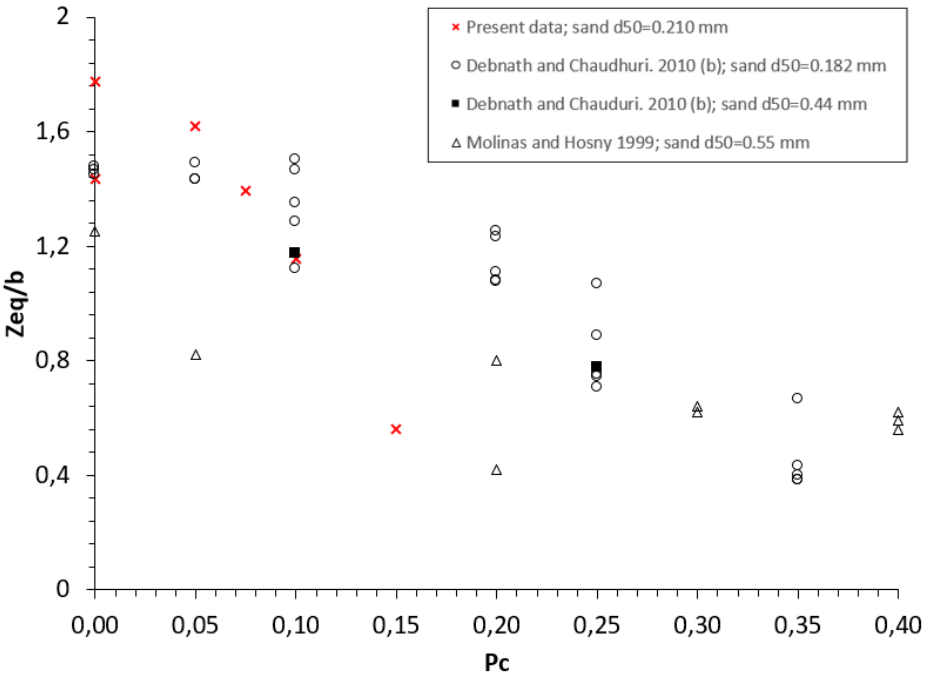

Figure IV.14: Plot of non-dimensional equilibrium scour depth Zeq/b as a function of percentage of clay Pc obtained from present data, Debnath and Chaudhuri. 2010 (b) [80] and Molinas and Hosny 1999 [173] for V/Vcr (sand) =0.99-1.1, where Vcr (sand) is the critical velocity of the sand used in the soil mixtures

IV.2.5 *Scour hole plane dimensions*

IV.2.5.1 *Temporal variation of the scour hole plane dimensions*

The temporal evolution of scour parameters in the horizontal plane is shown in Figure IV.15. The longitudinal extensions in the upstream and downstream directions are presented by Lu and Ld respectively. The transverse extensions to the right and to the left are named B1 and B2, respectively. In the upstream and downstream test campaigns, B1 and B2 are averaged to form Bu and Bd respectively. The figures on the left displaying Lu and Bu correspond to the upstream tests and those on the right Ld and Bd correspond to the downstream tests. Lu, Ld, B1, and B2 are determined along the pier's center, longitudinally or transversely. These represent the x or y values on the horizontal plane where the elevation exceeds -2 mm. The choice of -2 mm is a practical mean for delineating pit boundaries. For cohesive soils, the surface often remains nearly flat with values between -1.9 mm and 0 mm over a wide area, which is disregarded due to its very shallow depth and excluded from width or length considerations.

For pure sand and the M1 mixture (85% sand+15% silt), fluctuations appear in the experimental data (Figure IV.15, orange and purple crosses). The fluctuations are due to a competition between erosion and deposition in the moving bed regime. This is caused by the presence and disappearance of ripples.

The findings demonstrate that the temporal evolution of Lu, Ld, Bu, and Bd, for all the tested soils, can be described by hyperbolic functions of the form t/(at+b) (Figure IV.15). The minimum value of the regression coefficient R^2 observed between the experimental data and the fitted curve is of the order of 0.71. The initial rates of change are calculated from the hyperbolic curve equations obtained, which is the value 1/b. The values at the equilibrium state are calculated from the hyperbolic curve equation, corresponding to infinite time, which is the value 1/a in the equation. These values are illustrated in Table IV.8.

Concerning the rate of change in scour dimensions in the horizontal plane, no clear trend is observed with increasing percentage of fine particles in the soil mixtures. For dimensions in the longitudinal direction, $\dot{Lu}$ and $\dot{Ld}$ values are in the order of 4-18.5 mm/min. Unexpectedly high values of $\dot{Bu}$ and $\dot{Bd}$ are observed for M4 mixture (85% sand + 5% silt + 10 % clay) and M5 mixture (85% sand + 15% clay) in the order of 54-76.5 mm/min. These values can be explained by the mode of erosion by soil chunks or aggregates and not by soil particles [156]. Soil stripping near the pier on its sides may have occurred at the beginning of the scour process.

Additionally, a trend of decreasing pit dimensions in the horizontal plane at equilibrium with increasing percentage of fine particles in the soil mixtures is evident. In comparison to pure sand, the reduction factors range from 14.5-60% for (Lu)eq, 46-70% for (Bu)eq, 8-66% for (Ld)eq, and 1.5-77.5% for (Bd)eq (Table IV.8). These results show also that clay has a greater effect than silt in reducing the scour pit. It is important to note that among all the previous studies mentioned in chapter I, none of them have addressed the topic of temporal laws changes in dimensions in the horizontal plane for cohesive soils.

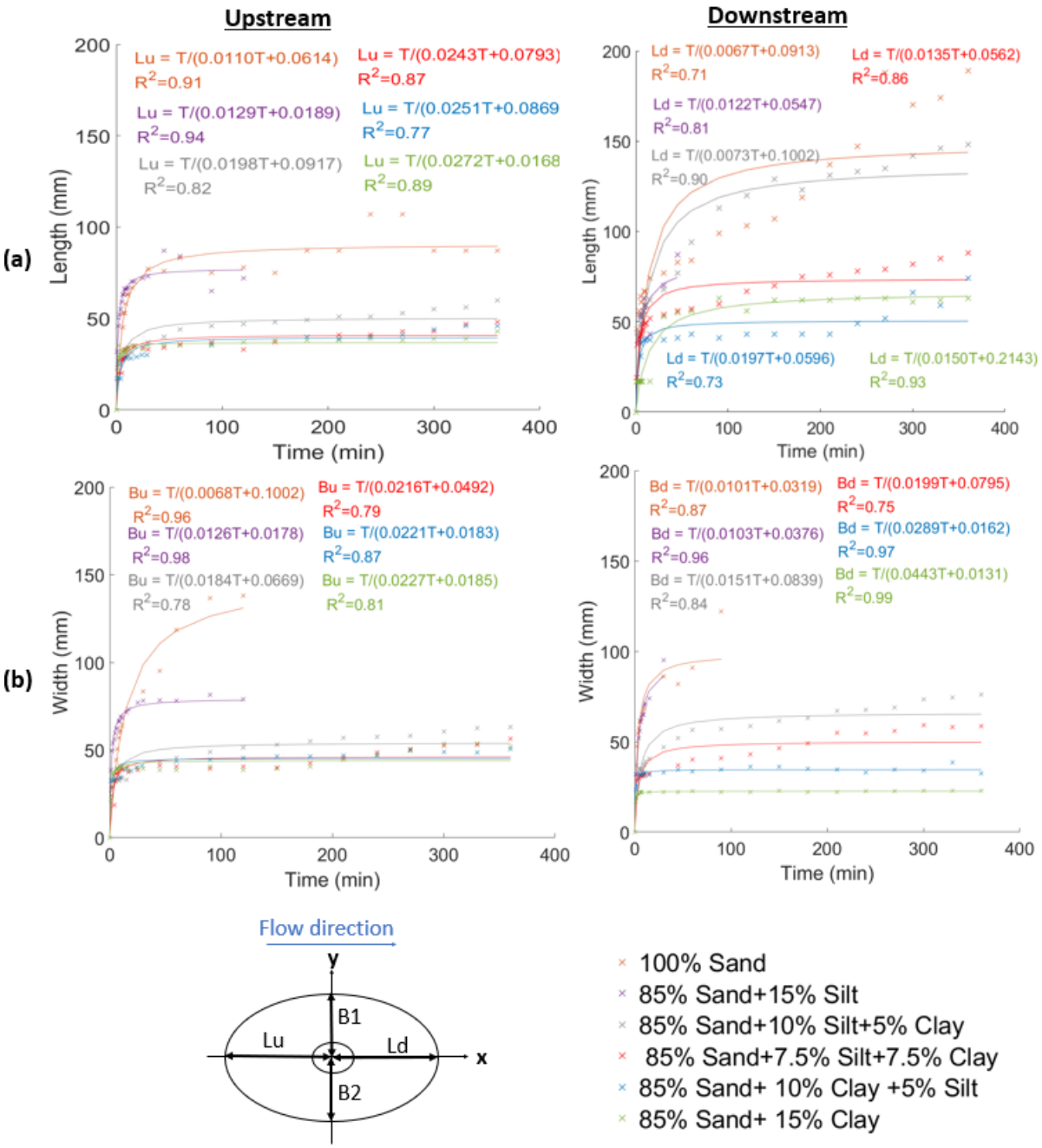

Figure IV.15: Temporal evolution of the plane parameters of the scour hole, (a) : length, (b): width, (x):experimental data, (-): hyperbolic best fit with the experimental data, the scheme illustrates the corresponding value of the length L and width B for the upstream and the downstream part

	Sand	M1 *	M2	M3	M4	M5
$\dot{Lu}$ **mm/min**	16.29	5.29	10.91	12.61	11.51	5.95
(Lu)eq mm	90.91	77.52	50.51	41.15	39.84	36.76
Reduction factor (Lu)eq (%) $(1-\frac{(Lu)eq}{((Lu)eq)Sand})\times 100$	–	14.73	44.44	54.74	56.18	59.56
$\dot{Bu}$ **mm/min**	9.98	56.18	14.95	20.33	54.64	54.05
(Bu)eq mm	147.08	79.37	54.35	46.29	45.25	44.05
Reduction factor (Bu)eq (%) $(1-\frac{(Bu)eq}{((Bu)eq)Sand})\times 100$	–	46.04	63.05	68.53	69.23	70.05
$\dot{Ld}$ **mm/min**	10.95	18.28	9.98	17.79	16.78	4.67
(Ld)eq mm	149.25	81.97	136.99	74.07	50.76	66.67
Reduction factor (Ld)eq (%) $(1-\frac{(Ld)eq}{((Ld)eq)Sand})\times 100$	–	45.08	8.21	50.37	65.99	55.33
$\dot{Bd}$ **mm/min**	31.35	26.59	11.92	12.58	61.73	76.34
(Bd)eq mm	99.01	97.09	66.23	50.25	34.60	22.57
Reduction factor (Bd)eq (%) $(1-\frac{(Bd)eq}{((Bd)eq)Sand})\times 100$	–	1.94	33.11	49.25	65.05	77.20

Table IV.8: Plane scour hole dimensions for tested soils; $\dot{Lu}$, $\dot{Bu}$, $\dot{Ld}$ and $\dot{Bd}$ are the initial rate of change in the length upstream, width upstream, length downstream and width downstream respectively; (Lu)eq, (Bu)eq, (Ld)eq, (Bd)eq are the values at the equilibrium state of length upstream, width upstream, length downstream and width downstream respectively; M1: 85% Sand +15% Silt, M2: 85 % Sand +10 % Silt +5 % Clay, M3: 85% Sand +7.5 % Silt +7.5 % Clay, M4: 85% Sand +5% Silt +10% Clay and M5: 85% Sand +15% Clay
*: *extrapolation from data measurements based on an upstream test lasting 120 min and a downstream test lasting 45 min instead of 360 min*

IV.2.5.2 *Scour hole diameter function of clay percentage*

Figure IV.16 presents the non-dimensional scour hole diameter B/b, where b is the pier diameter, as a function of clay content P_c for the present data as well as for that of Debnath and Chaudhuri. 2010 (b) [80] and Molinas and Hosny. 1999 [173]. In this study, the greatest value of (Lu)eq, (Ld)eq, (Bu)eq and (Bd)eq is taken as scour hole diameter Beq for each tested soil and Pc is the

fraction of the clay percentage in the mixture.

This figure shows a similar trend in our study than of Molinas and Hosny. 1999 [173] and Debnath and Chaudhuri. 2010 (b) [80] clearly a decrease in the scour hole diameter with increasing percentage of clay in the soil mixture. The Beq/b ratios reported in our study are lower than those of Molinas and Hosny. 1999 [173], which are themselves lower than Debnath and Chaudhuri. 2010 (b) [80] for a similar percentage of clay. It's difficult to find a clear explanation for this distinction from the obtained values because of the differences in the experimental conditions (in particular used soils) between the different studies.

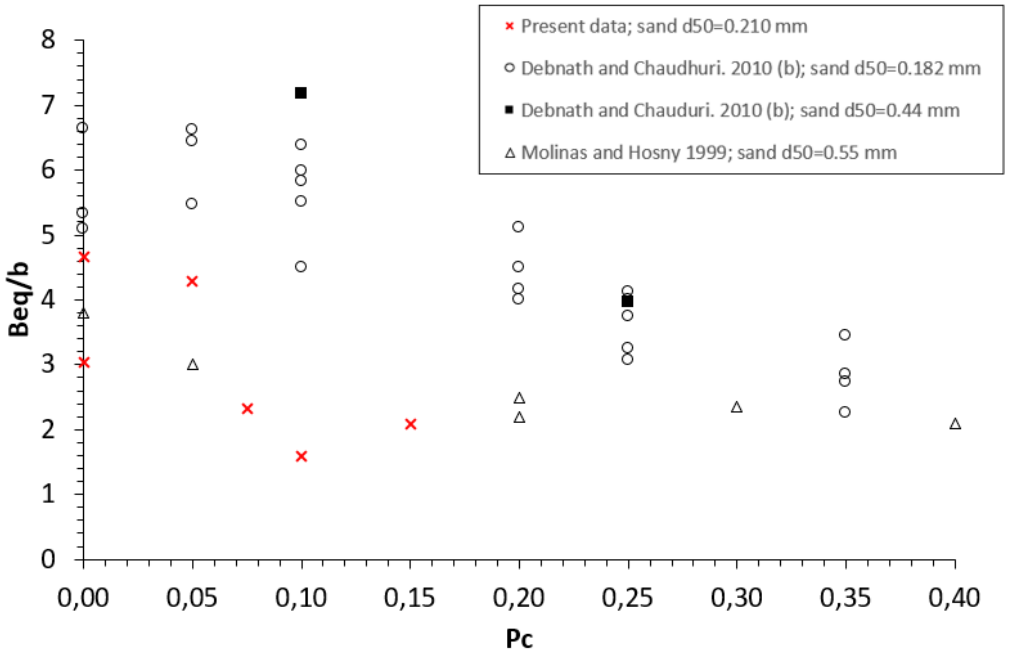

Figure IV.16: Plot of non-dimensional equilibrium scour diameter Beq/b function of percentage of clay Pc obtained from present data, Debnath and Chaudhuri. 2010 (b) [80] and Molinas and Hosny 1999 [173] for V/Vcr (sand) =0.99-1.1, where Vcr (sand) is the critical velocity of the sand used in the soil mixture

IV.2.6 *Temporal variation of the scour hole volumes*

Simultaneous data acquisition both upstream and downstream is not feasible, resulting in limited access to the entire scour hole volume. The scheme in Figure IV.17 illustrates the upstream and downstream scour pit volumes noted Vu for the upstream test and Vd for the downstream test. The volume is determined by summing the scour depths within the pit, delineated by its periphery. The pit's boundary is defined by points with depths exceeding -2 mm. For fine sand and the M1 mixture, the calculation does not include erosion occurring away from the pile. Figure IV.17

shows the evolution of volume Vu and Vd as a function of time.

It is observed that hyperbolic fitted trend curves describe well their evolution. The regression coefficients R^2 for all the fitted curves exceed 0.84.

The measured eroded volume values for fine sand and M1 mixture are similar, indicating minimal impact of silt on the scouring process. A noticeable reduction in Vu and Vd volumes becomes evident as the clay percentage rises. Using the same method previously described in section IV.2.5.1, the initial rate of change and the equilibrium values of volume for the upstream and downstream parts are calculated (Table IV.9). For the equilibrium state, a decreasing in the volume with the increase in the clay content is well observed. This observation is consistent with previous researches, illustrating a decrease of total equilibrium scour volume with increasing clay percentage in the bed [66, 173].

The reduction factors in volumes for all mixtures, when compared with pure fine sand, range from 23.68% to 94.05% for Vu and from 67.65% to 98.67% for Vd (as detailed in Table IV.9). For all tested soils, the scour hole volume in the downstream part is found greater than the scour hole volume in the upstream part. Concerning the initial rate of change in scour hole volumes, a decrease trend is observed with increasing percentage of clay particles in the soil mixtures. The values of the initial rate of change and the equilibrium values obtained for M1 mixture are less accurate compared with the others because of the limited number of values compared with the other soils containing fines.

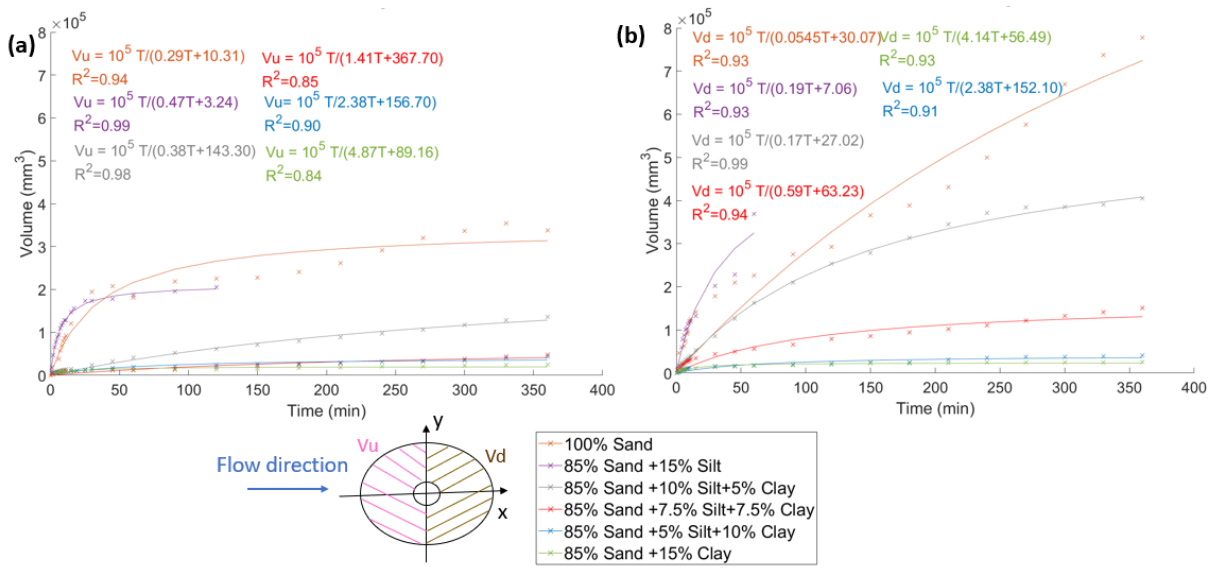

Figure IV.17: Temporal evolution of the scour volume (a): for the upstream part (Vu), (b): for the downstream part (Vd), the scheme illustrates the corresponding value of the volume for the upstream part Vu, and for the downstream part Vd

	Sand	**M1** *	**M2**	**M3**	**M4**	**M5**
$\dot{Vu}$ $10^4 mm^3/min$	0.97	3.09	0.07	0.03	0.06	0.11
(Vu)eq $10^5 mm^3$	3.45	2.13	2.63	0.71	0.42	0.21
Reduction factor (Vu)eq (%) $(1-\frac{(Vu)eq}{((Vu)eq)Sand})\times 100$	–	38.30	23.68	79.43	87.84	94.05
$\dot{Vd}$ $10^4 mm^3/min$	0.33	1.42	0.37	0.16	0.07	0.18
(Vd)eq $10^5 mm^3$	18.18	5.26	5.88	1.69	0.42	0.24
Reduction factor (Vd)eq (%) $(1-\frac{(Vd)eq}{((Vd)eq)Sand})\times 100$	–	71.05	67.65	90.68	97.67	98.67

Table IV.9: Volume of the scour hole for tested soils; $\dot{V}$u, $\dot{V}$d are the initial rate of change in the volume upstream and downstream respectively; (Vu)eq, (Vd)eq are the values at the equilibrium state of volume at the upstream part and downstream respectively; M1: 85% Sand +15% Silt, M2: 85 % Sand +10 % Silt +5 % Clay, M3: 85% Sand +7.5 % Silt +7.5 % Clay, M4: 85% Sand +5% Silt +10% Clay and M5: 85% Sand +15% Clay

*: *extrapolation from data measurements based on an upstream test lasting 120 min and a downstream test lasting 45 min instead of 360 min*

SYNTHESIS

New experimental data on scour at circular piers embedded vertically in mixed cohesive bed under steady current are presented. The new contribution of this work as regards to previous existing studies, is to determine whether the relative proportion of clay mixed with silt can affect the scour process. We compare the soil behavior from the starting mixture of 15% silt with the increasing of clay proportion in the sand-silt-clay mixture. So, the fines content remained constant (15%) but the clay fraction increased.
The study's main conclusions are as follows:

1. The type of cohesive soil added to the pure sand is a significant parameter that affect the scour process. Kaolinite clay is observed to have a greater effect than silt.

2. Soil mixture changes from cohesionless to cohesive scour behavior when the Kaolinite clay in the sediment mixture exceeds a threshold value of about 7.5-10 % in dry weight ratio. Cohesive scour hole topography is characterized by a flat region upstream and a scour propagation as well as a depth greater in the wake region compared to other sides.

3. The location of the scour initiation is observed on the sides, regardless of the soil type, oppositely to the location of maximum final scour depth.

4. With an increase in clay content, significant decrease in the amount of sediment deposition, maximum scour depth, scour hole dimensions with steeper downstream slopes are observed.

5. The SRICOS-EFA method works quite well for predicting the temporal evolution of the maximum scour depth measured in laboratory. The relative maximum error on the equilibrium scour depth between the measurement and SRICOS-EFA estimation is less than $\pm$ 25%. This value is within the $\pm$ 50 % range observed in [190]. It provides the best estimation values compared to all the other prediction equations evaluated for all the tested soils.

6. The temporal evolution of the measured maximum scour depth, scour hole horizontal plane dimensions and the volume at the upstream and downstream parts can be described by hyperbolic laws. Reduction factors compared to the sand at the equilibrium state range are 8.5-68.5 % for Zeq, 14.5-60 % for (Lu)eq, 46-70 % for (Bu)eq, 8-66 % for (Ld)eq, 1.5-77.5 % for (Bd)eq, 23.68-94.05 % for (Vu)eq and 67.65-98.67 % for (Vd)eq.

General Conclusion and Perspectives

CONTRIBUTIONS AND MAIN FINDINGS

Most studies were devoted to sand scour and few investigations were dedicated to cohesive soils involving clay. The contributions and main findings from the present investigation are summarized as follows.

In this thesis, a physical model of a bridge pier was implemented in a flume. The experimental protocol for carrying out the test was developed. A Vectrino Profiler method required to characterize the velocity profile was developed. The use of a 3D Laser Scanner to dynamically monitor the bed changes during the scour mechanism in laboratory setups was shown to be possible. An appropriate data processing approach was described to make the device operational and get accurate 3D digital elevation data of the formed scour hole with the best possible spatial accuracy. All preliminary results observed on medium sand in clear water scour regime (considered as benchmark test) using the 3D Scanner Laser were found to be in agreement with previous studies on sand using other instrumentation techniques. Repeatability tests indicated that a temporal standard deviation within an accepted range was observed. The 3D Scanner Laser measuring technique presents appreciated improvements in the pier scour instrumentation development in laboratory settings. It offers advantages over other instruments commonly found in the literature but also presents few limitations. It operates with rapid and automated procedures, ensuring high spatial accuracy in continuous temporal scour measurements, without the need for water drainage. However, it presents some limitations, including the selection of scanner positions due to the formation of shadows caused by objects and the restricted dimensions of the acquisition zone. Environmental factors, such as turbidity and waves, may affect the original data acquisition. The Plexiglas plate kept on the water's surface during pier scour measurement was found to have negligible impact on the scour hole's topography. In contrast, water evacuation was found to induce deformation in the topography of the scour hole.

The present study reports new experimental findings on pier scour around vertically circular piers embedded in a mixed cohesive bed under constant current conditions. A series of flume tests were conducted using soil mixtures including 85% fine sand and 15% fines. Silt, Kaolinite clay, and the two type of fines in varying quantities constitues the fines content used in the soil mixtures. The water velocity during the tests was maintained constant, slightly above the erosion critical velocity for the fine sand used in the mixtures. The results show that the type of fines added to the pure sand is an important factor that influences the scouring process. When the kaolinite clay in the cohesive sediment mixture exceeds a threshold value of roughly 7.5–10% in dry weight ratio, mixed soil is transformed from cohesionless to cohesive scour behavior. Flat region at the upstream of the pier, drop in the depth side, scour propagation, and depth larger in the wake region compared to other sides are the characteristics of cohesive scour hole topography. The scour start location was observed on the sides independent of the soil type, in contrast to the maximum final scour depth. Increase in clay content results in significant decrease in maximum scour depths, and scour hole widths with steeper downstream slopes. Hyperbolic laws was observed to describe well the temporal evolution of the recorded maximum scour depth, scour hole dimensions, and the volume at the upstream and downstream sections.

Using the SRICOS-EFA method, prediction of the temporal evolution of the maximum scour depth recorded in the laboratory has given good results. Between the measurement and the SRICOS-EFA estimation, the relative maximum error on the equilibrium scour depth was less than 25%. Compared to all other prediction equations considered for the tested soils, the SRICOS-EFA method offered the best estimation results.

SUGGESTIONS FOR FUTURE RESEARCH

This thesis provided an opportunity to investigate the phenomenon of scouring while concentrating on certain unresolved aspects. However, there are still a lot of raising questions regarding the topic of pier scour, and the current work could be expanded in a variety of ways.

1. A constraint linked to the positioning of the 3D laser scanner necessitated the conduction of each test twice for each bed. The purchase of an additional scanner with an extra Plexiglas plate is recommended. By synchronizing two scanners, one upstream and one downstream, it will become possible to scan the entire scour hole in a single flume test. To facilitate the merging of the two scans, it is essential to establish a reference object. This reduces the testing time required for the work carried out in this thesis by using only one available scanner device.

2. While our research allowed us to study the temporal progression of the topography of the scour hole, there is still a need for a more comprehensive grasp of the underlying hydrodynamics. A study of the hydrodynamics in the vicinity of the piers using the same cohesive soils in this thesis can complete the present findings. This may be done using the PIV (Particle Image Velocimetry) in the flume test or using numerical methods such as Computational Fluid Dynamics (CFD). The objective is to establish a relationship between the hydrodynamics and the resulting scour hole topography. In addition, it will allow an understanding of the changes in hydrodynamics that occur when fine particles are added to the sand.

3. The conducted study focuses on a simple configuration : an isolated circular pier, under constant velocity and in one uniform soil layer. It holds perspectives for exploring more configurations while making comparison with SRICOS-EFA method, such as changing the pier's shape, varying velocities as function of time, using different soil layers and several piers. Additionally, this study is limited on scenarios with a 15% fines content. However, exploring soil scour scenarios with higher fines contents which gives samples of soils less erodible (in Erosion Categories III and IV) can provide valuable insights. The consideration of geochemical and biological properties influencing cohesive sediment erodibility should also be incorporated.

4. This study represents a physical model of the pier scour process. It can be expanded by conducting numerical modeling, such as utilizing the HEC-RAS software, while employing the same input parameters as those used in the experimental study. This approach would enable a direct comparison between the results of the numerical modeling and the measurements obtained from the experimental data.

5. The need for more specific research on the maximum shear stress estimation for cohesive soils to clarify the definition of the generalized number of Shields.

6. This thesis markes the fist use of the SRICOS-EFA method in France. A comparison between scour depths measured in the flume and those predicted by SRICOS-EFA was carried out. However, it would be useful to extend this study by comparing scour depth data measured in the field for bridges located in France with the scour depths obtained by the SRICOS-EFA method. This would be in the ultimate aim of being able to integrate this methodology, while improving it, into the bridge design practices of French companies.

Appendix

Each point cloud has a roughness donated σ made of surface roughness and instrumented associated noise. In the figure below, it was assumed that S1 is the reference cloud and that Lt represents the true distance between the two clouds S1 and S2. For every point of S2, a distance"C2C" was calculated. The C2C method was based on finding the "nearest neighbour" point in the reference cloud S1 to each point in the cloud S2.

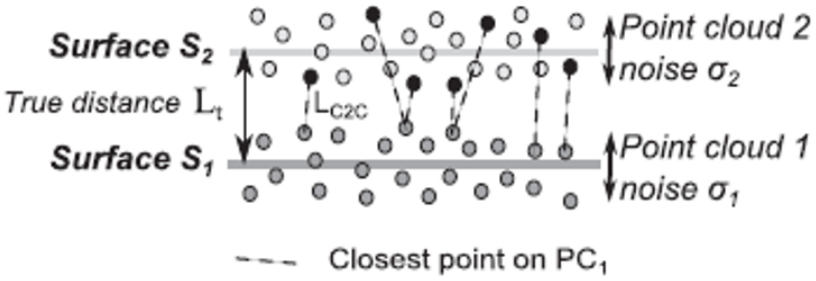

Figure : The "C2C (Cloud to Cloud) tools" in cloud compare software existing for calculating the distance between two point clouds [145]

39th IAHR WORLD CONGRESS GRANADA, SPAIN 2022 From Snow to Sea 19-24 June 2022

Proceedings of the 39th IAHR World Congress
19–24 June 2022, Granada, Spain
doi://10.3850/IAHR-39WC2521716X2022751

Continuous Monitoring of Local Scoured Bed in the Vicinity of Piers by 3D Scanner Laser Technique

ZAIDAN Jana [(1)(2)], POUPARDIN Adrien [(1)], BENNABI Abdelkrim [(1)], MARIN François [(2)] and BENAMAR Ahmed [(2)]

[(1)] Institut de Recherche en Construbilité, Ecole Spéciale des Travaux Publics, Université Paris Est, Champs-sur-Marne, France, e-mail jzaidan@estp-paris.eu
[(2)] Laboratoire Ondes et Milieux Complexes, UMR 6294 CNRS, Université Le Havre Normandie, Le Havre, France e-mail jana.zaidan@etu.univ-lehavre.fr

Abstract

Laboratory experiments constitute an essential part of scour investigation in the vicinity of embedded structures. Yet, no standard and robust instrumentation for monitoring the development of this physical process during laboratory tests is available. In this technical paper, a Laser Scanner has been tested to follow local scour around a circular pier in clear water regime in hydraulic flume, to demonstrate its efficiency. The results which are in good agreement with previous studies validate the performance of this technique. The initiation of local scour occurred at the close sides of the pier. The measured maximum final scour depth was found to be close to the pier diameter. The greatest advantages of this technique with regards to others, are the data acquisition rate which can reach a frequency of 0.5 Hz, especially at the beginning of the experiment, and the accurate continuous spatiotemporal resolution with dense data. Limitations of this device can be considered as very low with respect to the others.

Keywords Hydrodynamic; Instrumentation; Monitoring; Laser Scanner; Local Scour; Pier

1. INTRODUCTION

Scour is a complex process involving the interaction between the water flow, the bridge pier structure and the surrounding bed sediment. In the two past decades, important advancements have been carried out on laboratory investigation of bridge scour to better understand the physical mechanisms, and to study in controlled conditions the influence of various factors on the scour development. It aimed to assess a scour estimation equation, and also to develop the progress in scour countermeasure methods. An appropriate measurement technique needs to be implemented to record the evolution of the scour hole geometry during laboratory tests. Therefore, a wide range of instrumentation has been reported in the literature.

The traditional technique is based on the use of basic inexpensive tools such as a point gauge placed at the location of the bed's point of interest (Dey, 1999; Oliveto and Hager, 2002). They can only give a punctual measurement of the scour depth and are not fast enough to cover the three space dimensions of the scour hole topography formed instantaneously in particular at the beginning of the experiments, and thus, in this case, a global dynamic measurement is not possible. Alternatively, another simple method which has been used consists of measuring the scour depth in a calibrated pier model with a vertical scale. This model can be inspected visually or by using a camera installed inside a hollow transparent tube Debnath and Chaudhuri (2010). Due to the compared dimensions of the camera and the pile model, it is not practical to place a camera tool inside the pile in small scale tests. Moreover, it can provide information about the scour depth only at the region adjacent to the pile. Various set-up of photogrammetry technique has been applied in experimental studies. An illustrative example was the dynamic measurement of 3D scour hole by (Baglio et al., 2001; Sumer et al., 2013), through a stereo-vision approach. A grid of dots was created by lens on the soil bottom and two cameras were set outside of the flume to measure the variation in spatial position. However, in this type of system refraction through the flume wall was not taken into account. Foti et al. (2011) also indicate that the use of a grid lens at sand surface is inadequate, which results in a reduction of accuracy. Some authors have used various types of laser distance sensors to evaluate the scour depth in laboratory experiments. Laser profilometer (Lachaussee et al. (2017)) requires a complex mounting system, as the laser sheet must pass through different locations to collect the 3D shape. Since this method is fast, quasi-dynamic measurement can be likely done. However, there will be always a temporal gap between the profiles that should be regrouped in the post treatment step, then the topography measured cannot be considered instantaneous especially if the bottom has eroded rapidly. Another disadvantage of this technology is the presence of a white region close to the pile due to the shadow created when the height of the obstacle hides a part of sensor laser line. Auzerais et al. (2016) used an ultrasonic ranging system to obtain three-dimensional

(3D) bed profiles downstream a pile, only at the equilibrium state. Recently, Nagarajan and Arockiasamy (2020) studied the feasibility of a Terrestrial Laser Scanner to view a specific scour hole shape around a cylinder in presence of water at static state. They reported a high potential of the device but with reduced accuracy for high values of the water turbidity.

In light of the advantages and disadvantages of each technique, this paper investigates the potential of using a Terrestrial Laser Scanner (as in Nagarajan and Arockiasamy (2020)) to capture the dynamic topographic bed deformation induced by the pier scouring process in a laboratory flume experiment. After this introduction, the methodology and implementation of the laser scanner are detailed in section 2, the test results are discussed in section 3 and are followed by a conclusion in section 4.

2. METHODOLOGY AND IMPLEMENTATION OF SCANNER 3D TECHNIQUE

2.1 Experimental Setup and Procedure

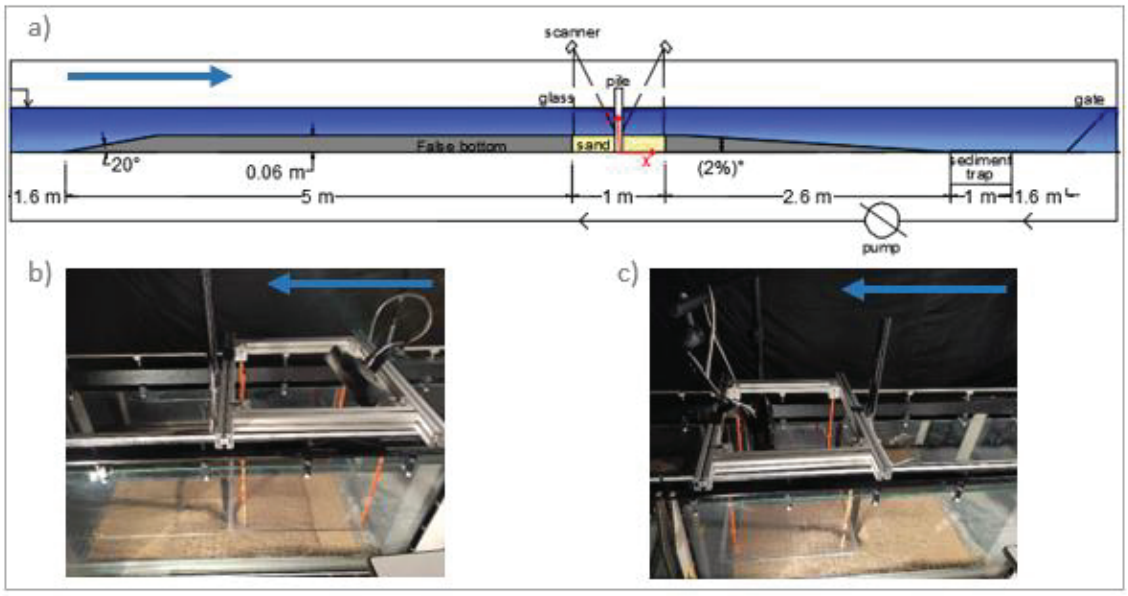

Figure 1. Pier scour experiments (a): scheme of the test flume set-up (not to scale), (b): photograph of test upstream of the pile, (c): photograph of test downstream of the pile, arrow represent the direction of flow

The experiments were carried out in a rectangular flume with dimensions of 13 m length, 0.41 m width and 0.5 m depth located in the Hydraulic Laboratory of ESTP Paris (Ecole Spéciale des Travaux Publics, Cachan, France). Water discharge in the flume was controlled by a variable speed electronic control unit, which allows to maintain a constant flow rate. Water height in the flume was controlled with a tail gate located at the downstream end of the flume. A false bottom made of PVC (Poly Vinyl Chloride) was constructed over the entire length of the flume. The sediment recess area, 1 m long and 0.062 m deep was located 5 m from the flume upstream opening.

A 32 mm filled PVC cylinder simulating a circular pier was firstly installed at the center of the recess area. The sediment used in this study was a typical medium sand, the Hostun Sand HN 1/2.5 which is uniformly grain distributed with a median grain size (d_{50}), a uniformity coefficient ($C_u = \frac{d_{60}}{d_{10}}$), a geometric standard distribution ($\sigma_g = (\frac{d_{84}}{d_{16}})^{0.5}$), a specific gravity ($\rho_s$) and a friction angle (Φ), whose values are 1.7 mm, 1.39, 1.15, 2.65 t/m3 and 35° respectively. The sand bed in the test section was carefully prepared and deposited. A 38 kg dry mass of sand was mixed homogeneously with 1.5 L of tap water in order to fix the initial density and the initial moisture content to 1.7 t/m^3 and 4%, respectively. The soil was saturated initially during 1h, in order to be in geotechnical conditions close to that in the field.

The depth averaged flow velocity U was maintained at a constant value of 0.29 m/s during the experiment. The average critical velocity of the initiation of the sand bed movement was determined preliminarily, visually in a non-pile experiment using the same geotechnical conditions described previously. The hydraulic conditions for particle detachment initiation correspond to the critical water discharge (Qcr) and the critical velocity (Vcr) values of 90 m3/h and 0.41 m/s, respectively. Therefore, for tests involving the pier, a flow intensity U/Ucr= 0.7 shows a clear water scour condition. The flow regime of performed tests was turbulent

since the Reynold's number based on the water depth was Re= 42920 Sleath (1984). The Froude number Fr= 0.24 indicates subcritical hydraulic conditions. The Reynold number based on the diameter of the cylinder ReD= 9280 points out a laminar boundary layer separation and a completely turbulent wake region Sumer and Fredsøe (2006).

The duration of the experiment was set at 6 hours to ensure a quasi-equilibrium scour geometry at the end of the test.

As mentioned before, a high-resolution Scanner laser technique was used in this study. It consists of a pattern projector of Laser class 3R with the signal wavelength in the red spectrum (approx. 639 nm) and a camera. This device relies on the principle of the triangulation plane for 3D surface Imaging allowing an automatic reconstruction of 3D object.

The scan area was around 360 × 286 mm, which was illuminated by the laser sheet. For this reason, the underwater test was composed of two similar separated tests, one focusing scanner to the upstream of the pile and another to the downstream of the pile, while putting a Plexiglas plate at the water surface. The Plexiglas plate used has at each longitudinal extremity a chamfer of 30 degrees to limit the generation of turbulence into the water surface. Using the 3D scanner at these two stations limits the occurrence of the shadow and coloring the pile in black by a marker avoids the reflection of the laser, which appears as an empty area. Then, the 3D scanner allows the capture of a complete half plane (180-degrees view per test) of the scour hole, with a presence of the maximum number of points of the cloud around the pile.

A sketch of the experimental set-up, photographs of tests acquired from the upstream and downstream of the pile are shown in Fig.1 (a), (b) and (c) respectively.

2.2 Methodology of Data Analysis

The laser scanner was connected through the data acquisition software Phoxi Control to obtain the 3D scans around the pile. Suitable acquisition parameters are chosen in our measurements. The values for laser power (4095 µWatt) and exposure time (20.48 milliseconds) were chosen to avoid the saturation of the camera. The shutter multiply, number of repetitions of a pattern (1) and scan multiply, number of repetitions of a scan (1) parameters provided a good density of original cloud data (up to 1.3 million 3D points). As the scour in sand is a rapid process especially at the beginning of the experiments, the frequency rate of acquisition was set to 0.5 Hz for the first 5 minutes (1 scan per 02 seconds) and then to 0.0033 Hz (1 scan per 5 minute) for the rest of the experiment. An automatic triggering of scans was set up with a fixed framerate and an automatic saving in ". ply" extension. Thus, in terms of acquisition, the main advantages of this instrument were the rapid acquisition and the ability to give a representation with millions of 3D points.

The refraction of light at the interface between two different materials modifies the trajectory of light rays and therefore measured elevations, hence a correction algorithm in Scilab software was written. This correction algorithm is based on the determination of the position of the interface 1 (between air and glass) and interface 2 (between glass and water) in function of the position of the camera and the laser. Two scans of a plate reference, object of known thickness at the two different positions, are done. For facility purposes, this step was performed in empty flume. To visualize the importance of this correction step, an application in case of the cylinder obstacle (D=32mm) alone is shown in Figure 2 (b). The green, blue and red surfaces refer respectively to scanned cylinder without water and glass, with water and glass before correction and with water and glass after correction. It was observed that the surface of the cylinder scanned in the presence of water and glass before correction is not a circle, which means that refraction can have the effect of modifying completely the shape of the scanned object. The correction gives back a cylinder of the same radius even if its relative spatial placement is not exactly the same. The amount of refraction depends mostly on the incident angle of water medium and therefore varies with the change in position of the scanner.

In addition, since the acquisition of all clouds is done in the camera spatial reference, an algorithm for changing the reference to a local orthonormal reference centered on the pile was also written in Scilab. This computing code contains a combination of translation and rotation matrices. An application in case of plate surface was displayed in the fig 2 (c). The blue, green and red surfaces correspond to the original scan, the scan after translation and the scan after translation and rotation, respectively. It is noticed the existence of small deviation at the corner.

The calibration previously described is valid only for one position of the laser scanner, so the operator should pay attention that the device is well fixed without any movement (example: vibration) during the test. These corrections were applied to all the data clouds acquired by the instrument.

In fact, the data acquired by the laser scanner always contain scatter points and noises. An example is shown in Fig.2 (d). Their presence do not allow a correct interpretation of the object details. Scatter points are points that do not belong to the target object "bed surface". In our model, the pile was colored in black which permits the elimination of the scatter points related to the pile. The noise is the result of the divergence of the laser beam. The cloud is cleaned by removing all the scatter points and reducing the noise as much as possible.

As the resolution of the scanner differs from one scan to another and is not homogenous within the same scan, decreasing while moving away from the scanner, and a small deviation exists at the corners of scans, a relative rasterization with the reference cloud, always being the initial state of the soil (flat bed surface) was done. Each 3D cloud is transformed into a matrix of altitude Z, with the lines and columns corresponding respectively to x and y coordinates. The digital elevation model was created with a fixed horizontal grid resolution of 1×1 mm. The data at time t was the difference between the Z matrix at time t and the Z matrix at the initial time (see figure 2 (e)). The post treatment step including cloud cleaning and relative rasterization was performed using Cloud Compare software, created by Girardeau-montaut (2006) and which have been used for post-treatment of laser scanner acquired clouds by many authors (Lague et al., 2013; Strange, 2019).

Finally, using MATLAB software, a linear interpolation was applied to replace the small missing data points referring to the shadow caused by the presence of the pile in order to obtain the best quality of the results, a proper and highly precise digital elevation model. Results can then be presented in different forms (counter map plot, section profiles, etc.).

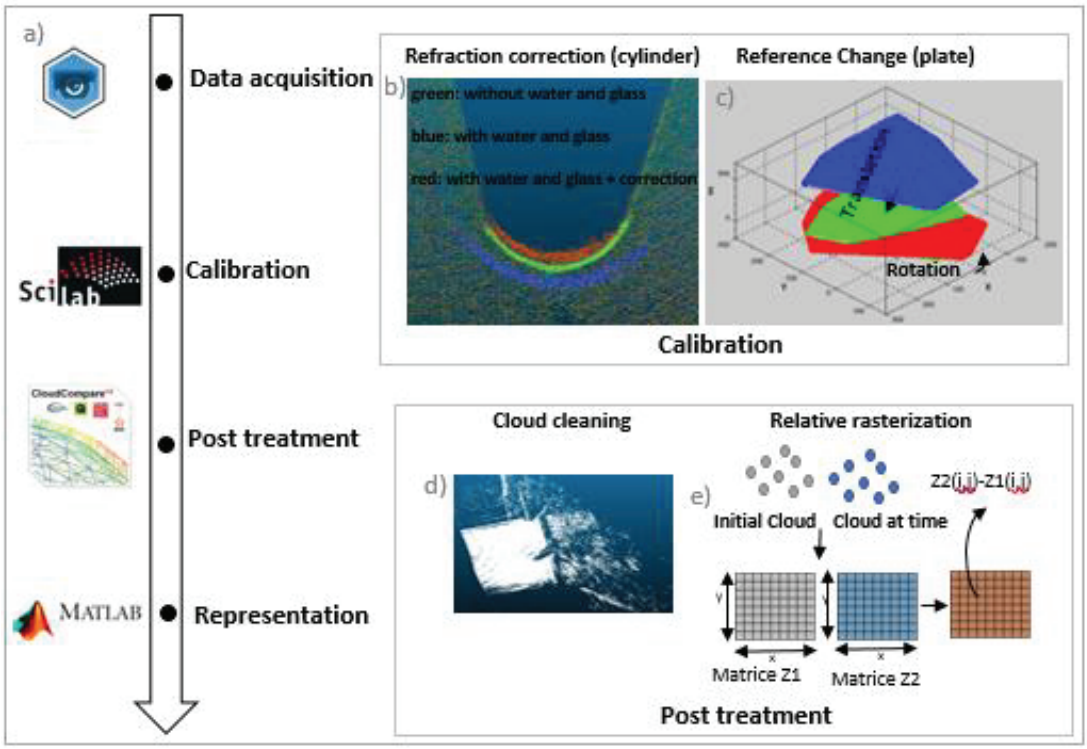

Figure 2. Methodology used for data processing

3. RESULTS AND DISCUSSION

The development of the scour hole topography after t=01min 36 sec,15 min and 06 h for monitored data upstream and downstream of the pile is shown in fig 3-4 as contour maps, longitudinal central sections (y=0) and transversal central sections (x=0). It was difficult to obtain results before 01 min 36 sec, the average time needed to set the water height with the gate in the flume to be aligned with the surface of the Plexiglas plate at the desired hydraulic conditions. Before this time, no depth can be monitored.

The general pattern of the scour process was distinguished by: the scour hole around the pier and a single dune. In fact, the scour hole started at the close sides of the pier, where small depressions were formed at 01min 36 sec. Then, the scoured region enlarged to cover all the area surrounding the cylinder after 15 minutes. It is observed that the maximum depth at the upstream region is close to the maximum depth at the side of the pile at this stage. Then the scour hole continued progressively to extend and deepen and the maximum final scour depth at the front of the pile becomes deeper than that at the side region at the end of the experiment. Whereas, the scour at the downstream region was always the smallest one. The contraction of the main flow due to the presence of the pier upstream accelerated the flow, sweeping then ejecting the eroded sediment from the scour hole to the downstream part. Those sediments deposited downstream the pile and formed the dune which increased progressively in height and reached finally a maximum value close to 0.8 times the pier diameter. Since the scour process is in progress, the sediment in the dune was always in

movement by the wake vortices to far downstream of the pier until the equilibrium state was reached. The periodic shedding of von Karman wake vortices made the transportation of the sediments quasi-periodic. The presence of this dune induced the formation of a small hole behind it. During the scour development, the shape of the scour hole remained nearly constant and nearly symmetric with respect to the flow direction. These findings are in agreement with previous studies (Umeda et al., 2008; Link et al., 2008). The artefact in the contour maps representation was caused by the presence of the light spot near the measurement zone.

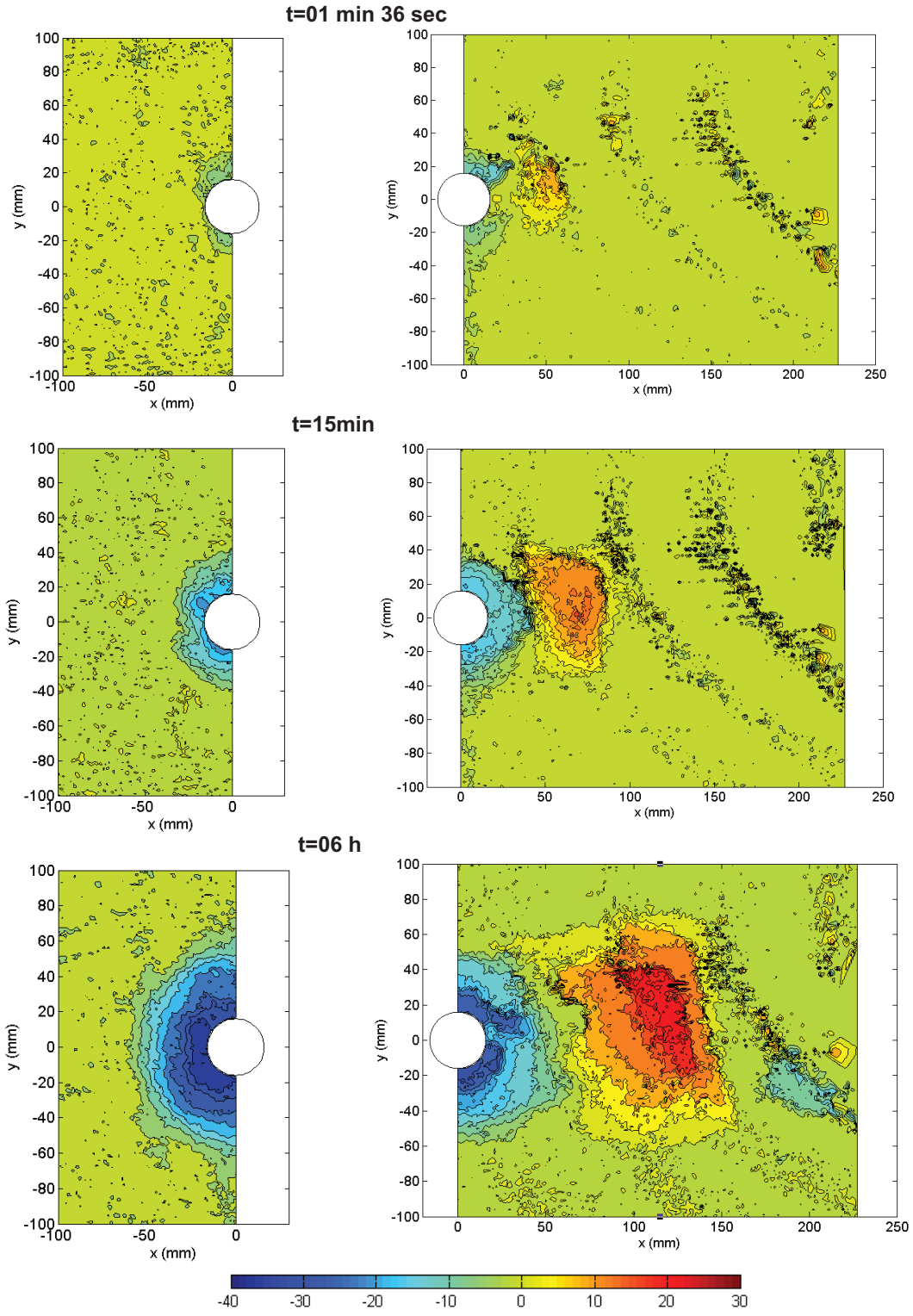

Figure 3. Relative elevation (ΔZ) contour maps at various instants during the experiments, t=time, flow direction is from left to right

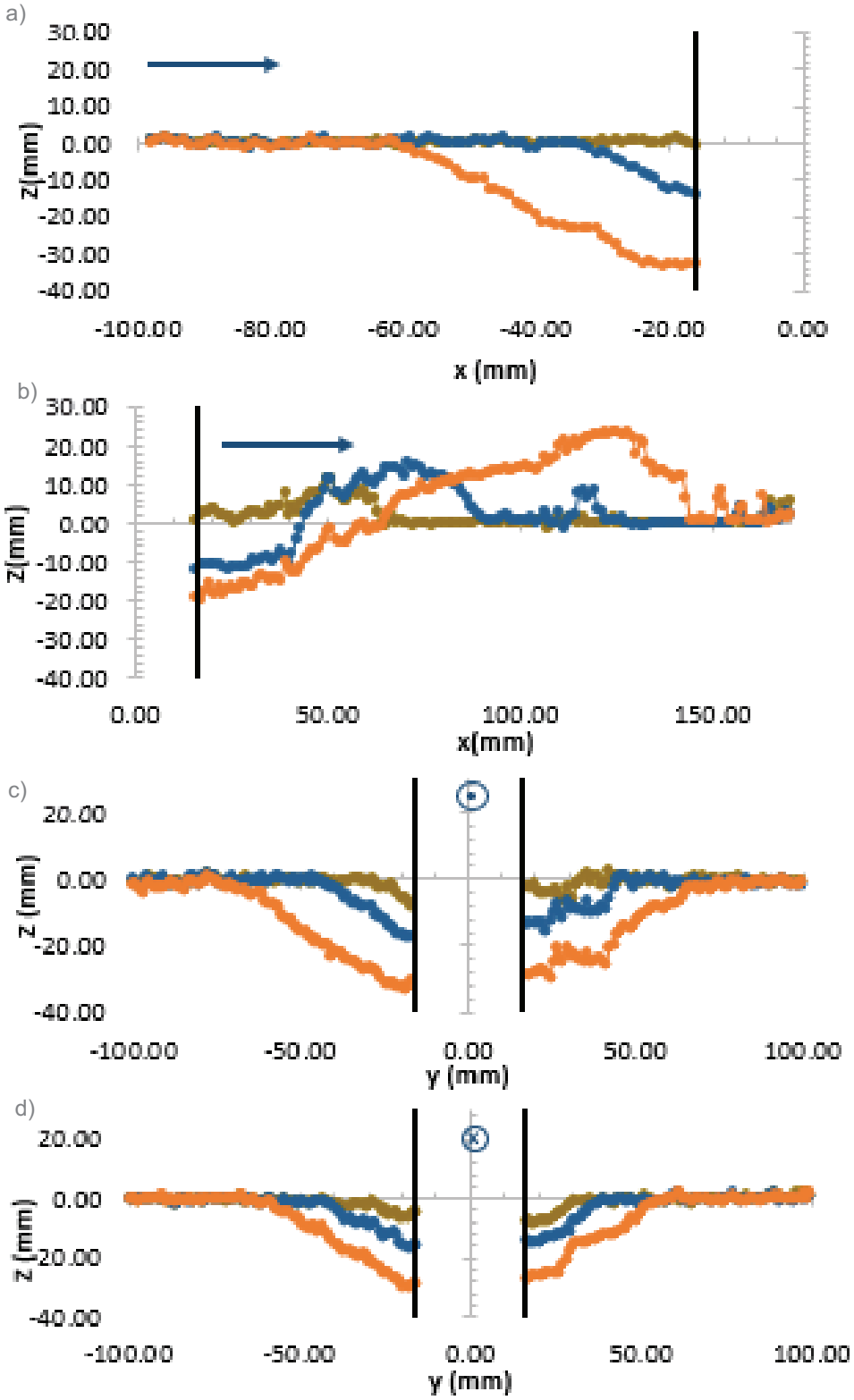

Figure 4. Profiles of scour hole at various instants during the experiments, t=time, flow direction is from left to right., Longitudinal: (a) upstream of the pile, (b) downstream of the pile, and transversal (c) upstream of the pile, (d): downstream of the pile

In longitudinal and transversal sections, we quantitatively identified the existence of a flat bottom region close to the cylinder. The measure of the topography at this region was rendered difficult by various monitoring devices due to the presence of the pier.

In the longitudinal section, the scour hole was steeper at upstream than downstream. At upstream, over this plat region, two slopes are recognized. At the final experiment state, the change in the average slope of the scour hole was from around 44 degrees in the middle part to around 41 degrees in the upper part corresponding to an average value of slope of around 40.9 degrees. As stated by LIU et al. (2019), in a region around the pier, the scour hole slope always exceeds the angle of repose of sediment particles. The average scour hole slope in this region is about 10%-15% sharper than the natural angle of repose of sediment particles according to Dey (1999). The differences in the slopes upstream of the pile suggested the action of the system of horseshoe vortex. This system has the most important contribution in the deformation of the bed during scour mechanism. If the measurement was made after water was paused or was drained out, the sediment will settle under gravity, then in this case the scour hole slopes will be equal to the natural angle of repose of the soil as obtained by (Melville, 1975; Yanmaz and Altmbilek, 1992), hence the scour hole will have the most usual described shape, an “inverted and truncated cone”.

Therefore, at the downstream part the average slope of the scour hole reaches around 26 degrees, beside 17 degrees at the dune. Sediment continuously slides upward on the upper slope of the dune, and downwards on the lower slope of the scour hole. The wake vortices picked the downward sliding sediments and transported them as bed load to the upward part. Some sediments passed through the dune, while others fed continuously and were deposited at the mount.

On the other hand, the central transversal profiles of the scour hole were very similar to the upstream profile, but with a relatively shallow average slope of around 32.7 degrees. The same side section in upstream and downstream tests was relatively close, but not exactly similar. This is explained by the uncertainty due to the manual soil preparation. The small noise observed in the cross sections is caused by the medium grain size distribution of the soil used.

The temporal variation of scour depth at the point of the final maximum scour depth was presented in Fig. 5. In the initial stage of the scour process, scour depth increased very rapidly. It attained above 60% of the final scour depth at the first 30 min, then increased more slowly to reach finally at 04h an asymptotic final state. The final scour depth measured was 1.1 times the diameter of the pile used, in accordance with the values reported in the literature (Roulund et al., 2005; Lachaussee et al., 2017).

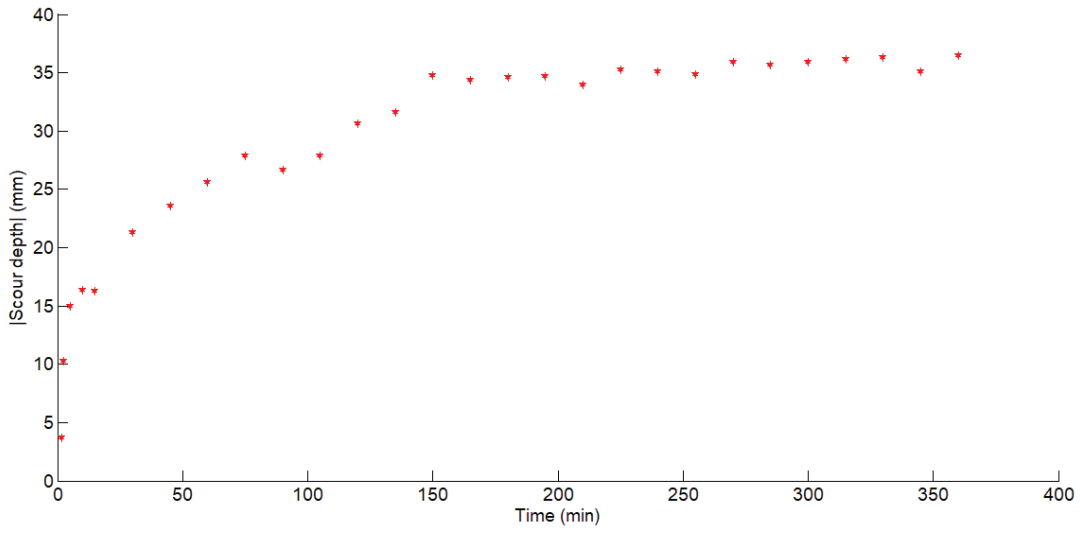

Figure 5. Scour depth function of time at the point of maximum final scour depth

4. CONCLUSIONS

The capability of a terrestrial laser scanner to dynamically measure the bed elevation change during the physical scour mechanism in laboratory setups is demonstrated. A suitable procedure is presented as a set of

actions for calibrate, treat the acquired data in order to make operational the device and obtain a correct 3D digital elevation data of the shaped scour hole with highest spatial accuracy. Such measurement approach provides appreciated advancements in monitoring the development of the scour hole around a pier. The discussed methodology is rapid, automatic and allows temporal scour measurement in a safe environment. In addition, it allows the measurement without the necessity to drain the water. However, limitations are related to the crucial position choice due to the shadow formed by the presence of object and the limited dimensions of acquisition zone. Turbidity and waves can also largely affect the original data acquisition and then can prevent the possibility of measurement.

The presented work provides an experimental database for numerical simulation of medium granular sediment scour models. The determination of the temporal variation of maximum scour depth position, and comparison of measurement with scour empirical prediction methods, could be very useful to complete this study.

5. ACKNOWLEDGEMENTS

A grateful acknowledged for the financial support of the present research project supported by the Normandy Region and ESTP Foundation.

6. REFERENCES

Auzerais, A., Jarno, A., Ezersky, A., and Marin, F. (2016). “Formation of localized sand patterns downstream from a vertical cylinder under steady flows: Experimental and theoretical study.” *Physical Review E*, 94(5), 1–7.

Baglio, S., Faraci, C., Foti, E., and Musumeci, R. (2001). “Measurements of the 3-D scour process around a pile in an oscillating flow through a stereo vision approach.” *Measurement: Journal of the International Measurement Confederation*, 30(2), 145–160.

Debnath, K., and Chaudhuri, S. (2010). “Laboratory experiments on local scour around cylinder for clay and clay-sand mixed beds.” *Engineering Geology*, Elsevier B.V., 111(1–4), 51–61.

Dey, S. (1999). “Time-variation of scour in the vicinity of circular piers.” *Proceedings of the Institution of Civil Engineers: Water, Maritime and Energy*, 136(2), 67–75.

Foti, E., Rabionet, I. C., Marini, A., Musumeci, R. E., and Sánchez-Arcilla, A. (2011). “Experimental investigations of the bed evolution in wave flumes: Performance of 2D and 3D optical systems.” *Coastal Engineering*, Elsevier B.V., 58(7), 606–622.

Girardeau-montaut, D. (2006). “Thèse présentée pour obtenir le grade de Docteur DANIEL GIRARDEAU-MONTAUT.” *Ph.D Thesis*.

Lachaussee, F., Bertho, Y., Morize, C., Sauret, A., and Gondret, P. (2017). “Érosion autour et en aval d ’ un cylindre Résumé : Abstract :” 1–7.

Lague, D., Brodu, N., and Leroux, J. (2013). “Accurate 3D comparison of complex topography with terrestrial laser scanner: Application to the Rangitikei canyon (N-Z).” *ISPRS Journal of Photogrammetry and Remote Sensing*, International Society for Photogrammetry and Remote Sensing, Inc. (ISPRS), 82, 10–26.

Link, O., PFLEGER, F., and ZANKE, U. (2008). “Characteristics of developing scour-holes at a sand-embedded cylinder.” *International Journal of Sediment Research*, International Research and Training Centre on Erosion and Sedimentation and the World Association for Sedimentation and Erosion Research, 23(3), 258–266.

LIU, Q., TANG, H., and WANG, H. (2019). “Topographic Evolution of Scour Hole Around a Cylindrical Pier: an Experimental Investigation.” *38th IAHR World Congress - “Water: Connecting the World,”* 38(November), 2564–2573.

Melville, B. W. (1975). “Local scour at bridge sites.”

Nagarajan, S., and Arockiasamy, M. (2020). “Non-Contact Scour Monitoring System for Railroad Bridges.” (November).

Oliveto, G., and Hager, W. H. (2002). “Temporal Evolution of Clear-Water Pier and Abutment Scour.” *Journal of Hydraulic Engineering*, 128(9), 811–820.

Roulund, A., Sumer, B. M., Fredsøe, J., and Michelsen, J. (2005). “Numerical and experimental investigation of flow and scour around a circular pile.” *Journal of Fluid Mechanics*, 534(January 2016), 351–401.

Sleath, J. (1984). *Sea Bed Mechanics*. *Wiley Interscience*.

Strange, E. M. (2019). “Monitoring survey of heritage listed fencing using terrestrial laser scanners and CloudCompare software . A Dissertation submitted by.”

Sumer, B. M., Petersen, T. U., Locatelli, L., Fredsøe, J., Musumeci, R. E., and Foti, E. (2013). “Backfilling of a Scour Hole around a Pile in Waves and Current.” *Journal of Waterway, Port, Coastal, and Ocean Engineering*, 139(1), 9–23.

Sumer, F. (2006). “Hydrodynamics around cylindrical strucures.” *World scientific.*, 26, 13, 14, 45.
Umeda, S., Yamazaki, T., and Ishida, H. (2008). “Time Evolution of Scour and Deposition Around a Cylindrical Pier in Steady Flow.” 140–146.
Yanmaz, A. M., and Altmbilek, H. D. (1992). “Study of time-dependent local scour around bridge piers.” *Journal of Hydraulic Engineering*, 118(11), 1595–1597.

Bibliography

[1] AASHTO. *AASHTO LRFD Bridge Design Specificaitons: Customary US Units 4th Edition-2007*. American association of state highway and transportation officials, 2007.

[2] NL Ackermann, HT Shen, and P Olsson. "Local scour around circular piers under ice covers." In: *International Symposium on Ice: 02/12/2002-06/12/2002*. Dep. of Physic, Univ. of Otago. 2002, pp. 149–155.

[3] SG Aghaji Zare, SA Moore, CD Rennie, O Seidou, H Ahmari, and J Malenchak. "Boundary shear stress in an ice-covered river during breakup." In: *Journal of Hydraulic Engineering* 142.4 (2016), p. 04015065.

[4] F Ahmed and N Rajaratnam. "Flow around bridge piers." In: *Journal of Hydraulic Engineering* 124.3 (1998), pp. 288–300.

[5] AO Aksoy, G Bombar, T Arkis, and MS Guney. "Study of the time-dependent clear water scour around circular bridge piers." In: *Journal of hydrology and hydromechanics* 65.1 (2017), pp. 26–34.

[6] M Al-Hammadi and RR Simons. "Local scour mechanism around dynamically active marine structures in noncohesive sediments and unidirectional current." In: *Journal of Waterway, Port, Coastal, and Ocean Engineering* 146.1 (2020), p. 04019026.

[7] AT Al-Madhhachi, GJ Hanson, GA Fox, AK Tyagi, and R Bulut. "Measuring erodibility of cohesive soils using laboratory jet erosion tests." In: *World Environmental and Water Resources Congress 2011: Bearing Knowledge for Sustainability*. 2011, pp. 2350–2359.

[8] KED Ambtman, FE Hicks, and PM Steffler. "Experimental investigation of the pressure distribution beneath a floating ice block." In: *Journal of Hydraulic Engineering* 137.4 (2011), pp. 399–411.

[9] H An, W Yao, L Cheng, S Draper, M Zhao, G Tang, Y Zhang, and P Hortin. "Detecting local scour using contact image sensors." In: *Journal of hydraulic engineering* 143.4 (2017), p. 04016100.

[10] SA Ansari. "Influence of cohesion on local scour." In: *Universitt of Roorkee, Roorkee, India* (1999).

[11] SA Ansari. "Discussion of "Flume Tests for Scour in Clay at Circular Piers" by Francis CK Ting, JL Briaud, HC Chen, Rao Gudavalli, Suresh Perugu, and Gengsheng Wei." In: *Journal of Hydraulic Engineering* 129.7 (2003), pp. 554–556.

[12] SA Ansari, UC Kothyari, and KG Ranga Raju. "Influence of clay content, dry density and soil moisture on bridge pier scour-I." In: *Int. Seminar on Sustainable Development in Road Transport, 1, New Delhi*. 2001, 1193–1201.

[13] SA Ansari, UC Kothyari, and KG Ranga Raju. “Influence of cohesion on scour around bridge piers.” In: *Journal of hydraulic research* 40.6 (2002), pp. 717–729.

[14] LA Arneson. *Evaluating scour at bridges*. Tech. rep. United States. Federal Highway Administration, 2012.

[15] A Auzerais. “Impact d’un cylindre vertical sur la dynamique sédimentaire sous l’action d’un courant.” PhD thesis. Normandie, 2017.

[16] A Auzerais, A Jarno, A Ezersky, and F Marin. “Formation of localized sand patterns downstream from a vertical cylinder under steady flows: Experimental and theoretical study.” In: *Physical Review E* 94.5 (2016), p. 052903.

[17] S Baglio, C Faraci, E Foti, and R Musumeci. “Measurements of the 3-D scour process around a pile in an oscillating flow through a stereo vision approach.” In: *Measurement* 30.2 (2001), pp. 145–160.

[18] C Baykal, BM Sumer, DR Fuhrman, NG Jacobsen, and J Fredsøe. “Numerical investigation of flow and scour around a vertical circular cylinder.” In: *Philosophical Transactions of the Royal Society A: Mathematical, Physical and Engineering Sciences* 373.2033 (2015), p. 20140104.

[19] S Beltaos. “River ice jams: theory, case studies, and applications.” In: *Journal of Hydraulic Engineering* 109.10 (1983), pp. 1338–1359.

[20] N Benahmed and S Bonelli. “Investigating concentrated leak erosion behaviour of cohesive soils by performing hole erosion tests.” In: *European Journal of Environmental and Civil Engineering* 16.1 (2012), pp. 43–58.

[21] N Benahmed, TK Nguyen, PY Hicher, and M Nicolas. “An experimental investigation into the effects of low plastic fines content on the behaviour of sand/silt mixtures.” In: *European Journal of environmental and civil engineering* 19.1 (2015), pp. 109–128.

[22] H Bénard. “Etude cinematogrphique des remous et rides produits par la translation d’un obstacle.” In: *Compt. Rend.* 147 (1908), p. 970.

[23] H Bénard. “Formation des centres de giration à l’arrière d’un obstacle en mouvement.” In: *Compt. rend.* 147 (1908), p. 839.

[24] A Bennabi, G Herrier, and D Lesueur. “Lime treated soil erodibility investigated by EFA erosion testing.” In: (2016).

[25] LG Bennetts, A Alberello, MH Meylan, C Cavaliere, AV Babanin, and A Toffoli. “An idealised experimental model of ocean surface wave transmission by an ice floe.” In: *Ocean Modelling* 96 (2015), pp. 85–92.

[26] AM Bento, L Couto, T Viseu, and JP Pêgo. “Image-based techniques for the advanced characterization of scour around bridge piers in laboratory.” In: *Journal of Hydraulic Engineering* 148.6 (2022), p. 06022004.

[27] A Bestawy, T Eltahawy, A Alsaluli, A Almaliki, and M Alqurashi. “Reduction of local scour around a bridge pier by using different shapes of pier slots and collars.” In: *Water Supply* 20.3 (2020), pp. 1006–1015.

[28] LC Bolduc. “Probabilistic models and reliability analysis of scour depth around bridge piers.” PhD thesis. Texas A & M University, 2010.

[29] LC Bolduc, P Gardoni, and JL Briaud. “Probability of exceedance estimates for scour depth around bridge piers.” In: *Journal of Geotechnical and Geoenvironmental Engineering* 134.2 (2008), pp. 175–184.

[30] MA Boukhemacha, I Bica, and K Mezouar. “New procedures to estimate soil erodibility properties from a hole erosion test record.” In: *Periodica Polytechnica Civil Engineering* 57.1 (2013), pp. 77–82.

[31] P Bouratsis, P Diplas, CL Dancey, and N Apsilidis. “High-resolution 3-D monitoring of evolving sediment beds.” In: *Water Resources Research* 49.2 (2013), pp. 977–992.

[32] P Bouratsis, P Diplas, CL Dancey, and N Apsilidis. “Quantitative spatio-temporal characterization of scour at the base of a cylinder.” In: *Water* 9.3 (2017), p. 227.

[33] Z Bozkus and O Yildiz. “Effects of inclination of bridge piers on scouring depth.” In: *Journal of Hydraulic Engineering* 130.8 (2004), pp. 827–832.

[34] A Brand, C Noss, C Dinkel, and M Holzner. “High-resolution measurements of turbulent flow close to the sediment–water interface using a bistatic acoustic profiler.” In: *Journal of atmospheric and oceanic technology* 33.4 (2016), pp. 769–788.

[35] L Brandimarte, A Montanari, JL Briaud, and P D’Odorico. “Stochastic flow analysis for predicting river scour of cohesive soils.” In: *Journal of hydraulic engineering* 132.5 (2006), pp. 493–500.

[36] L Brandimarte, P Paron, and G Di Baldassarre. “Bridge pier scour: A review of processes, measurements and estimates.” In: *Environmental Engineering and Management Journal* 11.5 (2012), pp. 975–989.

[37] T Branß, F Núñez-González, A Dittrich, and J Aberle. “A flume study to investigate the contribution of main-channel bedforms on levee formation.” In: *E3S Web of Conferences*. Vol. 40. EDP Sciences. 2018, p. 02018.

[38] M Brede, H Eckelmann, and D Rockwell. “On secondary vortices in the cylinder wake.” In: *Physics of Fluids* 8.8 (1996), pp. 2117–2124.

[39] HNC Breusers, G Nicollet, and HW Shen. “Local scour around cylindrical piers.” In: *Journal of hydraulic research* 15.3 (1977), pp. 211–252.

[40] JL Briaud. “Case histories in soil and rock erosion: Woodrow wilson bridge, brazos river meander, normandy cliffs, and new orleans levees.” In: *Journal of Geotechnical and Geoenvironmental Engineering* 134.10 (2008), pp. 1425–1447.

[41] JL Briaud. “Scour depth at bridges: Method including soil properties. I: Maximum scour depth prediction.” In: *Journal of Geotechnical and Geoenvironmental Engineering* 141.2 (2015), p. 04014104.

[42] JL Briaud. “Scour depth at bridges: Method including soil properties. II: Time rate of scour prediction.” In: *Journal of Geotechnical and Geoenvironmental Engineering* 141.2 (2015), p. 04014105.

[43] JL Briaud, L Brandimarte, J Wang, and P D'odorico. "Probability of scour depth exceedance owing to hydrologic uncertainty." In: *Georisk* 1.2 (2007), pp. 77–88.

[44] JL Briaud, HC Chen, AV Govindasamy, and R Storesund. "Levee erosion by overtopping in New Orleans during the Katrina Hurricane." In: *Journal of geotechnical and geoenvironmental engineering* 134.5 (2008), pp. 618–632.

[45] JL Briaud, HC Chen, K Kwak, SW Han, and FCK Ting. "Multiflood and multilayer method for scour rate prediction at bridge piers." In: *Journal of Geotechnical and Geoenvironmental Engineering* 127.2 (2001), pp. 114–125.

[46] JL Briaud, HC Chen, K Kwak, J Wang, and J Xu. "The SRICOS-EFA Computer Program For Bridge Scour." In: *Proceedings 2nd International Conference on Scour and Erosion (ICSE-2). November 14.–17., 2004, Singapore*. 2004.

[47] JL Briaud, HC Chen, Y Li, P Nurtjahyo, and J Wang. "SRICOS-EFA method for contraction scour in fine-grained soils." In: *Journal of geotechnical and geoenvironmental engineering* 131.10 (2005), pp. 1283–1294.

[48] JL Briaud, HC Chen, P Nurtjahyo, and J Wang. *Complex pier scour and contraction scour in cohesive soils*. NCHRP Report 24-15. Washington, D.C.: National Cooperative Highway Research Program - National Research Board National Research Council, 2003.

[49] JL Briaud, P Gardoni, and C Yao. "Statistical, risk, and reliability analyses of bridge scour." In: *Journal of Geotechnical and Geoenvironmental Engineering* 140.2 (2014), p. 04013011.

[50] JL Briaud, AV Govindasamy, and I Shafii. "Erosion charts for selected geomaterials." In: *Journal of geotechnical and geoenvironmental engineering* 143.10 (2017), p. 04017072.

[51] JL Briaud and B Hunt. "Bridge scour and the structural engineer." In: *Structure* 2006.Dec (2006), pp. 58–61.

[52] JL Briaud, S Hurlebaus, KA Chang, C Yao, H Sharma, OY Yu, C Darby, BE Hunt, and GR Price. *Realtime monitoring of bridge scour using remote monitoring technology*. Tech. rep. Texas Transportation Institute, 2011.

[53] JL Briaud and I Shafii. *NCHRP-Erosion spreadsheet*. Available at : https://www.trb.org/Publications/Blurbs/179128.aspx.

[54] JL Briaud, I Shafii, HC Chen, and Z Medina-Cetina. *Relationship between erodibility and properties of soils*. Project 24–43. 2019.

[55] JL Briaud, FCK Ting, HC Chen, Y Cao, SW Han, and K Kwak. "Erosion function apparatus for scour rate predictions." In: *Journal of geotechnical and geoenvironmental engineering* 127.2 (2001), pp. 105–113.

[56] JL Briaud, FCK Ting, HC Chen, R Gudavalli, S Perugu, and G Wei. "SRICOS: Prediction of scour rate in cohesive soils at bridge piers." In: *Journal of Geotechnical and Geoenvironmental Engineering* 125.4 (1999), pp. 237–246.

[57] GO Brown. "The history of the Darcy-Weisbach equation for pipe flow resistance." In: *Environmental and water resources history*. 2002, pp. 34–43.

[58] F Brunier-Coulin, P Cuéllar, and P Philippe. “Generalized Shields criterion for weakly cohesive granular materials.” In: *Physical Review Fluids* 5.3 (2020), p. 034308.

[59] GW Brunner. *HEC-RAS River Analysis System. Hydraulic User’s Manual. Version 1.0.* Tech. rep. Hydrologic Engineering Center Davis CA, 1995.

[60] W Cai, MJ Bora, S Pekkat, S Bordoloi, A Garg, and S Sekharan. “A new and simple model for predicting soil erosion based on hole erosion tests.” In: *Acta Geophysica* 71.2 (2023), pp. 823–836.

[61] AH Cardoso and R Bettess. “Effects of time and channel geometry on scour at bridge abutments.” In: *Journal of Hydraulic Engineering* 125.4 (1999), pp. 388–399.

[62] Cerema. *Analyse de risque des ponts en site affouillable*. Tech. rep. 2019.

[63] J Chabert. “Etude des affouillements autour des piles de ponts.” In: *Rep. Natl. Hydraul Lab., Chatou* (1956).

[64] WY Chang, LAI Jihn-Sung, YU Teng-Yi, LIN Franco, LEE Lung-Cheng, TSAI Whey-Fone, and LOH Chin-Hsiung. “Pier scour monitoring system by bed-level image tracking.” In: *International Journal of Sediment Research* 29.2 (2014), pp. 269–277.

[65] S Chaudhuri and K Debnath. “Observations on initiation of pier scour and equilibrium scour hole profiles in cohesive sediments.” In: *ISH Journal of Hydraulic Engineering* 19.1 (2013), pp. 27–37.

[66] S Chaudhuri, K Debnath, and G Oliveto. “A comparative study on equilibrium scour volume around circular cylinders in clay–sand mixed cohesive beds, at near threshold velocity of sand–an experimental approach.” In: *Water Supply* 22.8 (2022), pp. 6777–6791.

[67] S Chaudhuri, SK Singh, K Debnath, and MK Manik. “Pier scour within long contraction in cohesive sediment bed.” In: *Environmental Fluid Mechanics* 18 (2018), pp. 417–441.

[68] R Chavan and B Kumar. “Downward seepage effects on dynamics of scour depth and migrating dune-like bedforms at tandem piers.” In: *Canadian Journal of Civil Engineering* 47.1 (2020), pp. 13–24.

[69] HC Chen. “Numerical simulation of scour around complex piers in cohesive soil.” In: *First International Conference on Scour of Foundations. November 17-20, 2002, College Station, USA*. 2002, pp. 14–33.

[70] NP Cheremisinoff and SL Cheng. “Hydraulic Mechanics 2 Civil Engineering Practice.” In: *Technomic Published Company, Lancaster, Pennsylvania, USA* (1987).

[71] C Chevalier, D Pham Van Bang, E Durand, I Charles, and G Herrier. “Scour and erosion phenomena occurring in waterways–recent advances.” In: *Proc. 7th Int. Conf. Scour and Erosion (ICSE7, Perth, Australia)*. 2014, pp. 33–48.

[72] SU Choi and B Choi. “Prediction of time-dependent local scour around bridge piers.” In: *Water and Environment Journal* 30.1-2 (2016), pp. 14–21.

[73] S Chourasiya, PK Mohapatra, and S Tripathi. “Non-intrusive underwater measurement of mobile bottom surface.” In: *Advances in Water Resources* 104 (2017), pp. 76–88.

[74] MJ Crance and KM Frothingham. “The impact of ice cover roughness on stream hydrology.” In: *65th Eastern Snow Conference*. 2008, pp. 149–165.

[75] SH Crim Jr, F Parker Jr, JG Melville, JE Curry, and O Giiven. “Erosion Characteristics of Alabama Soils Obtained with the Erosion Function Apparatus and Correlations with Classification Properties.” In: *ALDOT Highway Research Centre, Project* (2003), pp. 930–490.

[76] P Dahal, D Peng, YL Yang, and H Sharif. “RSS based bridge scour measurement using underwater acoustic sensor networks.” In: *Communications and Network* 5.03 (2013), pp. 641–648.

[77] B Dargahi. “The turbulent flow field around a circular cylinder.” In: *Experiments in fluids* 8 (1989), pp. 1–12.

[78] B Dargahi. “Controlling mechanism of local scouring.” In: *Journal of Hydraulic Engineering* 116.10 (1990), pp. 1197–1214.

[79] S Das, R Midya, R Das, and A Mazumdar. “A study of wake vortex in the scour region around a circular pier.” In: *International Journal of Fluid Mechanics Research* 40.1 (2013).

[80] K Debnath and S Chaudhuri. “Bridge pier scour in clay-sand mixed sediments at near-threshold velocity for sand.” In: *Journal of Hydraulic Engineering* 136.9 (2010), pp. 597–609.

[81] K Debnath and S Chaudhuri. “Cohesive sediment erosion threshold: a review.” In: *ISH Journal of Hydraulic Engineering* 16.1 (2010), pp. 36–56.

[82] K Debnath and S Chaudhuri. “Laboratory experiments on local scour around cylinder for clay and clay–sand mixed beds.” In: *Engineering Geology* 111.1-4 (2010), pp. 51–61.

[83] K Debnath and S Chaudhuri. “Local scour around non-circular piers in clay–sand mixed cohesive sediment beds.” In: *Engineering geology* 151 (2012), pp. 1–14.

[84] K Debnath, V Nikora, and A Elliott. “Stream bank erosion: In situ flume tests.” In: *Journal of irrigation and drainage engineering* 133.3 (2007), pp. 256–264.

[85] S Dey. “Time-variation of scour in the vicinity of circular piers.” In: *Proceedings of the Institution of Civil Engineers-Water Maritime and Energy* 136.2 (1999), pp. 67–75.

[86] S Dey, SK Bose, and GLN Sastry. “Clear water scour at circular piers: a model.” In: *Journal of Hydraulic Engineering* 121.12 (1995), pp. 869–876.

[87] S Dey, A Helkjær, BM Sumer, and J Fredsøe. “Scour at vertical piles in sand-clay mixtures under waves.” In: *Journal of waterway, port, coastal, and ocean engineering* 137.6 (2011), pp. 324–331.

[88] S Dey and RV Raikar. “Characteristics of horseshoe vortex in developing scour holes at piers.” In: *Journal of Hydraulic Engineering* 133.4 (2007), pp. 399–413.

[89] R Diab, O Link, and U Zanke. “Geometry of developing and equilibrium scour holes at bridge piers in gravel.” In: *Canadian Journal of Civil Engineering* 37.4 (2010), pp. 544–552.

[90] RMAEA Diab. *Experimental investigation on scouring around piers of different shape and alignment in gravel*. Tu Darmstadt, 2011.

[91] HA Einstein. *The bed-load function for sediment transportation in open channel flows*. 1026. US Department of Agriculture, 1950.

[92] IH Elsebaie. "An experimental study of local scour around circular bridge pier in sand soil." In: *International Journal of Civil & Environmental Engineering IJCEE-IJENS* 13.01 (2013), pp. 23–28.

[93] B Etkin and HS Ribner. "Canadian research in aerodynamic noise." In: *UTIA Review, No. 13* (1958).

[94] R Ettema. "Scour at bridge piers (phd thesis)." In: *The University of Auckland, Auckland* (1980).

[95] R Ettema, BW Melville, and B Barkdoll. "Scale effect in pier-scour experiments." In: *Journal of Hydraulic Engineering* 124.6 (1998), pp. 639–642.

[96] R Ettema, BW Melville, and G Constantinescu. *Evaluation of bridge scour research: Pier scour processes and predictions*. Citeseer, 2011.

[97] R Ettema, T Nakato, and MVI Muste. *An illustrated guide for monitoring and protecting bridge waterways against scour*. Tech. rep. IIHR-Hydroscience & Engineering, University of Iowa, 2006.

[98] B Ettmer, F Orth, and O Link. "Live-bed scour at bridge piers in a lightweight polystyrene bed." In: *Journal of Hydraulic Engineering* 141.9 (2015), p. 04015017.

[99] CMS Fael, G Simarro-Grande, JP Martín-Vide, and AH Cardoso. "Local scour at vertical-wall abutments under clear-water flow conditions." In: *Water Resources Research* 42.10 (2006).

[100] R Fernandez Luque and R Van Beek. "Erosion and transport of bed-load sediment." In: *Journal of hydraulic research* 14.2 (1976), pp. 127–144.

[101] M Fisher, MN Chowdhury, AA Khan, and S Atamturktur. "An evaluation of scour measurement devices." In: *Flow Measurement and Instrumentation* 33 (2013), pp. 55–67.

[102] E Florens. "Couche limite turbulente dans les écoulements à surface libre: étude expérimentale d'effets de macro-rugosités." PhD thesis. Toulouse 3, 2010.

[103] E Foti, IC Rabionet, A Marini, RE Musumeci, and A Sánchez-Arcilla. "Experimental investigations of the bed evolution in wave flumes: Performance of 2D and 3D optical systems." In: *Coastal Engineering* 58.7 (2011), pp. 606–622.

[104] GA Fox, L Guertault, C Castro-Bolinaga, P Allen, KA Bigham, S Bonelli, SL Hunt, K Kassa, EJ Langendoen, E Porter, et al. "Perspective: Lessons learned, challenges, and opportunities in quantifying cohesive soil erodibility with the jet erosion test (JET)." In: (2022).

[105] J Fredsoe and BM Sumer. *Hydrodynamics around cylindrical structures (revised edition)*. Vol. 26. World Scientific, 2006.

[106] DC Froehlich. "Analysis of onsite measurements of scour at piers." In: *Hydraulic engineering: proceedings of the 1988 national conference on hydraulic engineering*. 1988, pp. 534–539.

[107] RJ Garde and KGR Raju. *Mechanics of sediment transportation and alluvial stream problems*. Taylor & Francis, 2000.

[108] D Girardeau-Montaut. "Détection de changement sur des données géométriques tridimensionnelles." PhD thesis. Télécom ParisTech, 2006.

[109] RC Grabowski, IG Droppo, and G Wharton. "Erodibility of cohesive sediment: The importance of sediment properties." In: *Earth-Science Reviews* 105.3-4 (2011), pp. 101–120.

[110] WH Graf and I Istiarto. "Flow pattern in the scour hole around a cylinder." In: *Journal of Hydraulic Research* 40.1 (2002), pp. 13–20.

[111] D Guan, YM Chiew, M Wei, and S Hsieh. "Characterization of horseshoe vortex in a developing scour hole at a cylindrical bridge pier." In: *International journal of sediment research* 34.2 (2019), pp. 118–124.

[112] R Gudavalli. *Prediction model for scour rate around bridge piers in cohesive soil on the basis of flume tests*. Texas A&M University, 1997.

[113] J Guo. "Pier scour in clear water for sediment mixtures." In: *Journal of hydraulic research* 50.1 (2012), pp. 18–27.

[114] M Gupta and N Nakhate. "A geometric perspective on structured light coding." In: *Proceedings of the European Conference on Computer Vision (ECCV)*. 2018, pp. 87–102.

[115] O Güven, JG Melville, JE Curry, and SH Crim Jr. "Observations and Evaluations of Scour at Two Bridge Sites with Cohesive Soils." In: *Erosion of Soils and Scour of Foundations*. 2005, pp. 1–13.

[116] I Haghighi, C Chevalier, M Duc, S Guédon, and P Reiffsteck. "Improvement of hole erosion test and results on reference soils." In: *Journal of Geotechnical and Geoenvironmental Engineering* 139.2 (2013), pp. 330–339.

[117] DB Hains. *An experimental study of ice effects on scour at bridge piers*. Lehigh University, 2004.

[118] JM Harris and RJS Whitehouse. "Marine scour: Lessons from nature's laboratory." In: *Scour* 766 (2014), p. 19.

[119] PA Hartvig, JMC Thomsen, P Frigaard, and TL Andersen. "Experimental study of the development of scour and backfilling." In: *Coastal Engineering Journal* 52.02 (2010), pp. 157–194.

[120] ZF Hassan, IR Karim, and AK Al-Shukur. "Effect of interaction between bridge piers on local scouring in cohesive soils." In: *Civil Engineering Journal* 6.4 (2020), pp. 659–669.

[121] T Hoshino and H Yasuda. "3D measurement of water and bed surface profiles during formation of sand waves with moving optical cutting method." In: *Proc. 9th Symposium on River, Coastal and Estuarine Morphodynamic (RCEM), Iquitos*. CREAR Lima. 2015.

[122] R Jain, AS Lodhi, G Oliveto, and M Pandey. “Influence of cohesion on scour at piers founded in clay–sand–gravel mixtures.” In: *Journal of Irrigation and Drainage Engineering* 147.10 (2021), p. 04021046.

[123] SUI Jueyi, WANG Jun, HE Yun, and KROL Faye. “Velocity profiles and incipient motion of frazil particles under ice cover.” In: *International Journal of Sediment Research* 25.1 (2010), pp. 39–51.

[124] JW Kamphuis and KR Hall. “Cohesive material erosion by unidirectional current.” In: *Journal of Hydraulic Engineering* 109.1 (1983), pp. 49–61.

[125] N Karimi, M Heidarnejad, and A Masjedi. “Scour depth at inclined bridge piers along a straight path: A laboratory study.” In: *Engineering science and technology, an international journal* 20.4 (2017), pp. 1302–1307.

[126] T Kawamura, M Hiwada, T Hibino, I Mabuchi, and M Kumada. “Flow around a finite circular cylinder on a flat plate: Cylinder height greater than turbulent boundary layer thickness.” In: *Bulletin of JSME* 27.232 (1984), pp. 2142–2151.

[127] A Khanal, GA Fox, and AT Al-Madhhachi. “Variability of erodibility parameters from laboratory mini jet erosion tests.” In: *Journal of Hydrologic Engineering* 21.10 (2016), p. 04016030.

[128] KT Kho, E Valentine, and S Glendinning. “An experimental study of local scour around circular bridge piers in cohesive soils.” In: *Proceedings 2nd International Conference on Scour and Erosion (ICSE-2). November 14.–17., 2004, Singapore*. 2004.

[129] G Kirkil, SG Constantinescu, and R Ettema. “Coherent structures in the flow field around a circular cylinder with scour hole.” In: *Journal of Hydraulic Engineering* 134.5 (2008), pp. 572–587.

[130] K Koca, C Noss, C Anlanger, A Brand, and A Lorke. “Performance of the Vectrino Profiler at the sediment–water interface.” In: *Journal of Hydraulic Research* 55.4 (2017), pp. 573–581.

[131] MJ Koob, JM Hanson, PW Deming, JP Gould, and P Edinger. “Collapse of the thruway bridge at Schoharie Creek.” In: *Final Rep. by Wiss, Janney, Elstner, and Associates and Mueser Rutledge Consulting Engineers* (1987).

[132] UC Kothyari and RK Jain. “Influence of cohesion on the incipient motion condition of sediment mixtures.” In: *Water resources research* 44.4 (2008).

[133] UC Kothyari, A Kumar, and RK Jain. “Influence of cohesion on river bed scour in the wake region of piers.” In: *Journal of Hydraulic Engineering* 140.1 (2014), pp. 1–13.

[134] S Krajnović. “Flow around a tall finite cylinder explored by large eddy simulation.” In: *Journal of Fluid Mechanics* 676 (2011), pp. 294–317.

[135] BG Krishnappan. “Laboratory verification of turbulent flow model.” In: *Journal of hydraulic engineering* 110.4 (1984), pp. 500–514.

[136] RA Kuhnle, CV Alonso, and FD Shields. “Geometry of scour holes associated with 90 spur dikes.” In: *Journal of Hydraulic Engineering* 125.9 (1999), pp. 972–978.

[137] V Kumar, KGR Raju, and N Vittal. “Reduction of local scour around bridge piers using slots and collars.” In: *Journal of hydraulic engineering* 125.12 (1999), pp. 1302–1305.

[138] K Kwak. *Prediction of scour depth versus time for bridge piers in cohesive soils in the case of multi-flood and multi-layer soil systems*. Texas A&M University, 2000.

[139] K Kwak, JL Briaud, Y Cao, M Chung, B Hunt, and S Davis. “Pier scour at Woodrow Wilson Bridge and SRICOS method.” In: *First International Conference on Scour of Foundations. November 17-20, 2002, College Station, USA*. 2002, pp. 227–241.

[140] K Kwak, JL Briaud, and HC Chen. “SRICOS: Computer program for bridge pier scour.” In: *International Conference on soil mechanics and geotechnical engineering*. 2001, pp. 2235–2238.

[141] J Lacey, J Duguay, and B MacVicar. “Comparison of velocity and turbulence profiles obtained with a Vectrino Profiler and PIV.” In: *E3S Web of Conferences*. Vol. 40. EDP Sciences. 2018, p. 05070.

[142] F Lachaussée. “Érosion et transport de particules au voisinage d’un obstacle.” PhD thesis. Université Paris-Saclay, 2018.

[143] F Lachaussée, Y Bertho, C Morize, A Sauret, and P Gondret. “Competitive dynamics of two erosion patterns around a cylinder.” In: *Physical Review Fluids* 3.1 (2018), p. 012302.

[144] PF Lagasse, JD Schall, F Johnson, EV Richardson, F Chang, et al. *Stream stability at highway structures.* Tech. rep. United States. Federal Highway Administration. Office of Technology Applications, 1995.

[145] D Lague, N Brodu, and J Leroux. “Accurate 3D comparison of complex topography with terrestrial laser scanner: Application to the Rangitikei canyon (NZ).” In: *ISPRS journal of photogrammetry and remote sensing* 82 (2013), pp. 10–26.

[146] RM Lança, CS Fael, and AH Cardoso. “Assessing equilibrium clear water scour around single cylindrical piers.” In: *River Flow 2010* (2010), pp. 1207–1213.

[147] RM Lança, CS Fael, RJ Maia, JP Pêgo, and AH Cardoso. “Clear-water scour at comparatively large cylindrical piers.” In: *Journal of Hydraulic Engineering* 139.11 (2013), pp. 1117–1125.

[148] MN Landers and DS Mueller. *Channel scour at bridges in the United States*. Tech. rep. 1996.

[149] F Larrarte, F Schmidt, E Durand, A Bontemps, Y Della Longa, M Cheetham, S de La Roque, M Hosseingholian, and C Chevalier. “A French experience of Structural Health Monitoring of scour affecting river infrastructures.” In: *PIANC-Smart Rivers 2019*. 2019, 3p.

[150] EM Laursen and A Toch. *Scour around bridge piers and abutments*. Vol. 4. Iowa Highway Research Board Ames, IA, 1956.

[151] JW Lavelle, HO Mofjeld, and ET Baker. “An in situ erosion rate for a fine-grained marine sediment.” In: *Journal of Geophysical Research: Oceans* 89.C4 (1984), pp. 6543–6552.

[152] SS Li. "Estimates of the Manning's coefficient for ice-covered rivers." In: *Proceedings of the Institution of Civil Engineers-Water Management*. Vol. 165. 9. Thomas Telford Ltd. 2012, pp. 495–505.

[153] Y Li. *Bridge pier scour and contraction scour in cohesive soils on the basis of flume tests*. Texas A&M University, 2002.

[154] O Link, C Gobert, M Manhart, and U Zanke. "Effect of the horseshoe vortex system on the geometry of a developing scour hole at a cylinder." In: *Proceedings 4th International Conference on Scour and Erosion (ICSE-4). November 5-7, 2008, Tokyo, Japan*. 2008, pp. 162–168.

[155] O Link, C González, M Maldonado, and C Escauriaza. "Coherent structure dynamics and sediment particle motion around a cylindrical pier in developing scour holes." In: *Acta Geophysica* 60 (2012), pp. 1689–1719.

[156] O Link, K Klischies, G Montalva, and S Dey. "Effects of bed compaction on scour at piers in sand-clay mixtures." In: *Journal of Hydraulic Engineering* 139.9 (2013), pp. 1013–1019.

[157] O Link, F Pfleger, and U Zanke. "Characteristics of developing scour-holes at a sand-embedded cylinder." In: *International Journal of Sediment Research* 23.3 (2008), pp. 258–266.

[158] Q Liu, H Tang, and H Wang. "TOPOGRAPHIC EVOLUTION OF SCOUR HOLE AROUND A CYLINDRICAL PIER: AN EXPERIMENTAL INVESTIGATION." In: *E-proceedings of the 38th IAHR World Congress, September 1-6, 2019, Panama City, Panama*. 2019, pp. 2564–2573.

[159] Z Liu. *Sediment Transport*. English. 1st ed. Aalborg Universitet, 2001, pp. 54–56.

[160] JY Lu, ZZ Shi, JH Hong, JJ Lee, and RV Raikar. "Temporal variation of scour depth at nonuniform cylindrical piers." In: *Journal of Hydraulic Engineering* 137.1 (2011), pp. 45–56.

[161] X Lyu, Y Cheng, W Wang, H An, and Y Li. "Experimental study on local scour around submerged monopile under combined waves and current." In: *Ocean Engineering* 240 (2021), p. 109929.

[162] L Ma, L Wang, Z Guo, H Jiang, and Y Gao. "Time development of scour around pile groups in tidal currents." In: *Ocean Engineering* 163 (2018), pp. 400–418.

[163] B Mahalder, JS Schwartz, AM Palomino, and J Zirkle. "Scour Hole Development in Natural Cohesive Bed Sediment around Cylinder-Shaped Piers Subjected to Varying Sequential Flow Events." In: *Water* 13.22 (2021), p. 3289.

[164] C Manes and M Brocchini. "Local scour around structures and the phenomenology of turbulence." In: *Journal of Fluid Mechanics* 779 (2015), pp. 309–324.

[165] DJ McGovern, S Ilic, AM Folkard, SJ McLelland, and BJ Murphy. "Time development of scour around a cylinder in simulated tidal currents." In: *Journal of Hydraulic Engineering* 140.6 (2014), p. 04014014.

[166] BW Melville. "Local scour at bridge sites." PhD thesis. researchspace@ auckland, 1975.

[167] BW Melville and YM Chiew. “Time scale for local scour at bridge piers.” In: *Journal of Hydraulic Engineering* 125.1 (1999), pp. 59–65.

[168] BW Melville and S E Coleman. *Bridge scour*. Water Resources Publication, 2000.

[169] BW Melville and AJ Sutherland. “Design method for local scour at bridge piers.” In: *Journal of Hydraulic Engineering* 114.10 (1988), pp. 1210–1226.

[170] E Meyer-Peter and R Müller. “Formulas for bed-load transport.” In: *IAHSR 2nd meeting, Stockholm, appendix 2*. IAHR. 1948.

[171] MF Mia and H Nago. “Design method of time-dependent local scour at circular bridge pier.” In: *Journal of Hydraulic Engineering* 129.6 (2003), pp. 420–427.

[172] H Mitchener and H Torfs. “Erosion of mud/sand mixtures.” In: *Coastal engineering* 29.1-2 (1996), pp. 1–25.

[173] A Molinas and MM Hosni. *Effects of gradation and cohesion on bridge scour: Volume 4: Experimental study of scour around circular piers in cohesive soils*. Tech. rep. Turner-Fairbank Highway Research Center, 1999.

[174] LF Moody. “Friction factors for pipe flow.” In: *Trans. Asme* 66 (1944), pp. 671–684.

[175] DK Muschenheim, J Grant, and EL Mills. “Flumes for benthic ecologists: theory, construction and practice.” In: *Mar. Ecol. Prog. Ser* 28 (1986), pp. 185–196.

[176] M Muste, F Braileanu, and R Ettema. “Flow and sediment transport measurements in a simulated ice-covered channel.” In: *Water Resources Research* 36.9 (2000), pp. 2711–2720.

[177] M Muzzammil, J Alama, and M Danish. “Scour prediction at bridge piers in cohesive bed using gene expression programming.” In: *Aquatic Procedia* 4 (2015), pp. 789–796.

[178] M Muzzammil and T Gangadhariah. “The mean characteristics of horseshoe vortex at a cylindrical pier.” In: *Journal of Hydraulic Research* 41.3 (2003), pp. 285–297.

[179] S Nagarajan and M Arockiasamy. *Non-Contact Scour Monitoring System for Railroad Bridges*. Tech. rep. 2020.

[180] S Nagarajan, M Arockiasamy, et al. “Non-Contact Scour Monitoring for Highway Bridges.” In: (2020).

[181] M Najafzadeh and GA Barani. “Experimental study of local scour around a vertical pier in cohesive soils.” In: *Scientia Iranica* 21.2 (2014), pp. 241–250.

[182] MR Namaee. “Experimental and Numerical Study of Local Scour Around Side-by-side Bridge Piers Under Ice-covered Conditions.” PhD thesis. University of Northern British Columbia, 2019.

[183] AW Niedoroda and C Dalton. “A review of the fluid mechanics of ocean scour.” In: *Ocean Engineering* 9.2 (1982), pp. 159–170.

[184] P Nielsen. *Coastal and estuarine processes*. Vol. 29. World Scientific Publishing Company, 2009.

[185] FN Nnadi and KC Wilson. “Motion of contact-load particles at high shear stress.” In: *Journal of Hydraulic Engineering* 118.12 (1992), pp. 1670–1684.

[186] Nortek. *MIDAS Data Acquisition Software: Software User Guide*. 2015.

[187] Nortek. *The Comprehensive Manual for Velocimeters*. Technical Report, 2018. Available online: https://support. nortekgroup.com . . . 2018.

[188] NortekAs. *Vectrino profiler*. Available at : http://www.nortek-as.com/en/products/velocimeters/vectrino-ii.

[189] PY Nurtjahyo. *Chimera RANS simulations of pier scour and contraction scour in cohesive soils*. Texas A&M University, 2003.

[190] SJ Oh. *Experimental study of bridge scour in cohesive soil*. Vol. 71. 03. 2009.

[191] G Oliveto and WH Hager. "Temporal evolution of clear-water pier and abutment scour." In: *Journal of Hydraulic Engineering* 128.9 (2002), pp. 811–820.

[192] G Oliveto and WH Hager. "Further results to time-dependent local scour at bridge elements." In: *Journal of Hydraulic Engineering* 131.2 (2005), pp. 97–105.

[193] S Pagliara and I Carnacina. "Scour and dune morphology in presence of large wood debris accumulation at bridge pier." In: *River Flow*. Vol. 2. 2010, pp. 1223–1230.

[194] G Palau-Salvador, T Stoesser, J Fröhlich, M Kappler, and W Rodi. "Large eddy simulations and experiments of flow around finite-height cylinders." In: *Flow, turbulence and combustion* 84 (2010), pp. 239–275.

[195] TM Parchure and AJ Mehta. "Erosion of soft cohesive sediment deposits." In: *Journal of Hydraulic Engineering* 111.10 (1985), pp. 1308–1326.

[196] E Partheniades. "Erosion and deposition of cohesive soils." In: *Journal of the Hydraulics Division* 91.1 (1965), pp. 105–139.

[197] RJ Pattenden, SR Turnock, and X Zhang. "Measurements of the flow over a low-aspect-ratio cylinder mounted on a ground plane." In: *Experiments in Fluids* 39 (2005), pp. 10–21.

[198] H Persillon and M Braza. "Physical analysis of the transition to turbulence in the wake of a circular cylinder by three-dimensional Navier–Stokes simulation." In: *Journal of Fluid Mechanics* 365 (1998), pp. 23–88.

[199] TU Petersen, BM Sumer, and J Fredsøe. "Time scale of scour around a pile in combined waves and current." In: *International Conference on Coastal Engineering*. Vol. 30. 2012, p. 08.

[200] Pierre Fitou Photo NR. *La Nouvelle Republique : Il y a quarante ans le pont Wilson à Tours s'effondrait*. Available at : https://www.lanouvellerepublique.fr/tours/il-y-a-quarante-ans-le-pont-wilson-a-tours-s-effondrait.

[201] Photoneo. *PhoXi 3D Scanner S Datasheet*. Available at : https://www.photoneo.com/products/phoxi-scan-s/.

[202] D Poggi and NO Kudryavtseva. "Non-intrusive underwater measurement of local scour around a bridge pier." In: *Water* 11.10 (2019), p. 2063.

[203] K Porter, R Simons, and J Harris. "Comparison of three techniques for scour depth measurement: photogrammetry, echosounder profiling and a calibrated pile." In: *Coastal Engineering Proceedings* 34 (2014), pp. 64–64.

[204] H Postma. "Sediment transport and sedimentation in the estuarine environment." In: *American Association of Advanced Sciences* 83 (1967), pp. 158–179.

[205] WG Qi and FP Gao. "Physical modeling of local scour development around a large-diameter monopile in combined waves and current." In: *Coastal Engineering* 83 (2014), pp. 72–81.

[206] YD Rajendra, SC Mehrotra, KV Kale, RR Manza, RK Dhumal, AD Nagne, and AD Vibhute. "Evaluation of Partially Overlapping 3D Point Cloud's Registration by using ICP variant and CloudCompare." In: *The International Archives of the Photogrammetry, Remote Sensing and Spatial Information Sciences* 40 (2014), pp. 891–897.

[207] RD Raju, S Nagarajan, M Arockiasamy, and S Castillo. "Feasibility of Using Green Laser in Monitoring Local Scour around Bridge Pier." In: *Geomatics* 2.3 (2022), pp. 355–369.

[208] VS Ramachandran, KP Kacker, and NK Patwardhan. "Adsorption of dyes by clay minerals." In: *American Mineralogist* 47.1-2 (Feb. 1962), pp. 165–169.

[209] M Rambabu, S Narasimha Rao, and V Sundar. "Current-induced scour around a vertical pile in cohesive soil." In: *Ocean Engineering* 30.7 (2003), pp. 893–920.

[210] AJ Raudkivi. "Loose boundary hydraulics, Balkema, Rotterdam." In: *The Netherland* (1998).

[211] AJ Raudkivi and R Ettema. "Clear-water scour at cylindrical piers." In: *Journal of hydraulic engineering* 109.3 (1983), pp. 338–350.

[212] JS Ribberink. "Bed-load transport for steady flows and unsteady oscillatory flows." In: *Coastal Engineering* 34.1-2 (1998), pp. 59–82.

[213] A Rieux, P Weill, D Mouaze, C Poirier, F Nechenache, L Perez, and B Tessier. "Threshold of motion and settling velocities of mollusc shell debris: Influence of faunal composition." In: *Sedimentology* 66.3 (2018), pp. 895–916.

[214] I Rifai, V Schmitz, S Erpicum, P Archambeau, D Violeau, M Pirotton, B Dewals, and K El Kadi Abderrezzak. "Continuous monitoring of fluvial dike breaching by a laser profilometry technique." In: *Water Resources Research* 56.10 (2020), e2019WR026941.

[215] LC van Rijn. "Erodibility of mud–sand bed mixtures." In: *Journal of Hydraulic Engineering* 146.1 (2020), p. 04019050.

[216] A Rogers, C Manes, and T Tsuzaki. "Measuring the geometry of a developing scour hole in clear-water conditions using underwater sonar scanning." In: *International Journal of Sediment Research* 35.1 (2020), pp. 105–114.

[217] A Roulund, BM Sumer, J Fredsøe, and J Michelsen. "Numerical and experimental investigation of flow and scour around a circular pile." In: *Journal of Fluid mechanics* 534 (2005), pp. 351–401.

[218] B Ruonan, C Liekai, W Xingkui, and L Danxun. "Comparison of ADV and PIV measurements in open channel flows." In: *Procedia Engineering* 154 (2016), pp. 995–1001.

[219] K Sarkar, C Chakraborty, and BS Mazumder. "Variations of bed elevations due to turbulence around submerged cylinder in sand beds." In: *Environmental Fluid Mechanics* 16 (2016), pp. 659–693.

[220] F Scarano and C Poelma. "Three-dimensional vorticity patterns of cylinder wakes." In: *Experiments in fluids* 47 (2009), pp. 69–83.

[221] RJ Schindler, S Stripling, RJS Whitehouse, and JM Harris. "The influence of physical cohesion on scour around a monopile." In: *Proc., 8th Int. Conf. on Scour and Erosion, J. Harris, R. Whitehouse, and S. Moxon, CRC, Boca Raton, FL*. 2016, pp. 325–334.

[222] I Shafii. "Relationship between erodibility and properties of soils." PhD thesis. 2018.

[223] I Shafii, JL Briaud, H Chen, and A Shidlovskaya. "Relationship between soil erodibility and engineering properties." In: (2016).

[224] I Shafii, Z Medina-Cetina, A Shidlovskaya, and JL Briaud. "Relationship between Soil Erodibility and Soil Properties." In: *Journal of Geotechnical and Geoenvironmental Engineering* 149.1 (2023), p. 04022121.

[225] HW Shen, VR Schneider, and S Karaki. "Local scour around bridge piers." In: *Journal of the Hydraulics Division* 95.6 (1969), pp. 1919–1940.

[226] DM Sheppard. *LARGE SCALE AND LIVE BED LOCAL PIER SCOUR EXPERIMENTS. PHASE 1: LARGE SCALE, CLEARWATER SCOUR EXPERIMENTS*. Tech. rep. 2003.

[227] DM Sheppard. *LARGE SCALE AND LIVE BED LOCAL PIER SCOUR EXPERIMENTS. PHASE 2: LIVE BED EXPERIMENTS*. Tech. rep. 2003.

[228] DM Sheppard, B Melville, and H Demir. "Evaluation of existing equations for local scour at bridge piers." In: *Journal of Hydraulic Engineering* 140.1 (2014), pp. 14–23.

[229] DM Sheppard and W Miller Jr. "Live-bed local pier scour experiments." In: *Journal of Hydraulic Engineering* 132.7 (2006), pp. 635–642.

[230] DM Sheppard, M Odeh, and T Glasser. "Large scale clear-water local pier scour experiments." In: *Journal of Hydraulic Engineering* 130.10 (2004), pp. 957–963.

[231] A Shields. "Anwendung der Aehnlichkeitsmechanik und der Turbulenzforschung auf die Geschiebebewegung." In: *PhD Thesis Technical University Berlin* (1936).

[232] AM Shirole and RC Holt. "Planning for a comprehensive bridge safety assurance program." In: *Transportation Research Record* 1290 (1991), pp. 39–50.

[233] G Simarro, CMS Fael, and A Cardoso. "Estimating equilibrium scour depth at cylindrical piers in experimental studies." In: *Journal of Hydraulic Engineering* 137.9 (2011), pp. 1089–1093.

[234] DAB Sirianni, C Valela, CD Rennie, I Nistor, and H Almansour. "Effects of developing ice covers on bridge pier scour." In: *Journal of Hydraulic Research* 60.4 (2022), pp. 645–655.

[235] JFA Sleath. *Sea Bed Mechanics*. Wiley, New York, 1984.

[236] R Soulsby. *Dynamics of marine sands*. T. Telford London, UK, 1997.

[237] BM Spears, JE Saunders, I Davidson, and DM Paterson. "Microalgal sediment biostabilisation along a salinity gradient in the Eden Estuary, Scotland: unravelling a paradox." In: *Marine and Freshwater Research* 59.4 (2008), pp. 313–321.

[238] EM Strange. "Monitoring survey of heritage listed fencing using terrestrial laser scanners and CloudCompare software." In: (2019).

[239] TD Straub and TM Over. *Pier and contraction scour prediction in cohesive soils at selected bridges in Illinois*. Tech. rep. Illinois Center for Transportation, 2010.

[240] V Strouhal. *Über eine besondere Art der Tonerregung*. Stahel, 1878.

[241] BM Sumer, N Christiansen, and J Fredsøe. "Influence of cross section on wave scour around piles." In: *Journal of waterway, port, coastal, and ocean engineering* 119.5 (1993), pp. 477–495.

[242] BM Sumer, J Fredsøe, and N Christiansen. "Scour around vertical pile in waves." In: *Journal of waterway, port, coastal, and ocean engineering* 118.1 (1992), pp. 15–31.

[243] BM Sumer, TU Petersen, L Locatelli, J Fredsøe, RE Musumeci, and E Foti. "Backfilling of a scour hole around a pile in waves and current." In: *Journal of Waterway, Port, Coastal, and Ocean Engineering* 139.1 (2013), pp. 9–23.

[244] BM Sumer et al. *The mechanics of scour in the marine environment*. World Scientific, 2002.

[245] D Sumner, JL Heseltine, and OJP Dansereau. "Wake structure of a finite circular cylinder of small aspect ratio." In: *Experiments in Fluids* 37 (2004), pp. 720–730.

[246] S Tanaka and S Murata. "An investigation of the wake structure and aerodynamic characteristics of a finite circular cylinder: time-averaged wake structures behind circular cylinders with various aspect ratios." In: *JSME International Journal Series B Fluids and Thermal Engineering* 42.2 (1999), pp. 178–187.

[247] F Ternat, P Boyer, F Anselmet, and M Amielh. "Erosion threshold of saturated natural cohesive sediments: Modeling and experiments." In: *Water resources research* 44.11 (2008).

[248] Q Tian, KT Lowe, and RL Simpson. "A laser-based optical approach for measuring scour depth around hydraulic structures." In: *Scour and Erosion*. 2010, pp. 787–796.

[249] FCK Ting, JL Briaud, HC Chen, R Gudavalli, S Perugu, and G Wei. "Flume tests for scour in clay at circular piers." In: *Journal of hydraulic engineering* 127.11 (2001), pp. 969–978.

[250] FCK Ting, AL Jones, RJ Larsen, et al. *Evaluation of SRICOS method on cohesive soils in South Dakota*. Tech. rep. South Dakota. Dept. of Transportation. Office of Research, 2008.

[251] S Umeda. "Scour regime and scour depth around a pile in waves." In: *Journal of Coastal Research* (2011), pp. 845–849.

[252] S Umeda, T Yamazaki, and H Ishida. "Time evolution of scour and deposition around a cylindrical pier in steady flow." In: *Proceedings 4th International Conference on Scour and Erosion (ICSE-4). November 5-7, 2008, Tokyo, Japan*. 2008, pp. 140–146.

[253] J Unger and WH Hager. "Down-flow and horseshoe vortex characteristics of sediment embedded bridge piers." In: *Experiments in Fluids* 42 (2007), pp. 1–19.

[254] C Valela, DAB Sirianni, I Nistor, CD Rennie, and H Almansour. "Bridge pier scour under ice cover." In: *Water* 13.4 (2021), p. 536.

[255] T Von Karman. "Über den Mechanismus des Widerstandes, den ein bewegter Körper in einer Flüssigkeit erfährt." In: *Nachrichten von der Gesellschaft der Wissenschaften zu Göttingen, Mathematisch-Physikalische Klasse* 1911 (1911), pp. 509–517.

[256] CF Wan and R Fell. "Investigation of rate of erosion of soils in embankment dams." In: *Journal of geotechnical and geoenvironmental engineering* 130.4 (2004), pp. 373–380.

[257] C Wang, X Yu, and F Liang. "A review of bridge scour: mechanism, estimation, monitoring and countermeasures." In: *Natural Hazards* 87 (2017), pp. 1881–1906.

[258] J Wang. *The SRICOS-EFA method for complex pier and contraction scour*. Texas A&M University, 2004.

[259] J Wang, J Sui, and BW Karney. "Incipient motion of non-cohesive sediment under ice cover—An experimental study." In: *Journal of Hydrodynamics* 20.1 (2008), pp. 117–124.

[260] G Wei. "Numerical simulation of scour process around bridge piers in cohesive soil." PhD thesis. Texas A&M University, 1997.

[261] R Whitehouse. *Scour at marine structures: A manual for practical applications*. Thomas Telford, 1998.

[262] JC Winterwerp and WGM Van Kesteren. *Introduction to the physics of cohesive sediment dynamics in the marine environment*. Elsevier, 2004.

[263] P Wu, R Balachandar, and J Sui. "Local scour around bridge piers under ice-covered conditions." In: *Journal of Hydraulic Engineering* 142.1 (2016), p. 04015038.

[264] O Yagci, I Yildirim, MF Celik, V Kitsikoudis, Z Duran, and VSO Kirca. "Clear water scour around a finite array of cylinders." In: *Applied Ocean Research* 68 (2017), pp. 114–129.

[265] H Yang, M Omidalizarandi, X Xu, and I Neumann. "Terrestrial laser scanning technology for deformation monitoring and surface modeling of arch structures." In: *Composite Structures* 169 (2017), pp. 173–179.

[266] AM Yanmaz and HD Altinbilek. "Study of time-depenbent local scour around bridge piers." In: *Journal of Hydraulic Engineering* 117.10 (1991), pp. 1247–1268.

[267] C Yao, JL Briaud, and P Gardoni. "LRFD Calibration of Bridge Foundations Subjected to Scour." In: *Geo-Congress 2014: Geo-characterization and Modeling for Sustainability*. 2014, pp. 890–899.

[268] M Yilmaz, AM Yanmaz, and M Koken. "Clear-water scour evolution at dual bridge piers." In: *Canadian Journal of Civil Engineering* 44.4 (2017), pp. 298–307.

[269] BD Younkin and DF Hill. “Rapid profiling of an evolving bed form using planar laser sheet illumination.” In: *Journal of Hydraulic Engineering* 135.10 (2009), pp. 852–856.

[270] LJ Zabilansky. *Ice force and scour instrumentation for the White River, Vermont.* Tech. rep. COLD REGIONS RESEARCH and ENGINEERING LAB HANOVER NH, 1996.

[271] LJ Zabilansky, DB Hains, and JI Remus. “Increased bed erosion due to ice.” In: *Current Practices in Cold Regions Engineering*. 2006, pp. 1–12.

[272] W Zhang, MU Zapata, X Bai, D Pham-Van-Bang, and KD Nguyen. “Three-dimensional simulation of horseshoe vortex and local scour around a vertical cylinder using an unstructured finite-volume technique.” In: *International Journal of Sediment Research* 35.3 (2020), pp. 295–306.

[273] M Zhao, L Cheng, and Z Zang. “Experimental and numerical investigation of local scour around a submerged vertical circular cylinder in steady currents.” In: *Coastal Engineering* 57.8 (2010), pp. 709–721.

[274] M Zhao, X Zhu, L Cheng, and B Teng. “Experimental study of local scour around subsea caissons in steady currents.” In: *Coastal Engineering* 60 (2012), pp. 30–40.

[275] Photoneo s.r.o. *PhoXi Control 1.10 - User Manual*. Available at : https://www.photoneo.com/downloads/phoxi-control/. 2023.

List of Figures

List of Tables

Abstract

Local scour is considered to be one of the main causes of bridge failure and collapse. Laboratory experiments are a crucial and important approach for the scour process investigation. Yet, there is no robust and standard instrumentation for tracking the evolution of this physical phenomenon in laboratory studies. There are several flume-based studies of scour around a circular bridge pier on cohesionless soil. However, the bed of natural alluvial channels often contains cohesive sediments. Comparatively, there is a limited research on local scour around circular pier founded in cohesive beds that has been documented. In this PhD research, a 3D Laser Scanner is used to monitor scour around a circular pier. The results obtained with this technique, in line with previous research, in particular that carried out on a sandy bed, demonstrate its effectiveness. The technique offers advantages such as continuous spatiotemporal monitoring, but also many limitations. In a next step, the study focused on the effect of the type and proportion of fines in the sediment mixture on the depth and the shape of the scour hole and the temporal propagation of scour process around a circular pier. Results show that increasing the clay in the fine fraction reduce significantly the scour. The mixture with a range around 7.5-10 % of clay fines content provides the threshold composition for coherent soil behavior in scouring process. In addition, scour depth prediction for bridge piers in cohesive soil is not yet fully developed. In engineering practice, scour depth estimation methods currently used are those proposed for sand bed. Many researches aimed to adress a method to optimize the design of bridge piers in the case of cohesive soil. Among the different methods, the one based on the use of the EFA (Erosion Function Apparatus) erodimeter and called SRICOS (Scour Rate In COhesive Soil) was examined as part of this work in order to predict the deepest scour in cohesive bed.

Keywords: Local Scour, 3D Scanner Laser, Cohesive bed, SRICOS-EFA

Résumé

L’affouillement local autour des piles est considéré comme un des principaux risques de ruptureet d’effondrement des ponts. Les expériences en laboratoire sont un élément crucial de l’étude du processus d’affouillement. Pourtant, il n’existe pas d’instrument robuste et standard pour suivrel’évolution de ce phénomène physique dans les études de laboratoire. Les études expérimentalesen canal sur l’affouillement autour d’une pile circulaire dans un sol non cohésif sont nombreuses. Cependant, le lit des canaux alluviaux naturels contient souvent des sédiments cohésifs. Comparativement, il existe peu de recherches sur l’affouillement local autour des piles circulaires fondés dans des lits cohésifs. Dans le cadre de cette recherche doctorale, un scanner laser 3D est utilisé pour suivre l’affouillement local autour d’une pile circulaire. Les résultats obtenus avec cette technique, en accord avec les recherches précédentes, notamment celles effectuées sur un lit de sable, démontrent son efficacité. Elle offre des avantages tels qu’une résolution spatio-temporelle continue, mais aussi de nombreuses limitations. Dans une seconde étape, l’étude a porté sur l’effet du type et de la proportion des fines sur la profondeur et la forme de lafosse d’affouillement et sur la propagation temporelle du processus d’affouillement autour du pile circulaire. Les résultats montrent que l’augmentation de l’argile dans la fraction fine réduitsignificativement l’affouillement. Le mélange avec une gamme d’environ 7.5-10 % de teneur en argile fournit la composition seuil pour un comportement cohérent du sol dans le processus d’affouillement. En outre, la prédiction de la profondeur d’affouillement dans les sols cohésifsdans la conception des fondations de ponts n’est pas encore complètement développée. Dans la pratique, les méthodes d’estimation de la profondeur d’affouillement actuellement utilisées sont celles proposées pour des sols non cohérents. De nombreux chercheurs ont mis au point des méthodes pour optimiser la conception des piles de pont dans le cas d’un sol cohésif. Parmi elles, celle basée sur l’utilisation de l’érodimètre EFA (Erosion Function Apparatus) et appelée SRICOS (Scour Rate In COhesive Soil) a été examinée dans le cadre de ce travail afin de prédire la profondeur d’affouillement maximal dans un lit cohésif.

Mot-clés: Affouillement local, Scanner laser 3D, lit cohésif, SRICOS-EFA